



UNIL | Université de Lausanne

Unicentre
CH-1015 Lausanne
<http://serval.unil.ch>

Year: 2024

Exploiting chemokine receptors as targets for non-invasive imaging in cancer and immunology

Martin Sebastian

Martin Sebastian, 2024, Exploiting chemokine receptors as targets for non-invasive imaging in cancer and immunology

Originally published at : Thesis, University of Lausanne

Posted at the University of Lausanne Open Archive <http://serval.unil.ch>

Document URN : [urn:nbn:ch:serval-BIB_E75F46676FC70](http://nbn:ch:serval-BIB_E75F46676FC70)

Droits d'auteur

L'Université de Lausanne attire expressément l'attention des utilisateurs sur le fait que tous les documents publiés dans l'Archive SERVAL sont protégés par le droit d'auteur, conformément à la loi fédérale sur le droit d'auteur et les droits voisins (LDA). A ce titre, il est indispensable d'obtenir le consentement préalable de l'auteur et/ou de l'éditeur avant toute utilisation d'une oeuvre ou d'une partie d'une oeuvre ne relevant pas d'une utilisation à des fins personnelles au sens de la LDA (art. 19, al. 1 lettre a). A défaut, tout contrevenant s'expose aux sanctions prévues par cette loi. Nous déclinons toute responsabilité en la matière.

Copyright

The University of Lausanne expressly draws the attention of users to the fact that all documents published in the SERVAL Archive are protected by copyright in accordance with federal law on copyright and similar rights (LDA). Accordingly it is indispensable to obtain prior consent from the author and/or publisher before any use of a work or part of a work for purposes other than personal use within the meaning of LDA (art. 19, para. 1 letter a). Failure to do so will expose offenders to the sanctions laid down by this law. We accept no liability in this respect.



UNIL | Université de Lausanne

Faculté de biologie
et de médecine

Département d'oncologie

**Exploiting chemokine receptors as targets for non-invasive
imaging in cancer and immunology**

Thèse de doctorat ès sciences de la vie (PhD)

présentée à la

Faculté de biologie et de médecine
de l'Université de Lausanne

par

Sebastian MARTIN

Master diplômé, l'Université de Freiburg i. Breisgau, Allemagne

Jury

Prof. Isabelle Décosterd, Présidente
Prof. Margret Schottelius, Directrice de thèse
Prof. Niklaus Schäfer, Co-directeur de thèse
Prof. Melpomeni Fani, Experte
Dr. Martin Behe, Expert

Lausanne, 2024



UNIL | Université de Lausanne

Faculté de biologie
et de médecine

Ecole Doctorale

Doctorat ès sciences de la vie

Imprimatur

Vu le rapport présenté par le jury d'examen, composé de

Président·e	Madame	Prof.	Isabelle	Décosterd
Directeur·trice de thèse	Madame	Prof.	Margret	Schottelius
Co-directeur·trice	Monsieur	Prof.	Niklaus	Schäfer
Expert·e·s	Madame	Prof.	Melpomeni	Fani
	Monsieur	Dr	Martin	Behe

le Conseil de Faculté autorise l'impression de la thèse de

Sebastian Martin

Master - Pharmaceutical Science, Albert-Ludwigs-Universität Freiburg, Allemagne

intitulée

Exploiting chemokine receptors as targets for non-invasive imaging in cancer and immunology

Lausanne, le 19 juin 2024

pour le Doyen
de la Faculté de biologie et de médecine

Prof. Isabelle Décosterd

Wings are a constraint that makes
it possible to fly.
— Robert Bringhurst

To my parents...

Acknowledgments

A great time passes fast, and so did the five years of my PhD journey. The tremendous support of my colleagues at the TRS lab made it all possible. I am particularly grateful to my supervisor, Prof. Margret Schottelius, for her good leadership, encouragement and trust. Under her guidance, I was able to develop skills that I would not have acquired otherwise. Being part of the newly inaugurated Agora institute (2018) and establishing a research lab from the scratch made this experience unique. This stimulating atmosphere wouldn't have been the same without the researchers from the 3rd floor. The coffee breaks and fruitful (non)scientific conversations were always a great opportunity to share ideas and opinions. Special thanks to the Pittet lab for their contribution with biological experiments. It was intense and without them, I would not have been able to produce the data for my projects. I also want to thank my former supervisor Mark Bartholomä for his restless support. Together we successfully completed two articles based on my master projects. Mark even facilitated a small clinical trial involving one of my synthesized compounds. Thanks again to him and his lab members for their invaluable contributions.

Lastly, I would like to express my heartfelt gratitude to my family, girlfriend, and friends for their great support and unforgettable moments we shared. Living with in a French-speaking environment allowed my to fulfill my long-held desire of mastering a third language.

Contents

Acknowledgments	i
Contents	iii
Abstract	ix
Résumé	xi
List of Abbreviations	xiii
List of Figures	xvii
List of Tables	xix
1 Introduction	1
1.1 Cancer, therapy and diagnostics	1
1.2 Chemokine Receptors	6
1.2.1 Exploiting CC-chemokine receptors as leukocyte infiltration marker	8
1.2.2 Exploiting CXCR3 as a biomarker of T cell activation	11
1.2.3 Exploiting CXCR4 for imaging and targeted radioligand therapy . . .	15
2 Summary of results and contributions	19
2.1 Article 1: Validation of the C-X-C chemokine receptor 3 (CXCR3) as a potential biomarker for T cell activation	19
2.2 Article 2: Influence of corticosteroid treatment on CXCR4 expression in DLBCL	20

2.3	Article 3: Conjugation of unprotected macrocyclic chelators using solid-phase peptide synthesis	21
2.4	Article 4: Validation of a size exclusion method for concomitant purification and formulation of peptide radiopharmaceuticals	22
3	Materials and methods	25
3.1	Mass spectrometry	25
3.2	Nuclear magnetic resonance spectroscopy	26
3.3	High performance liquid chromatography	26
3.4	General Procedures	29
3.4.1	GP01: Peptide synthesis	29
3.4.2	GP02: Coupling cycles	29
3.4.3	GP03: Peptide cleavage and deprotection	30
3.4.4	GP04: Radiolabeling using ⁶⁸ Ga-labeling	30
3.4.5	GP05: PET/CT scans	30
3.5	Synthesis of CCR-targeted radiotracers	31
3.5.1	Method-M1: Conjugate synthesis using DOTA in solution	31
3.5.2	Method-M2: Conjugate synthesis using DOTA-tris(tert-butyl)ester	31
3.5.3	Method-M3: Conjugate Synthesis using unprotected macrocyclic chelators on 2CTC resin	32
3.5.4	Synthesis of compound RAP-103y	33
3.5.5	Synthesis of compound RAP-103-Hx-N3	34
3.5.6	Synthesis of compound TRAP-103	34
3.5.7	Synthesis of compound NO-Y	35
3.5.8	Synthesis of compound NO-Y-103 and NO-Y-Hx	35
3.6	Iodinating proteins using Iodogen	38
3.7	Iodinating proteins using the Bolton-Hunter reagent	38
3.8	Synthesis of piperazinylpiperidine based radiotracers	39
3.8.1	Synthesis of compound XC3-1a	39

Contents

3.8.2	Synthesis of compound XC3-2a	40
3.8.3	Synthesis of compound XC3-3	40
3.8.4	Synthesis of compound XC3-6	41
3.8.5	Synthesis of compound XC3-1b	41
3.8.6	Synthesis of compound XC3-2b	42
3.8.7	Synthesis of compound XC3-B6	42
3.8.8	Synthesis of compound [^{nat} F] FXC3-5	43
3.8.9	Synthesis of compound [^{nat} F] FXC3-7	43
3.8.10	Synthesis of compound [^{nat} F] FXC3-B7	44
3.8.11	Synthesis of compound [¹⁸ F] FXC3-5	44
3.8.12	¹⁸ F-click labeling to obtain compound [¹⁸ F] FXC3-7 and [¹⁸ F] FXC3-B7	45
3.9	Synthesis of CXCR4-targeted ligands	45
3.10	Serum protein binding	46
3.11	Stability in human serum	47
3.12	Distribution coefficient	47
3.13	<i>In vitro</i> experimentation	47
3.13.1	Cell culture	47
3.13.2	Cell transfection	48
3.13.3	Flow cytometry	48
3.13.4	IC50 determinations on CXCR4-expressing cells	49
3.13.5	Cell-based radioligand binding assay on CCR transfected cells	49
3.13.6	Radioligand binding assay using ⁶⁸ Ga-labeled DOTA-DAPTA	50
3.13.7	Membrane binding assay	50
3.14	Internalization assay	51
3.15	<i>In vitro</i> fluorescence microscopy	51
3.16	<i>In vivo</i> experiments	52
3.16.1	Mouse models	52
3.16.2	Immunofluorescence cryoslides	52
3.16.3	Biodistribution assay	53

3.17 Data analysis	53
4 Investigating CC-chemokine receptors	55
4.1 Characterization of the tumor microenvironment	55
4.2 Synthesis of CCR-targeted peptide radiotracers	56
4.3 <i>In vitro</i> evaluations	59
4.4 <i>In vivo</i> radiotracer evaluation	63
5 Exploiting CXCR3 as target for T cell activation imaging	67
5.1 Synthesis and characterization of small piperazinylpiperidine-based radio- tracers	67
5.1.1 <i>In vitro</i> characterization of small molecular weight radiotracers . . .	69
5.1.2 PET/CT imaging using [¹⁸ F]FXC3-7	70
5.2 Validation of the C-X-C chemokine receptor 3 (CXCR3) as a target for PET imaging of T cell activation	72
6 Exploiting CXCR4 as target for imaging and radioligand therapy	119
6.1 Development of CXCR4-directed ligands	120
6.2 Synthesis of L6-CPCR4 derivatives	120
6.3 IC50 determinations of L6-CPCR4 derivatives	121
6.4 Internalization studies	122
6.5 Influence of corticosteroid treatment on CXCR4 expression in DLBCL . . .	126
7 Methodological developments	135
7.1 Conjugation of macrocyclic chelators using solid-phase peptide synthesis .	136
7.2 Validation of a size exclusion method for concomitant purification and for- mulation of peptide radiopharmaceuticals	144
8 Discussion	163
8.1 Targeting chemokine receptors for molecular imaging and radioligand therapy	163
8.2 The challenges of tumor micro-environment imaging	165

Contents

8.2.1	Challenge 1: Target expression and cell abundance	166
8.2.2	Challenge 2: The pharmacokinetic and -dynamic properties of a ra- diotracer	167
8.2.3	Challenge 3: The molar activity of a radiotracer preparation	168
8.3	Outlook of chemokine receptor targeting	169
	Bibliography	171
	Curriculum vitae	189

Abstract

Novel therapeutic modalities such as immunotherapy and radioligand therapy (RLT) show significant anti-cancer effects, yet a subset of patients demonstrates limited response. In the context of immunotherapy, an immunosuppressive tumor micro-environment (TME) contributes to absent efficacy, while targeted RLT is only beneficial for patients with cancers revealing stable overexpression of the drug target. Within the scope of this thesis, we investigated chemokine receptors, for non-invasive imaging of the TME and for potential RLT. Regarding molecular imaging of the TME, we aimed to exploit chemokine receptors (CCRs e.g., CCR5) as predictive biomarker to quantify the leukocyte infiltration in tumors and as biomarker for T cell activation (CXCR3) to monitor immunotherapy response. The third pillar of this thesis is dedicated to CXCR4-directed imaging and therapy of B cell lymphoma.

In the first project, we aimed to quantify leukocyte infiltration by targeting CC chemokine receptors using radiotracers based on the lead sequence RAP-103 (H₂N-ttnyt-OH). Although developed radiotracers, such as monomeric [⁶⁸Ga]Ga-DOTA-RAP-103 and its trimeric counterpart [⁶⁸Ga]Ga-TRAP-103, lacked specificity in vivo, we established two synthesis methodologies. The first method involved direct conjugation of unprotected chelators like DOTA to peptides immobilized on 2CTC resin, successfully synthesizing radiotracer precursors **DOTA-RAP-103** and **CC-1** to **CC-7**. The second method allowed simultaneous purification and formulation of peptide radiopharmaceuticals in physiologic solution using size exclusion cartridges (G10, 700 kDa cut-off). Results demonstrated consistently high radiochemical purities (>99%) for eluted tracers, even at increased elution volumes, with product recovery higher than 85% for peptides with molecular weights ≥2 kDa.

CXCR3 was explored as a biomarker for T cell activation during immune checkpoint inhibitor (ICI) treatment. Therefore, C57BL/6 mice bearing MC38 tumors were treated with ICIs (α -PD-1/ α -CTLA-4). In-depth TME analysis by flow cytometry and immunofluorescence in MC38 tumors revealed a significant increase of CXCR3⁺ T cells five days post-treatment. Two radiotracer types, an antibody-based tracer ($[^{64}\text{Cu}]\text{Cu-NOTA-}\alpha\text{-CXCR3}$) and small molecular weight radiotracers ($[^{18}\text{F}]\text{FXC3-7}$ and $[^{18}\text{F}]\text{FXC3-B7}$) were synthesized. The antibody-based target validation showed specific radiotracer uptake in lymph nodes and spleen, but not in tumors. However, systemic T cell activation in the spleen correlated with biomarker kinetics found in the flow cytometry analysis.

The third project investigated corticosteroids influence on CXCR4 regulation in diffuse large B-cell lymphoma (DLBCL) cells to understand their potential impact on CXCR4-directed RLT. Treatment with dexamethasone and prednisolone led to cell line-dependent upregulation of CXCR4 expression, notably in B lymphoma cell lines. Dexamethasone treatment in vivo increased the uptake of $[^{68}\text{Ga}]\text{Ga-PentixaTher}$ in OCI-LY1 tumors, suggesting that corticosteroids can be administered in conjunction with CXCR4-targeted RLT. Furthermore, highly potent ligands based on the L6-CPCR4 moiety were synthesized and characterized *in vitro*, thereby expanding the scope of CXCR4-targeted applications towards $[^{18}\text{F}]\text{AIF}$ radiolabeling, fluorescence imaging, and hybrid tracers, enabling both fluorescence and nuclear imaging.

Key words: Chemokine receptor imaging, tumor micro-environment, CCR5, CXCR3, CXCR4.

Résumé

Les nouvelles modalités thérapeutiques telles que l'immunothérapie et la thérapie radio-ligand (RLT) montrent des effets anticancéreux significatifs, mais un sous-ensemble de patients présentent une réponse limitée. Dans le contexte de l'immunothérapie, un micro-environnement tumoral (TME) immunosuppresseur contribue à une efficacité absente, tandis que la RLT ciblée est uniquement bénéfique pour les patients présentant une surexpression stable de la cible du médicament. Dans le cadre de cette thèse, nous avons étudié les récepteurs des chimiokines, pour l'imagerie non invasive du TME et pour la RLT potentielle. En ce qui concerne l'imagerie moléculaire du TME, nous avons cherché à exploiter les récepteurs des chimiokines (CCR, par exemple CCR5) comme biomarqueur prédictif pour quantifier l'infiltration des leucocytes dans les tumeurs et comme biomarqueur de l'activation des lymphocytes T (CXCR3) pour surveiller la réponse à l'immunothérapie. Le troisième volet de cette thèse est consacrée à l'imagerie et à la thérapie dirigée par CXCR4 du lymphome B.

Dans le premier projet, nous avons cherché à quantifier l'infiltration des leucocytes en ciblant les récepteurs des chimiokines CC à l'aide de radiotraceurs basés sur la séquence plomb RAP-103 (H₂N-ttnyt-OH). Bien que les radiotraceurs développés, tels que le monomère [⁶⁸Ga]Ga-DOTA-RAP-103 et son homologue trimérique [⁶⁸Ga]Ga-TRAP-103, manquaient de spécificité in vivo, nous avons établi deux méthodologies de synthèse. La première méthode impliquait la conjugaison directe de chélateurs non protégés comme le DOTA à des peptides immobilisés sur de la résine 2CTC, permettant ainsi de synthétiser avec succès les précurseurs de radiotraceurs DOTA-RAP-103 et CC-1 à CC-7. La deuxième méthode permettait la purification et la formulation simultanée des radiopharmaceutiques peptidiques dans

une solution physiologique en utilisant des cartouches d'exclusion de taille (G10, coupure de 700 kDa). Les résultats ont montrés des puretés radiochimiques élevées et cohérentes (>99%) pour les traceurs éludés, même à des volumes d'élution accrus, avec un taux de récupération du produit supérieur à 85% pour les peptides avec des poids moléculaires ≥ 2 kDa.

CXCR3 a été exploré comme biomarqueur de l'activation des lymphocytes T pendant le traitement par inhibiteur des points de contrôle immunitaires (ICI). Par conséquent, des souris C57BL/6 portant des tumeurs MC38 ont été traitées avec des ICI (α -PD-1/ α -CTLA-4). Une analyse approfondie du TME par cytométrie en flux et immunofluorescence dans les tumeurs MC38 a révélé une augmentation significative des lymphocytes T CXCR3⁺ cinq jours après le traitement. Deux types de radiotraceurs, un traceur à base d'anticorps (⁶⁴Cu]Cu-NOTA- α -CXCR3) et des radiotraceurs de faible poids moléculaire (¹⁸F]FXC3-7 et ¹⁸F]FXC3-B7), ont été synthétisés. La validation de la cible à base d'anticorps a montré une captation spécifique du radiotraceur dans les ganglions lymphatiques et la rate, mais pas dans les tumeurs. Cependant, l'activation systémique des lymphocytes T dans la rate était corrélée avec la cinétique des biomarqueurs trouvés dans l'analyse par cytométrie en flux.

Le troisième projet a étudié l'influence des corticostéroïdes sur la régulation de CXCR4 dans les cellules de lymphome B diffus à grandes cellules (DLBCL) pour comprendre leur impact potentiel sur la RLT dirigée par CXCR4. Le traitement par dexaméthasone et prednisolone a entraîné une surexpression dépendante de la lignée cellulaire de CXCR4, notamment dans les lignées cellulaires de lymphome B. Le traitement par dexaméthasone *in vivo* a augmenté la captation de ⁶⁸Ga]Ga-PentixaTher dans les tumeurs OCI-LY1, suggérant que les corticostéroïdes peuvent être administrés conjointement avec la TRL ciblée par CXCR4. De plus, des ligands hautement puissants basés sur la fraction L6-CPCR4 ont été synthétisés et caractérisés *in vitro*, élargissant ainsi le champ des applications ciblées par CXCR4 vers le marquage radiologique ¹⁸F]AIF, l'imagerie par fluorescence et les traceurs hybrides, permettant à la fois la fluorescence et l'imagerie nucléaire.

Mots clés : Imagerie des récepteurs des chimiokines, micro-environnement tumoral, CCR5, CXCR3, CXCR4.

List of Abbreviations

AA	amino acid
ACN	acetonitrile
APC	antigen presenting cell
avB_{max}	average number of binding sites in a tissue
BAT	brown adipose tissue
B_{max}	number of binding sites per cell
BPDS	bathophenanthroline disulfonate
CAR	chimeric antigen receptor
CCL	CC chemokine ligand
CCR	CC chemokine receptor
CCR2	CC chemokine receptor 2
CCR5	CC chemokine receptor 5
CAF	cancer associated fibroblast
CT	computed tomography
CTLA-4	cytotoxic T-lymphocyte-associated protein 4
CXCL9	C-X-C chemokine ligand 9
CXCL10	C-X-C chemokine ligand 10
CXCL11	C-X-C chemokine ligand 11
CXCR3	C-X-C chemokine receptor 3
CXCR4	C-X-C chemokine receptor 4
DAPTA	D-ala peptide T-amide
DC	dendritic cell

List of Abbreviations

DCM	dichloromethane
DCE	dichlorethane
DEE	diethylether
DC	dendritic cell
dGK	deoxyguanosine kinase
DIPEA	N,N-diisopropylethylamine
DLBCL	diffuse large B cell lymphoma
DMF	N,N-dimethylformamid
DOTA	1,4,7,10-Tetraazacyclododecane-1,4,7,10-tetraacetic acid
EDCI	1-ethyl-3-(3-dimethylaminopropyl)carbodiimide
EPR	enhanced permeability and retention
EtOAc	ethylacetate
FAP	fibroblast activation protein
FDA	food and drug administration
GLUT	glucose transporter
GPCR	G-protein coupled receptor
GZB	granzyme B
HPLC	high performance liquid chromatography
HOBt	hydroxybenzotriazole
IC50	half-maximal inhibitory concentration
ICOS	inducible T cell co-stimulator
IHC	immunohisotchemistry
IFN-γ	interferon gamma
IC50	half-maximal inhibitory concentration
ICI	immune checkpoint inhibitor
IL-2R	interleukin-2 receptor
MA	molar activity
mAb	monoclonal antibody
MDSC	myeloid-derived suppressor cell

List of Abbreviations

MeOH	methanol
MM	multiple myeloma
MRI	magnetic resonance imaging
MS	mass spectrometry
MSI	microsatellite instability
NHS	N-hydroxysuccinimide
NOTA	2,2,2-(1,4,7-triazacyclononane-1,4,7-triyl)triacetic acid
NOTI	1,4,7-tris((1H-imidazol-2-yl)methyl)-1,4,7-triazonane
PE	phycoerythrin
PD-1	programmed cell death protein 1
PD-L1	programmed cell death ligand 1
PET	positron emission tomography
PFP	pentafluorophenol
PSMA	prostate-specific membrane antigen
R_f	retention factor
p.i.	post-injection
RLT	radioligand therapy
R_t	retention time
RT	room temperature
SPE	solid phase extraction
SPECT	single photon emission computed tomography
SPPS	solid phase peptide synthesis
SulfoCy5	sulfo-cyanine5
SUV	standardized uptake value
TACN	1,4,7-triazacyclononane
TAM	tumor associated macrophage
TAN	tumor associated neutrophil
TBTU	2-(1H-benzotriazole-1-yl)-1,1,3,3-tetramethylammonium tetrafluoroborate
TEA	triethylamine

List of Abbreviations

TFA	trifluoroacetic acid
THF	tetrahydrofuran
TIL	tumor infiltrating lymphocyte
TIPS	triisopropyl silane
TLC	thin layer chromatography
TMB	tumour mutational burden
TME	tumor micro-environment
Treg	regulatory T cell
WHO	world health organization

List of Figures

1.1	The tumor immune phenotypes	3
1.2	Predictive vs responsive biomarkers	5
1.3	Scheme of CXCR3 dependent T cell migration and activation during immune checkpoint blockade.	14
1.4	The PET imaging agent [⁶⁸ Ga]Ga-PentixaFor and the therapeutic counterparts [¹⁷⁷ Lu]Lu/[⁹⁰ Y]Y-PentixaTher	16
4.1	Immunofluorescence evaluation of MC38 tumors	56
4.2	IC50 evaluations on CCR5 membrane preparations	61
4.3	Inhibitor screening on CCR5 membranes	62
4.4	<i>In vivo</i> evaluation of CC-chemokine receptor specific radiotracers	66
5.1	CXCR3 radiotracer synthesis using click chemistry	68
5.2	Maximum intensity projections of radiotracer [¹⁸ F]FXC3-7	71
6.1	Synthesized CXCR4 inhibitors based on the L6-CPCR4 moiety	121
6.2	Internalization studies of the hybrid compound using immunofluorescence	124
6.3	Internalization studies of the radiolabeled hybrid compound	125
8.1	Challenges of tumor micro-environment imaging using PET radiotracers	166

List of Tables

1.1	Overview of the three relevant chemokine receptors	8
1.2	Investigated biomarkers for T cell activation	13
4.1	Sequences of all DOTA-conjugated radiotracer precursor	57
4.2	Overview of radiotracers tested <i>in vitro</i> characterization	60
5.1	Preliminary evaluation of [¹⁸ F]FXC3-7 and [¹⁸ F]FXC3-B7	69
6.1	Affinities of CXCR4-targeted peptides on human and murine CXCR4	122

1 Introduction

1.1 Cancer, therapy and diagnostics

Cancer stands as a predominant epidemiological menace, globally claiming millions of lives every year [1, 2, 3]. While the world health organization (WHO) anticipates increased cancer incidence, successful cancer treatment remains challenging. Immunotherapy has emerged as one of the most promising treatment strategies, comprising both cell-based therapy such as chimeric antigen receptor (CAR) T cells [4] and immune checkpoint inhibitor (ICI) therapy [5]. These therapies, exemplified by ipilimumab (target: cytotoxic T-lymphocyte-associated protein 4 (CTLA-4), approved in 2011) and tisagenlecleucel as the first CAR T cell therapy (target: CD19, approved in 2017), aim to mount an efficient anti-tumor immunity via activated T cells in the tumor micro-environment (TME). Notably, ICIs function by blocking immune checkpoint proteins like CTLA-4 or programmed cell death protein 1 (PD-1), thus counteracting immunosuppressive signaling by the tumor cells and immunosuppressive components of the TME and reinvigorating tumor infiltrating lymphocytes (TILs) to eliminate cancer cells. In contrast, exploiting cell-based therapies involve the injection of leukocytes which are typically primed against tumor (neo)antigens and ultimately infiltrate into the TME and exert their cytotoxic activity. These treatments have shown remarkable efficacy in the last decade, significantly increasing survival rates of highly aggressive cancers such as melanoma

or lung cancer [6, 7]. However, the recent success of immunotherapeutic approaches is not universal. For certain cancer types response rates are low or absent [8, 9, 10]. Thus, the main challenges associated with immunotherapies are, as in all cancer therapies, limited tumor response rates and relapse. Both are predominantly related to an immunosuppressive TME. The immunosuppressive TME is usually characterized by hypoxic conditions, the presence of tumor promoting leukocytes (myeloid-derived suppressor cells (MDSCs), tumor associated macrophages (TAMs), tumor associated neutrophils (TANs)) as well as by physical barriers such as a stiff extracellular matrix and the prevalence of cancer associated fibroblasts (CAFs) which limit T cell infiltration and create dysfunctional T cells [11]. Depending on the composition of the TME, tumors are commonly classified as immune infiltrated, immune excluded, or immune desert phenotype, which is based on the location and spatial distribution of immune cells. In all cases, cytokines play a role in establishing an immunosuppressive TME which promotes immune evasion, cancer progression, and metastasis (see Figure 1.1) [12, 13]. Notably, the absence of CD8⁺ effector T cells correlates with unfavorable response to ICI treatment, particularly in the immune desert phenotype [11, 13]. Again, depending on the composition and dynamic changes within the TME, immunotherapies are highly potent but require nuanced clinical decision-making prior to and during the treatment. Diagnostic biomarkers allowing improved selection of patients for a given (combination) treatment or monitoring the response early after drug administration are thus of great importance.

Typically, cancer localization and staging are conducted through non-invasive imaging techniques such as magnetic resonance imaging (MRI) or positron emission tomography (PET)/computed tomography (CT). PET harnesses molecular targets such as glucose transporter (GLUT) (2-[¹⁸F]FDG), C-X-C chemokine receptor 4 (CXCR4) ([⁶⁸Ga]Ga-PentixaFor) or prostate-specific membrane antigen (PSMA) ([⁶⁸Ga]Ga-PSMA-11) for cancer imaging using specific radiotracers (see Figure 1.2). Following detection of cancer in a patient using these techniques, assessments of the TME prior to initiating immunotherapy are crucial for predicting treatment response. As presented in Figure 1.2, several predictive biomarkers have been investigated, primarily using biopsy samples. These samples were analyzed *ex vivo*

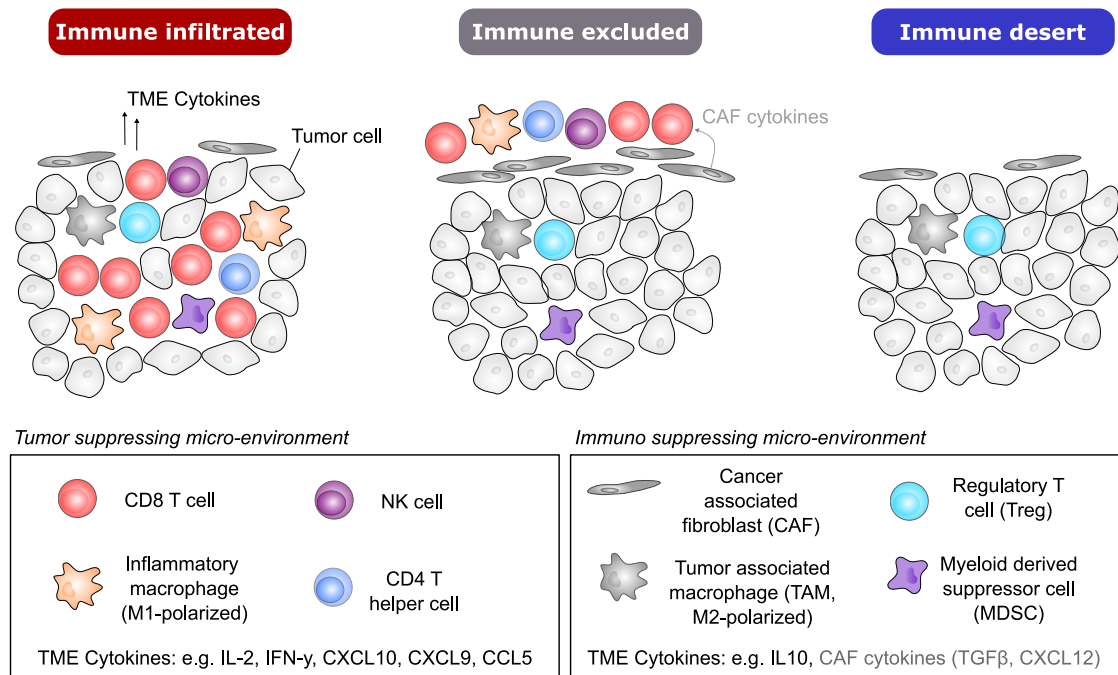


Figure 1.1: The tumor immune phenotypes [12, 13, 14]. From immune infiltrated (immune cells infiltrate, but their effects are inhibited), to immune excluded (immune cells are present but do not efficiently infiltrate), to desert (immune cells are absent from the tumor and its periphery).

to provide the tumour mutational burden (TMB) [15], microsatellite instability (MSI) [16], leukocyte infiltration (e.g., CD8⁺ T cells, regulatory T cells (Tregs), M1/M2 macrophages [17, 18]), programmed cell death ligand 1 (PD-L1) expression [19], or fibroblast activation protein (FAP) (expressed by CAFs) [20]. Although almost all predictive biomarkers have shown significance, their predictive value might be limited as the reported studies were primarily performed on single tumor biopsy samples per patient. In fact, previous studies exemplify that inter- as well as intra-tumoral heterogeneity is widely observed in tumors [21, 22, 23, 19]. For example, biopsies from the same patient with no PD-L1 expression in the primary tumor lesion showed substantial expression of the predictive biomarker in nodal metastasis, allowing for selection of eligible patients for anti-PD-L1 therapy [19]. Thus, extensive tumor sampling is advised to reduce the chance of potentially misleading analysis based on a single tumor biopsy. Since this strategy, however, is neither ethically nor practically implementable, molecular imaging represents a powerful alternative to invasive techniques.

Molecular imaging using PET radiotracers offers several advantages over immunohistochemistry (IHC) specimens. In contrast to IHC, PET imaging can provide information of the entire tumor heterogeneity in a patient non-invasively and in real-time. Additionally, PET allows for the quantification of radiotracer uptake through standardized metrics such as standardized uptake value (SUV), facilitating objective assessment and comparison of data across different imaging studies, while standardization of IHC from biopsy sampling to analysis is challenging [24]. Given these advantages, molecular targets such as PD-1, PD-L1, or CD3 were investigated towards predictive characterization of the TME using PET radiotracers in order to select the best therapy prior to treatment [25].

During immunotherapy treatment, it is highly important to verify the efficacy and to adapt the treatment if necessary. Again, this requires repetitive TME assessments where non-invasive imaging can be readily repeated multiple times to verify response to therapy. In this context, MRI is used based on iRECIST protocols to assess the response to immunotherapy [26]. However, with anatomical imaging, it takes up to three months to delineate real tumor progression or hyperprogression from pseudo-progression, which is characterized by an increased tumor volume through immune cell infiltration and proliferation [27]. Therefore, molecular imaging targeting biomarkers of T cell activation is highly promising for monitoring early immunotherapy response (see Figure 1.2). T cell activation biomarkers such as granzyme B (GZB) [28], interferon gamma (IFN- γ) [29], and CD69 [30] have shown encouraging preclinical results for early therapy-induced response monitoring using PET radiotracers. Thus, exploring biomarkers (predictive, as well as responsive) for molecular imaging to characterize the TME *in vivo* using molecular imaging is of high (pre-)clinical interest to understand, improve and ensure the efficacy of novel immunotherapy treatment modalities.

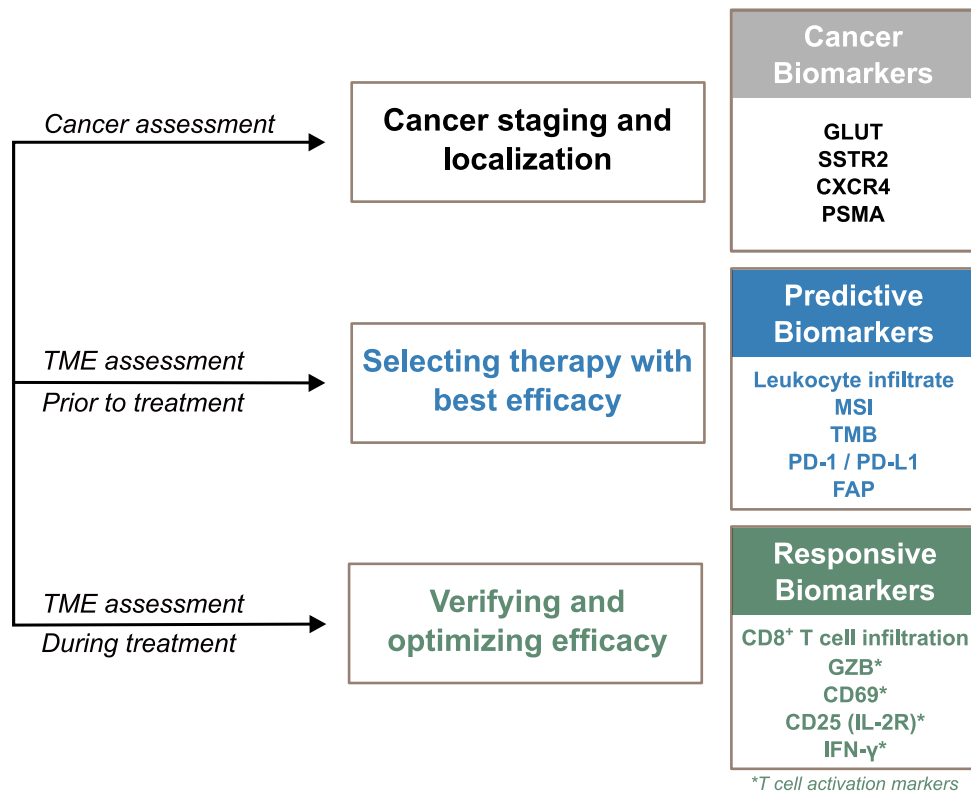


Figure 1.2: Cancer imaging is typically performed with magnetic resonance imaging (MRI) or positron emission tomography (PET). PET uses radiotracers for example targeting the glucose transporter (GLUT, radiotracer: 2- ^{18}F FDG), somatostatin receptor 2 (SSTR2, radiotracer: ^{68}Ga DOTA-TOC), C-X-C chemokine receptor 4 (CXCR4, radiotracer: ^{68}Ga Ga-PentixaFor), or prostate-specific membrane antigen (PSMA, radiotracer: ^{68}Ga Ga-PSMA-11). Predictive biomarkers are applied to select the best matching (combination) therapy regimen prior to treatment start: leukocyte infiltration (e.g., CD8⁺ T cells infiltration); MSI, microsatellite instability; TMB, tumor mutational burden; PD-1, programmed cell death protein-1; PD-L1, programmed cell death ligand-1; FAP, fibroblast activation protein. In contrast, responsive biomarkers can indicate/confirm response to immunotherapy: CD8⁺ T cell infiltration, GZB, Granzyme B; CD69, cluster of differentiation 69; IL-2R, interleukin-2 receptor; IFN- γ , interferon- γ .

1.2 Chemokine Receptors

Chemokine receptors play a crucial role in physiological as well as in pathological processes. Their ligands, called chemokines, are small chemotactic cytokines with a size ranging between 8-12 kDa and are classified by their structure [31]. According to the number and location of conserved N-terminal cysteines, ligands are classified into four subgroups (XC, CC, CXC, CX₃C). To date, approximately 20 receptors and 50 ligands are known, with one native chemokine oftentimes targeting multiple chemokine receptors [31, 32]. Chemokine receptors are a family of seven-transmembrane spanning G-protein coupled receptors (GPCRs) which are primarily expressed on migratory cells and, consequently, lead to chemotaxis of these cells along a chemokine gradient towards sites of high chemokine concentration. In analogy to their ligands, typical chemokine receptors are divided into XC-, CC-, CXC- and CX₃C chemokine receptors [31, 33].

The seven-transmembrane receptors have dual roles in homeostasis and inflammation. A prime example for a highly relevant homeostatic chemokine receptor is the CXCR4 which plays an important role in blood cell homing in the bone marrow and serves essential functions during organogenesis [33]. As opposed to other chemokine receptors, CXCR4 has one native ligand called CXCL12 (or SDF-1). A well-investigated representative is CC chemokine receptor 5 (CCR5), which is mainly expressed on immune cells, such as antigen presenting cells (APCs), T cells (effector and memory phenotype), or NK cells. This receptor has inflammatory functions and binds several chemokine ligands such as CCL3, CCL4 and CCL5 [31]. The CCR5-dependent recruitment of T cells towards mature dendritic cells (DCs) allows the priming of naïve CD8⁺ T cells and the receptor is also involved in the migration of APCs towards their site of inflammation [34, 35]. Interestingly, despite their fundamentally different physiological roles and functions, both CXCR4 and CCR5, appear to be the two major co-receptors for the HIV entry into CD4⁺ leukocytes [31]. Over the last decades, both receptors were therefore investigated as druggable HIV target. For both receptors, food and drug administration (FDA) approved pharmaceuticals are on the

market, both with different applications. Maraviroc, a CCR5 inhibitor, is approved for the treatment of patients infected with CCR5-dependent (R5-tropic) HI viruses and plerixafor, an antagonist of CXCR4, is used for stem cell mobilization. Due to its strong overexpression on hematological malignancies, CXCR4 has emerged as a highly relevant molecular target for non-invasive imaging and radioligand therapy (RLT) during the last decades. In addition, dedicated CXCR4-targeted radiopharmaceuticals, namely [^{68}Ga]Ga-PentixaFor [36], [$^{99\text{m}}\text{Tc}$]Tc-PentixaTec [37], and [^{177}Lu]Lu-PentixaTher [38], have found their way into clinical practice. Besides the undisputed value of CXCR4-targeted imaging and therapy for oncological applications, CXCR4-targeted PET as well as single photon emission computed tomography (SPECT) has gained considerable attention for the sensitive detection and quantification of immune cell infiltration in inflammatory conditions, such as atherosclerosis, stroke, myocardial infarction and myocarditis, amongst others [39]. At a first glance, this also suggests a potential role of these imaging modalities in TME imaging, since recruitment of immune cells to the TME is strongly dominated by the CXCL12/CXCR4 axis. However, many (solid) cancers also display strong CXCR4 expression on tumor cells, prohibiting selective imaging of tumor-infiltrating immune cells via CXCR4 targeting.

This, however, is not a problem regarding immune-cell specific chemokine receptors, such as CCR5 or the C-X-C chemokine receptor 3 (CXCR3). Both receptors are involved in the inflammatory chemokine axis and play an important role for the infiltration and function of TILs and in creating a tumor-suppressive environment [40, 41, 42]. Importantly, CXCR3, expressed on activated T cells [43], is necessary for functional T cells in the TME, while impaired CXCR3 signaling has been shown to limit anti-PD-1 therapy [41, 44]. In contrast, circulating CCR5⁺CCR2⁺ monocytes are recruited to the TME where these cells commonly differentiate to TAMs (M2-polarized) promoting tumor progression [45]. Previous studies have reported that blocking of the CCR5/CCR2 axis leads to a reduced number of TAMs, inciting better therapy responses, [45], and CCR5-antagonism with maraviroc induces M1-like polarization of tumor residing macrophages mediating tumor-suppression [46]. Another tumor promoting signaling axis/pathway is elicited by CAF secreted CXCL12, restraining leukocyte infiltration

Table 1.1: Overview of the three relevant chemokine receptors, their expression in leukocytes and role in cancer. Abbreviations: CD#, cluster of differentiation; CCR, CC chemokine receptor; CXCR, C-X-C chemokine receptor; DC, dendritic cell; Mo, monocyte; M Φ , macrophage; NK, natural killer cell. Data taken from [31].

Receptor	CD#	Relevant leukocyte subpopulations	Native ligands	Major role in cancer
CCR5	CD195	M Φ , Mo, DC, NK and T cells	CCL3, CCL4, CCL5	Macrophage and T cell infiltration
CXCR3	CD183	NK and T cells	CXCL9, CXCL10, CXCL11	NK and T cell infiltration
CXCR4	CD184	most leukocyte subpopulations	CXCL12	Metastasis

[14]. The inhibition of CXCR4 using antagonist Peptide-R54 increases T cell infiltration in tumors, potentiating the response to ICI treatment [47]. Collectively, these investigations highlight the critical role of chemokine receptors in cancer biology and their emerging role as druggable targets. A thorough understanding can be achieved by comprehensively analyzing chemokine receptors both on cancer cells and in the TME. Nuclear imaging emerges as an indispensable tool for elucidating chemokine receptors *in vivo*. Thus, this thesis focuses on evaluating receptors from the CC and CXC families as potential targets for non-invasive imaging of the immune cell populations in the TME (CCR5, CXCR3), but also explores new routes towards optimized CXCR4-targeted radiopharmaceuticals and a better understanding of CXCR4 regulation in cancer. An overview of the investigated receptors is summarized in Table 1.1.

1.2.1 Exploiting CC-chemokine receptors as leukocyte infiltration marker

The chemokine network regulates immune cell trafficking, development, and progression. CC chemokine receptors (CCRs) and their ligands play important roles in shaping the TME. Some of the CC chemokine ligands (CCLs) bind to CCR5 (e.g., CCL4, CCL5) or CC chemokine

receptor 2 (CCR2) (e.g., CCL2, CCL5) directing T cell migration in the tumor to deliver an effective anti-tumor immune response [48, 40]. In contrast, CCL1 signaling contributes to maintain a tumor-suppression activating CCR8 on Tregs [48]. Adding to the complexity, most tumors shape their own chemokine network which contributes to a pro-tumorigenic microenvironment by recruiting TAMs, MDSCs, TANs, and Tregs [48]. Thus, the same chemokine axis contributes to anti- and -protumorigenic immune responses.

Despite the reported ambiguity, CCRs share a restricted expression on almost all immune cell subtypes [31]. These characteristics can be exploited for pan-immune cell imaging, presenting a robust strategy to target and quantify a wide array of immune cell types for the monitoring of the overall immune cell infiltration allowing the delineation of tissue-specific leukocyte infiltration. The utilization of a viral CCL-based radiotracer, namely [⁶⁴Cu]Cu-DOTA-vMIP-II, has demonstrated high sensitivity as a PET imaging probe in detecting immune cell recruitment in a mouse model of atherosclerosis, targeting six different CC-chemokine receptors [49]. For the quantification of T cell populations, CD3 represents a more specific biomarker. Studies have demonstrated the utility of ⁸⁹Zr-DFO-anti-CD3 for the quantification of global T cell infiltration [50], with Larimer et al. [51] establishing the prognostic value of global CD3⁺ T cell infiltrate in predicting responses to ICI therapy. However, CD3-targeted imaging intrinsically relies on the use of antibody-based tracers, with all associated disadvantages concerning pharmacokinetics and dosimetry. In contrast, radiopharmaceutical development for CCR targeting is facilitated by the availability of multiple small, high affinity lead structures with inherently much more favorable pharmacokinetic profiles.

Extensive HIV-related studies [52, 53] have identified CCR5 as the best characterized representative of the CC-receptor family. The GPCR comprises two transmembrane pockets (a minor transmembrane site 1 and a major transmembrane site 2) where the small molecular weight pharmaceutical maraviroc binds and blocks the interaction with the viral chemokine analogue gp120 [54]. Notably, before maraviroc was discovered as an entry inhibitor of R5-tropic HI viruses [55], the octapeptide D-ala peptide T-amide (DAPTA) was established as a potent anti-retroviral agent in the early 90's [56]. Based on the DAPTA sequence, a

series of all-D pentapeptides, all of which showing surprisingly high activities on CCR5, has been developed and patented as potent neuroinflammation antagonists [57]. Out of these, the lead sequence, termed RAP-103 (H₂N-ttnyt-OH) shows excellent inhibitory activity towards CCR5 (0.18 pM [58]), CCR2 (4.2 pM [58]) as well as CCR8 (7.7 fM [59]). The resulting inhibition of microglial cell signaling of orally applied CCR-antagonist RAP-103 attenuated neuropathic pain in rodents [58]. Overall, this data suggests that highly potent binding motifs are available for developing high-affinity radiotracers for leukocyte targeting. That this is a viable approach has been recently demonstrated by the evaluation of the DAPTA-based sequence to synthesize the radiotracer [¹¹¹In]In-DOTA-DAPTA that allowed sensitive and specific detection of atherosclerotic plaque-related inflammation in mice [60]. Another study of inflammation imaging, targeting CCR2, demonstrated that the peptide radiotracer [⁶⁴Cu]Cu/[⁶⁸Ga]Ga-DOTA-ECL1i is capable of imaging heart- and lung inflammation [61, 62]. Both, these CCR5 and CCR2, targeting approaches exploited small peptide radiotracers to effectively monitor inflammation and correlate it with leukocyte density. Again, the pentapeptide RAP-103 and its analogous peptides are highly appropriate structural scaffolds to target CCRs as they show high affinities to multiple chemokine receptors such as CCR5, CCR2, and CCR8, thereby targeting a large scope of immune cell subsets such as macrophages, T cells or NK cells. This potentially allows a discrimination between a leukocyte rich (immune infiltrated phenotype) and poorly infiltrated (immune desert phenotype) TME. To date, no radiotracers utilizing these sequences are reported, but based on the available data, they might have potential for monitoring immune cell infiltration in the context of immuno-oncology and immunology. Consequently, the primary objective of this project was to develop RAP-103-based radiotracers for non-invasive imaging of the leukocyte infiltrate in cancer.

To this aim, we synthesized a small compound library using the lead compound Rap-103 and further reported pentapeptide sequences [57] as binding motifs. The binding motifs were conjugated with aminohexanoic acid and 1,4,7,10-Tetraazacyclododecane-1,4,7,10-tetraacetic acid (DOTA). Since the trimerization of small targeted peptides has been shown to

enhance apparent binding affinity and tracer uptake in the target tissue [63], this strategy was also implemented in the CCR targeting strategy. Two different trimers (**NO-Y-103** and **TRAP-103**) were synthesized and evaluated in comparison to the respective monomeric tracers. The trimers were radiolabeled either with ^{68}Ga or ^{64}Cu . Subsequently, binding affinities on CCR5 and possible imaging properties were tested *in vitro*, and ^{68}Ga -labeled **DOTA-DAPTA**, **DOTA-RAP-103** and **TRAP-103** were evaluated *in vivo*. The results of these evaluations are summarized in chapter 4. In addition, two novel methodologies were developed: (1) a resin-based synthesis of peptide radiotracer precursors using unprotected macrocyclic chelator, and (2) a size exclusion purification method based on commercially available G10 cartridges to directly obtain pure peptide radiotracers in a physiological solution (see chapter 7).

1.2.2 Exploiting CXCR3 as a biomarker of T cell activation

The efficacy of immunotherapies relies on the presence and activity of CD8⁺ T cells residing in the TME [64, 65]. As anti-cancer effects are primarily triggered by the activation of these T cells in the tumor milieu, T cell activation serves as a crucial parameter in assessing the response to immunotherapy. Different T cell activation markers have been targeted for non-invasive PET imaging so far, and various studies revealed a robust correlation between T cell activation and therapy-related responses. These biomarkers were OX40 [66], CD69 [30], inducible T cell co-stimulator (ICOS) [67], IFN- γ [29], interleukin-2 receptor (IL-2R) [68], GZB [69] as well as T cell metabolism [70]. Table 1.2 summarizes the preclinical PET imaging studies performed with full-sized antibodies (OX40, CD69, ICOS, IFN- γ), proteins (IL-2R), peptides (GZB) or small molecules (metabolism, deoxyguanosine kinase (dGK)). All of these studies demonstrated that early response to therapy is detectable using the proposed by the established radiotracers only few days post-treatment. Notably, T cell activation markers follow distinct kinetics. For example, OX40, dGK, and ICOS demonstrated early T cell activation only two days post-therapy initiation, with the signals of OX40 and dGK returning to baseline level despite continuous immunotherapy [67, 66, 69]. In contrast, other biomarkers (GZB, CD69, IFN- γ , IL-2R) were evaluated at least six days after therapy

initiation showing all T cell activation, with GZB and CD69 facilitating the differentiation between treatment responders vs treatment non-responders in the context of ICI therapy [69, 30, 29, 68]. This data emphasizes the critical role of T cell activation in determining and predicting treatment outcomes and suggests the potential utility of these imaging modalities in clinical decision making.

Another relevant biomarker associated with T cell activation is CXCR3 [71, 42, 41]. CXCR3 was first reported for its important role in T cell recruitment and its exclusive expression on activated T cells [72]. Through its IFN- γ inducible ligands C-X-C chemokine ligand 9 (CXCL9), CXCL10, and CXCL11 T cells and NK cells are directed to sites of inflammation [73]. Multiple studies have demonstrated that the efficacy of cell-based and checkpoint inhibitor-based immunotherapies depends on CXCR3-related T cell recruitment and activation [41, 44, 74, 75]. Furthermore, CXCR3 is indispensable for the response to ICI treatment involving T cell activation, invasion and expansion in the TME. For example, Chow et al. [41] demonstrated that CXCR3-expressing CD8⁺ T cells are required in the TME for effective anti-tumor activity, while a CXCR3-knockout in mice dramatically reduced the anti-tumor response to anti-PD-1 therapy [41]. Iwai et al. [44] showed that blocking of CXCR3 signaling restrains T cell infiltration into the tumor tissue [44]. Based on these investigations, two central functions can be attributed to the CXCR3 axis during ICI therapy: (a) T cell recruitment into the TME [44, 74, 76] and (b) T cell activation through APCs [41], as shown in Figure 1.3. Therefore, CXCR3 represents an interesting molecular target for nuclear imaging of T cell activation and infiltration in response to immunotherapy. Although this receptor has never been investigated in the context of nuclear imaging during immunotherapy, two reports on CXCR3-targeted inflammation imaging have been published. Both studies use inflammation models (allograft rejection and atherosclerosis) for tracer evaluation and both radiopharmaceuticals investigated, [¹²⁵I]-CXCL10 [77] and an ¹⁸F-labeled small molecule CXCR3 inhibitor [78] accumulated specifically in inflammatory regions infiltrated with CXCR3-expressing T cells. Overall, respective PET signal was found to correlate well with CXCR3 related T cell infil-

Table 1.2: Overview of recently investigated biomarkers for T cell activation in nuclear medicine. Abbreviations: mAb, monoclonal antibody; ICOS, inducible T cell co-stimulator; IFN- γ , interferon-gamma; IL-2R, interleukin-2 receptor; GZB, granzyme B; dGK, deoxyguanosine kinase.

Biomarker	Radiotracer	Radiotracer class	Reference
OX40	[⁶⁴ Cu]Cu-DOTA-AbOX40	mAb	[66]
CD69	[⁸⁹ Zr]Zr-DFO-H1.2F3	mAb	[30]
ICOS	[⁸⁹ Zr]Zr-DFO-ICOS	mAb	[67]
IFN- γ	[⁸⁹ Zr]Zr-anti-IFN γ	mAb	[29]
IL-2R	[¹⁸ F]FB-IL-2	protein	[68]
GZB	[¹⁸ F]AIF-mNOTA-GZP	peptide	[69]
dGK	[¹⁸ F]F-AraG	small molecule	[70]

tration. Based on these encouraging findings, we designed a proof-of-concept to validate CXCR3 as a potential T cell activation marker during ICI therapy.

Monoclonal antibodies are characterized by intrinsic high binding affinities, which makes them an ideal vector for preclinical target evaluations in nuclear medicine. Therefore, we exploited an anti-mouse CXCR3 monoclonal antibody (mAb) (α -CXCR3) as a starting proof-of-concept vector for the validation of CXCR3. The mAb was conjugated with the chelator 2,2,2-(1,4,7-triazacyclononane-1,4,7-triyl)triacetic acid (NOTA) by a site specific conjugation method [79] and subsequently radiolabeled with the radioisotope ⁶⁴Cu. The affinity and stability of the resulting radiotracer [⁶⁴Cu]Cu-NOTA- α -CXCR3 was confirmed by *in vitro* assays. To assess therapy-related CXCR3 upregulation within the TME in comparison to baseline expression a MC38 syngeneic colon carcinoma model was used. MC38 tumors are known to show a strong response to ICI therapy, based on a highly immune-infiltrated TME [80, 81]. During this study, ICI therapy (anti-PD-1/anti-CTLA-4) was applied, and the treatment-related changes in CXCR3 expression level were investigated in-depth by flow cytometry as well as by immunohistochemistry and immunofluorescence of tissue specimens. Ultimately, use CXCR3 targeting efficiency of the radiotracer [⁶⁴Cu]Cu-NOTA-

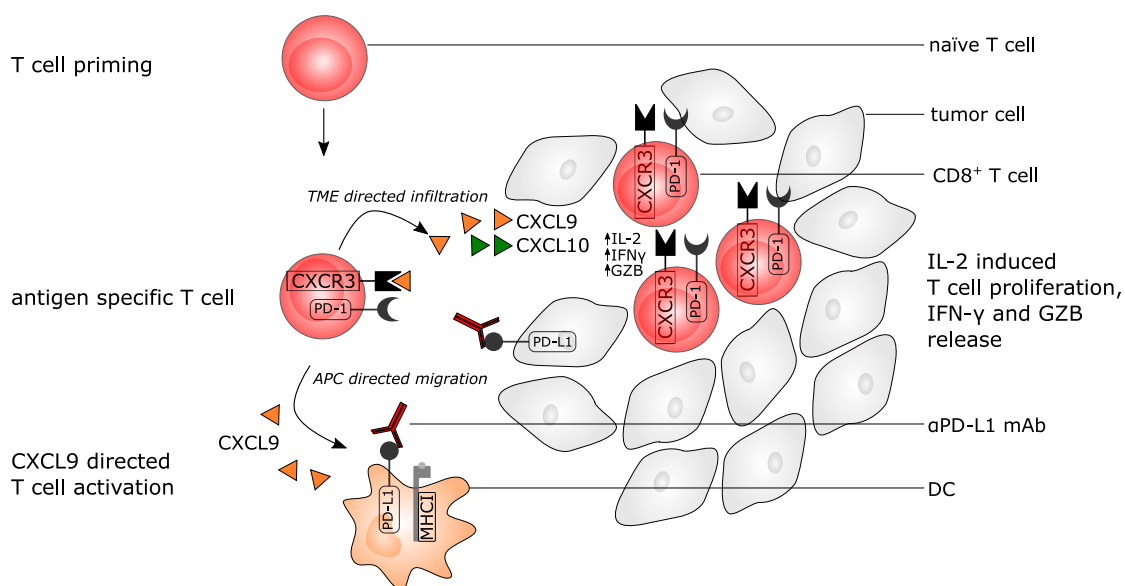


Figure 1.3: Proposed function of CXCR3 during immune checkpoint inhibitor therapy according to Iwai et al. [44] and Chow et al. [41]. CXCR3 driven chemotaxis of activated T cells towards dendritic cells and a directed migration for the tumor-specific infiltration during immune checkpoint blockade, ultimately leading to a higher CXCR3⁺ T cell density in the tumor micro-environment. Abbreviations: CTL, cytotoxic T lymphocyte; CXCR3, C-X-C chemokine receptor 3; PD-1, programmed cell death protein-1; PD-L1, programmed cell death ligand-1; CXCL9, C-X-C chemokine ligand 9; CXCL10, C-X-C chemokine ligand 10; IL-2, interleukin-2; IFN- γ interferon-gamma; GZB, Granzyme B; mAb, monoclonal antibody; DC, dendritic cell; MHC I, major-histocompatibility complex I.

anti- α -CXCR3 was investigated *in vivo*, both via PET imaging and biodistribution studies using different molar activities, antibody doses, and time points. These results have been summarized in a publication (see manuscript section 5.2, which has been submitted to npj Imaging). Additionally, to cross validate the *in vivo* results obtained with [⁶⁴Cu]Cu-NOTA-**anti- α -CXCR3**, small molecular weight ¹⁸F-labeled radiotracers ([¹⁸F]FXC3-7 and [¹⁸F]FXC3-B7) based on a piperazinyl-piperidine binding motif [82] were synthesized. Additionally, the small molecular weight radiotracer [¹⁸F]FXC3-7 was evaluated *in vivo* using PET imaging. This data is presented in section section 5.1.

1.2.3 Exploiting CXCR4 for imaging and targeted radioligand therapy

CXCR4 is a key chemokine receptor which plays a role in stem cell homing, hematopoiesis, and immune cell trafficking [31]. Its ligand, CXCL12 (also known as SDF-1), is highly expressed in various tissues and organs, including the bone marrow, lymph nodes, spleen, liver, and sites of tissue injury [33]. Moreover, CXCR4-mediated signaling via CXCL12 can modulate immune cell function and distribution within the TME, leading to immunosuppression and tumor immune evasion [83]. The finding that CAFs create an immunosuppressive TME is based on CXCL12 secretion by CAFs [84]. CXCL12-mediated activation of CXCR4 inhibits the chemotactic functions of immune cells, thereby compromising tumor infiltration of multiple immune cells, rendering immunotherapies less efficient [85, 83]. Conversely, many tumors highly express CXCR4 on the tumor cell surface, which is strongly associated with promoting tumor growth, metastasis, and resistance to therapy [86]. CXCR4 facilitates tumor cell migration, invasion, and angiogenesis, contributing to the formation of a supportive niche for tumor progression in CXCL12 rich tissues such as lung, liver, brain, and bone [86]. CXCR4 expression is particularly high in hematological malignancies such as multiple myeloma or B cell lymphoma, correlating with advanced disease stage and poor prognosis [87, 88, 89]. Consequently, tumoral upregulation of CXCR4 is linked to worse prognosis and both the CXCR4 receptor expressed on tumor cells as well as its ligand CXCL12 secreted in the TME are considered tumor promoting mediators.

Given the reported high expression of CXCR4 in various tumors, this chemokine receptor is a relevant drug target for anti-cancer interventions [90, 47, 91] and imaging [92, 36]. Particularly, in hematologic malignancies, characterized by substantially increased CXCR4 expression, cancer diagnosis and staging via CXCR4-targeted PET using [^{68}Ga]Ga-PentixaFor (see Figure 1.4) [36] plays an increasingly important role. Furthermore, the availability of the therapeutic companion in the context of a theranostic concept, namely [^{177}Lu]Lu/[^{90}Y]Y-PentixaTher, has opened up new perspectives for CXCR4-directed RLT [91].

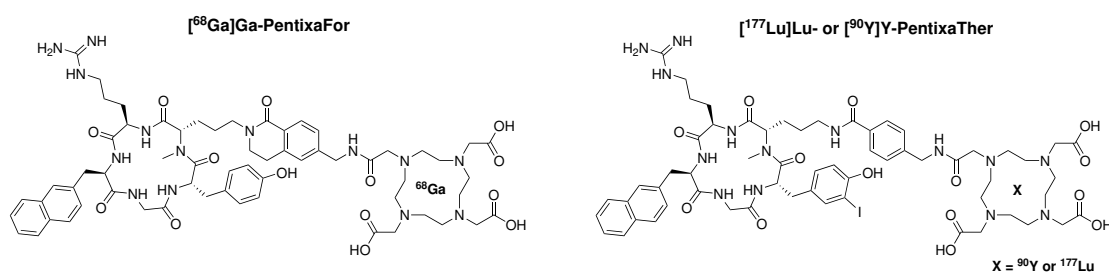


Figure 1.4: Structures of the PET imaging agent [^{68}Ga]Ga-PentixaFor and the radiotracers [^{177}Lu]Lu/[^{90}Y]Y-PentixaTher used as theranostic analogue for CXCR4-directed radioligand therapy (RLT) [91].

In small cohorts of heavily pretreated patients with multiple myeloma, T-cell lymphoma, acute myeloblastic leukemia and diffuse large B-cell lymphoma (DLBCL) encouraging responses to [^{177}Lu]Lu/[^{90}Y]Y-PentixaTher were observed [91, 38], leading to the initiation of a prospective phase I/II study (COLPRIT trial; Eudra-CT 2015-001817-28). Since the majority of these patients suffer from advanced stages of their disease, [^{177}Lu]Lu/[^{90}Y]Y-PentixaTher RLT was used as last-line therapy in the reported patient studies. To prevent further tumor progression at this stage, concomitant or bridging chemotherapy between the diagnostic imaging and RLT is required. These therapeutic regimens typically consist of multiple chemotherapeutic drugs alongside with glucocorticoid treatment to manage side effects of anti-cancer therapies. However, a recent clinical trial involving three multiple myeloma (MM) patients revealed a significant downregulation of CXCR4 expression by bridging chemotherapy, potentially compromising the efficacy of CXCR4-targeted radiopharmaceuticals [93]. The dynamic (up and down) regulation of CXCR4 expression in response to chemotherapy agents or glucocorticoid treatment has been observed previously *in vitro* [94, 95].

In the clinical management of diffuse large B cell lymphoma (DLBCL), the conventional first-line therapy, representing the established standard of care, involves the integration of CHOP regimen (Cyclophosphamide, Doxorubicin, Vincristine, and Prednisone) with rituximab [96]. Second-line treatment regimen comprises DHAP (Dexamethasone, Cytarabine, Cisplatin) [97]. Thus, patients suffering from DLBCL undergo these treatment protocols (CHOP or

DHAP) typically entailing the use of glucocorticoids (Prednisolone or Dexamethasone). Again, the reported treatment agents altered the CXCR4 expression from cancer patients initially eligible for RLT with [^{177}Lu]Lu/[^{90}Y]Y-PentixaTher. To investigate the impact of glucocorticoid treatment on CXCR4 regulation in B cell lymphoma, six different DLBCL cell lines (Daudi, SUDHL-4, SUDHL-5, SUDHL-8, OCY-LY1) and the T cell lymphoma cell line (Jurkat) were treated with glucocorticoids (Prednisolone 5 μM [98] or Dexamethasone 0.5 μM [99]), and the kinetics of the receptor regulation were investigated. Flow cytometry expression analysis in conjunction with radioligand binding assays using [^{125}I]CPCR4.3 were conducted in parallel, and CXCR4 expression and radioligand uptake were correlated. To elucidate the effects of glucocorticoid therapy on CXCR4 expression *in vivo*, mice bearing DLBCL tumors were treated with received glucocorticoids starting six days prior a biodistribution study using high-affinity ligand [^{68}Ga]Ga-PentixaTher. All results obtained in this study, that was conducted in the context of a service contract with PentixPharm, were published in EJNMMI Research as short communication and can be found in section 6.5.

In addition to investigating CXCR4 receptor regulation, we aimed to improve and expand their current applications. Unfortunately, [^{68}Ga]Ga-PentixaFor and its theranostic analogues, [^{177}Lu]Lu/[^{90}Y]Y-PentixaTher, exhibit limited flexibility towards structural changes without a substantial decrease in affinity [100, 101, 102] precluding the implementation of alternative radiolabeling strategies. As shown by Osl et al. [101] and further implemented by Lorenz Konrad [103], extended linker structures with specific amino acid sequences provide both enhanced CXCR4 affinity and greatly improved structural flexibility towards even bulky modifications to CPCR4-based receptor ligands. Thus, based on the excellent *in vitro* and *in vivo* characteristics of [$^{99\text{m}}\text{Tc}$]Tc-PentixaTec ([$^{99\text{m}}\text{Tc}$]Tc-N4-L6-CPCR4 [37]), the highly potent L6-CPCR4 scaffold was exploited to generate novel CXCR4-targeted imaging agents for an expanded set of applications such as ^{18}F -PET, and a hybrid (fluorescent/radioactive) compound for potential application as a preclinical imaging tool. This involved development of appropriate precursors for [^{18}F]AlF-labeling (NOTA, NODA-GA) and sulfo-cyanine5 (SulfoCy5) containing analogs as well as their non-radioactive Al^{nat}F- and ^{nat}Ga-counterparts. Their

affinity was assessed *in vitro* on human as well as on mouse CXCR4 expressing cell lines and compared to the clinical gold standard [⁶⁹Ga]Ga-PentixaFor. The results from the *in vitro* evaluation can be found in section 6.1.

2 Summary of results and contributions

2.1 Article 1: Validation of the C-X-C chemokine receptor 3 (CXCR3) as a potential biomarker for T cell activation

Authors: Sebastian Martin, Lennard Wendlinger, Béatrice Zitti, Mehdi Hicham, Viktoriia Postupalenko, Léo Marx, Greta Giordano-Attianese, Elisabetta Cribioli, Melita Irving, Alexandra Litvinenko, Radmila Faizova, David Viertl, Margret Schottelius

Summary

The study aimed to evaluate CXCR3 expression as a potential T cell activation marker in the tumor microenvironment (TME) during immune checkpoint inhibitor therapy with α -PD-1/ α -CTLA-4 antibody treated mice. Exploiting α -CXCR3-PE as well as ^{64}Cu -labeled NOTA- α -CXCR3 antibody, T cell activation within MC38 tumors in B57BL/6 mice were analyzed by flow cytometry and biodistribution analyses. Flow cytometry analysis confirmed a significant increase in CXCR3⁺ T cells five days post-immune checkpoint inhibitor (ICI) treatment. These findings were in conjunction with immunofluorescence analysis of tumor cryoslices. In vivo PET imaging utilizing [^{64}Cu]Cu-NOTA- α -CXCR3 demonstrated a specific accumulation in secondary lymphoid organs. Specifically, at high molar activities

(300 GBq μmol^{-1}), specificity was observed in lymph nodes and spleen. Spleen-to-liver ratios indicated a time-dependent systemic immune response, exhibiting a steady increase over multiple ICI cycles. The study concludes that in vivo imaging of CXCR3 upregulation under immunotherapy using antibodies is feasible, provided by optimal conditions of high molar activities and low antibody doses for sensitive detection in lymphoid organs. However, assessing therapy-induced alterations in CXCR3⁺ T cell populations within tumors was not possible. Nevertheless, CXCR3 remains a promising candidate for response imaging, with potential enhancements in sensitivity anticipated through the utilization of alternative tracers with increased affinities (pM) and favorable pharmacokinetic properties.

Authors' contributions

MS and SM were involved in the conceptualization and experimental design of this study. BZ and SM performed the flow cytometry experiments. MH and SM carried out the Qupath evaluations. EC and GGA were responsible for CXCR3 transduction of CHO cells. SM carried out the radiotracer synthesis and in vitro evaluations. DV, AL, LW and SM carried out the PET imaging and biodistribution studies. All authors read and approved the current version of the manuscript.

2.2 Article 2: Influence of corticosteroid treatment on CXCR4 expression in DLBCL

Authors: Sebastian Martin, David Viertl, Anna Janz, Stefan Habringer, Ulrich Keller, Margret Schottelius

Summary

The study investigated the influence of corticosteroids on CXCR4 regulation in diffuse large B-cell lymphoma (DLBCL) cells, aiming to understand their impact on the efficacy of CXCR4-

targeted radioligand therapy ($[^{177}\text{Lu}]\text{Lu}/[^{90}\text{Y}]\text{Y-PentixaTher}$). DLBCL cell lines and a T-cell lymphoma cell line were treated with dexamethasone and prednisolone at different concentrations and time points. Results revealed a cell line-dependent upregulation of CXCR4 expression upon dexamethasone and prednisolone treatment, with notable increases observed in B lymphoma cell lines. Moreover, dexamethasone treatment in vivo led to enhanced uptake of $[^{68}\text{Ga}]\text{Ga-PentixaTher}$ in OCI-LY1 tumors, indicating elevated CXCR4 expression. These findings suggest that corticosteroids, a crucial component of chemotherapy regimens, may not adversely impact CXCR4 expression in DLBCL cells. Instead, they may potentially enhance the efficacy of CXCR4-targeted radioligand therapy.

The short communication can be found in section 6.5.

Authors' contributions

SM, DV and MS carried out the in vitro and in vivo experiments. AJ, SH, UK and MS designed the study, and MS wrote the manuscript. All authors were involved in the analysis and interpretation of the data and in revising the manuscript. All authors read and approved the final manuscript.

2.3 Article 3: Conjugation of unprotected macrocyclic chelators using solid-phase peptide synthesis

Authors: Sebastian Martin, Tobias Stemler and Margret Schottelius

Summary

Peptide-based radiotracers exhibit clinical success due to unique properties: fast clearance, low background accumulation, and renal excretion. They can be easily modified, allowing precise tuning of receptor affinity and pharmacokinetics. A novel synthetic strategy was developed, directly coupling unprotected macrocyclic chelators on peptides immobilized

on 2CTC resin. This method, exemplified by the synthesis of PSMA-617, demonstrated improved efficiency and yield compared to conventional approaches. The same strategy was successful with NOTA as well as various peptide sequences. Overall, on-resin coupling of unprotected chelators in aqueous solvent systems presents a straightforward strategy for peptide radiotracer precursor synthesis.

Authors' contributions:

MS and SM were involved in the conceptualization and experimental design of this study. TS carried out the synthesis of the PSMA binding motif. SM carried out the peptide synthesis and method development. All authors read and approved the current version of the manuscript.

2.4 Article 4: Validation of a size exclusion method for concomitant purification and formulation of peptide radiopharmaceuticals

Authors: Sebastian Martin, Lennard Wendlinger, Alexandra Litvinenko, Radmila Faizova, Margret Schottelius

Summary

The study investigated an alternative purification method for radiometal-labeled peptide radiotracers, comparing it to the standard reversed-phase solid phase extraction (RP-SPE) technique. Sephadex G10 cartridges were utilized for purification of peptide radiotracers with molecular weights exceeding 1 kDa. Results showed effective retention of unreacted radiometal salts on the G10 cartridges, with high radiochemical purities (>99%) achieved for eluted radiopeptides, even at increased elution volumes. Product recovery from the G10 cartridges was consistently >85% for peptides with molecular weights ≥ 2 kDa, albeit slightly lower for [^{68}Ga]Ga-PSMA-617. Notably, the G10 cartridges maintained robust performance

over multiple uses (up to 20 times) and were successfully integrated into automated radiosynthesis procedures. Overall, size exclusion purification yielded excellent radiochemical purities (>99%) for all investigated peptide radiotracers, without the use of organic solvents.

The original article can be found in section 7.2.

Authors' contributions

SM, LW, AL and MS were involved in the conceptualization and experimental design of this study. SM and LW carried out the labeling procedures, prepared the draft, collected, and analyzed the data. SM, LW, AL, RF and MS contributed to the writing and revision of the manuscript. All authors have read and agreed to the current version of the manuscript.

3 Materials and methods

All chemicals and solvents were of analytical grade and used without further purification. Amino acids for the solid phase peptide synthesis were purchased from Iris Biotech (Marktrewitz, Germany), chelator derivatives were acquired from Chematech (Dijon, France) and Fosfinos (Perucká, Czech Republic). Solvents and reactants for organic synthesis were ordered from Sigma-Aldrich (Buchs, Switzerland) and VWR (Nyon, Switzerland). Monoclonal antibodies were purchased from Biolegend (San Diego, USA) and chemokine ligands from Preprotech (London, UK). All procedures involving radioactivity were performed according to Swiss radiation protection and safety regulations.

3.1 Mass spectrometry

Mass spectrometry (MS) was performed with electron spray ionization MS by using a Advion Expression compact mass spectrometer (Ithaca, USA) including an additional thin layer chromatography (TLC)/MS plate express. Liquid samples were manually injected using 0.3 mL min^{-1} flow of methanol (MeOH) containing 0.1% formic acid mobile phase.

3.2 Nuclear magnetic resonance spectroscopy

NMR spectra were recorded on a Bruker Avance II WB (^1H 400 MHz, ^{13}C 101 MHz) at 298 K. NMR solvents was d_6 -DMSO. Spectra were calibrated on solvent signals (2.54 ppm for d_6 -DMSO). Chemical shifts were given in parts per million (ppm) and reported relative to trimethylsilane (TMS). Coupling constants are reported in hertz (Hz). The multiplicity of the NMR signals is described as follows: s = singlet, d = duplet, t = triplet, q = quartet, m = multiplet.

3.3 High performance liquid chromatography

Analytical and preparative high performance liquid chromatography (HPLC) was conducted on a Shimadzu LC-40D equipped with a SPD-M40 DAD UV detector (UV detection at 220 nm) a DGU-405 degassing unit and a CTO-40C column oven (column temperature at 40 °C, A = 0.1% TFA in H_2O and B = 0.1% TFA in acetonitrile (ACN)).

For **analytical HPLC** a 150x4.6 mm MultiKrom 100-5 C18 (CS-Chromatographie Service GmbH, Langerwehre) column was used. Following methods were used:

ANALYTICAL-10-90ACN: 0-15 min 10-90% B, 15-16 min 90% B, 16-18 min 10% B, 18-20 min 10% B at a flow rate of 1 mL min^{-1} .

ANALYTICAL-5-40ACN: 0-1 min 5% B, 1-25 min 5-40% B, 25-26 min 40-80% B, 26-28 min 80% B, 28-29 min 80-5% B, 29-32 min 5% B at a flow rate of 1 mL min^{-1} .

ANALYTICAL-10-40ACN: 0-15 min 10-40% B, 15-16 min 40% B, 16-18 min 90% B, 18-19 min 10% B, 19-22 min 10 B at a flow rate of 1 mL min^{-1} .

ANALYTICAL-15-25ACN: 0-15 min 15-25% B, 15-16 min 90% B, 16-18 min 90% B, 18-19 min 25% B, 19-22 min 25 B at a flow rate of 1 mL min^{-1} .

Preparative HPLC was conducted on a Shimadzu LC-40D equipped with a SPD-M40 DAD UV detector (UV detection at 220 nm) and a DGU-405 degasing unit. For the purification using a 250x10 mm MultoKrom 100-5 C18 (CS-Chromato-graphie Service GmbH, Langwehre) column following methods were used (A = 0.1% TFA in H₂O and B = 0.1% TFA in ACN):

PURIFICATION-5-20ACN-a: 0-1 min 5% B, 1-15 min 5-20% B, 15-16 min 20-80% B, 16-18 min 80% B, 18-19 min 80-5% B, 19-22 min 5% B at a flow rate of 5 mL min⁻¹.

PURIFICATION-5-20ACN-b: 0-1 min 5% B, 1-15 min 5-20% B, 15-18 min 20-23% B, 18-19 min 23-80% B, 19-21 min 80% B, 21-22 min 80-5% B, 22-24 min 5% B at a flow rate of 5 mL min⁻¹

PURIFICATION-10-60ACN: 0-12 min 10-60% B, 15-16 min 80% B, 16-17 min 80% B, 17-18 min 10% B at a flow rate of 4 mL min⁻¹.

PURIFICATION-10-25ACN: 0-30 min 15-25% B, 30-31 min 25-90% B, 31-34 min 90% B, 34-35 min 15% B, 35-38 min 15% at a flow rate of 5 mL min⁻¹.

PURIFICATION-15-45ACN 0-25 min 15-45% B, 25-26 min 45-90% B, 26-28 min 90% B, 28-29 min 15% B, 29-30 min 15% at a flow rate of 5 mL min⁻¹.

PURIFICATION-10-45ACN 0-30 min 10-45% B, 30-31 min 45-90% B, 31-34 min 90% B, 34-35 min 10% B, 35-38 min 10% at a flow rate of 5 mL min⁻¹.

PURIFICATION-10-30ACN: 0-15 min 10-30% B, 15-16 min 80% B, 13-14 min 10% B, 14-16 min 10% B at a flow rate of 4 mL min⁻¹.

For crude crude purification using a 250x20 mm MultoKrom 100-5 C18 (CS-Chromatographie Service GmbH, Langwehre) column, semi-preparative HPLC settings were used as follows (A = 0.1% TFA in H₂O and B = 0.1% TFA in ACN): PURIFICATION-30-80ACN: 0-15 min 30-80% B, 15-16 min 80-30% B, 16-18 min 30% B at a flow rate of 9 mL min⁻¹.

Samples were lyophilized using a Christ Alpha 1-2 LD plus lyophilizer.

Radio-HPLC was performed on a Shimadzu LC-20AT equipped with a SPD-M20A UV-VIS detector and a Elysia Raytest γ -ray detector. For analytical radio-HPLC of the radiolabeled CC-peptides method a 150x4.6 mm MultiKrom 100-5 C18 (CS-Chromatographie Service GmbH, Langerwehre) was used (A = 0.1% TFA in H₂O and B = 0.1% TFA in ACN). Gradient setting RADIO-5-50ACN: 0-7 min 5-50% B, 7-8 min 50-80% B, 8-9 min 80% B, 9-10 min 80-5% B, 10-12 min 5% B at a flow rate of 1 mL min⁻¹.

For analytical radio-HPLC of the trimers analytical measurements using method RADIO-Chromo-10-70ACN a Chromolith Performance RP-18e 100-4.6 mm (Merck, Darmstadt) HPLC column was used (A = 0.1% TFA in H₂O and B = 0.1% TFA in ACN). Gradient setting RadioChromo-10-70ACN: 0-5 min 10-70% B, 5-6 min 70-10% B, 6-8 min 10% B at a flow rate of 2 mL min⁻¹.

For the in process and quality control of compound [¹⁸F]FXC3-7 and [¹⁸F]FXC3-B7 system was connected to a Thermo Electron Corporation BDS HYPERSIL C18 RP 5 μ m column (Thermo Scientific), 250x4.6 mm. The solvent composition was A = 0.1% TFA in H₂O; B = 0.1% TFA in ACN.

Gradient setting RADIO-20-60ACN: 0-10 min 20-60% B, 10-11 min 60-90% B, 11-13 min 90% B, 13-14 min 90-20%, 14-17 min 20% B at a flow rate of 1 mL min⁻¹.

The work-up of ¹⁸F-labeled radiotracers was conducted on a XBridge C18 BEH, 130 Å, 250x10 mm (Waters, USA). Gradient setting Tracer-PURIFICATION-20-60ACN: 0-10 min 20-60% B, 10-11 min 60-90% B, 11-13 min 90% B, 13-14 min 90-20%, 14-17 min 20% B. The purification was performed at a flow rate of 4 mL min⁻¹.

3.4 General Procedures

3.4.1 GP01: Peptide synthesis

The starting amino acid (AA) Fmoc-AA-OH (1.5 eq.) was immobilized on 2-chlorotrityl resin (200-400 mesh, Iris Biotech) in DCM supplemented with N,N-diisopropylethylamine (DIPEA) (1.25 eq). Another 2.5 eq DIPEA were added after 5 min of shaking. The resin was capped after 120 min with MeOH (1 mL g⁻¹) for 10 min and then washed (2x each dichloromethane (DCM), N,N-dimethylformamid (DMF), MeOH). Next, the resin was dried *in-vacuo* and weighed for the calculation of the resin load according to the formula below:

$$\text{resin-load [mmol/g]} = \frac{(m_2 - m_1) \times 1000}{(Mw - 36.461 \text{ [g/mol]}) \times m_2} \quad (3.1)$$

*m*₁ = mass of the net resin before coupling [g]

*m*₂ = mass of the dried resin after coupling in [g]

Mw = molecular weight of the Fmoc-OH in [g/mol]

3.4.2 GP02: Coupling cycles

The resin-bound Fmoc-AA was treated with 20% piperidine in DMF (v/v) for 10 min and a second time for 5 min. After the resin was washed (5x with DMF) the subsequent Fmoc-AA-OH was activated using 2-(1H-benzotriazole-1-yl)-1,1,3,3-tetramethylaminium tetrafluoroborate (TBTU) (1.5 eq), hydroxybenzotriazole (HOBT) (1.5 eq) and DIPEA (4.5 eq) in DMF. The resin was then shaken for 2.5 hours and washed 5-times with DMF.

3.4.3 GP03: Peptide cleavage and deprotection

A mixture of trifluoroacetic acid (TFA), triisopropyl silane (TIPS), water (95:2.5:2.5, v/v/v) was added to the resin to cleave the peptide. After 60 min of incubation at room temperature (RT) the peptide was precipitated in 45 mL–50 mL of cold diethylether (DEE). The precipitated peptide was centrifuged (3 min, 3000 rcf). Next, the crude was dried *in vacuo* and redissolved in HPLC eluent or MeOH for the work-up by preparative HPLC.

3.4.4 GP04: Radiolabeling using ^{68}Ga -labeling

Radiotracer precursor (10 nmol–25 nmol) was added into a 10 mL glass reaction vial containing NaOAc buffer (0.2 N, pH = 4.0, 1 mL–2 mL). ^{68}Ga was manually eluted from a $^{68}\text{Ge}/^{68}\text{Ga}$ generator (Eckert & Ziegler GalliaPharmTM, Berlin) using 0.1 N hydrochloric acid. A volume of 0.5 mL–1.5 mL 0.1 N of the active fraction were added to the reaction vial. The labeling took place for 15 min at 95 °C. The reaction mixture was aspirated in a shielded 20 mL syringe and passed through an C18 SepPak light cartridge (Waters, 120 mg sorbent) which was equilibrated with 5 mL ethanol and 5 mL water. After adding the crude mixture, the column was washed with 1 mL of water. The radiotracer was eluted with 1.5 mL ethanol. Subsequently, the organic solvent was evaporated at 95 °C under nitrogen flow and the dried product was redissolved in PBS for *in vitro* or 0.9% NaCl for *in vivo* studies. Quality control by Radio-TLC: Buffer solution: 1 M NH_4OAc in MeOH 1:1, pH = 7.0; retention factor (R_f) of free and colloidal ^{68}Ga : 0-0.3; R_f radiotracer: 0.8-1.0.

3.4.5 GP05: PET/CT scans

PET/CT images were acquired on an Albira PET/SPECT/CT (Bruker Biospin Corporation, Woodbridge, CT, USA). A volume of 100 μL of radiotracer in 0.9% NaCl was injected into the tail vein (1 MBq–3 MBq, 10 pmol–250 pmol). Blocking was carried out by co-injection of a 1000-fold excess of cold tracer analogue. The images were acquired 60 min–90 min post-injection. The animals were anesthetized using isoflurane (1.5% alveolar concentration)

during the static scans (20 min, 32x32 0.5 mm) or dynamic scans (60 min, 32x32 0.5 mm). Followed by a 10 min CT scan. During the whole imaging procedures, the body temperature and respiration rate was monitored. Reconstruction was performed by using Albira reconstructor (version NMI3.3) and the images were processed by PMOD (V6.3.4, Bruker).

3.5 Synthesis of CCR-targeted radiotracers

3.5.1 Method-M1: Conjugate synthesis using DOTA in solution

Route A1 was performed according to the literature [104]. Briefly, DOTA (4 eq), NHS (5 eq) and 1-ethyl-3-(3-dimethylaminopropyl)carbodiimide (EDCI) (5 eq) were dissolved in water, and DIPEA (8 eq) is added. After 15 min the respective peptide (1 eq.) was added in an equal volume of water. Progress of the coupling reaction is monitored using HPLC. If the conversion was incomplete another equivalent of DOTA, N-hydroxysuccinimide (NHS) and EDCI was added. Upon completion of the reaction (approximately 1 hour), the solvents are evaporated *in vacuo*.

Compound **DOTA-DAPTA** (DOTA-D-Ala-Ser-Tre-Tre-Tre-Asn-Tyr-Tre-OH) MS m/z (%): calculated for $C_{51}H_{83}N_{14}O_{22}^+$ [M+H]⁺ 1243.58, found 1243.5 (85%); calculated for $C_{51}H_{82}N_{14}O_{22}Na^+$ 1265.56, found 1265.6 (100%). Retention time (R_t) (analytical HPLC, method ANALYSIS-5-40ACN): 7.95 min, > 99% purity. Yield: 5.41 mg (42%).

3.5.2 Method-M2: Conjugate synthesis using DOTA-tris(tert-butyl)ester

DOTA-tris(tert-butyl)ester (1.5 eq) was activated with TBTU (1.5 eq), HOBt (1.5 eq) and DIPEA (4.5 eq) in DMF. The resin was then shaken for 2.5 hours and washed 5-times in DMF.

Compound **CC-8** (DOTA-Glu-D-Tre-D-Trp-D-Tyr-D-Ser-OH) MS m/z (%): calculated for $C_{54}H_{78}N_{11}O_{19}^+$ [M+H]⁺ 1184.55, found 1184.3 (85%); cald for $C_{54}H_{77}N_{11}O_{19}Na^+$ 1120.51, found

1120.4 (100%). R_t (analytical HPLC, method ANALYSIS-5-40ACN): 14.20 min, 96.6% purity. Yield: 3.28 mg (7%).

3.5.3 Method-M3: Conjugate Synthesis using unprotected macrocyclic chelators on 2CTC resin

Macrocyclic chelator NOTA (2 eq) or DOTA (2 eq) was added to 400 μ L of MilliQ water and was dissolved in an ultrasonic bath. The resin with the immobilized peptide was pre-soaked in tetrahydrofuran (THF) for at least 5 minutes in 3 mL THF. To this suspension, pentafluorophenol (PFP) in THF (1 $\text{mg}\mu\text{L}^{-1}$, 2.5 eq) was added. EDCI (2.5 eq) was dissolved in a reaction tube with water 100 μ L, followed by adding 100 μ L THF. Next, DIPEA (10 eq) was added to the EDCI solution. This solution was added to the suspension while vigorously stirred. Subsequently, the clear reaction solution was added to the resin (1 eq) and mixed for 2 hours. The resin was washed two times each in THF, DMF and MeOH followed by drying *in vacuo* and cleavage in TFA/water/TIPS (95:2.5:2.5).

Compound **CC-1** (DOTA-Ahx-D-Ser-D-Ser-D-Tre-D-Tyr-D-Arg-OH) MS m/z (%): calculated for $\text{C}_{47}\text{H}_{78}\text{N}_{13}\text{O}_{18}^+$ $[\text{M}+\text{H}]^+$ 1112.59, found 1112.4 (100%). R_t (analytical HPLC, method ANALYSIS-5-40ACN): 8.37 min, > 99% purity. Yield: 10.12 mg (18%).

Compound **CC-2** (DOTA-Ahx-D-Tre-D-Tre-D-Ser-D-Tyr-D-Tre-OH) MS m/z (%): calculated for $\text{C}_{46}\text{H}_{75}\text{N}_{10}\text{O}_{19}^+$ $[\text{M}+\text{H}]^+$ 1071.52, found 1071.4 (100%). R_t (analytical HPLC, method ANALYSIS-5-40ACN): 9.74 min, 96.5% purity. Yield: 9.73 mg (15%).

Compound **CC-3** (DOTA-Ahx-D-Asn-D-Tre-D-Arg-D-Tyr-D-Arg-OH) MS m/z (%): calculated for $\text{C}_{51}\text{H}_{86}\text{N}_{17}\text{O}_{17}^+$ $[\text{M}+\text{H}]^+$ 1208.64, found 1208.5 (100%). R_t (analytical HPLC, method ANALYSIS-5-40ACN): 8.20 min, 91.8% purity. Yield: 4.14 mg (7%).

Compound **CC-4** (DOTA-Ahx-D-Ile-D-Asp-D-Asn-D-Tyr-D-Tre-OH) MS m/z (%): calculated for $\text{C}_{49}\text{H}_{78}\text{N}_{11}\text{O}_{19}^+$ $[\text{M}+\text{H}]^+$ 1124.55, found 1124.3 (100%). R_t (analytical HPLC, method ANALYSIS-5-40ACN): 13.31 min, > 99% purity. Yield: 8.95 mg (13%).

Compound **CC-5** (DOTA-Ahx-D-Asn-D-Tre-D-Ser-D-Tyr-D-Arg-OH) MS m/z (%): calculated for $C_{48}H_{79}N_{14}O_{18}^+ [M+H]^+$ 1139.57, found 1139.5 (100%). R_t (analytical HPLC, method ANALYSIS-5-40ACN): 8.32 min, > 99% purity. Yield: 8.67 mg (17%).

Compound **CC-6** (DOTA-Ahx-D-Ile-D-Asn-D-Asn-D-Tyr-D-Tre-OH) MS m/z (%): calculated for $C_{49}H_{79}N_{12}O_{18}^+ [M+H]^+$ 1123.56, found 1123.5 (100%). R_t (analytical HPLC, method ANALYSIS-5-40ACN): 13.01 min, > 99% purity. Yield: 4.24 mg (13%).

Compound **CC-7** (DOTA-Ahx-D-Asn-D-Tre-D-Ser-D-Tyr-Gly-OH) MS m/z (%): calculated for $C_{44}H_{70}N_{11}O_{18}^+ [M+H]^+$ 1040.49, found 1040.5 (100%). R_t (analytical HPLC, method ANALYSIS-5-40ACN): 8.40 min, > 97.9% purity. Yield: 8.23 mg (26%).

Compound **DOTA-RAP-103** (DOTA-Ahx-D-Tre-D-Tre-D-Asn-D-Tyr-D-Tre-OH) MS m/z (%): calculated for $C_{47}H_{76}N_{11}O_{19}^+ [M+H]^+$ 1098.53, found 1098.5 (80%); calculated for $C_{47}H_{74}N_{11}O_{19}Na^+$ 1120.51, found 1120.4 (100%). R_t (analytical HPLC, method ANALYSIS-5-40ACN): 9.54 min, > 99% purity. Yield: 12.43 mg (19%).

Compound **PSMA-617** MS m/z (%): calculated for $C_{49}H_{72}N_9O_{16}^+ [M+H]^+$ 1042.50, found 1042.2 (100%). R_t (analytical HPLC, method ANALYSIS-5-40ACN): 18.7 min, > 97.9% purity. Yield: 2.56 mg (21%).

Compound **NOTA-617** (MS m/z (%): calculated for $C_{45}H_{65}N_8O_{14}^+ [M+H]^+$ 941.45, found 941.2 (100%). R_t (analytical HPLC, method ANALYSIS-5-40ACN): 19.4 min, > 95.5% purity. Yield: 2.22 mg (18%).

3.5.4 Synthesis of compound RAP-103y

5-Hexynoic acid (1.5eq) was coupled to the resin-bound binding motif RAP-103 (H_2N -D-Tre-D-Tre-D-Asn-D-Tyr-D-Tre-2CTC resin) applying GP02. After the peptide cleavage (GP03), the curde was purified using method PURIFICATION-10-60ACN ($R_t = 5.7$ min).

Compound **RAP-103y** MS m/z (%): calculated for $C_{31}H_{45}N_6O_{12}^+$ [M+H]⁺ 693.30, found 693.2 (50%). R_t (analytical HPLC, method ANALYSIS-10-90ACN): 5.01 min, 95.5% purity. Yield: 26.75 mg (18%).

3.5.5 Synthesis of compound RAP-103-Hx-N3

6-Azido-hexanoic acid (1.5eq) was coupled to the resin-bound binding motif **RAP-103** (H₂N-D-Tre-D-Tre-D-Asn-D-Tyr-D-Tre-2CTC resin) applying GP02. After the peptide cleavage (GP03), the curde was purified using method PURIFICATION-10-60ACN (R_t = 6.5 min).

Compound **RAP-103-Hx-N3** MS m/z (%): calculated for $C_{31}H_{48}N_9O_{12}^+$ [M+H]⁺ 737.33, found 737.3 (30%). R_t (analytical HPLC, method ANALYSIS-10-90CN): 7.3 min, 97.1% purity. Yield: 6.75 mg (15%).

3.5.6 Synthesis of compound TRAP-103

An aqueous solution of TRAP-Triazide (Fisfinos s.r.o., Czech Republic) was prepared in MilliQ water (0.1 mg μ L⁻¹, 1 eq, 0.007 mmol). The alkyne RAP-103y (3.3 eq, 0.022 mmol) which has been dissolved in 720 μ L 1:1 DMF/MilliQ water (v/v) was added into a 5 mL Eppendorf reaction tube. Subsequently, an aqueous solution of L-ascorbic acid (50 mM, 50 eq) was added. A solution of CuSO₄ (110 mM, 1.2eq) in water was added and the reaction mixture. The mixture was heated in an oil bath at 60 °C for 30-60 min without stirring. The product formation was verified by analytical HPLC. In case of the presence of unreacted azide, a second aliquot of copper (1.2 eq) was added, and the reaction mixture was heated again for 30 min. Subsequently, NOTA (20 eq.) dissolved in 1 mL MilliQ was added, and the reaction mixture was heated again for 2 hours at 60 °C. The compound was purified using the method PURIFICATION-10-60ACN.

Compound **TRAP-103** MS m/z (%): calculated for $C_{120}H_{184}N_{33}O_{45}P_3^{2-}$ $[M-2H]^{2-}$ 1450.13, found 1450.5 (45%). R_t (analytical HPLC, method ANALYSIS-5-40ACN): 13.8 min, 90.3% purity. Yield: 9.30 mg (46%).

3.5.7 Synthesis of compound NO-Y

1,4,7-Triazacyclononane (1 eq., 50 mg, 0.21 mmol) was dissolved in dry ACN and K_2CO_3 (15 eq., 435 mg, 3.2 mmol). Propargylchlorid (2.9 eq, 44.1 μ L) which had been diluted in 1 mL ACN was added dropwise and the reaction mixture was stirred at RT for 10 hours. Subsequently, the solvent was evaporated, redissolved in MeOH and filtered through a 0.22 μ m filter (Ministart RC 4, Sartorius). The work up was conducted using method PURIFICATION-10-60ACN R_t 7.5min.

Compound **NO-Y** (1,4,7-tri(prop-2-yn-1-yl)-1,4,7-triazonane) MS m/z (%): calculated for $C_{15}H_{22}N_3^+$ $[M+H]^+$ 244.17, found 244.1 (100%). R_t (analytical HPLC, method ANALYSIS-5-40ACN): 16.6 min, 98.9% purity. Yield: 4.85 mg (4%).

3.5.8 Synthesis of compound NO-Y-103 and NO-Y-Hx

The alkyne **NO-Y** (1 eq) was dissolved in DMF to obtain a solution of 0.1 mg μ L⁻¹. Next, the azide **RAP-103-Hx-N3** (3.3 eq, 0.009 mmol) or 5-Hexynoic acid (3.3 eq, 0.005 mmol) dissolved in 1:1 MilliQ water/DMF was added. Subsequently, an aqueous solution of L-ascorbic acid (50 mM, 50 eq) was added. A solution of $CuSO_4$ (110 mM, 1.2 eq) in MilliQ water was added and the reaction mixture and was heated in an oil bath at 60 °C for 30-60 min without stirring. The product formation was verified by analytical HPLC. In case of the presence of unreacted alkyne, a second aliquot of copper (1.2 eq) was added, and the reaction mixture was heated again for 30 min. Subsequently, NOTA (20 eq.) dissolved in 1 mL MilliQ water was added, and the reaction mixture was heated again for 2 hours at 60 °C. The compounds were purified using the method PURIFICATION-10-60ACN.

Compound **NO-Y-Hx** MS m/z (%): calculated for $C_{33}H_{55}N_{12}O_6^+$ [M+H]⁺ 715.43, found 715.5 (15%). R_t (analytical HPLC, method ANALYSIS-5-40ACN): 16.6 min, 98.9% purity. Yield: 2.07 mg (65%).

Compound [⁶⁴Cu]Cu-**NO-Y-Hx** MS m/z (%): calculated for $CuC_{33}H_{56}N_{12}O_6^{2+}$ [M+2H]²⁺ 389.68, found 389.0 (55%). R_t (analytical HPLC, method ANALYSIS-5-40ACN): 14.5 min, 94.5% purity. Yield: 1.19 mg (35%).

Compound **NO-Y-103** MS m/z (%): calculated for $C_{108}H_{160}N_{30}O_{36}^{2-}$ [M-2H]²⁻ 1226.6, found 1227.0 (40%). R_t (analytical HPLC, method ANALYSIS-5-40ACN): 14.9 min, 77.2% purity. Yield: 1.99 mg (36%).

Synthesis of ^{nat}Ga and ^{nat}Lu complexes

Non-radioactive reference compounds were prepared with GaNO₃ or LuCl₃. A stock solution (0.032 mmol/mL) was prepared in 0.1 N hydrochloric acid. 500 μL sodium acetate buffer (NaOAc, pH = 4.5, 0.2 mmol) was given into an Eppendorf tube (1.8 mL). Next, the precursor was added. The stock solution of the trivalent metal ions was added to the mixture and heated for 10 minutes at 95 °C. Meanwhile, a SepPak C18 light cartridge (120 mg sorbents) was equilibrated using ethanol (5 mL) and water (10 mL). After equilibration to RT the reaction mixture was slowly passed through the equilibrated cartridge and rinsed with water (2 mL). The labeled compound was eluted with ethanol (5 mL). The product was freeze-dried and weighed.

Compound [^{nat}Ga]Ga-**CC-1** MS m/z (%): calculated for $C_{47}H_{75}N_{13}O_{18}Ga^+$ [M+H]⁺ 1178.46, found 1178.4 (100%). R_t (analytical HPLC, method ANALYSIS-5-40ACN): 8.33 min, 95.9% purity. Yield: 2.32 mg (80%).

Compound [^{nat}Ga]Ga-**CC-2** MS m/z (%): calculated for $C_{46}H_{72}N_{10}O_{19}Ga^+$ [M+H]⁺ 1137.42, found 1137.3 (100%). R_t (analytical HPLC, method ANALYSIS-5-40ACN): 9.76 min, 98.3% purity. Yield: 1.91 mg (75%).

Compound [^{nat}Ga]Ga-CC-3-Ga MS m/z (%): calculated for C₅₁H₈₃N₁₇O₁₇Ga⁺ [M+H]⁺ 1274.54, found 1174.4 (87%); calculated for C₅₁H₈₃N₁₇O₁₇Ga²⁺ [M+2H]²⁺ 637.77, 637.8 (100%). R_t (analytical HPLC, method ANALYSIS-5-40ACN): 8.33 min, 95.9% purity. Yield: 2.10 mg (78%).

Compound [^{nat}Ga]Ga-CC-4-Ga MS m/z (%): calculated for C₄₉H₇₅N₁₁O₁₉Ga⁺ [M+H]⁺ 1190.45, found 1190.3 (100%). R_t (analytical HPLC, method ANALYSIS-5-40ACN): 13.52 min, 97.9% purity. Yield: 1.60 mg (65%).

Compound [^{nat}Ga]Ga-CC-5 MS m/z (%): calculated for C₄₈H₇₆N₁₄O₁₈Ga⁺ [M+H]⁺ 1205.47, found 1205.2 (100%). R_t (analytical HPLC, method ANALYSIS-5-40ACN): 8.45 min, 95.1% purity. Yield: 1.75 mg (65%).

Compound [^{nat}Ga]Ga-CC-6 MS m/z (%): calculated for C₄₉H₇₆N₁₂O₁₈Ga⁺ [M+H]⁺ 1189.47, found 1189.3 (100%). R_t (analytical HPLC, method ANALYSIS-5-40ACN): 13.21 min, 97.1% purity. Yield: 1.33 mg (57%).

Compound [^{nat}Ga]Ga-CC-7 MS m/z (%): calculated for C₄₄H₆₇N₁₁O₁₈Ga⁺ [M+H]⁺ 1106.39, found 1106.2 (100%). R_t (analytical HPLC, method ANALYSIS-5-40ACN): 8.47 min, 97.3% purity. Yield: 2.11 mg (80%).

Compound [^{nat}Ga]Ga-CC-8 MS m/z (%): calculated for C₅₄H₇₅N₁₁O₁₉Ga⁺ [M+H]⁺ 1250.45, found 1250.1 (90%); calculated for C₅₄H₇₆N₁₁O₁₉Ga²⁺ [M+2H]²⁺ 625.73, found 625.8 (100%). R_t (analytical HPLC, method ANALYSIS-5-40ACN): 14.35 min, 94.1% purity. Yield: 1.35 mg (60%).

Compound [^{nat}Ga]Ga-DOTA-RAP-103 MS m/z (%): calculated for C₄₇H₇₃N₁₁O₁₉Ga⁺ [M+H]⁺ 1164.43, found 1164.4 (100%). R_t (analytical HPLC, method ANALYSIS-5-40ACN): 9.63 min, > 99% purity. Yield: 2.37 mg (85%).

Compound [^{nat}Ga]Ga-DOTA-DAPTA MS m/z (%): calculated for C₅₁H₈₀N₁₄O₂₂Ga⁺ [M+H]⁺ 1309.48, found 1309.3 (50%); calculated for C₅₁H₇₉N₁₄O₂₂GaNa⁺ 1331.46, found 1331.4 (100%).

R_t (analytical HPLC, method ANALYSIS-5-40ACN): 7.53 min, > 99% purity. Yield: 1.83 mg (75%).

Compound [^{nat}Lu]Lu-DOTA-DAPTA MS m/z (%): calculated for C₅₁H₈₀N₁₄O₂₂Lu⁺ [M+H]⁺ 1415.50, found 1415.4 (70%); calculated for C₅₁H₇₉N₁₄O₂₂LuNa⁺ 1437.48, found 1437.3 (100%).

R_t (analytical HPLC, method ANALYSIS-5-40ACN): 8.18 min, 98.5% purity. Yield: 2.03 mg (80%).

Compound [^{nat}Ga]Ga-TRAP-103 MS m/z (%): calculated for C₁₂₀H₁₈₉N₃₃O₄₅P₃Ga³⁺ [M+3H³⁺] 990.39, found 990.9 (100%); calculated for C₁₂₀H₁₈₈N₃₃O₄₅P₃Ga²⁺ 1485.59, found 1486.1 (80%).

R_t (analytical HPLC, method ANALYSIS-5-40ACN): 12.9 min, 92.2% purity. Yield: 1.5 mg (70%).

3.6 Iodinating proteins using Iodogen

The recombinant protein was dissolved in PBS and aliquots were created using low bind Eppendorf tubes. 10 µg–20 µg of recombinant protein were dissolved in 100 µL TRIS buffer (25 mM TRIS, 0.4 M NaCl, pH 7.5). Additionally, 5 µL DMSO were added. The mixture was transferred to an Eppendorf reaction tube precoated with 50 µg of Iodogen. Upon addition of Na¹²⁵I (20 MBq–25 MBq (Hartmann Analytic, Braunschweig) the radiolabeling was performed for 15 min at RT. Next, the liquid was purified by a PD MidiTrap G-25 (Cytiva, Uppsala) column which was saturated by 1 mL BSA (20 g L⁻¹). The purification was performed according to the manufacturer's protocol. 10% (v/v) ethanol were added to the final product to prevent radiolysis.

3.7 Iodinating proteins using the Bolton-Hunter reagent

The iodination was performed according to the general procedures recommended by Fisher Scientific (protocol no. 0476.1). In brief, 0.5 mg of the Bolton-Hunter reagent (*N*-succinimidyl-3-[4-hydroxyphenyl]propionate, #cat: 27710) were dissolved in 1 mL DMSO. A volume

of 2 μL of this solution were added to the labeling buffer (50 mM sodium phosphate buffer, pH 7.5 containing 25 MBq of Na^{125}I). Immediately, chloramine T (100 μg in 50 μL of labeling buffer 50 mM sodium phosphate buffer, pH = 7.5) was added. After 15 seconds the reagent was extracted by the addition of 100 μL of benzene and 5 μL DMF. The organic phase was collected and dried in a V-shaped glass vial with a gentle stream of nitrogen gas. 250 ng of the protein (human recombinant CXCL10, Preprotech, #Cat: 300-12) which was dissolved in ice-cold sodium borate buffer (50 mM, pH = 8.5) before were added in a volume of 2.5 μL and allowed to react for 2 hours at RT. The reagents were dissolved in 500 μL of PBS and purified using a PD MidiTrap G-25 (Cytiva, Uppsala) column which was saturated by 1 mL BSA (20 g L^{-1}). The purification was performed according to the manufacturers' protocol.

3.8 Synthesis of piperazinylpiperidine based radiotracers

3.8.1 Synthesis of compound XC3-1a

5,6-Dichloronicotinic acid (1 eq, 9.33 mmol) was dissolved in dry 12 mL of dry DMF:DCM (3:1). Propargylamide (1.5 eq, 14 mmol), EDCI (1.5 eq, 14 mmol) and Triethylamine (1.6 eq, 14.9 mmol) were added and the reactants were stirred for 16 hours at RT. The solvent was removed under reduced pressure at 50 $^{\circ}\text{C}$. The residue was dissolved in DCM (50 mL) and washed with 1 M HCl (50 mL) and water (50 mL). The organic layer was collected, dried over MgSO_4 , filtered and concentrated under vacuum. Column chromatography was performed (eluent: ethylacetate (EtOAc)/Petrol ether, 1:1) to give the product as yellowish solid.

Compound **XC3-1a** (5,6-dichloro-*N*-(prop-2-yn-1-yl)nicotinamide) MS m/z (%): calculated for $\text{C}_9\text{H}_5\text{Cl}_2\text{N}_2\text{O}$ [$\text{M}-\text{H}^-$] 227.0, found 226.8 (100%). R_t (analytical HPLC, method Analytical-10-90ACN): 9.2 min, > 99% purity. Yield: 488.2 mg (23%). $^1\text{H-NMR}$: 9.292 (t, JHz = 5.2, 1H), 8.801 (d, JHz = 2.20, 1H), 8.497 (d, JHz = 2.20, 1H), 4.100 (dd, JHz = 2.60, 2H), 3.200 (t, JHz = 2.51, 1H). $^{13}\text{C-NMR}$: 150.472, 147.352, 138.617, 130.451, 129.734, 80.927, 74.011, 29.179.

3.8.2 Synthesis of compound XC3-2a

Compound **XC3-1a** (1.05 eq, 2.44 mmol), (S)-1-Boc-2-ethylpiperazine (1 eq, 2.33 mmol) and K_2CO_3 (3 eq) were stirred at 85°C in 5 mL DMF (anhydrous) overnight. The DMF was evaporated under reduced pressure. Then the residue was dissolved in DCM (3 mL) and washed with water (30 mL) two times. The organic layer was dried over $MgSO_4$, and the DCM was evaporated under reduced pressure. The yellowish oil was dissolved in 5 mL DCM/TFA (3:2) for 5 min. The solvents were again removed under reduced pressure. The residue was dissolved in 25 mL DCM and washed with 1 M NaOH (25 mL) and a second time with water (25 mL). The collected organic layer was dried over $MgSO_4$, filtered and concentrated under reduced pressure. Column chromatography was applied to gain the product as yellowish oil. The crude was purified by means of column chromatograph. Gradient: EtOAc/triethylamine (TEA) (99:1) to EtOAc/MeOH/TEA (80:20:1).

Compound **XC3-2a** ((S)-5-chloro-6-(3-ethylpiperazine-1-yl)-N-(prop-2-yn-1-yl)nicotinamide) MS m/z (%): calculated for $C_{15}H_{20}ClN_4O$ $[M+H]^+$ 307.8, found 307.0 (100%). R_t (analytical HPLC, method Analytical-10-90ACN): 6.0 min, > 99% purity. Yield: 373 mg (52%).

3.8.3 Synthesis of compound XC3-3

Piperidin-4-one (1 eq, 10.10 mmol), 1-chloro-4-(chloromethyl)benzene (2.5 eq, 25.25 mmol) and Triethylamine (3 eq, 30.3 mmol) were stirred for 48 hours at 60 °C in dichloroethane (DCE). The solvent was removed *in vacuo* and column chromatography was applied using EtOAc/TEA (99:1) to obtain the product as brownish oil.

Compound **XC3-3** (1-(4-chlorobenzyl)piperidine-4-one) MS m/z (%): calculated for $C_{12}H_{14}ClNO$ $[M+H]^+$ 224.1, found 224.0 (80%). R_t (analytical HPLC, method Analytical-10-90ACN): 6.0 min, > 99% purity. Yield: 373 mg (52%). 1H -NMR: 7.373 (s, 4H), 3.587 (s, 2H), 2.657 (t, 4H), 2.335 (t, 4H).

3.8.4 Synthesis of compound XC3-6

Compound **XC3-2a** (1 eq, 0.23 mmol) and compound **XC3-3** (2 eq, 0.46 mmol) were dissolved in THF (anhydrous) and heated to 50 °C for 3 h. After agitation at RT NaBH(OAc)₃ (1.9 eq, 0.48 mmol) was added stepwise. After 16 hours of stirring, the solvent was evaporated *in vacuo* and the residue was dissolved in EtOAc (30 mL). After washing the organic phase with 1 M NaOH and water, the combined organic phases were dried with MgSO₄, filtered and evaporated under reduced pressure. The crude was redissolved in MeOH for the work-up by semi-preparative HPLC using method PURIFICATION-30-80ACN.

Compound **XC3-6** ((*S*)-5-chloro-6-(4-(1-(4-chlorobenzyl)piperidine-4-yl)-3-ethylpiperazine-1-yl)-*N*-(prop-2-yn-1-yl)nicotinamide) MS m/z (%): calculated for C₂₇H₃₃Cl₂N₅O [M+H]⁺ 514.5, found 514.2 (100%). R_t (analytical HPLC, method Analytical-10-90ACN): 7.1 min, >98.5% purity. Yield: 67.7 mg (57%).

3.8.5 Synthesis of compound XC3-1b

3-amino-5,6-dichloro-*N*-methylpyrazine-2-carboxamide (1.22 mmol, 1.05 eq), K₂CO₃ (3.5 mmol, 3 eq) and (*S*)-1-Boc-2-ethylpiperazine (1.17 mmol, 1 eq) were stirred in DMF (anhydrous) at 85 °C for 16 hours. After evaporation of the DMF under reduced pressure at 50 °C the residue was dissolved in 25 mL DCM and washed with 1 M NaOH (25 mL) and water (25 mL) one time. After evaporation of the organic phase, a mixture of 9 mL MeOH/water/THF (6:2:1) was added to the yellowish oil. Next, LiOH (4 eq) was added and stirred for 16 hours at RT. The solvent was removed *in vacuo* and the residue was dissolved in EtOAc, washed with water two times, dried over MgSO₄. Subsequently, the organic solvent was removed under reduced pressure. The lyophilized product was used without further purification.

Compound **XC3-1b** ((*S*)-3-amino-5-(4-(tert-butoxycarbonyl)-3-ethylpiperazine-1-yl)-6-chloropyrazine-2-carboxylic acid) MS m/z (%): calculated for C₁₆H₂₅ClN₅O₄ [M+H]⁺ 386.9,

found 386.1 (100%). R_t (analytical HPLC, method Analytical-10-90ACN): 12.5 min, 69.7% purity. Yield: 250 mg (56%).

3.8.6 Synthesis of compound XC3-2b

Compound **XC3-1b** (0.13 mmol, 1 eq) was dissolved in DCE. Propargylamine (0.28 mmol, 2.2 eq), TEA (0.78 mmol, 6 eq) was added, and the mixture was cooled to 0 °C. The acid was activated by addition of thionyl chloride (0.76 mmol, 6 eq) at 0 °C. Subsequently, the mixture was stirred for 15 min at RT. The solvent was removed under reduced pressure and the residue was redissolved in EtOAc (30 mL). The organic phase was washed with saturated NaHCO_3 and water one time each. After rotary evaporation of the organic phase, silica gel column chromatography was applied with EtOAc/TEA (99:1). The organic solvent of the collected fractions was removed *in vacuo*. Subsequently, the Boc protection group was removed by addition of 5 mL of DCM/TFA (3:2) for 5 minutes. Rotary evaporation and lyophilization resulted in compound **2a** as a yellow oil.

Compound **XC3-2b** ((*S*)-3-amino-6-chloro-5-(3-ethylpiperazine-1-yl)-*N*-(prop-2-yn-1-yl)-pyrazine-2-carboxamide) MS m/z (%): calculated for $\text{C}_{14}\text{H}_{23}\text{ClN}_7\text{O}$ [$\text{M}+\text{NH}_4^+$] 340.8, found 340.1 (25%). R_t (analytical HPLC, method Analytical-10-90ACN): 7.0 min, 70.2% purity. Yield: 32.6 mg (78%).

3.8.7 Synthesis of compound XC3-B6

Compound **XC3-2b** (0.31 mmol, 1 eq) and compound **XC3-3** (0.46 mmol, 2 eq) were dissolved in THF (anhydrous) and heated to 50 °C for 3 h. After agitation to RT $\text{NaBH}(\text{OAc})_3$ (0.59 mmol, 1.9 eq) were added stepwise. After 16 hours of stirring, the solvent was evaporated *in vacuo* and the residue was dissolved in EtOAc (30 mL). After washing the organic phase with 1 M NaOH and water, the EtOAc was dried with MgSO_4 , filtered and evaporated under reduced pressure. The crude was redissolved in MeOH for the work-up by semi-preparative HPLC using method PURIFICATION-30-80ACN.

Compound **XC3-B6** ((*S*)-3-amino-6-chloro-5-(4-(1-(4-chlorobenzyl)piperidine-4-yl)-3-ethylpiperazine-1-yl)-*N*-(prop-2-yn-1-yl)pyrazine-2-carboxamide) MS *m/z* (%): calculated for $C_{26}H_{34}Cl_2N_7O$ [$M+NH_4^+$] 530.22, found 530.4 (100%). R_t (analytical HPLC, method 10-90ACN): 7.8 min, 90.1% purity. Yield: 34.6 mg (21%).

3.8.8 Synthesis of compound [^{nat}F]FXC3-5

The synthesis of compound [^{nat}F]FXC3-5 (2-Fluoroethylazide) was conducted according to Glaser et al. [105]. In brief, 2-fluoroethyl-4-toluenesulfonate (0.24 mmol, 1 eq) was dissolved in 0.5 mL DMF (anhydrous). Sodium azide (0.73 mmol, 3 eq) was added and the suspension was stirred for 24 hours at RT. The undissolved residues were centrifuged, and the supernatant was filtered through a 0.2 μ m filter (Sartorius RC 4 minisart). The filter was further rinsed with 200 μ L DMF. TLC using EtOAc as eluent was applied to monitor of the reaction.

3.8.9 Synthesis of compound [^{nat}F]FXC3-7

Compound **XC3-6** (0.03 mmol, 1 eq) was dissolved in 5 mL DMF. First, 328 μ L (0.13 mmol, 4.5 eq) of a freshly prepared stock solution of L-Ascorbic acid (100 mg/mL in water) was added. Subsequently, 328 μ L (0.13 mmol, 4.5 eq) of a $CuSO_4 \cdot 5H_2O$ stock solution (100 mg/mL in water). Finally, compound **XC3-5** (0.08 mmol, 2.7 eq) in 200 μ L DMF was added under vigorous stirring. The reaction mixture was stirred for 15 minutes at RT. The solution was then diluted with 40 mL water and 10 mL saturated $NaHCO_3$, and subsequently extracted three times with 50 mL EtOAc. The organic phase was collected, dried over $MgSO_4$ and evaporated under reduced pressure. The residue was redissolved in MeOH for the work-up by semi-preparative HPLC using method PURIFICATION-30-80ACN.

Compound [^{nat}F]FXC3-7 ((*S*)-5-chloro-6-(4-(1-(4-chlorobenzyl)piperidine-4-yl)-3-ethylpiperazine-1-yl)-*N*-((1-(2-fluoroethyl)-1*H*-1,2,3-triazol-4-yl)methyl)nicotinamide) MS *m/z* (%): calculated for $C_{29}H_{38}Cl_2FN_8O$ [$M+H$]⁺ 603.25, found 603.1 (100%). R_t (analytical HPLC, method 10-90ACN): 7.0 min, > 99% purity. Yield: 3.3 mg (18%).

3.8.10 Synthesis of compound [^{nat}F]FXC3-B7

Compound **XC3-B6** (0.03 mmol, 1 eq) was dissolved in 0.5 mL DMF. First, 359 μ L (0.2 mmol, 7 eq) of a freshly prepared stock solution of L-Ascorbic acid (100 mg mL⁻¹ in water) was added. Subsequently, 328 μ L (0.13 mmol, 4.5 eq) of a CuSO₄·5H₂O stock solution (100 mg/mL in water). Lastly, compound **XC4-5** (0.08 mmol, 2.7 eq) in 200 μ L DMF was added under vigorous stirring. The reaction mixture was stirred for 15 minutes at RT. The solution was then diluted with 40 mL water and 10 mL saturated NaHCO₃, and subsequently extracted three times with 550 mL EtOAc. The organic phase was collected, dried over MgSO₄ and evaporated under reduced pressure. The residue was redissolved in MeOH for the work-up by semi-preparative HPLC using method PURIFICATION-30-80ACN.

Compound [^{nat}F]**FXC3-B7** ((S)-3-amino-6-chloro-5-(4-(1-(4-chlorobenzyl)piperidine-4-yl)-3-ethyl-piperazine-1-yl)-N-((1-(2-fluoroethyl)-1H-1,2,3-triazol-4-yl)methyl)pyrazine-2-carboxamide) MS m/z (%): calculated for C₂₈H₃₈Cl₂FN₁₀O [M+H]⁺ 619.26, found 619.1 (100%). R_t (analytical HPLC, method 10-90ACN): 7.3 min, > 99% purity. Yield: 2.64 mg (14%).

3.8.11 Synthesis of compound [¹⁸F]FXC3-5

The protocol was performed according to Zhou et al. [106]. Briefly, ¹⁸F-fluoride (500 MBq) was added into a septum-screw-capped 10 mL V-vial and azeotropically dried in the presence of K₂CO₃ (2 mg) and kryptofix (K₂₂₂, 0.8 mg) with ACN (3 × 1 mL) under nitrogen flow at 105 °C. Tosylate precursor 2-azidoethyl-4-toluenesulfonate (0.35 mg, 1.5 μ mol) in ACN (0.2 mL) was added to the dried vial while the reaction took place at 80 °C–90 °C for 10 min. Subsequently, 10 mL water was added to quench the reaction. By pressurising the vessel the mixture was passed through a C18 plus (Waters, 5404 Baden) and an Oasis HLB (Waters, 5404 Baden) solid phase extraction (SPE) column which had been assembled in series. Before use, the cartridges were activated with MeOH (10 mL) and water (10 mL). The reaction vial was rinsed one more time with water (10 mL), followed by air (20 mL) to remove the residual water from

the cartridges. For in-process control, the residing activity on the HLB cartridge containing compound [^{18}F]FXC3-5 (2- ^{18}F Fluoroethyl azide) was measured (120 MBq–160 MBq).

3.8.12 ^{18}F -click labeling to obtain compound [^{18}F]FXC3-7 and [^{18}F]FXC3-B7

The radiolabeling using C18 plus (waters, USA) and HLB cartridges (waters, USA) in series was performed according to [106]. A solution of the alkyne substrate **XC3-6** or **XC3-B6** in DMF (0.4 mg, 450 μL) and 50 μL of the Cu(I) reagent (mixture of 5 mg of CuSO_4 in 50 μL water, 15 mg sodium ascorbate in 50 μL water, and 6 mg bathophenanthroline disulfonate (BPDS) in 100 μL 4:1 water/DMF) were loaded slowly onto the 2- ^{18}F fluoroethyl azide containing HLB cartridge. The eluate during the loading was discarded. The reaction was allowed to proceed for 10 min at RT (compound **XC3-6**) or 10 min (**XC3-B6**) at 60 °C. Acetonitrile (0.5 mL) was used to elute the reaction mixture followed by water (up to 2 mL–3 mL). The crude was purified by radio-HPLC using method Tracer-Purification-10-60ACN. Subsequently, the solvents were evaporated under nitrogen flow at 100 °C until dryness.

Compound [^{18}F]FXC3-7: R_t (analytical radio-HPLC, method Radio-20-60ACN): 8.1 min.

Compound [^{18}F]FXC3-B7: R_t (analytical radio-HPLC, method Radio-20-60ACN): 8.5 min.

3.9 Synthesis of CXCR4-targeted ligands

Starting material was the L6-CPCR4 building block Cyclo(D-Tyr-NMe-D-Orn(D-Dap(Boc)-D-Arg(Pbf)-D-Ala-4-Abz)-Arg(Pbf)-2-Nal-Gly) which was commercially purchased (Senn Chemicals AG, Dielsdorf). The synthesis of the final products was carried out based on previously published protocols [37]. After the deprotection (GP-03), the products were purified by means of preparative HPLC. Method PURIFICATION-10-25ACN: **NODAGA-L6-CPCR4** (R_t : 25.7 min), **NOTA-L6-CPCR4** (R_t : 26.8 min); method PURIFICATION-15-45ACN: **SulfoCy5-L6-CPCR4** (R_t : 14.6 min); method PURIFICATION-10-40ACN: **SulfoCy5-Ahx-dap(DOTA)-L6-CPCR4** (R_t : 19.5 min).

The labeling of **NODAGA-L6-CPCR4** and **NOTA-L6-CPCR4** was performed in NaOAc buffer (0.5 M, pH = 4). A solution of 8 mM AlF in NaOAc labeling buffer was added to obtain a final concentration of 2 mM concentration. The labeling conducted at 95 °C for 20 min.

Compound **NODAGA-L6-CPCR4**: MS m/z (%): calculated for $C_{70}H_{98}N_{20}O_{17}$ $[M+H]^{1+}$ 1492.7, found 1491.7 (20%), 745.9 $[M+2H]^{2+}$ (100%). R_t (analytical HPLC, method ANALYTICAL-15-25ACN): 10.4 min, purity 98.4%.

Compound **Al-NODAGA-L6-CPCR4**: MS m/z (%): calculated for $C_{70}H_{98}N_{20}O_{17}Al$ $[M+H]^{1+1+}$ 1518.66, found 1538.7 (25%), 758.7 $[M+2H]^{2+}$ (30%). R_t (analytical HPLC, method ANALYTICAL-15-25ACN): 10.5 min, purity 95.3%.

Compound **NOTA-L6-CPCR4**: MS m/z (%): calculated for $C_{67}H_{94}N_{20}O_{15}$ $[M+H]^{1+1+}$ 1419.61, found 1420.6 (100%), found 710.4 $[M+2H]^{2+}$ (40%). R_t (analytical HPLC, method ANALYTICAL-15-25ACN): 11.0 min, purity 96.7%.

Compound $[^{nat}F]AlF$ -**NOTA-L6-CPCR4**: MS m/z (%): calculated for $C_{67}H_{94}N_{20}O_{15}AlF$ $[M+H]^{1+}$ 1466.6, found 732.4 $[M+2H]^{2+}$ (30%). R_t (analytical HPLC, method ANALYTICAL-15-25ACN): 10.5 min, purity 84.1%.

Compound **SulfoCy5-L6-CPCR4**: MS m/z (%): calculated for $C_{87}H_{111}N_{19}O_{17}S_2$ $[M+H]^{1+}$ 1759.08, found 880.6 $[M+2H]^{2+}$ (80%). R_t (analytical HPLC, method ANALYTICAL-15-45ACN): 13.8 min, purity >99%.

Compound **SulfoCy5-dap(DOTA)-L6-CPCR4**: MS m/z (%): calculated for $C_{112}H_{154}N_{26}O_{26}S_2$ $[M+H]^{1+}$ 2344.10, found 1172.9 $[M+2H]^{2+}$ (12%), 782.7 $[M+3H]^{3+}$ (5%). R_t (analytical HPLC, method ANALYTICAL-10-40ACN): 12.0 min, purity 95.4%.

3.10 Serum protein binding

To determine the ratio of protein bound radiotracer, 20 μ L–50 μ L of the radio-labeled molecule in PBS was added directly into preheated human serum (1000 μ L, 37 °C). Triplicates were

generated. The incubation took place in a cell-incubator (37°C) for 1 hour. The samples were centrifuged utilizing centrifuge filters (molecular cutoff 30 kDa) at 10,000 rcf for 5 minutes at 4°C. The filters were further rinsed twice using cold PBS buffer (100 µL). A subsequent gamma counting was applied to determine the counts per minute of the filters and the liquid. The percentage of protein bound ratio was calculated.

3.11 Stability in human serum

To a volume of 500 µL of human serum, 50 µL–100 µL of radiotracer were added. The mixture was incubated at 37°C. Analyses were undertaken after 24 and 48 hours of incubation. Before the analysis 100 µL of the sample were passed through a 0.2 µm filter before the radio-HPLC analysis.

3.12 Distribution coefficient

Distribution coefficient (Log D) determinations were performed in the two-phase system n-octanol (500 µL) and PBS buffer (490 µL, pH 7.4). Radio-labeled compound (10 µL) was added to the mixture, thoroughly mixed and incubated in a shaker for 1 hour at room temperature. The two-phase system was centrifuged at 4xG for 5 minutes. Triplicates of both phases were prepared. 100 µL of each phase was taken for the gamma counting and common logarithm was applied to calculate the n-octanol/PBS distribution coefficient Log D.

3.13 *In vitro* experimentation

3.13.1 Cell culture

Cells were maintained in a 5% CO₂ humid atmosphere at 37°C either using RPMI GlutaMAX media (HEK293, Jurkat, MDA-MB231 X4, 4T1, MC38) or Ham's F-12 Nutrient Mix (CHO). The cell culture media was supplemented with 10% fetal bovine serum and 1% penicillin/strep-

tomycin. Transiently transfected HEK293 cells were cultured in GlutaMAX containing 10% fetal bovine serum, 1% penicillin/streptomycin, and 1 mg/mL geneticin (G418).

3.13.2 Cell transfection

HEK293 cells were transfected according to the instructions of the manufacturers protocol for the TransIT® -293 transfection reagent. Therefore, one million cells were transfected with the plasmide of one of the six Chemokine receptors (human CCR2, -5, -8 or murine CCR2, CCR5, or CCR8). Positive selection was performed by addition of 1 mg/mL geneticin (G418) at day two post-transfection.

3.13.3 Flow cytometry

The cells were washed twice with cold flow cytometry buffer (1% fetal bovine serum in PBS). For the staining, triplicates of 1×10^6 cells were prepared and incubated 30 min on ice using a concentration of $1 \mu\text{g mL}^{-1}$ of antibody using PE anti-human CCR2 (BioLegend, #Cat: 357205, Clone K036C2), PE anti-human CCR5 (BioLegend, #Cat: 359105, Clone: J418F1), PE anti-human CCR8 (BioLegend, #Cat: 360603, Clone: L263G8), PE anti-mouse CCR2 (BioLegend, #Cat: 150609, Clone: SA203G11), PE anti-mouse CCR5 (BioLegend, #Cat: , Clone: SA203G11), PE anti-mouse CCR8 (BioLegend, #Cat: 150311, Clone: SA214G2), PE anti-mouse CXCR3 (BioLegend, #Cat: 126505, Clone: CXCR3-173), PE anti-human CXCR4 (BioLegend, #Cat: 306506, Clone: 12G5), or PE mouse IgG, α isotype Ctrl (BioLegend, #Cat: 400212, Clone: MOPC-173). The freshly prepared staining dilution (100 μL in flow cytometry buffer) was added to the cells. The cells were spun down at 300xg after the incubation and the staining agent was discarded. Subsequently, the cells were washed twice and resuspended in 500 μL of cold FACS buffer. In addition, DAPI was added to each sample shortly before the analysis to yield a final concentration of $0.5 \mu\text{g mL}^{-1}$. The flow cytometry analyses were conducted on the same day on a Beckman Coulter Gallios flow cytometer. The acquired data were analyzed with FlowJo v10.7.1. Control of the surface expression was realized by flow cytometry and its

specific phycoerythrin (PE)-mAb (Biolegend, London). HEK293-hCCR2: 49.7% positive cells; HEK293-hCCR5: 88.6% positive cells; HEK293-hCCR8: 67.9% positive cells; HEK293-mCcr2: 13.6% positive cells; HEK293-mCcr5: 53.7% positive cells; HEK293-mCcr8: 56.7% positive cells.

3.13.4 IC50 determinations on CXCR4-expressing cells

Binding experiments were performed on Jurkat (human CXCR4) and transfected HEK293 (murine CXCR4) cells. The cell suspension was washed three times and 10^6 cells were added to each γ -counter tube (V-shape, 4.5 mL) in 200 μ L assay buffer (HBSS, supplemented with 1% BSA). The competitors were added in concentrations ranging from 10^{-11} to 10^{-4} M (n = 3 per concentration) in a volume of 25 μ L. Next, the radioligand [125 I]-FC131 (Jurkat) or [125 I]-CPCR4.3 (HEK293) was added in a volume of 25 μ L in assay buffer. Specific binding of the radioligands [125 I]-FC131 (Jurkat) or [125 I]-CPCR4.3 (HEK293) was at 5-15% without competitor. The samples were incubated at RT for 1 hour. Subsequently, the cells were for 3 min at 400 rcf and the supernatant was removed with a pipette and placed in a corresponding empty γ -counter tube (V-shape, 4.5 mL) with the pipette tip used. The cells were washed with 200 μ L of assay buffer and spun down again. The supernatant was added to the previously removed fraction, again with the respective pipette tip. The γ -counter tubes were analyzed using a Perkin Elmer Wizard 3. The corresponding supernatant of each sample was used to determine the percentage of binding.

3.13.5 Cell-based radioligand binding assay on CCR transfected cells

To conduct binding experiments on the transfected (CCR2, CCR5, CCR8) HEK293 cells, the number of cells used per γ -counter tube (V-shape, 4.5 mL) were tested between 2×10^5 to 1×10^6 cells per vial, aiming to obtain 5–15% specific binding of the added radioactive ligand. The Assay buffer was prepared freshly as follows: RPMI medium supplemented with 0.5-5% BSA or HBSS supplemented with 0.5-5% BSA. Using 10 pM–50 pM 125 I-labeled recombinant

protein (e.g., murine [^{125}I]I-CCl5) in 225 μL assay buffer). The inhibitor was titrated in 25 μL (0.1 nM–1 nM). The γ -counter tubes were analyzed using a Perkin Elmer Wizard 3. Specific binding was determined comparing transfected and blocked cells as well as looking at total activity added.

3.13.6 Radioligand binding assay using ^{68}Ga -labeled DOTA-DAPTA

500,000 cells of human CCR5 transfected HEK293 cells were added in a volume of 200 μL of assay medium (HBSS suppl. with 1% BSA). Non-transfected HEK293 cells were used for unspecific binding per tube. 25 μL of either HBSS or a 1 mM Dapta stock solution in HBSS was supplemented to the cell suspension. Freshly radiolabeled [^{68}Ga]Ga-DAPTA-DOTA in a stock solution of 10 nM. The incubation took place either at RT or at 37 °C. After one hour the cells were spun down at 1300 rcf, washed one time with ice-cold HBSS. Subsequently, a gamma-counting of the collected supernatants Perkin Elmer Wizard 3 and the corresponding cells was performed and the specific binding was determined.

3.13.7 Membrane binding assay

The membrane binding assay was carried out according to Schottelius et al. [107] using commercially available membrane preparations (DiscoverX, France) and ^{125}I -labeled radioligands (Perkin Elmer ([^{125}I]I-MIP-1 α , #Cat: NEX298005UC or Chelatec, [^{125}I]I-CXCL10). Briefly, the radioligands were dissolved in a volume of 1.5 mL of binding buffer (Binding Buffer contained 50 mM HEPES, 5 mM MgCl_2 , 1 mM CaCl_2 and 0.2% BSA, pH 7.4.). 5 μL of CCR5 or CXCR3 cell membrane preparation (1 unit per well, Eurofins) were added to a flat-bottom 96-well polystyrene plate. Wash buffer contained 50 mM HEPES, pH = 7.4, 500 mM NaCl, 0.1% BSA. The competitor was titrated in a volume of 10 μL . To each well 10 μL (approx. 1.22 kBq per well, 0.15 nM final assay concentration in 100 μL) of reconstituted radioligand in binding buffer. All wells were brought to a final volume of 100 μL) using binding buffer and incubated for 90 min at RT. After the incubation the liquid was spun down a centrifuge

for 30 sec at 100-150 rcf and the liquid was transferred on the filter mat using the Cell Harvester. The filter mat was preconditioned with 0.33% polyethylenimine for 30 min and then washed 7x times with 150 μ L wash buffer using the Cell Harvester (Perkin Elmer, USA). The dry filter membrane was cropped with a scissors and the corresponding wells were counted in γ -counter tubes using a γ -counter (Perkin Elmer Wizard 3).

3.14 Internalization assay

One day before the experiment, MCF-7 cells were plated in a 24-well plate (200.000 cells/well). Freshly ^{68}Ga -radiolabeled **SulfoCy5-dap**([^{68}Ga]**Ga-DOTA**)-**L6-CPCR4** was mixed with [^{125}I]I-FC131 obtain a 1 mM solution of both radiotracer in HBSS, 1% BSA. The plated cells were washed one time using 200 μ L of HBSS, 1% BSA. To the cells 200 μ L HBSS 1% BSA and 25 μ L of the radiotracer preapartion were added and incubated for 15 min–90 min at 37 °C. At each time point (n = 3), the supernatant was removed and added in the corresponding wells. The cells were washed with 300 μ L of ice-cold PBS and both fractions were pooled, representing the unbound radioligand. Next the cells were washed with 250 μ L of sodium acetate buffer (0.02 M, pH = 5, 0.9% NaCl) which represented the cell bound fraction. The cells were lysed with 300 μ L of NaOH (1 M) and washed again with 300 μ L of PBS. Both collected fractions represented the internalized radiotracer. The tubes were analyzed in a γ -counter (Perkin Elmer Wizard 3) to determine the activity of ^{68}Ga on the same day of the experiment. The next day, the activity of the added internal standard [^{125}I]I-FC131 was determined.

3.15 *In vitro* fluorescence microscopy

MDA-MB-231 X4 cells expressing eGFP-CXCR4 were seeded on glass coverslips in a 24-well plate (200.000 cells/well). The cells werre incubated for 72 hours at 37 °C. The plated cells were washed one time using 200 μ L of HBSS, 1% BSA. After adding 200 μ L of HBSS, 1% BSA the cells were incubated for 30 min at 4 °C. Next, either 25 μ L of HBSS, 1% BSA or the hybrid compound **SulfoCy5-dap**([$^{\text{nat}}\text{Ga}$]**Ga-DOTA**)-**L6-CPCR4** (250 mM in HBSS, 1% BSA) were

added. Blocking was conducted with 25 μ L of AMD3100 (1 mM, in water). The final assay volume was 250 μ L. The cells were incubated for 5, 15, 30 and 60 min at 37 °C. After the respective incubation time, the cells were washed two times with cold HBSS, 1% BSA. Cell nuclei were stained using 300 μ L of DAPI (300 nM) for 3 min. The cells were washed again two times and mounted on the coverslips with mounting medium (ProLong Antifade Glass).

3.16 *In vivo* experiments

3.16.1 Mouse models

Animal experimentations were conducted according to the protocols approved by the Veterinary Authorities of the Canton Vaud and in concordance with the Swiss Animal Welfare Act. Six to eight-week old female C57Bl/6 or Balb/C mice were purchased from Charles River Laboratories (France, L'Arbresle). The MC38 tumors cell line was engrafted (2×10^6 cells) on the right flank of female C57Bl/6 mice. The 4T1 tumor cells (1×10^5) were injected into the 5th mammary fat pad of female Balbc mice. Tumor size was monitored by applying following formula: tumor size = $\frac{1}{2} \times \text{length} \times \text{width}^2$

3.16.2 Immunofluorescence cryoslides

Immunofluorescence stainings were conducted on acetone fixed slices. The tissues were blocked with donkey and goat serum (10%) for 20 min. After washing the samples in 0.3% triton in PBS the primary antibodies (1:50, diluent DAKO S3022) were incubated 60 min, RT. After another wash step the staining was completed with the fluorescent antibody (1:500, diluent DAKO S3022) for 30 min at room temperature. DAPI (Sigma, #Cat: D9542, 1:3000 dilution in PBS) was used as control color. After the slices had been rinsed with distilled water, the slices were treated with fluorescent mounting medium (DAKO S3023). Negative controls were carried out by using fluorescent antibodies only.

3.16.3 Biodistribution assay

At a tumor size between 400-800 mm² the radiotracer preparation was injected in a volume of 100 µL i.v. and blocking was performed by the coinjection of a 1000-fold molar excess of cold compound or DAPTA for [⁶⁸Ga]Ga-DOTA-DAPTA. The animals were sacrificed 1 hour post-injection and the organs were harvested. The collected organs were analyzed by a Wizard 3 γ-counter (Perkin Elmer, Schwerzenbach) and the corresponding tissue weight was determined. Tail vein correction was applied and the data are expressed in %IA/mL tissue (mean ± SD).

3.17 Data analysis

All data were evaluated using GraphPad Prism version 9.1.0 for Windows, GraphPad Software, San Diego, California USA.

4 Investigating CC-chemokine receptors

Exploiting CCRs to image lymphocyte infiltration has been thoroughly investigated in recent preclinical studies [108, 61, 49]. The goal of the present investigation was to translate this approach to quantify global leukocyte infiltration in tumors using peptide radiotracers. In theory, this concept should allow to distinguish between the immune infiltrated vs immune desert cancer phenotype. The recently reported all-D pentapeptides based on the RAP-103 sequence all showed high activity on CCR2, CCR5 and CCR8 in functional binding assays [57, 59]. Of note, the sequence RAP-103 (H₂N-ttnyt-OH) was investigated more thoroughly, revealing extremely low half-maximal inhibitory concentrations (IC₅₀s) (< 1 nM [58, 59]) which makes them ideal candidates for binding vectors of peptide radiotracers. Since CCR5 is one of the best-characterized receptors within the CC-family, we focused the validation on this receptor to assess the presence in the TME and affinity of the synthesized compounds.

4.1 Characterization of the tumor microenvironment

Several preclinical tumor models, notably the syngenic tumors MC38, CT27, and 4T1 are highly infiltrated by leukocytes [80]. Of these, the MC38 tumor model was selected for its particularly high immune cell infiltration, and MC38 tumor cryoslides was characterized with respect to immune cell infiltration. The presence of CCR5 expressing cells in the inner and

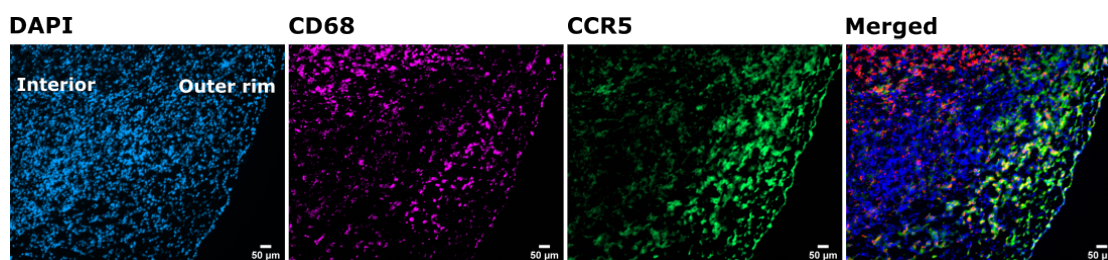


Figure 4.1: Immunofluorescence evaluation of MC38 tumors. Detection of CD68⁺ T cells (red) and CCR5⁺ cells (green). DAPI in blue.

outer rim of the tumor indicated substantial leukocyte infiltration (Figure 4.1). Moreover, the CCR5 signal partly co-localized with CD68 expressing cells confirming the presence of CD68⁺CCR5⁺ macrophages in these tumors. This motivated us to proceed with the development and characterization of potential radiotracers to ultimately image leukocyte infiltration in these tumors.

4.2 Synthesis of CCR-targeted peptide radiotracers

The reported all-D pentapeptides with the lead sequence RAP-103 (H₂N-ttnyt-OH) showed high activity on CCR2, CCR5 and CCR8 on functional binding assays [57, 59, 58]. Based on this promising data, a first set of pentapeptides was synthesized using solid phase peptide synthesis (SPPS) (GP01-GP03) and an additional aminohexanoic acid was used as spacer moiety, followed by the chelator DOTA to complete the radiotracer precursor. Additionally, the reported CCR5-specific radiotracer precursor DOTA-DAPTA [60] was synthesized as a reference compound. All peptide sequences investigated are summarized in Table 4.1.

To conjugate the terminal building block DOTA on the peptides Method-M1 was used which was performed according to a previously reported protocol [104]. This method was performed using unprotected DOTA and the cleaved and purified peptides in solution and yielded compound **DOTA-DAPTA** in a yield of 42% for this reaction step. However, the coupling of HO-ttnyt-Ahx-NH₂ revealed high amounts of side products and low product yields (<30%). In contrast, the developed method (Method-M3) aims to couple unprotected DOTA directly

Table 4.1: Sequences of all DOTA-conjugated radiotracer precursors. DOTA: 1,4,7,10-Tetraazacyclododecane-1,4,7,10-tetraacetic acid; Ahx: aminohexanoic acid.

Compound	Chelator	Linker	Binding sequence ^a
CC-1	DOTA	Ahx	H ₂ N-sstyr-OH ^b
CC-2	DOTA	Ahx	H ₂ N-ttsyt-OH ^b
CC-3	DOTA	Ahx	H ₂ N-ntryr-OH ^b
CC-4	DOTA	Ahx	H ₂ N-idnyt-OH ^b
CC-5	DOTA	Ahx	H ₂ N-ntsyr-OH ^b
CC-6	DOTA	Ahx	H ₂ N-innyt-OH ^b
CC-7	DOTA	Ahx	H ₂ N-ntsyg-OH ^b
CC-8	DOTA	Ahx	H ₂ N-etwys-OH ^b
DOTA-RAP-103	DOTA	Ahx	H ₂ N-ttnyt-OH ^c
DOTA-DAPTA^d	DOTA	-	H ₂ N-aSTTTNYT-CONH ₂

^a Small letters indicate D-amino acids, capital letters indicate L-configuration.

^b Binding sequences taken from Ruff [57]

^c Binding sequence RAP-103 taken from Noda et al. [59]

^d Compound DOTA-DAPTA reported from Wei et al. [60]

on 2CTC-bound peptides providing compound **CC-1** - **CC-7** and **DOTA-RAP-103**. The corresponding method development for this reaction is summarized in section 7.1.

To expand the library, a trimerization approach was tested with the aim to potentially amplify the specific uptake to the target cells. This was recently shown by several studies using RGD-peptides [109, 63]. Therefore, resin bound sequence **RAP-103** (Resin-tyntt-NH₂) was prolonged using 5-Hexynoic acid acid (GP02-GP03) to obtain the alkyne **RAP-103y**. Using commercially available TRAP-Triazide, the pre-purified alkyne derivative **RAP-103y** was coupled via Cu(I)-catalyzed azide-alkyne cycloaddition yielding compound **TRAP-103**. The synthesis was performed similarly to Baranyai et al. [110]. However, the coupling was commonly incomplete and prolonged reaction times with heating at 60 °C did not yield in higher product formation. We found that the addition of an additional aliquot of CuSO₄ was re-

quired to obtain almost complete conversion of the educts obtaining product **TRAP-103** in satisfactory yields (46%).

Additionally, an alternative chelator construct was synthesized (**NO-Y**) to allow trimerization similarly to the concept of TRAP-based molecules. The scaffold of the synthesized trimers (**NO-Y-103** and **NO-Y-Hx-OH**) are based on the design of the 1,4,7-tris((1H-imidazol-2-yl)methyl)-1,4,7-triazonane (NOTI)-chelator [63] with the difference that the imidazol-arms were replaced by the triazide-arms. Compared to the TRAP scaffold, these chelators are chemically easier to synthesize which is one of the major advantages. Noteworthy, the reported NOTI chelator shows excellent complexation properties on both radionuclides ^{68}Ga as well as ^{64}Cu [111, 63]. Using Propargylchlorid and 1,4,7-triazacyclononane (TACN) in ACN/ K_2CO_3 allowed the alkylation on all three secondary amines of the macrocycle. Surprisingly, the product yields of compound **NO-Y** were below 5% after the work-up with semi-preparative HPLC. However, this one-step synthesis allowed us to proceed directly with the trimer synthesis. To obtain the final trimer, a cycloaddition using **NO-Y** and either commercially available 6-azido-hexanoic acid or **Rap-103-Hx-N3** was performed on the three alkynes using CuSO_4 and L-ascorbic acid at 60 °C. This resulted in product **NO-Y-Hx** and **NO-Y-103**. Both compounds were used to conduct preliminary radiolabeling and stability experiments using relevant radioisotopes ^{68}Ga and ^{64}Cu for imaging. Radiolabeling with ^{68}Ga (GP04) showed no complexation of the trivalent metal-ion. In contrast, radiolabeling using divalent ^{64}Cu revealed complete incorporation of the radiometal to compound **NO-Y-Hx** as well as **NO-Y-103**. This was not surprising since cold ^{63}Cu -complexes of compound **NO-Y-Hx** were identified and isolated after the cycloaddition using Cu(I), followed by the transchelation with NOTA. Stability of [^{64}Cu]Cu-**NO-Y-Hx** was confirmed *in vitro* by incubation in human serum for 24 hours at 37 °C. The *in vivo* biodistribution was assessed by injecting [^{64}Cu]Cu-**NO-Y-Hx** (3 MBq, 300 pmol) in a healthy BALB/C mouse. The PET/CT image was acquired 24 hours post-injection (p.i.) and revealed a high abdominal uptake showing a liver uptake of 15.5%IA/mL. Likely, the triazide-arms are not or very weakly involved in the metal complexation, leading to an incomplete coordination of the radiometal. Thus,

exclusively the trimer based on the well-established TRAP scaffold (compound **TRAP-103**) was included in further evaluations since it offers excellent complexation of ^{68}Ga with high molar activities (MAs) and *in vivo* stability [112, 113]

4.3 *In vitro* evaluations

The ^{68}Ga -labeled radiotracers were characterizations *in vitro* by a Log D determination and binding to human serum. A comprehensive table is represented in Table 4.2. The lead compound [^{68}Ga]Ga-**DOTA-RAP-103** was completely stable after 1 hour and 2 hours incubation in human serum at 37 °C. The Log D value was ranging from -4.41 ([^{68}Ga]Ga-**DOTA-RAP-103**) for the monomer to 2.41 ([^{68}Ga]Ga-**TRAP-103**) for the trimer. The CC-peptide series showed all serum protein binding below 5%, while the trimer revealed a significantly higher serum protein binding of roughly 50%. Affinity data was required to facilitate the selection of the best candidates. Therefore, six different CCR-transfected strains (murine/human CCR2, CCR5, CCR8) were kindly provided and characterized by the research group of Professor Melita Irving (Ludwig institute of cancer, Epalinges). We performed first cellular experiments with ^{125}I -radiolabeled ligands using the Iodogen method and the transfected HEK293 cells expressing either CCR2 or CCR5. Although, the binding assay was performed similarly as reported in the literature [114, 115, 116, 117] a specific binding of the iodinated radioligand (mouse/human CCL2, CCL3 or CCL5 using the Iodogen method) was not achieved. Flow cytometry based cell sorting of transfected mouse CCR5-expressing cells was conducted to sort exclusively CCR5^{high} expressing HEK cells. Unfortunately, a radioligand binding assay was unsuccessful using the sorted cells with freshly iodinated mouse CCL5 as well as CCL3, also known as MIP-1 α , using the Iodogen iodination method. Other iodinated proteins such as murine [^{125}I]I-CCL2 to CCR2-transfected HEK cells showed the same results. Furthermore, we performed a cell assay which was designed similarly to Wei et al. [60], utilizing the human CCR5 transfected cells and the published compound DOTA-DAPTA [108]. Modifications were as follows: ^{68}Ga instead of ^{111}In was used as radionuclide, the assay concentration was adjusted from 0.27 nM to 1 nM and in the final assay volume of

Table 4.2: Overview of radiotracers tested *in vitro* characterization.

Compound	Log D	SPB [%] ^a	Rt [min] ^b	Purity [%] ^c
[^{nat} Ga/ ⁶⁸ Ga]Ga-DOTA-RAP-103	-4.41 ± 0.69	1.77 ± 0.66	9.63	>99
[^{nat} Ga/ ⁶⁸ Ga]Ga-TRAP-103	2.41 ± 0.04	49.12 ± 1.10	12.9	92
[^{nat} Ga/ ⁶⁸ Ga]Ga-CC-1	n/a	2.7	8.3	95.9
[^{nat} Ga/ ⁶⁸ Ga]Ga-CC-2	n/a	3.2	9.8	98.3
[^{nat} Ga/ ⁶⁸ Ga]Ga-CC-3	n/a	2.6	8.3	95.9
[^{nat} Ga/ ⁶⁸ Ga]Ga-CC-4	n/a	2.9	13.5	97.9
[^{nat} Ga/ ⁶⁸ Ga]Ga-CC-5	n/a	1.4	8.5	95.1
[^{nat} Ga/ ⁶⁸ Ga]Ga-CC-6	n/a	2.7	13.2	97.1
[^{nat} Ga/ ⁶⁸ Ga]Ga-CC-7	n/a	3.7	8.5	97.3
[^{nat} Ga/ ⁶⁸ Ga]Ga-CC-8	-3.87 ± 0.35	2.5	14.4	94.1
[^{nat} Ga/ ⁶⁸ Ga]Ga-DOTA-DAPTA	n/a	1.1	7.5	>99

^a SPB, serum protein binding

^b Rt, retention time analyzed with analytical HPLC method Analytical-5-40ACN

^c Purity of the ^{nat}Ga-labeled complexes by analytical HPLC.

250 µL was used including 5x10⁵ cells. The binding assay was performed at room temperature and at 37 °C. However, specific binding for the radiolabeled molecule [⁶⁸Ga]Ga-DOTA-DAPTA was lacking.

Since the binding assays with the transfected cells and the freshly iodinated radioligands failed, binding assays based on membrane preparations were performed. To conduct the assay, commercially available human [¹²⁵I]I-MIP-1α and human CCR5 membrane preparations were used, while murine CCR5 membranes were not commercially available. Using a cell harvester, IC50 determinations were successfully established with homologous competitor human CCL3 (IC50 = 0.1 nM) which was used as positive control in all assays. The binding curves of the investigated compounds are presented in Figure 4.2. Both reported lead sequences RAP-103 and DAPTA show extremely high affinities on CCR5 (< 1 nM [58, 59,

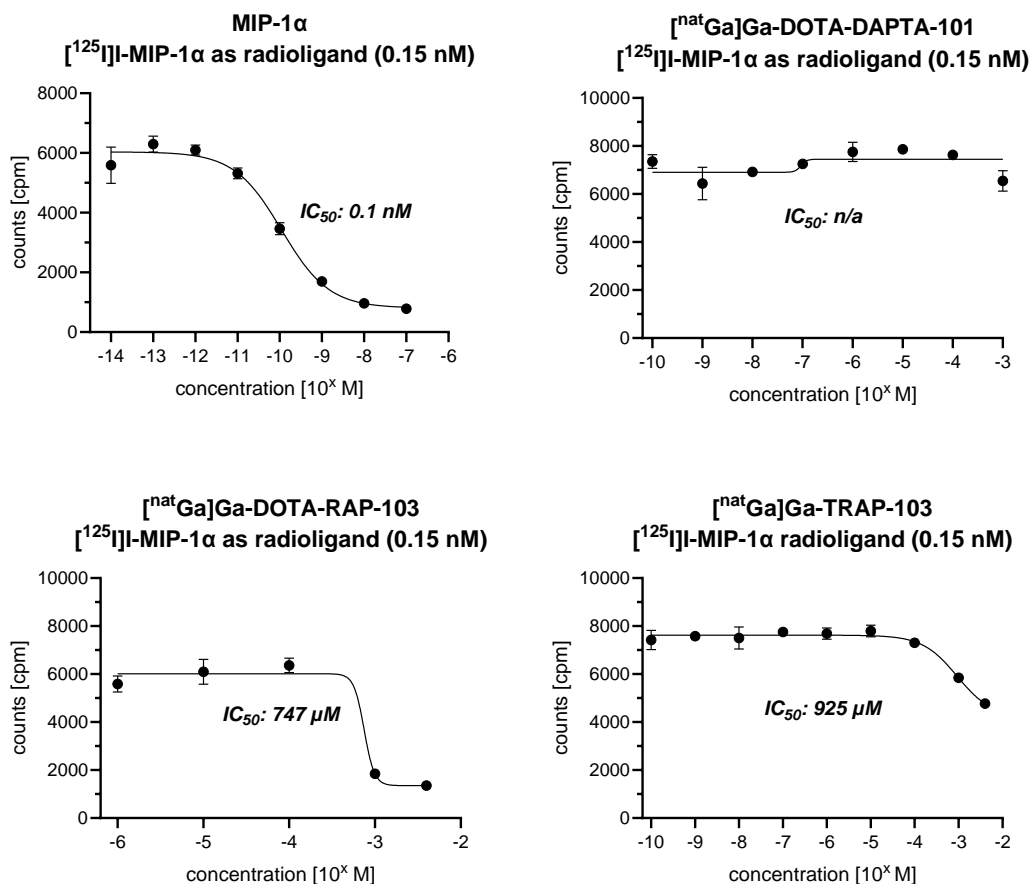


Figure 4.2: IC₅₀ evaluation on CCR5 membrane preparations of the reference ligand MIP-1α (CCL3) and the cold complexes [^{nat}Ga]Ga-DOTA-DAPTA (IC₅₀ = n/a), [^{nat}Ga]Ga-DOTA-RAP-103 (IC₅₀ = 747 μM), [^{nat}Ga]Ga-TRAP-103 (IC₅₀ = 925 μM).

118)). In addition, all reported binding determinations of these peptides were performed on cell-based assays. Surprisingly, the reference compound [^{nat}Ga]Ga-DOTA-DAPTA-101 showed no activity on the CCR5 membranes. An IC₅₀ using ^{nat}Ga-DOTA-RAP-103 exhibited a value of 747 μM, whereas the trimeric counterpart [^{nat}Ga]Ga-TRAP-103 showed a lower affinity (IC₅₀ = 925 μM). The unexpectedly high IC₅₀ values of these molecules prompted us to conduct a preliminary drug screening of the whole set of synthesized compounds including compound [^{nat}Ga]Ga-CC-1-^{nat}Ga]Ga-CC-8, [^{nat}Ga]Ga-DOTA-RAP-103 and [^{nat}Ga]Ga-DOTA-DAPTA-101 to isolate potentially high affinity molecules (see Figure 4.3). Using competitor concentrations of 10 μM and 100 μM, respectively. At a concentration of 10 μM

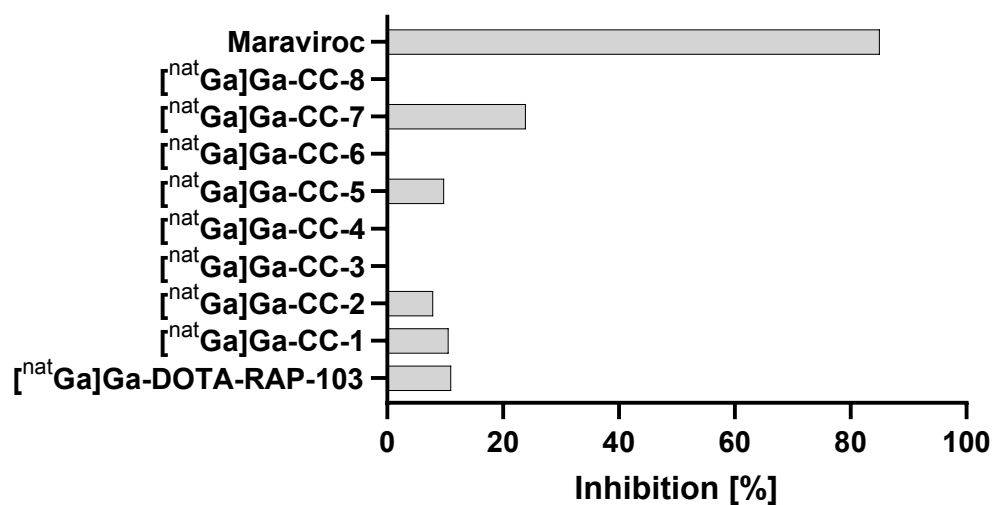


Figure 4.3: Inhibitor screening on CCR5 membranes. Inhibition is indicated relative to [¹²⁵I]I-MIP-1 α binding on CCR5 membranes at an inhibitor concentration of 10 μ M. The compounds were plated in duplicates on a 96-well plate containing [¹²⁵I]I-MIP-1 α (0.15 nM) as radiotracer.

only compound [^{nat}Ga]Ga-DOTA-RAP-103 (11%), [^{nat}Ga]-CC-1 (10.6%), [^{nat}Ga]Ga-CC-2 (7.9%), [^{nat}Ga]Ga-CC-5 (9.8%), [^{nat}Ga]Ga-CC-7 (23.9%) showed activity on the receptor. In contrast, the approved CCR5 inhibitor maraviroc showed more than 85% inhibition in both concentrations in this drug screening.

The cell-free membrane binding assays showed low activity of all the synthesized compounds. For example, investigations showed CCR5 specific uptake on CD4⁺CCR5⁺ cells using the radiotracer [¹¹¹In]In-DOTA-DAPTA [60]. The membrane binding assay showed no activity on isolated CCR5⁺ membranes using [^{nat}Ga]Ga-DOTA-RAP-103. However, the reported compound [¹¹¹In]In-DOTA-DAPTA reveals uptake on inflammation sites in mice [60], which motivated us to confirm the specificity ideally in MC38 tumors which showed considerable leukocyte infiltration of CCR5⁺ cells, notably on macrophages. Another aim was to confirm specificity at least in lymphoid organs such as the spleen and the lymph nodes, since many CCR-expressing leukocytes are present in these tissues [119, 120].

4.4 *In vivo* radiotracer evaluation

Previous studies have shown that immune cell imaging is feasible in mice through CCR-targeting [60, 61]. Despite the readout on human CCR5 membranes, the reported compound [^{111}In]In-DOTA-DAPTA was already successfully established as CCR5-specific radiotracer to monitor atherosclerotic inflammation in mice [60]. This motivated us to show that possible targeting of multiple CCRs can in principle lead to a specific binding *in vivo* (e.g., tumor, spleen or lymph node). As previously demonstrated using the ^{111}In -labeled peptide DOTA-DAPTA [60], we investigated the identical ^{68}Ga -labeled peptide radiotracer with the same sequence named [^{68}Ga]Ga-DOTA-DAPTA-101 in this study. A wild-type C57Bl/6 mouse model was selected bearing MC38 tumors on the right flank. A dose of 200 pmol of radiotracer [^{68}Ga]Ga-DOTA-DAPTA-101 ($15 \text{ GBq } \mu\text{mol}^{-1}$, $n = 3$) was injected. The biodistribution results are presented in Figure 4.4. Surprisingly, tracer specificity remained unconfirmed in the spleen and lymph nodes as well as in the tumor. Although a trend was visible for [^{68}Ga]Ga-DOTA-DAPTA-101 showing reduced tumor-to-blood ratios (1.41 ± 0.28 control vs. 1.05 ± 0.22 blocking) and spleen-to-blood ratios (0.42 ± 0.16 control vs. 0.30 ± 0.05 blocking), an unambiguous confirmation of tracer specificity with P-values < 0.05 was not possible. Thus, we decided to investigate one of the monomers bearing an all-D-pentapeptide as binding vector. Since the binding motif RAP-103 of molecule DOTA-RAP-103 is already thoroughly investigated in the literature, showing extremely potent affinities on functional binding assays on several chemokine receptors ($< 1 \text{ nM}$ [59, 58]), we wanted to investigate the behavior of the compound more thoroughly. Despite limited activity on human CCR5 *in vitro*, a biodistribution assay would bring more clarity of eventual binding on multiple murine CCRs resulting in specific uptake in at least large lymphoid organs. As for compound DOTA-DAPTA-101, a dose of 200 pmol of radiotracer [^{68}Ga]Ga-DOTA-DAPTA-103 ($15 \text{ GBq } \mu\text{mol}^{-1}$, $n = 5$) was injected in a mice bearing MC38 tumors. Interestingly, a competition with 1000-fold excess of cold [$^{\text{nat}}\text{Ga}$]Ga-DOTA-RAP-103 ($n = 3$) showed the same trend as observed for the radiotracer [^{68}Ga]Ga-DOTA-RAP-103 by creating tumor-to-blood ratios (2.77 ± 0.75 vs.

1.75 ±0.89). However, no significant differences in the tumor, pancreas or lymph nodes for this radiotracer were detected during target blocking with cold compound.

Additionally, PET/CT images were recorded to show the complete biodistribution *in vivo* and to obtain more details of the pharmacokinetics of the radiotracers. Illustrated in Figure 4.4C shows a rapid renal elimination of the small, hydrophilic radiotracer. Aiming to show at least 2-fold reduction during competition with cold compound PET/CT images were acquired 1 hour p.i. (n = 2). The tumor uptake of radiotracer [⁶⁸Ga]Ga-DOTA-DAPTA-101 and [⁶⁸Ga]Ga-DOTA-RAP-103 was at 0.32 ±0.09%IA/mL and 0.32 ±0.04%IA/mL, respectively. Target saturation exhibited no substantial decrease of the signal (0.23 ±0.08%IA/mL for [⁶⁸Ga]Ga-DOTA-DAPTA-101 and 0.44 ±0.049%IA/mL for [⁶⁸Ga]Ga-RAP-103. Showing rapid tracer elimination, we decided to change the radiotracer strategy by exploiting the properties of the trimer **TRAP-103**.

Despite the lower IC₅₀ of the trimer, the TRAP-based molecule [⁶⁸Ga]Ga-TRAP-103 entails two major advantages for imaging over the DOTA-based monomeric counterpart [⁶⁸Ga]Ga-DOTA-RAP-103. First, the higher protein binding of approximately 50% offers slower elimination favoring target accumulation and second the higher molar activities which can be readily achieved with the TRAP-scaffold [112] can avoid target saturation of unlabeled radiotracer, especially when target expression is scarce. So that, the dose of radiotracer [⁶⁸Ga]Ga-TRAP-103 was reduced 20-times compared to its DOTA-counterpart and 10 pmol (300 GBq μmol⁻¹) were injected while the injected activity remained identical (3 MBq) to the DOTA-based monomeric structure. An initial PET/CT imaging on MC38 bearing mice showed similar results compared to [⁶⁸Ga]Ga-DOTA-RAP-103. Both cohorts (n = 2) showed similar uptake (0.35 ±0.03 vs. competition 0.34 ±0.04%IA/mL). Showing a tumor uptake similar to the monomer, the animal model was changed from a subcutaneous MC38 tumor model to an orthotopic 4T1 tumor model using Balb/C mice which is also characterized by high leukocyte infiltration [80]. A biodistribution assay (n = 5) showed no significant differences between the control and blocking cohort. The radiotracer uptake in the tumor (0.84 ±0.18 control vs. 0.69 ±0.11%IA/g blocking) as well as in the spleen (0.84 ±0.40 control

vs. 0.39 ± 0.15 blocking) was reduced in the blocked cohort. Additionally, spleen-to-blood ratios showed small differences (1.33 ± 0.45 vs. 1.20 ± 0.57) but not tumor-to-blood ratios (1.32 ± 0.17 vs. 2.10 ± 0.63).

Overall, the monomers [^{68}Ga]Ga-DOTA-RAP-103, [^{68}Ga]Ga-DOTA-DAPTA-101 and [^{68}Ga]Ga-DOTA-RAP-103 as well as the trimer [^{68}Ga]Ga-TRAP-103 showed a fast renal elimination and target specificity remained unconfirmed for the investigated radiotracers *in vivo*. Unexpectedly, the specificity in lymph nodes or spleen remained unconfirmed by blocking with 1000-fold molar excess of cold compound or DAPTA. The D-pentapeptide based radiotracers [^{68}Ga]Ga-RAP-103 and the trimer [^{68}Ga]Ga-TRAP-103 lacked specificity in lymphoid organs as well. Showing improved pharmacokinetic properties, the trimer [^{68}Ga]Ga-TRAP-103 exhibited higher uptake in the spleen compared to the blocked cohort but this result remained statistically insignificant. Therefore, tracer optimization is required to obtain molecules with higher plasma protein binding for slower elimination and higher affinities to ultimately increase the specific uptake in leukocyte infiltrated tissues. Using [^{111}In]In-DOTA-DAPTA investigators demonstrated specificity exclusively at inflammatory sites, exhibiting low specific uptake values in conjunction with small animal cohorts [60]. However, to increase the credibility of preclinical studies in immunology, the inclusion of blocking cohorts would be highly appreciated which involves large lymphoid organs confirming radiotracer specificity. This strategy was pursued by exploiting CXCR3 as a biomarker for T cell activation which is described in more detail in chapter 5.

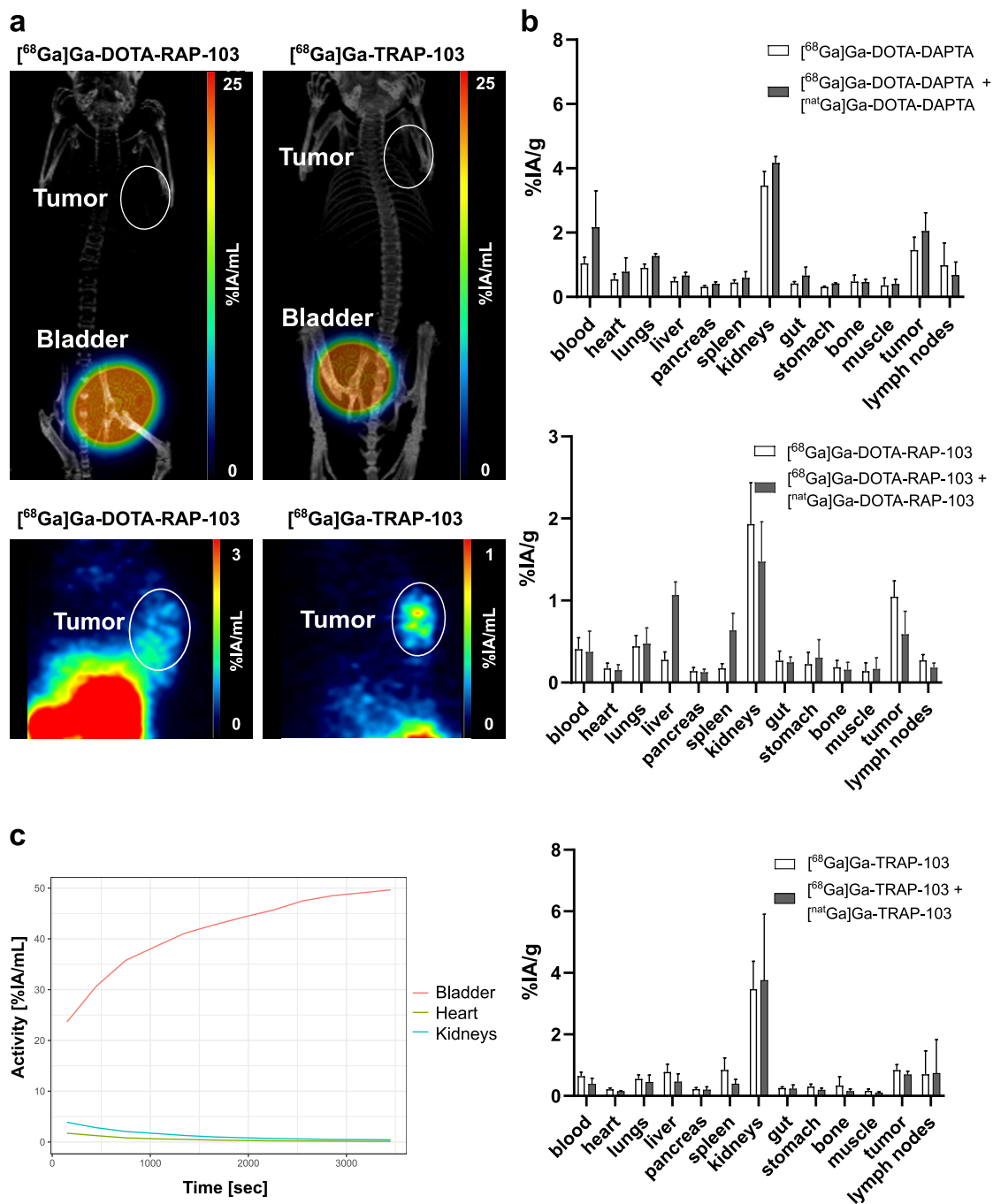


Figure 4.4: *In vivo* evaluation of CC-chemokine receptor specific radiotracers. (A) PET/CT acquisitions 1 h p.i. on B57Bl/6 mice bearing MC38 tumors; (B) Biodistribution assay of $[^{68}\text{Ga}]\text{Ga-DOTA-DAPTA-101}$ (McC38 tumor model, n=5 unblocked, n=3 blocking), $[^{68}\text{Ga}]\text{Ga-DOTA-RAP-103}$ (n=5 per group, MC38 tumor model), $[^{68}\text{Ga}]\text{Ga-TRAP-103}$ (n=5 per group, 4T1 tumor model); (C) Dynamic PET/CT of $[^{68}\text{Ga}]\text{Ga-DOTA-RAP-103}$ (60 min).

5 Exploiting CXCR3 as target for T cell activation imaging

Two different radiotracer types were prepared simultaneously. A radiotracer based on a monoclonal antibody [^{64}Cu]Cu-NOTA- α -CXCR3 was prepared as well as small ^{18}F -labeled radiotracers which were based on a piperazinylpiperidine scaffold similar to highly potent CXCR3 inhibitors reported by Jenh et al. [82] were synthesized. A comprehensive target characterization was performed *in vivo* using the radiotracer [^{64}Cu]Cu-NOTA- α -CXCR3 using a thoroughly characterized MC38 mouse model treated with ICIs, and the corresponding manuscript is currently under revision in npj Imaging (see section 5.2).

5.1 Synthesis and characterization of small piperazinylpiperidine-based radiotracers

Through organic synthesis two radiotracer precursors **XC3-6** and **XC3-B6** were synthesized. Compound **XC3-3** was produced at first by heating piperidine-4-one and 1-chloro-4-(chloromethyl)benzene under basic conditions. This compound was further used for a reductive amination as a final reaction in both synthesis routes. To obtain compound **XC3-6**, 5,6-dichloronicotinic acid was used as starting material and conjugated with propargyl amine. The aromate of the resulting compound **XC3-1a** was subsequently substituted by (S)-1-Boc-2-ethylpiperazine. The Boc protection group was removed under acidic condi-

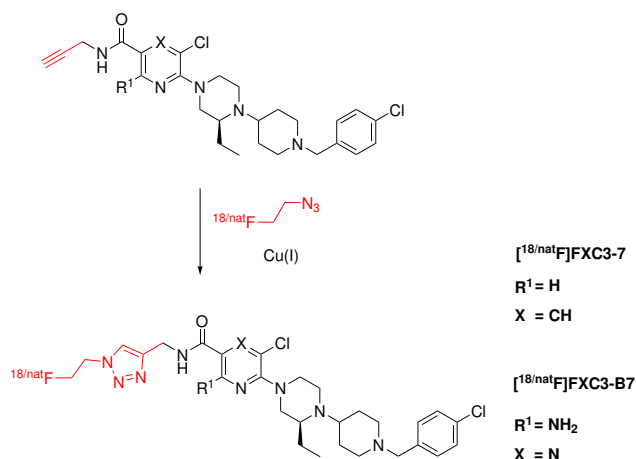


Figure 5.1: Radiotracer synthesis using click chemistry

tions and the resulting compound **XC3-2a** was next reacted with with compound **XC3-3**. To obtain compound **XC3-B6** commercially available starting material 3-amino-5,6-dichloro-N-methylpyrazine-2-carboxamide was utilized. Compound **XC3-1b** was synthesized by aromatic substitution using (S)-1-Boc-2-ethylpiperazine. Under basic conditions with LiOH the methyl ester was hydrolyzed. Since the resulting carbocyclic acid is unreactive most likely through a hydrogen bond with the neighbouring amine, a mild conjugation using EDCI and propargylamine was unsuccessful. Therefore, the carbocyclic acid of compound **XC3-1b** was activated by thionylchloride prior conjugation to the alkyne. The last step included compound **XC3-2b** and **XC3-3** to obtain the final radiotracer precursor **XC3-B6**. Using both precursors **XC3-6** and **XC3-B6**, cold compounds $[^{19}\text{F}]\text{FXC3-7}$ and $[^{19}\text{F}]\text{FXC3-B7}$ were synthesized by click chemistry with freshly produced 2-fluoroethylazide (compound $[^{19}\text{F}]\text{FXC3-5}$) using CuSO_4 and ascorbic acid in a mixture of DMF/water at 60 °C.

To produce the radiotracers a dual-column concept was applied by combining a C18 and a HLB cartridge [106]. The combination allowed the direct isolation of the 2- $[^{18}\text{F}]\text{fluoroethylazide}$ for the on-site click reaction on the HLB cartridge (see Figure 5.1). However, only compound $[^{18}\text{F}]\text{FXC3-7}$ was obtained at room temperature, while the click reaction for compound $[^{18}\text{F}]\text{FXC3-B7}$ and 2- $[^{18}\text{F}]\text{fluoroethylazide}$ (compound $[^{18}\text{F}]\text{FXC3-5}$) required elevated tem-

Table 5.1: Preliminary evaluation of [^{18}F]FXC3-7 and [^{18}F]FXC3-B7. R_t : retention time of the γ -ray detector, gradient: RADIO-20-60ACN.

Compound	R_t [min]	%RCC	Log D	Serum protein binding [%]
[^{18}F]FXC3-7	8.1	45.6 \pm 5.1 (n=3)	1.45 \pm 0.07	98.3 \pm 0.38
[^{18}F]FXC3-B7	8.5	71.6 (n=1)	1.43 \pm 0.03	94.9 \pm 1.21

perature of 60 °C. Applying this dual column synthesis strategy, the radiotracers [^{18}F]FXC3-7 and [^{18}F]FXC3-B7 were isolated by means of radio-HPLC.

5.1.1 *In vitro* characterization of small molecular weight radiotracers

The radiotracers were further evaluated *in vitro* according to their lipophilicity and serum protein binding. Both radiotracers showed a high lipophilicity with Log D values of 1.45 \pm 0.07 ([^{18}F]FXC3-7) and 1.43 \pm 0.03 ([^{18}F]FXC3-B7), respectively. The serum protein binding of the radiotracers was at 98.3 \pm 0.38 for compound [^{18}F]FXC3-B7 and at 94.9 \pm 1.21 for compound [^{18}F]FXC3-7. Binding assays based on membrane preparations were carried out. Due to the discontinuation of [^{125}I]I-CXCL10 (#Cat: NEX348) by the provider, an IC₅₀ study with the cold compounds [^{18}F]FXC3-7 and [^{18}F]FXC3-B7 could not be performed according to specifications of the recommended protocol (Eurofins, France). A membrane binding assay with freshly iodinated CXCL10 using the Iodogen method as well as the corresponding Bolton-Hunter iodinated ligand did not provide any specific membrane binding of the radioiodinated chemokines. Hence, we decided to purchase a customized manufactured [^{125}I]I-CXCL10 (Chelatec, France) with identical specifications to the previous product (MA of 81.4 TBq mmol⁻¹, 185 MBq mL⁻¹, 185 kBq). Although the product showed an identical specification to the radioligand suggested in the original assay protocol (Eurofins, France) and identical assay conditions were used as for the successfully established CCR5-based membrane binding assay (see chapter 4), CXCR3-specific binding of the radiotracer to the membranes could not be observed. However, to provide first vivo data of the radiotracers, non-invasive PET/CT imaging using [^{18}F]FXC3-7 was carried out.

5.1.2 PET/CT imaging using [¹⁸F]FXC3-7

For pilot PET/CT imaging, C57Bl/6 mice bearing MC38 tumors were used. The radiotracer [¹⁸F]FXC3-7 was selected due to higher yields in the precursor synthesis, a more robust click synthesis on the HLB cartridge as well as better synthetic accessibility of [¹⁹F]FXC3-7 as blocking agent. The blocking was carried out by co-injection with an 1000-fold excess of cold [¹⁸F]FXC3-7. Two C57Bl/6 mice of each cohort (control vs blocking) bearing a MC38 tumor on the right flank were injected i.v. with 0.1 nmol of radioligand for the PET/CT imaging. Of note, the initial MA of the injected radiotracer preparation was (19.22 ± 0.53) GBq μmol^{-1} (n=3) and the purity of the isolated radiotracer was >99%. The reconstructed images showed a high uptake in the liver and intestines as well as an uptake in the brown adipose tissue (BAT) (see Figure 5.2). The liver uptake was at $20.1 \pm 7.3\%IA/mL$ (blocking $23.8 \pm 4.4\%IA/mL$), in the spleen $13.1 \pm 1.4\%IA/mL$ (blocking: $17.2 \pm 4.3\%IA/mL$), the BAT $10.0 \pm 0.8\%IA/g$ (blocking: $12.4 \pm 3.9\%IA/mL$), and the kidneys $16.9 \pm 1.6\%IA/mL$ (blocking: $19.9 \pm 2.4\%IA/mL$). The tumor uptake was $2.9 \pm 1.1\%IA/mL$, while the blocking was marginally higher ($3.3 \pm 1.3\%IA/mL$).

Overall, the acquired PET images were in concordance with the recently published study by Alluri et al. [78] using the CXCR3 specific radiotracer [¹⁸F]1 with a similar structure. Our data confirmed significant abdominal uptake of the lipophilic radiotracer (log D = 1.5), leading to a considerable first-pass effect in the liver. Both lipophilic radiotracers [¹⁸F]FXC3-7 investigated in this study and [¹⁸F]1 [78] showed a similar uptake in the BAT of roughly 10%IA/mL and 20%IA/mL in the liver. However, in comparison to the findings using compound [¹⁸F]1 [78] we could not confirm a decrease in BAT uptake by coinjection of cold ligand (blocking). This suggests predominant non-specific accumulation of [¹⁸F]FXC3-7 in fat tissue due to the high lipophilicity of the radiotracer. Of note, specific (blockable) radiotracer uptake was exclusively observed during the validation of the mAb-based radiotracer [⁶⁴Cu]Cu-NOTA- α -CXCR3 which showed specificity in spleen and lymph nodes. In contrast, the small-molecular weight radiotracer [¹⁸F]FXC3-7 did not show specific uptake in these

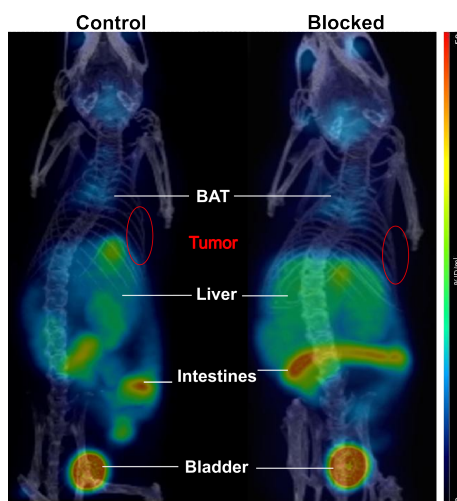


Figure 5.2: Maximum intensity projections of radiotracer $[^{18}\text{F}]\text{FXC3-7}$ (injected activity: 2 MBq; injected dose: 0.1 nmol). Blocking was performed with co-injection a 1000-fold molar excess of $[^{\text{nat}}\text{F}]\text{FXC3-7}$. Images were acquired 1 hour post-injection. BAT: brown adipose tissue.

highly T cell infiltrated tissues. Noteworthy, the radiotracer preparation showed a 15-fold reduced MA compared to the ^{64}Cu -mAb which is likely contributing to this observation. In addition, affinity data was lacking which is a relevant criterion to obtain sufficient radiotracer uptake as reported for $[^{64}\text{Cu}]\text{Cu-NOTA-}\alpha\text{-CXCR3}$ (KD = 3.3 nM). Due to the absence of affinity data and the results of the ^{64}Cu -mAb evaluations, which demonstrated the challenges associated with *in vivo* imaging of CXCR3, further investigations were omitted.

Taken together, we propose a refinement of the small molecular weight radiotracers to achieve satisfactory biodistribution for non-invasive imaging using radiotracer preparations with increased MA and optimized pharmacokinetics (Log D -1 to -3), ideally showing picomolar affinities on CXCR3, to overcome the addressed challenges of imaging the TME discussed in section 8.2.

5.2 Validation of the C-X-C chemokine receptor 3 (CXCR3) as a target for PET imaging of T cell activation

This article was submitted to EJNMMI Research in May 2024.

Validation of the C-X-C chemokine receptor 3 (CXCR3) as a target for PET imaging of T cell activation

Sebastian Martin^{1,2,3}, Lennard Wendlinger^{1,2,3}, Béatrice Zitti^{2,5}, Mehdi Hicham^{2,5}, Viktoriia Postupalenko⁴, Léo Marx⁴, Greta Giordano-Attianese⁶, Elisabetta Cribioli⁶, Melita Irving⁶, Alexandra Litvinenko^{1,2,3}, Radmila Faizova^{1,2,3}, David Viertl^{1,2,3}, Margret Schottelius^{1,2,3}

¹*Translational Radiopharmaceutical Sciences, Department of Nuclear Medicine and Department of Oncology, Centre Hospitalier Universitaire Vaudois (CHUV) and University of Lausanne (UNIL), 1011 Lausanne, Switzerland*

²*AGORA, Pôle de recherche sur le cancer, 1011 Lausanne, Switzerland*

³*SCCL Swiss Cancer Center Leman, 1011 Lausanne, Switzerland*

⁴*Debiopharm Research & Manufacturing SA, Campus “après-demain”, Rue du Levant 146, 1920 Martigny, Switzerland*

⁵*Department of Pathology and Immunology, University of Geneva, Geneva, Switzerland*

⁶*Ludwig Institute for Cancer Research, University of Lausanne, 1066 Epalinges, Switzerland; Department of Oncology, University Hospital of Lausanne, 1011 Lausanne, Switzerland*

***Corresponding Author:**

Prof. Dr. Margret Schottelius

Phone +41.21.545.1120

Mobile +41.79.556.0143

Email: margret.schottelius@chuv.ch

Keywords: CXCR3, Immunotherapy, chemokine receptor, T cell activation imaging

Abstract

Purpose: CXCR3 is expressed on activated T cells and plays a crucial role in T-cell recruitment to the tumor microenvironment (TME) during cell-based and immune checkpoint inhibitor (ICI) immunotherapy. This study utilized a ^{64}Cu -labeled NOTA- α -CXCR3 antibody to assess CXCR3 expression in the TME and validate it as a potential T cell activation biomarker in vivo.

Procedures: CXCR3⁺ cells infiltrating MC38 tumors (B57BL/6 mice, untreated and treated with α PD-1/ α CTLA-4 ICI) were quantified using fluorescence microscopy and flow cytometry. A commercial α -CXCR3 mAb was site-specifically conjugated with 2,2,2-(1,4,7-triazacyclononane-1,4,7-triyl)triacetic acid (NOTA) and radiolabeled with ^{64}Cu . Saturation binding of [^{64}Cu]Cu-NOTA- α -CXCR3 was investigated using CHO cells stably transfected with murine CXCR3. Biodistribution and PET imaging studies both at baseline and after 1 to 3 cycles of ICI, respectively, were carried out using different molar activities (10 GBq/ μmol to 300 GBq/ μmol) of [^{64}Cu]Cu-NOTA- α -CXCR3.

Results: Flow cytometry analysis at baseline confirmed the presence of CXCR3⁺ T-cells in MC38 tumors, which was significantly increased at day five after ICI (treated 33.8 ± 17.4 vs control 8.8 ± 6.2 CD3⁺CXCR3⁺ cells/mg). These results were qualitatively and quantitatively confirmed by immunofluorescence of tumor cryoslices. In vivo PET imaging of MC38 tumor bearing mice before, during and after ICI using [^{64}Cu]Cu-NOTA- α -CXCR3 (Kd = 3.3 nM) revealed a strong dependence of CXCR3-specificity of tracer accumulation in secondary lymphoid organs on molar activity. At 300 GBq/ μmol (1.5 μg of antibody/mouse), a specific signal was observed in lymph nodes (6.33 ± 1.25 control vs 3.95 ± 1.23 %IA/g blocking) and the spleen (6.04 ± 1.02 control vs 3.84 ± 0.79 %IA/g

blocking) at 48 hours p.i. Spleen-to-liver ratios indicated a time dependent systemic immune response showing a steady increase from 1.08 ± 0.19 (untreated control) to 1.54 ± 0.14 (three ICI cycles).

Conclusions: This study demonstrates the feasibility of in vivo imaging of CXCR3 upregulation under immunotherapy using antibodies. However, high molar activities and low antibody doses are essential for sensitive detection in lymph nodes and spleen. Detecting therapy-induced changes in CXCR3⁺ T cell numbers in tumors was challenging due to secondary antibody-related effects. Nonetheless, CXCR3 remains a promising target for imaging T cell activation, with anticipated improvements in sensitivity using alternative tracers with high affinities and favorable pharmacokinetics.

Introduction

Generally, the success and therapeutic efficacy of immunotherapies intrinsically rely on the presence and activity of T cells in the TME. Both for ICI as well as cell-based immunotherapies (adoptive tumor infiltrating lymphocyte (TIL) and chimeric antigen receptor T cell (CART cell)), no or negligible anti-tumor responses are observed, when CD8⁺ effector and CD4⁺ helper T cells are sparse or absent from the TME or if they are inactive due to immunosuppressive signaling in and by the tumor and TME [1-3]. Unfortunately, tumor biopsies can only provide spatial and temporal spotlight information on the composition of the TME in a given cancer lesion and do not capture the dynamics of the immune cell infiltrate over time and in response to therapy. In contrast, nuclear imaging methods such as positron emission tomography (PET) and single photon emission computed tomography (SPECT) allow the longitudinal non-invasive whole-body visualization of distinct cell populations. Fueled by the development of dedicated, highly specific radiopharmaceuticals in recent years, the

non-invasive quantification of tumor infiltration with distinct immune cell subsets, e.g. CD8⁺ cytotoxic T cells [4], is now rapidly entering clinical practice, providing crucial information for patient selection and on early response to immune checkpoint blockade. Furthermore, ongoing efforts are directed towards not only visualizing the presence, quantity and localization of T cells in the TME, but on imaging their activation state, which may represent a more robust predictor for the success of immunotherapies than T cell presence alone [5]. Various molecular targets have been investigated as biomarkers for T cell activation in recent years. These include OX40 [6], CD69 [7], inducible T cell costimulator (ICOS) [8, 9], interleukin-2 receptor (IL-2R) [10, 11], interferon gamma (INF- γ) [12], Granzyme B [13], and T-cell metabolism [14]. In preclinical PET imaging studies using specifically designed targeted tracers, ranging from full-sized antibodies (OX40, CD69, ICOS, INF- γ) over proteins (IL-2) and peptides (Granzyme B) to small molecules (metabolism), all these targets were found to be relevant molecular markers for T-cell activity, with the accumulation of the respective targeted tracer in the tumor or site of inflammation (pre and/or post-therapy) closely correlating with the presence of activated T cells in the tissue of interest and with therapy response [6-14]. Of these, both the metabolic tracer [¹⁸F]F-AraG (NCT04726215, NCT05096234) as well as the human Granzyme B targeted [⁶⁸Ga]Ga-NOTA-human-GZP (NCT04169321) have recently been translated into clinical studies.

Another highly interesting cell surface marker associated with T cell activation is the CXCR3 [15]. CXCR3 directs the temporal and spatial migration of activated T cells and natural killer cells towards sites of high expression of its native ligands, the INF- γ inducible proteins, C-X-C chemokine ligands 9 (CXCL9), CXCL10, and CXCL11 [16,

17] creating an inflammatory environment. Both in the context of ICI and of TIL-therapies, the CXCR3-chemokine axis was identified as a key player in the efficient recruitment of T cells to the TME as well as their expansion in the TME and their antitumor-activity [15, 18, 19]. Thus, CXCR3 represent a highly promising target for nuclear imaging, possibly allowing the visualization of T-cell distribution, homing and activation in the immunotherapy setting, both as a pretherapeutic prognostic marker as well as for assessing response to treatment. To date, only two reports on CXCR3-targeted nuclear imaging have been published, both of which use inflammation models (allograft rejection, atherosclerosis) for tracer evaluation [20, 21]. However, both radiopharmaceuticals investigated, [^{125}I]CXCL10 [20] and an ^{18}F -labeled small molecule CXCR3 inhibitor [21] accumulated specifically in inflammatory regions infiltrated with CXCR3-expressing T cells, and the respective signal intensity correlated with CXCR3⁺ T cell density.

Based on these encouraging findings, we designed the present study to validate CXCR3 as an imaging target in the TME and as a potential biomarker for therapy control and the prediction of therapy outcome in the immunotherapy setting. For the initial quantification of target expression at baseline and after several cycles of immunotherapy (anti-programmed cell death protein 1 ($\alpha\text{PD-1}$)/anti-cytotoxic T-lymphocyte-associated protein 4 ($\alpha\text{CTLA-4}$)) in a MC38 syngeneic colon cancer model via CXCR3-targeted PET, we used a commercially available anti-mouse CXCR3 antibody ($\alpha\text{-CXCR3}$). The monoclonal antibody (mAb) was site-specifically conjugated with a 2,2,2-(1,4,7-triazacyclononane-1,4,7-triyl)triacetic acid (NOTA) chelator using the AbYlink™ technology and radiolabeled with ^{64}Cu .

Methods

Antibody conjugation and characterization

Upon buffer exchange using an Amicon 50 kDa centrifugal filter, a commercially available anti-mouse CXCR3 mAb (clone: CXCR3-173, #Cat: BE0249, BioXcell) was site-specifically conjugated with NOTA according to a previously published protocol conjugated with (AbYlink™, Debiopharm) [22]. The average degree of conjugation (DoC) was determined by mass spectrometry analysis operating in protein mode (Sion, EPFL) and the final antibody concentrations were determined by a NanoDrop One/One spectrophotometer (Thermo Fisher).

Radiolabeling

A solution of ^{64}Cu dichloride in 0.1 N HCl was obtained from ARRONAX (Saint Herblain, France). To a defined volume of the $^{64}\text{CuCl}_2$ solution supplied by the manufacturer, 1/10 (v/v) of metal free sodium acetate 2.5 M (pH 8.5) was added. Then, the radiolabeling precursor (30-80 μg) in acetate buffer (0.1 M, pH 5.5) was added. After 30 min incubation at 40°C, 1 mM ethylenediaminetetraacetic acid (EDTA) (pH 7.0, Sigma Aldrich, St. Quentin Fallavier, France) was added to obtain a final concentration of 0.01 mM to complex free $^{64}\text{Cu}^{2+}$.

Size exclusion chromatography

Size exclusion chromatography (SEC) was performed on a Shimadzu (LC20AT, SPD-M20A) system using a XBridge protein BEH 200A SEC 3.5 μm , 7.8 x 300mm (Waters, Baden-Dättwil, Switzerland) size exclusion column and phosphate buffer (pH 6.8, 0.1 M) containing 342 mM NaCl at a constant flow of 1 mL/min as mobile phase. UV

detection was performed at 220, 254 and 280 nm, and the radioactivity signal was detected using a GABI well-type scintillation detector (Elisa-Raytest). Unconjugated α -CXCR3: R_t (retention time) 8.5 min, purity 99.2%; NOTA- α -CXCR3: R_t 8.5 min, purity 98.8%; [^{64}Cu]Cu-NOTA- α -Cxc3: R_t 8.6 min, radiochemical purity (RCP) >99%.

Stability in human serum

To a volume of 500 μL of human serum, 50 μL of radiotracer were added. The mixture was incubated at 37°C. SEC analyses were carried out after 24 and 48 hours of incubation. Before injection, 100 μL of the sample were passed through a 0.2 μm filter.

[^{64}Cu]Cu-NOTA- α - CXRCR3: R_t = 8.6 min, RCP after 24 and 48 hours >95%.

Instant thin layer chromatography (iTLC)

In-process reaction controls were performed using iTLC. The radiochemical yield (RCY) of [^{64}Cu]Cu-NOTA- α -CXCR3 was determined by instant thin layer chromatography (iTLC) using dried iTLC-SG Glass microfiber chromatography paper impregnated with silica gel (Agilent Technologies, Folsom, CA 95630) as stationary phase and citrate buffer (0.1 M, pH 4.5) as eluent. For iTLC evaluation, a Scan-RAM radio-TLC scanner (LabLogic) and Laura software (LabLogic, Version 6.0.3) were used.

[^{64}Cu]Cu-EDTA, R_f = 1; [^{64}Cu]Cu-NOTA- α -CXCR3, R_f = 0.

Saturation binding assay

Transfected CHO-CXCR3 cells were maintained and expanded using Ham's F-12 Nutrient Mix cell culture media (Thermo Fisher Scientific) supplemented with 10% fetal bovine serum (FBS) and 1% penicillin/streptomycin in a cell incubator at 37°C, 5% CO_2 .

2×10^6 CHO-CXCR3 cells were seeded in a 6-well plate one day before the experiment. On the day of the experiment, the growth medium was removed and the cells were washed once with cold assay buffer (0.5% BSA in PBS). Then, 800 μ L of assay buffer were added into each well, and the radiolabeled antibody (100 μ L, increasing concentrations, n=3 per concentration) was added. Additionally, 100 μ L assay buffer were added to the wells to reach a final volume of 1 mL. Final concentrations of [64 Cu]Cu-NOTA- α -CXCR3 were as follows: 25, 10, 1, 0.5, 0.25, 0.125 and 0.063 nM (n=3 per radioligand concentration). To determine non-specific binding at each radioligand concentration, radioligand binding was also investigated in the presence of a 100-fold excess of unlabeled α -CXCR3. Here, 100 μ L of α -CXCR3 antibody in assay buffer was added to the well to reach a final volume of 1 mL (n=3 per radioligand concentration). Plates were incubated for 2 hours at 4 °C. The supernatant was removed and combined with 1 mL of assay buffer using for washing the cells. The cells were then lysed with 1 M NaOH. The cell lysate was then combined with 1 mL of assay medium using for washing the wells. Both the activities in the supernatants and the respective lysates were quantified using a γ -counter (Wizzard 3, Perkin Elmer). Non-specific binding and total binding were analysed by GraphPad prism version 9.1.0.

Animal experiments

Animal experiments were conducted according to the protocols approved by the Veterinary Authorities of the Canton Vaud (license VD 3781) and in accordance with the Swiss Animal Welfare Act. Six to eight week-old female B157/6 mice were purchased from Charles River Laboratories (France, L'Arbresle). MC38 cells were maintained in RPMI 1640 GlutaMAXTM cell culture media (Thermo Fisher Scientific) supplemented with 10%

FBS and 1% penicillin/streptomycin in a cell incubator at 37°C, 5% CO₂. Tumor engraftment and the subsequent treatment schedule were conducted as described previously [23]. Briefly, MC38 tumors were engrafted on the right flank by subcutaneous injection of 2x10⁶ cells in 100 uL PBS. The first treatment with immune checkpoint inhibitors (ICIs) was initiated at day 7 post-engraftment. The checkpoint inhibitor combination consisted of 200 µg αCTLA-4 (clone: 9D9, #Cat: BP0164, BioXCell) and 200 µg αPD-1 (clone: 29F.1A12, #Cat: BE0273, BioXCell) and was injected i.p. in a total volume of 100 µL of sterile PBS. Additional treatments were administered on day 10 and on day 13 after tumor inoculation. At day 10 (untreated and 1xICI treated) and day 12 (2xICI treated) post-inoculation, MC38 tumors were dissected for flow cytometry, immunofluorescence, or immunohistochemistry analysis. Tumor size was monitored using caliper measurements and by applying the following formula to calculate the tumor volume: *tumor volume = (length/2) *width²*.

Flow cytometry

After harvesting the MC38 tumors, single cell suspensions were immediately generated by cutting the tumor in small pieces and incubating the tissue in 1 mL FBS containing collagenase IV (0.2 mg/L) and DNase I (2 µg/L). Upon incubation at 37 °C for 20 minutes, the tissue was passed through a cell strainer and the cell suspension was washed two times with cold PBS. The stainings were carried out at room temperature for 25 minutes in flow cytometry buffer (PBS suppl. with 1 mM EDTA, 1% FBS). Control stainings and FMO stainings were performed on splenocytes. The following antibodies were utilized: Fc block (clone: 93, #Cat: 101302, Biologend), DAPI (Invitrogen), CD45 (clone: 30-F11, #Cat: 103132, Biologend), CD3 (clone: 145-2c11, #Cat: 100306, Biologend), CD4 (clone: Gk-

1.5, #Cat: 552051, Biolegend), CD8: (clone 53-6.7, #Cat: 100712, Biolegend), CXCR3 (clone: CXCR3-173, #Cat: 126502, Biolegend). The antibody concentrations were 1 µg/mL in flow cytometry buffer. DAPI was added to each sample to yield a final concentration of 0.5 µg/mL and the cells were washed once. The cells were fixed with 2% PFA in PBS on ice. Precision count beads (#Cat: 424902, Biolegend) were added to each tumor sample and compensation beads were used (#Cat: 01-3333-42, Thermo Scientific) to set up the panel. The analysis was performed on a BD FACSymphony A5 Flow Cytometer on the same day. The data was evaluated using FlowJo V10.7.1.

Immunofluorescence

Immunofluorescence stainings were performed using acetone fixed tissue slices. The tissues were blocked with donkey and goat serum (10%) for 20 min. After washing the samples in 0.3% triton in PBS, tissues were incubated with the primary antibodies (1:50, diluent DAKO S3022) for 60 min at RT. After another washing step, the staining was completed by incubation with the respective fluorescent secondary antibody (1:500, diluent DAKO S3022) for 30 min at room temperature. DAPI (Sigma, #Cat: D9542, 1:3000 dilution in PBS) nuclear staining was used as control color. After the slices had been rinsed with distilled water, the slices were coverslipped with water-based mounting media (DAKO S3023). Negative controls were incubated with the fluorescent secondary antibodies only. For fluorescence microscopy image evaluation, the QuPath version 0.3.2 software for digital pathology image analysis was used by applying a trained object classifier for the positive cell annotation [24].

Immunohistochemistry

Immunohistochemistry stainings were performed on acetone fixed slices. The tissues were

blocked with goat serum (10%) for 20 min. After washing the samples in 0.3% triton in PBS, tissues were incubated with the respective primary antibodies (1:200, diluent DAKO S2022) at room temperature for 40 min. After another washing step, the staining was completed by incubating the slices with the secondary antibody (HRP-conjugated anti-rabbit, DAKO K4003) for 30 min at room temperature. After another washing step, the staining was completed by DAB chromogen revelation (DAKO K3468). Harris Gill II was applied as control color. Subsequently, the slides were dehydrated in xylol and covered with permanent mounting. Negative tissues were stained with the secondary antibody (HRP anti-rabbit) only.

Autoradiography

Autoradiography experiments were performed on a BeaQuant S real time autoradiography instrument (ai4R, Nantes). The radiotracer [⁶⁴Cu]Cu-NOTA- α -CXCR3 (2-3 MBq, 3 μ g, containing 50 μ g polyclonal Armenian hamster IgG (BioXCell, #BE0091)) was injected, and at 24h p.i., the spleens were harvested and transferred to optimal cutting temperature compound (O.C.T. Tissue-Tek, Sakura Finetek). Spleens were immediately frozen on dry ice. Slices (8 μ m) were cut and left to dry on the glass plate for 2 hours at RT. The autoradiography measurement was performed overnight for 24 hours. Images were analyzed using BEAMAGE (v3.3.X) software.

Biodistribution study

ICI treated MC38 tumor bearing mice were injected intravenously into the tail vein with 1.5 μ g (3 MBq) or 15 μ g (1 MBq) [⁶⁴Cu]Cu-NOTA- α -CXCR3 in 100 μ L sterile 0.9% NaCl on day 9 (untreated and 1xICI treated) and on day 12 (2xICI treated) post-

inoculation. To reduce Fc-mediated non-specific tracer accumulation, mice were coinjected with 50 μg polyclonal Armenian hamster IgG (BioXCell, #BE0091). To quantify CXCR3-specific tracer accumulation, an additional group of mice ($n = 3-5$) was coinjected with a 100-fold excess of unconjugated α -CXCR3. The animals were sacrificed 24 hours (15 μg , 1 MBq injected activity) or 48 hours (1.5 μg , 3 MBq injected activity) post-injection of the ^{64}Cu -labeled antibody, and the organs of interest were dissected. The activity in the weighed tissue samples was quantified using a Wizard 3 y-counter (Perkin Elmer, Schwerzenbach). Data are expressed in %IA/g tissue (mean \pm SD) and are corrected for residual injection-related activity in the tail.

PET/CT imaging

PET/CT images were acquired at 24 h p.i. on an Albira PET/SPECT/CT scanner (Bruker Biospin Corporation, Woodbridge, CT, USA) Mice were injected intravenously with [^{64}Cu]Cu-NOTA- α -CXCR3 (3 MBq, 1.5 μg) in saline. As described for the biodistribution study, CXCR3-specificity of tracer accumulation was determined by coinjection of a 100-fold excess of unlabeled α -CXCR3 mAb. During image acquisition (static scan, 20 min, 32x32 0.5 mm, followed by a 10 min CT scan), the animals were anesthetized using isoflurane (1.5% alveolar concentration). During imaging, the body temperature and respiration rate was constantly monitored. Image reconstruction was performed by using Albira reconstructor (version NMI3.3), and the images were analyzed using PMOD software (V6.3.4, Bruker).

Statistical analysis

All data were evaluated using GraphPad Prism version 9.1.0 for Windows, GraphPad

Software, San Diego, California USA. A two-way Anova test followed by a Tukey's multiple comparisons test was applied to determine the significance ($P < 0.05$) between the respective cohorts of the flow cytometry and biodistribution experiments. A one-way Anova test followed by a Tukey's multiple comparisons test was applied to determine the significance ($P < 0.05$) of the organ/liver or organ/blood ratios.

Results

Confirmation of therapy dependent infiltration of MC38 tumors with CXCR3⁺ cells

To confirm and quantify the infiltration of subcutaneous MC38 syngeneic colon cancer tumors with CXCR3-expressing T cells both at baseline and after ICI therapy (α -PD-1/ α -CTLA-4 combination treatment) in a sufficient number for imaging, the following cohorts were investigated using immunohistochemistry (IHC) and immunofluorescence (IF) methods: (1) an untreated control group, (2) a treated group receiving one cycle of ICI therapy and (3) a treated group receiving two cycles of ICI therapy at days 7 and 10 post tumor inoculation, respectively. IHC of untreated tumors and tumors treated with only one dose of ICI showed weak CD3⁺ cell infiltration that was restricted to the outer rim of the tumor (Figure 1A). In contrast, after two therapy cycles, the tumors showed an increased and more homogeneous infiltration with CD3⁺ T cells. Immunofluorescence staining for CXCR3 revealed the presence of CXCR3-expressing T cells both in untreated and in treated tumors as well as in the control tissues spleen and lymph nodes. The corresponding annotated tissue slides are shown in Figure 1A-D. While only 3.4 \pm 1.9% CXCR3⁺ cells were detected in the untreated MC38 tumor tissues, two cycles of therapy cycles led to a significant increase in CXCR3⁺ cells (9.7 \pm 2.8%). This observation is in accordance with the findings in CD3⁺ IHC. Again, treated tumors show increased and more homogenous infiltration than untreated tumors, where CXCR3⁺ cells are mainly localized on the outer rim of the tumor. Furthermore, more CXCR3⁺ cell clusters were detected in the interior of the tumors which received two treatment cycles (Figure 1C).

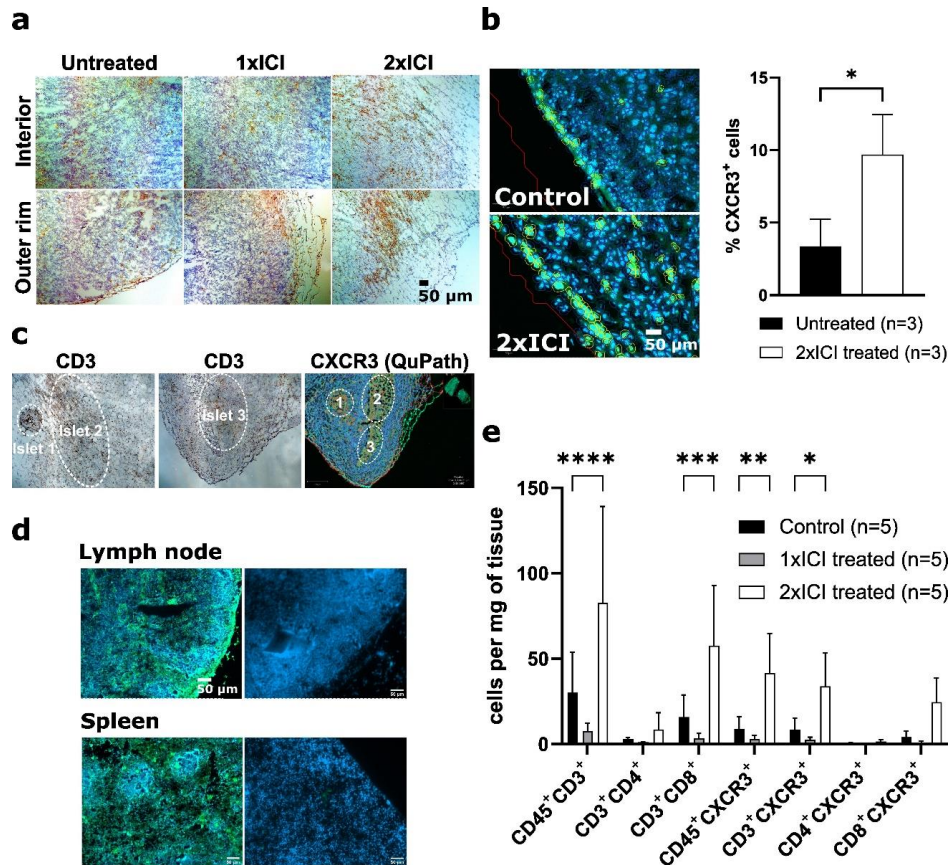


Figure 1 (a) CD3 immunohistochemistry of MC38 tumors treated with either one (1xICI) or two cycles of α PD-1/ α CTLA-4 ICI (2xICI); (b) Fluorescence microscopy of MC38 tumor slices. Cells (DAPI in blue, CXCR3 in green) were annotated and counted using Qupath; (c) Overlap regions of MC38 cryoslices from immunohistochemistry (CD3) and immunofluorescence (CXCR3) images; (d) Baseline CXCR3 immunofluorescence in untreated lymphoid tissues (left), with negative controls (stained without primary antibody) on the right; (e) Flow cytometry analysis of MC38 tumors treated either with one or two cycles of ICI.

To further corroborate the above data from the tissue analysis via IHC and IF, we additionally performed an in-depth analysis of the composition of the TME by flow cytometry, with lymphocytes being gated using CD45 as global immune cell marker. The tumors of the cohort which had received two therapy cycles showed a significant increase in CD3⁺ T cells as well as in the CD8⁺ T cell fraction (see Figure 1E). This

cohort also exhibited a global increase in CXCR3⁺ lymphocytes (8.7±6.6 vs 41.7±20.5 CXCR3⁺ cells/mg). This and a significant increase in CD3⁺CXCR3⁺ T cell numbers (8.8±6.2 vs 33.8±17.4 CD3⁺CXCR3⁺ cells/mg) confirmed the observation from the IF analysis. After one treatment cycle, however, no changes in immune cell infiltration were observed three days after therapy. As demonstrated, T cell infiltration in the MC38 tumors was robust and up to threefold enhanced after ICI therapy, and therefore the chosen MC38 tumor model seemed appropriate for subsequent imaging studies.

Antibody conjugation and radiolabeling

The Fc-specific conjugation of the commercially available α -CXCR3 mAb with the NOTA chelator using the AbYlinkTM technology (see Suppl. Figure S 1) [22] proceeded efficiently, yielding NOTA- α -CXCR3 in 98.8% purity and with a final average degree of conjugation (DoC) of 1.5, as determined by mass spectrometry (Suppl. Figure S 2). Of note, NOTA- α -CXCR3 was found to remain fully stable for > 12 months at 4 °C in labeling buffer (NaOAc, 0.1 M, pH 5.5). Since high molar activities (MAs) are indispensable for sensitive target detection at comparably low expression levels, the same amount of NOTA- α -CXCR3 (31.3 μ g, 0.2 nmol) was labeled with increasing ⁶⁴Cu activities (10 to 50 MBq). The maximum achievable MA for [⁶⁴Cu]Cu-NOTA- α -CXCR3 under the used standard labeling conditions was 690 GBq/ μ mol, with a radiochemical yield (RCY) of 96.8% (Suppl. Figure S 3). For preparations with lower MA, RCYs of > 99% were consistently obtained (see Figure 2A).

In vitro characterization of [⁶⁴Cu]Cu-NOTA- α -CXCR3

The binding affinity (K_D) of the radiolabeled mAb was determined by a saturation

binding assay using CHO cells stably transfected with CXCR3 (see Figure 2B and Suppl. Figure S 4). The antibody showed specific binding to the transfected cells with a K_D of 3.26 nM and a B_{max} of 8.8 fmol CXCR3 receptors per 10^6 cells (5280 receptors per cell). Additionally, [^{64}Cu]Cu-NOTA- α -CXCR3 was found to be stable in human serum for 48 hours at 37 °C (Suppl. Figure S 5).

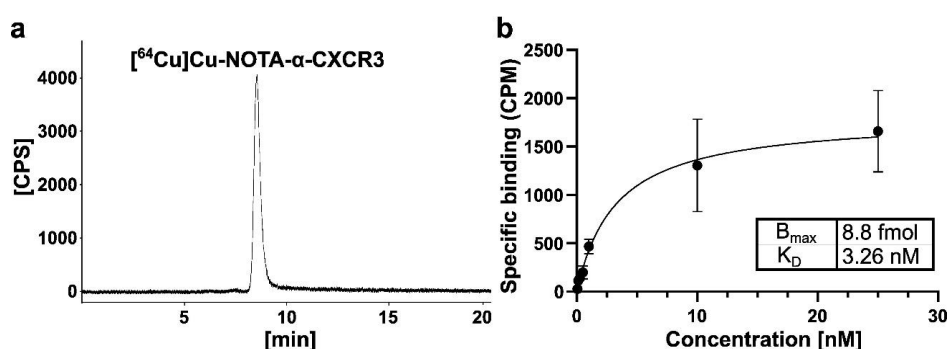


Figure 2: (a) Radio-SEC chromatogram of [^{64}Cu]Cu-NOTA- α -CXCR3 ($R_t = 8.6$ min, RCP > 99%); (b) Saturation binding of [^{64}Cu]Cu-NOTA- α -CXCR3 to murine CXCR3 (stably transfected CHO cells).

In vivo characterization of [^{64}Cu]Cu-NOTA- α -CXCR3 in tumor-free mice

To evaluate the general biodistribution of the ^{64}Cu -labeled antibody *in vivo*, orienting PET/CT imaging was performed 48 hours p.i. in a tumor-free WT mouse (see Figure 3A). This preliminary image demonstrated a potentially CXCR3-mediated radiotracer accumulation in the spleen and cervical lymph nodes as well as excretion-related uptake in the liver. To investigate whether a systemic activation induced by ICI treatment could be detected in healthy mice, an initial autoradiography experiment (see Figure 3B) was performed. Spleens from an untreated control and an ICI treated mouse were dissected and snap-frozen, and tissue slices were prepared. Quantitative real-time autoradiography revealed a significant increase in activity, from 0.36 ± 0.002 (control) to 0.45 ± 0.01 (2xICI)

counts per second (cp/s), was observed, hinting towards an increase in CXCR3-expression in the spleen due to systemic T-cell activation by ICI treatment. However, to prove CXCR3-specificity of [⁶⁴Cu]Cu-NOTA- α -CXCR3 uptake in lymphoid tissues, detailed biodistribution and imaging studies were performed in MC38 tumor bearing mice.

Biodistribution of [⁶⁴Cu]Cu-NOTA- α -CXCR3 in MC38 bearing mice

The biodistribution of [⁶⁴Cu]Cu-NOTA- α -CXCR3 in C57BL/6 mice bearing subcutaneous MC38 tumors at 24 hours p.i. was first investigated using an antibody dose of 15 μ g (MA = 10 GBq/ μ mol) per animal (Suppl. Figure S 6). To evaluate CXCR3-specificity of tracer binding to secondary lymphoid organs (lymph nodes, spleen), mice were either injected with tracer only (control group) or coinjected with a 100-fold molar excess of unlabeled antibody (blocking). Under these conditions, no CXCR3-specific tracer accumulation was observed in the target organs. Since target expression was assumed to be comparably low at baseline (no treatment), the presence of relatively high amounts of unlabeled antibody in the low-molar-activity-preparation of [⁶⁴Cu]Cu-NOTA- α -CXCR3 was thought to be responsible for already blocking all available binding sites, even in the control group. Thus, and due to the relatively high blood concentration of [⁶⁴Cu]Cu-NOTA- α -CXCR3 at 24 hours post-injection (p.i.), a second set of biodistribution studies was performed at 48 hours p.i. and at a ten-fold lower antibody dose (1.5 μ g, MA = 300 GBq/ μ mol) (Table 1). Under these conditions, specific binding of [⁶⁴Cu]Cu-NOTA- α -CXCR3 to CXCR3-expressing cells in spleen and lymph nodes was confirmed (control vs control blocking: P = 0.005 and 0.007, unpaired Student's T test).

Table 1: Biodistribution of [⁶⁴Cu]Cu-NOTA- α -CXCR3 in MC38 tumor bearing C57Bl/6 mice at 48 hours p.i.. Uptake values are expressed as %IA/g (%-injected activity per gram of tissue) and are means \pm SD (n=5 mice per group). Groups include untreated mice (Control), mice treated with 1 cycle of ICI (1xICI), mice treated using 3 cycles of ICI (3xICI). Blocking of 3xICI treated and blocking of untreated control mice was conducted using a 100-fold molar excess of α -CXCR3 antibody.

Organ	Control	Blocking (untreated control)	1xICI	3xICI	Blocking (3xICI)
Blood	19.3 \pm 2.1	19.96 \pm 2.36	16.69 \pm 1.37	16.30 \pm 4.29	20.10 \pm 1.56
Heart	4.62 \pm 0.45	5.31 \pm 1.64	4.62 \pm 0.95	5.14 \pm 1.86	6.27 \pm 1.03
Lungs	7.30 \pm 0.94	8.91 \pm 2.61	6.10 \pm 0.63	6.85 \pm 3.58	7.21 \pm 0.53
Liver	5.62 \pm 0.39	5.85 \pm 1.30	5.79 \pm 0.28	4.46 \pm 1.44	5.34 \pm 0.41
Pancreas	1.85 \pm 0.14	1.82 \pm 0.47	1.69 \pm 0.22	2.59 \pm 0.57	2.55 \pm 0.91
Spleen	6.04 \pm 1.02	3.84 \pm 0.79	6.48 \pm 0.45	6.19 \pm 2.11	3.51 \pm 0.99
Kidneys	5.22 \pm 0.26	5.65 \pm 1.08	5.45 \pm 0.46	5.01 \pm 1.35	6.08 \pm 0.80
Intestines	2.09 \pm 0.36	1.54 \pm 0.78	2.06 \pm 0.25	1.78 \pm 0.46	1.99 \pm 0.22
Stomach	1.97 \pm 0.16	1.92 \pm 0.35	1.69 \pm 0.38	1.82 \pm 0.68	1.95 \pm 0.23
Bone	2.38 \pm 0.33	1.83 \pm 0.54	2.14 \pm 0.38	1.91 \pm 0.78	2.08 \pm 0.08
Muscle	0.89 \pm 0.08	1.16 \pm 0.18	0.90 \pm 0.14	1.09 \pm 0.20	1.10 \pm 0.38
Tumor	11.45 \pm 1.77	10.67 \pm 2.85	13.86 \pm 3.10	9.42 \pm 3.68	10.85 \pm 2.39
Lymph nodes	6.33 \pm 1.25	3.95 \pm 0.73	5.50 \pm 1.07	4.78 \pm 1.40	2.51 \pm 1.23

Unexpectedly, no CXCR3-specific activity accumulation was observed in the MC38 tumors at baseline. To investigate the in vivo effects of ICI therapy on CXCR3 in the TME as well as systemic effects, two therapy cohorts receiving either one (1xICI) or three (3xICI) cycles of checkpoint inhibitor treatment (α -PD1/ α -CTLA-4) were investigated. Previous experiments in our lab using flow cytometry and IF had revealed that therapy response in the TME can be visualized earliest at five days post-treatment. Thus, [⁶⁴Cu]Cu-NOTA- α -CXCR3 was injected on day five post-therapy for the cohort which received two treatment cycles. Of note, a third treatment cycle was applied on day 13 post-inoculation (i.e. during the circulation time of the radiotracer) to ensure the therapy effectiveness and sustained T cell activation over this period (see Suppl. Figure S 6). Since the absolute organ uptakes both in reference organs such as blood or liver and in the target organs (tumor, spleen, lymph nodes) were found to vary between mice in the respective

cohorts, uptake ratios (spleen/liver, spleen/blood, tumor/liver, tumor/blood) were calculated for intra-individual normalization and better comparability. Interestingly, the spleen-to-liver ratio (SLR) increased steadily from 1.08 ± 0.19 (untreated cohort) to 1.12 ± 0.09 (1xICI), and 1.54 ± 0.14 (3xICI) during treatment and was the lowest in the blocking cohorts (0.66 ± 0.083 control blocking and 0.65 ± 0.15 3xICI blocking), demonstrating CXCR3-specificity of [^{64}Cu]Cu-NOTA- α -CXCR3 uptake in these tissues. Although differences between spleen-to-blood ratios (SBRs) were less significant, they showed identical trends. In contrast, a substantial increase in tracer accumulation (from 0.42 ± 0.20 (control) to 0.77 ± 0.47 (1xICI) to 1.13 ± 0.35 (3xICI) %IA/g, see Suppl. Figure S 8) was observed for the lymph-node-to-liver ratio but not for the lymph node-to-blood ratio. Unfortunately, this treatment-dependent increase in tracer uptake was not observed for the MC38 tumors. Although tumor-to-liver ratios were marginally higher in treated mice, this increase was not significant.

In vivo [^{64}Cu]Cu-NOTA- α -CXCR3 PET/CT imaging in MC38 bearing mice

To validate the findings from the biodistribution studies and to investigate the sensitivity of [^{64}Cu]Cu-NOTA- α -CXCR3 for detecting the observed ICI treatment effects in the secondary lymphoid organs, small animal [^{64}Cu]Cu-NOTA- α -CXCR3 PET/CT imaging at 24 hours p.i. was also performed (Figure 3). SLRs obtained from the representative PET/CT scans confirmed the results from the biodistribution experiment (see Suppl Figure S 7). Figure 3C summarizes the imaging results obtained for representative mice ($n = 1$ per condition) taken from the respective cohorts used for the biodistribution study at 48 hours p.i. (see previous section).

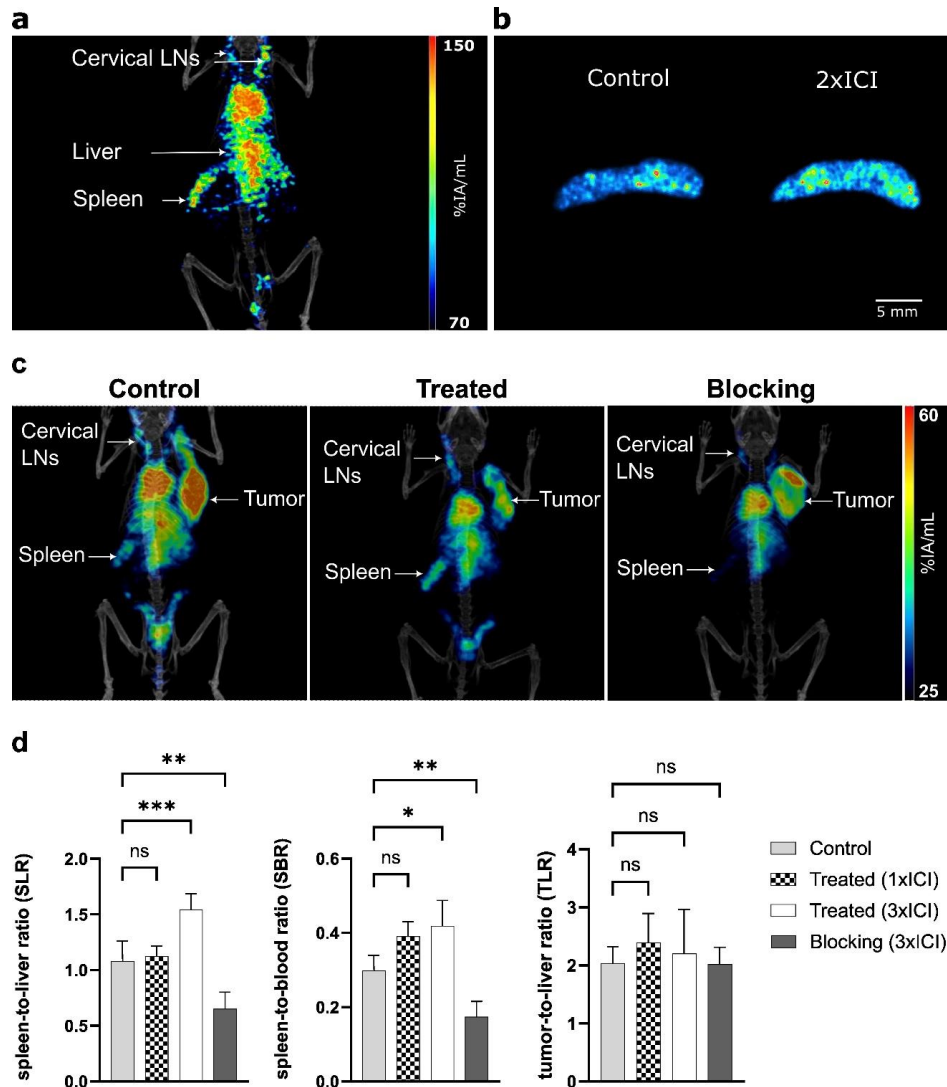


Figure 3: (a) PET/CT of a healthy C57Bl/6 mouse 48 p.i. of $[^{64}\text{Cu}]\text{Cu-NOTA-}\alpha\text{-CXCR3}$ (b) Autoradiography of spleens of healthy mice, either untreated (control, $n=1$) or treated with 2 cycles of ICI (2xICI, $n=1$); (b) Representative $[^{64}\text{Cu}]\text{Cu-NOTA-}\alpha\text{-CXCR3}$ PET/CT images (maximum intensity projections, MIP) of mice bearing MC38 tumors on the right flank at 24 hours p.i. Images show an untreated control mouse (left), a mouse having received 3 cycles of ICI (middle) and a mouse which received 3 cycles of ICI, coinjected with an 100-fold excess of $\alpha\text{-CXCR3}$ mAb (blocking, right) (c) Spleen-to-liver, spleen-to-blood and tumor-to-liver ratios for the different cohorts as determined via the biodistribution study (Table 1).

Discussion

As already demonstrated in the literature [15, 25], T cell function as well as infiltration into the tumor is strongly dependent on CXCR3. High CXCR3 expression on activated T cells has not only been shown to be a robust predictor for the success of cell-based immunotherapies [19] but may also be upregulated in tumor-resident T cells due to immune checkpoint inhibition-induced T cell activation. [15, 19].

This effect was also observed in the pilot experiments in this study in which a progressive, ICI-induced increase in CXCR3⁺ T cell numbers and an improved tumor infiltration with these cells was observed in MC38 tumors by IF as well as by flow cytometry after two ICI treatment cycles. These data were also in accordance with results from CD3 immunohistochemistry stainings of MC38 tumor slices, which in turn confirmed data from the literature [23]. An additional factor of high relevance for targeted imaging of immune-cell targets in the TME are the kinetics of T cell activation and expansion. In this study, flow cytometry analysis indicated that a single treatment cycle (three days post-treatment) did not yet have a detectable effect on activation and thus CXCR3 expression on tumor-infiltrating T cells, but was only observed after 2 cycles of checkpoint inhibition five days post-treatment. This is a highly interesting finding and underlines the importance of characterizing the kinetics of the up- (and down)regulation of individual T cell activation markers in response to therapy. For example, another T cell activation marker, OX40 [26], was found to display very distinct kinetics compared to CXCR3. For OX40, imaging of early response at two days post-treatment was feasible, whereas at nine days post-treatment, the signal returned to baseline level.

Motivated by the sufficient baseline infiltration and increasing number of CXCR3⁺ T

cells in the TME observed for the MC38 tumors under ICI therapy, the major aim of this study was to validate CXCR3 as an imaging target for T cell activation in the TME using the radiotracer [^{64}Cu]Cu-NOTA- α -CXCR3. Being the largest lymphoid organ, the spleen inherently showed a comparably high density of CXCR3⁺ cells in the initial IF experiments (Figure 1D). Consequently, during the subsequent *in vivo* evaluation of [^{64}Cu]Cu-NOTA- α -CXCR3, the spleen was considered as a positive control to verify the specificity of the radiotracer. Interestingly, even in this positive control tissue, low molar activities of the injected [^{64}Cu]Cu-NOTA- α -CXCR3 and thus the comparably high amount of coinjected, unlabeled antibody (15 μg) precluded CXCR3-specific tracer accumulation (Suppl. Figure S 7). Apparently, at this antibody dose, available CXCR3 receptors on splenic lymphoid T cells are already saturated by the excess of unlabeled antibody present in the radiopharmaceutical preparation. This observation is fully in line with previous results, where imaging of PD-1 expression was only feasible when small doses (2 μg) of the respective ^{64}Cu -labeled PD-1 targeted antibody were used [27]. To circumvent these drawbacks, the following adjustments were implemented: (1) A 10-fold reduction of the injected dose to 1.5 μg per mouse, based on an optimized molar activity of [^{64}Cu]Cu-NOTA- α -CXCR3 (300 GBq/ μmol vs 10 GBq/ μmol), and (2) a later time point for the *ex vivo* biodistribution study (48 hours *p.i.*) to allow more efficient tracer clearance and CXCR3-mediated accumulation. These adjustments resulted in specific and therapy-dependent radiotracer uptake observed in the spleen and lymph nodes (Table 1 and Figure 3C-D), both of which highly express CXCR3 tissues according to IF.

Despite significant therapy-induced changes in specific uptake of [^{64}Cu]Cu-NOTA- α -CXCR3 in the spleen and lymph nodes, limitations were encountered with respect to

imaging changes in CXCR3⁺ T cell infiltration or CXCR3 upregulation on tumor-resident T cells. Under the chosen experimental conditions, no significant therapy-related change in tumor uptake of [⁶⁴Cu]Cu-NOTA- α -CXCR3 was observed. We propose two possible explanations for this observation. First, the relatively low quantity of CXCR3⁺ expressing cells in the TME, even after 2 cycles of ICI treatment, limits the maximal achievable specific signal. For example, in the MC38 tumor model used in this study, a 6.7-fold increase in CXCR3⁺ T cell density was observed after ICI therapy. However, the cellular densities determined in the flow cytometry experiment ranged from 1524 \pm 579 CXCR3⁺ T cells/tumor (untreated control) to 9979 \pm 6369 cells/tumor (2xICI treated). This very low number of target-expressing cells as well as a probably low expression level per cell are insufficient to obtain a CXCR3-specific signal using [⁶⁴Cu]Cu-NOTA- α -CXCR3. With its affinity in the low nanomolar region ($K_D = 3.3$ nM), [⁶⁴Cu]Cu-NOTA- α -CXCR3 aligns well with other radiolabeled antibodies used for imaging [28], but this affinity is not sufficient to sensitively detect low-level CXCR3 expression in the TME. Here, dramatically enhanced CXCR3-affinity (ideally in the pM region) would be required to obtain the desired sensitive signal such as for radiotracers based on e.g. pembrolizumab [29]. Second, the inherent pharmacokinetic properties of the full-sized antibody radiotracer lead to high background uptake in tumor tissue. On the one hand, the EPR effect and Fc γ receptor-mediated uptake, which is well documented for antibody-based tracers [29, 30] contributes to significant non-specific accumulation of the [⁶⁴Cu]Cu-NOTA- α -CXCR3 macromolecule in the tumor tissue. This, as observed in the present study, may mask small, but significant differences of in CXCR3-mediated radiotracer uptake by CXCR3-positive T cells in the TME. On the other hand, as an inverse effect, efficient

extravasation of macromolecules such as full-size antibodies into the tumor tissue is limited [31], and thus, [^{64}Cu]Cu-NOTA- α -CXCR3 may be unable to reach the T cells residing in the TME. Thus, the present antibody-based approach for imaging T cell activation in the TME via CXCR3 targeting is not suited for imaging such small T cell (sub)populations in the TME. As mentioned, this would require radiotracers with extremely high affinities (pM), and ideally, rapid blood clearance and small background accumulation.

However, [^{64}Cu]Cu-NOTA- α -CXCR3 allowed in vivo imaging of systemic T cell activation, as demonstrated by an increased tracer uptake in the spleen and in the lymph nodes (Figure 3C-D) upon ICI treatment. Thus, the present approach may at least serve as a broader strategy [32] to image T cell activation. High splenic activity was recently proposed as a positive indicator of successful immunotherapy in melanoma and Hodgkin lymphoma patients using 2- ^{18}F FDG [33, 34]. Furthermore, previous studies have shown that the T cell activation marker CD69 exhibits increased expression in spleens of mice responding to ICI, whereas non-responders and untreated mice showed lower splenic uptake of the CD69-targeted [^{89}Zr]-DFO-H1.2F3 [35]. This suggests that, triggered by ICI, the number of effector T cells in the lymphatic circulation increases and immunological remodeling is taking place in the spleen [36]. As shown for the spleen-to-liver and spleen-to-blood ratios used in this study (Figure 3D), systemic response imaging could thus be feasible using [^{64}Cu]Cu-NOTA- α -CXCR3 PET. However, this assumption requires thorough further investigation since in the present study, animal cohorts were not sufficiently large to differentiate between ICI therapy responders and non-responders. Only if a correlation between the spleen-to-liver and spleen-to-blood ratios of [^{64}Cu]Cu-NOTA- α -CXCR3 uptake of responders

and non-responders can be observed, [⁶⁴Cu]Cu-NOTA- α -CXCR3-based PET imaging may qualify as an imaging approach for assessing systemic T cell activation as a surrogate marker for tumor response to ICI therapy.

Conclusions

In summary, the results of this study suggest, that in principle, CXCR3 represents a relevant molecular marker for T cell activation in an immunotherapy setting. The antibody-based imaging approach using [⁶⁴Cu]Cu-NOTA- α -CXCR3 was able to unambiguously demonstrate systemic T cell activation, as reflected by tracer uptake in CXCR3⁺ T cell rich organs such as spleen and lymph nodes. To be able to further exploit this highly interesting molecular marker as a target for imaging T cell activation in the TME, however, an optimized tracer design is required, providing not only very high affinity to CXCR3, ideally in the pM range, but also reduced background accumulation and faster general accumulation and clearance kinetics. First attempts in this direction have been reported [21] but require further optimization. Overall, this study represents an important first step towards establishing CXCR3 as an important (early) T cell activation marker alongside CD69, OX40, ICOS, IL-2R, IFN- γ , Granzyme B as well as T-cell metabolism and in the future may attract considerable clinical interest, as soon as an optimized tracer concept is available.

Author contributions

MS and SM were involved in the conceptualization and experimental design of this study. BZ and SM performed the flow cytometry experiments. MH and SM carried out the Qupath evaluations. EC and GGA were responsible for CXCR3 transduction of CHO cells. SM carried out the radiotracer synthesis and in vitro evaluations. DV, AL, LW and SM carried out the PET imaging and biodistribution studies. All authors read and approved current version of the manuscript.

Acknowledgements

SM thanks the AGORA institutional core facilities (flow cytometry and immunohistochemistry) for their excellent technical support.

Data availability

Data sharing not applicable to this article as no datasets were generated or analyzed during the study.

Funding

The authors declare that no funds, grants, or other support were received during the preparation of this manuscript.

Conflict of interest

The author LM is employed by Debiopharm which is IP holder for the AbYlink technology. Materials for the antibody conjugation were provided from Debiopharm under MTA.

Ethical approval

All applicable institutional and/or national guidelines for the care and use of animals were followed.

Abbreviations

CXCR3 C-X-C chemokine receptor 3

TME tumor micro-environment

ICI immune checkpoint inhibitor

NOTA 2,2,2-(1,4,7-triazacyclononane-1,4,7-triyl)triacetic acid

TIL tumor infiltrating lymphocyte

CAR-T chimeric antigen receptor T cell

PET positron emission tomography

SPECT single photon emission computed tomography

ICOS inducible T cell COStimulator

IL-2R interleukin-2 receptor

CXCL9 C-X-C chemokine ligand 9

PD-1 programmed cell death protein 1

CTLA-4 cytotoxic T-lymphocyte-associated protein 4

mAb monoclonal antibody

DoC degree of conjugation

EDTA ethylenediaminetetraacetic acid

SEC size exclusion chromatography

RCP radiochemical purity

iTLC instant thin layer chromatography

RCY radiochemical yield

BSA bovine serum albumine

FBS fetal bovine serum

IHC immunohistochemistry

IF immunofluorescence

MA molar activity

K_D dissociation constant

SLR spleen-to-liver ratio

SBR spleen-to-blood ratio

References

1. Edwards, J., et al., *CD103+ Tumor-Resident CD8+ T Cells Are Associated with Improved Survival in Immunotherapy-Naïve Melanoma Patients and Expand Significantly During Anti-PD-1 Treatment*. *Clinical Cancer Research*, 2018. **24**(13): p. 3036-3045.
2. Raskov, H., et al., *Cytotoxic CD8+ T cells in cancer and cancer immunotherapy*. *British Journal of Cancer*, 2021. **124**(2): p. 359-367.
3. Murciano-Goroff, Y.R., A.B. Warner, and J.D. Wolchok, *The future of cancer immunotherapy: microenvironment-targeting combinations*. *Cell Research*, 2020. **30**(6): p. 507-519.
4. Kist de Ruijter, L., et al., *Whole-body CD8+ T cell visualization before and during cancer immunotherapy: a phase I/2 trial*. *Nature Medicine*, 2022. **28**(12): p. 2601-2610.
5. Sako, M.O. and B.M. Larimer, *Imaging of Activated T Cells*. *Journal of Nuclear Medicine*, 2023. **64**(1): p. 30-33.
6. Alam, I.S., et al., *Visualization of Activated T Cells by OX40-ImmunoPET as a Strategy for Diagnosis of Acute Graft-versus-Host Disease*. *Cancer Research*, 2020. **80**(21): p. 4780-4790.
7. Nisnboym, M., et al., *Immuno-PET Imaging of CD69 Visualizes T-Cell Activation and Predicts Survival Following Immunotherapy in Murine Glioblastoma*. *Cancer Research Communications*, 2023. **3**(7): p. 1173-1188.
8. Xiao, Z., et al., *ICOS Is an Indicator of T-cell-Mediated Response to Cancer Immunotherapy*. *Cancer Res*, 2020. **80**(14): p. 3023-3032.
9. Simonetta, F., et al., *Molecular Imaging of Chimeric Antigen Receptor T Cells by*

- ICOS-ImmunoPET*. Clin Cancer Res, 2021. **27**(4): p. 1058-1068.
10. van de Donk, P.P., et al., *Interleukin-2 PET imaging in patients with metastatic melanoma before and during immune checkpoint inhibitor therapy*. Eur J Nucl Med Mol Imaging, 2021. **48**(13): p. 4369-4376.
 11. Hartimath, S.V., et al., *Noninvasive monitoring of cancer therapy induced activated T cells using [(18)F]FB-IL-2 PET imaging*. Oncoimmunology, 2017. **6**(1): p. e1248014.
 12. Gibson, H.M., et al., *IFN γ PET Imaging as a Predictive Tool for Monitoring Response to Tumor Immunotherapy*. Cancer Res, 2018. **78**(19): p. 5706-5717.
 13. Larimer, B.M., et al., *The Effectiveness of Checkpoint Inhibitor Combinations and Administration Timing Can Be Measured by Granzyme B PET Imaging*. Clin Cancer Res, 2019. **25**(4): p. 1196-1205.
 14. Levi, J., et al., *(18)F-AraG PET for CD8 Profiling of Tumors and Assessment of Immunomodulation by Chemotherapy*. J Nucl Med, 2021. **62**(6): p. 802-807.
 15. Chow, M.T., et al., *Intratumoral Activity of the CXCR3 Chemokine System Is Required for the Efficacy of Anti-PD-1 Therapy*. Immunity, 2019. **50**(6): p. 1498-1512.e5.
 16. Bachelierie, F., et al., *International Union of Basic and Clinical Pharmacology. [corrected]. LXXXIX. Update on the extended family of chemokine receptors and introducing a new nomenclature for atypical chemokine receptors*. Pharmacol Rev, 2014. **66**(1): p. 1-79.
 17. Nakajima, C., et al., *Induction of the chemokine receptor CXCR3 on TCR-stimulated T cells: dependence on the release from persistent TCR-triggering and requirement for IFN- γ stimulation*. European Journal of Immunology, 2002. **32**(6):

- p. 1792-1801.
18. Iwai, T., et al., *Both T cell priming in lymph node and CXCR3-dependent migration are the key events for predicting the response of atezolizumab*. Scientific Reports, 2021. **11**(1): p. 13912.
 19. Schmidt, J., et al., *Neoantigen-specific CD8 T cells with high structural avidity preferentially reside in and eliminate tumors*. Nat Commun, 2023. **14**(1): p. 3188.
 20. Sun, H., et al., *Monitoring Early-Stage Acute Rejection by Imaging CXCR3-Positive Cell Infiltration: Evaluation of ¹²⁵Iodine-Labeled CXCL10*. Exp Clin Transplant, 2020. **18**(3): p. 368-374.
 21. Alluri, S.R., et al., *Synthesis and preclinical evaluation of a novel fluorine-18 labeled small-molecule PET radiotracer for imaging of CXCR3 receptor in mouse models of atherosclerosis*. Res Sq, 2023.
 22. Postupalenko, V., et al., *Site-selective template-directed synthesis of antibody Fc conjugates with concomitant ligand release*. Chemical Science, 2024. **15**(4): p. 1324-1337.
 23. Selby, M.J., et al., *Preclinical Development of Ipilimumab and Nivolumab Combination Immunotherapy: Mouse Tumor Models, In Vitro Functional Studies, and Cynomolgus Macaque Toxicology*. PLoS One, 2016. **11**(9): p. e0161779.
 24. Bankhead, P., et al., *QuPath: Open source software for digital pathology image analysis*. Sci Rep, 2017. **7**(1): p. 16878.
 25. Dangaj, D., et al., *Cooperation between Constitutive and Inducible Chemokines Enables T Cell Engraftment and Immune Attack in Solid Tumors*. Cancer Cell, 2019. **35**(6): p. 885-900.e10.
 26. Alam, I.S., et al., *Imaging activated T cells predicts response to cancer vaccines*.

- J Clin Invest, 2018. **128**(6): p. 2569-2580.
27. Hettich, M., et al., *High-Resolution PET Imaging with Therapeutic Antibody-based PD-1/PD-L1 Checkpoint Tracers*. *Theranostics*, 2016. **6**(10): p. 1629-40.
 28. Krutzek, F., K. Kopka, and S. Stadlbauer, *Development of Radiotracers for Imaging of the PD-1/PD-L1 Axis*. *Pharmaceuticals (Basel)*, 2022. **15**(6).
 29. van der Veen, E.L., et al., *(89)Zr-pembrolizumab biodistribution is influenced by PD-1-mediated uptake in lymphoid organs*. *J Immunother Cancer*, 2020. **8**(2).
 30. Knight, J.C., et al., *Dual-isotope imaging allows in vivo immunohistochemistry using radiolabelled antibodies in tumours*. *Nuclear Medicine and Biology*, 2019. **70**: p. 14-22.
 31. Thurber, G.M., M.M. Schmidt, and K.D. Wittrup, *Antibody tumor penetration: transport opposed by systemic and antigen-mediated clearance*. *Adv Drug Deliv Rev*, 2008. **60**(12): p. 1421-34.
 32. Xing, X., et al., *Positron emission tomography molecular imaging to monitor anti-tumor systemic response for immune checkpoint inhibitor therapy*. *European Journal of Nuclear Medicine and Molecular Imaging*, 2023. **50**(6): p. 1671-1688.
 33. Dercle, L., et al., *(18)F-FDG PET and CT Scans Detect New Imaging Patterns of Response and Progression in Patients with Hodgkin Lymphoma Treated by Anti-Programmed Death 1 Immune Checkpoint Inhibitor*. *J Nucl Med*, 2018. **59**(1): p. 15-24.
 34. Tsai, K.K., et al., *Increased FDG avidity in lymphoid tissue associated with response to combined immune checkpoint blockade*. *J Immunother Cancer*, 2016. **4**: p. 58.
 35. Edwards, K.J., et al., *Using CD69 PET Imaging to Monitor Immunotherapy-*

Induced Immune Activation. *Cancer Immunology Research*, 2022. **10**(9): p. 1084-1094.

36. Markel, J.E., et al., *Using the Spleen as an In Vivo Systemic Immune Barometer Alongside Osteosarcoma Disease Progression and Immunotherapy with α -PD-L1*. *Sarcoma*, 2018. **2018**: p. 8694397.

Electronic Supplementary Material
Validation of the C-X-C chemokine receptor 3
(CXCR3) as a target for PET imaging of T cell
activation

Sebastian Martin^{1,2,3}, Lennard Wendlinger^{1,2,3}, Béatrice Zitti^{2,5}, Mehdi Hicham^{2,5},
Viktoriia Postupalenko⁴, Léo Marx⁴, Greta Giordano-Attianese⁶, Elisabetta Cribioli⁶,
Melita Irving⁶, Alexandra Litvinenko^{1,2,3}, Radmila Faizova^{1,2,3}, David Viertl^{1,2,3}, Margret
Schottelius^{1,2,3}

¹ *Translational Radiopharmaceutical Sciences, Department of Nuclear Medicine
and Department of Oncology, Centre Hospitalier Universitaire Vaudois (CHUV)
and University of Lausanne (UNIL), 1011 Lausanne, Switzerland*

² *AGORA, Pôle de recherche sur le cancer, 1011 Lausanne, Switzerland*

³ *SCCL Swiss Cancer Center Lemman, 1011 Lausanne, Switzerland*

⁴ *Debiopharm Research & Manufacturing SA, Campus "après-demain", Rue du
Levant 146, 1920 Martigny, Switzerland*

⁵ *Department of Pathology and Immunology, University of Geneva, Geneva,
Switzerland*

⁶ *Ludwig Institute for Cancer Research, University of Lausanne, 1066 Epalinges,
Switzerland; Department of Oncology, University Hospital of Lausanne, 1011
Lausanne, Switzerland*

***Corresponding Author:**

Prof. Dr. Margret Schottelius

Phone +41.21.545.1120

Mobile +41.79.556.0143

Email: margret.schottelius@chuv.ch

Protein Mass Spectrometry

The mass spectrometry was performed on a Q ExactiveTM HF Orbitrap operating in the protein mode in mass ranges of 15 kDa (EPFL, Sion). The scans were set in the range of 1200-4000 m/z at a resolution of 15 k and a SID of 25 eV. The mass spectra were deconvolved using Protein Deconvolution 4.0 (Thermo Scientific). For the measurement the samples were passed through a Acquity UPLC Protein BEH C4 column (1x150mm, 1.7µm, 300 Å, Waters) at a flow rate of 90 µL/min. The column oven was set at 60°C. Gradient: from 25% to 40% within 12 min. Solvent A: water +0.1% formic acid, solvent B: acetonitrile + 0.1% formic acid. Before the injection of 6 µL sample volume the samples were diluted 100 times with solvent A.

Cell transfection

For the retroviral harvest 293T cells were used as packaging cell line. 8×10^6 cells were seeded in a T150 flask the day before of the transfection in 16.5 mL of complete RPMI media. The cells were transfected by using Turbofect with 42 µg of total DNA (gagpol 14 µg, transfer vector 21 µg, envelop 7 µg). Turbofect and Optimem have been used according to the manufacturer's instructions. 48 hours after the transfection the supernatant was collected and concentrated by a ultracentrifugation at $24 \times 10^5 \times g$ for 1.5 h. Next, 300×10^5 CHO cells were infected with 100 µL of concentrated virus. Phenotype control of the target protein was performed 5 days after transduction by flow cytometry. The cells were maintained and expanded in DMEM/F12 containing 10% FBS and 1% Penicillin/Streptomycin.

Flow cytometry of in vitro cultivated cells

CHO-CXC3 or MC38 cells were detached using 2 mM EDTA in PBS for 15-20 min at 37°C. The cells were washed twice with cold flow cytometry buffer (1% fetal bovine serum in PBS). For the staining, 1×10^6 cells were prepared and incubated for 30 min on ice with 100 μ L flow cytometry buffer containing 1 μ g/mL of PE anti-mouse CXCR3 (BioLegend, #Cat: 126505, Clone: CXCR3-173). An unstained sample was used as negative control. The cells were washed two times with 200 μ L cold flow cytometry buffer. DAPI was added to each sample shortly before the analysis to yield a final concentration of 0.5 μ g/mL. The flow cytometry analyses were conducted on the same day on a Beckman Coulter Gallios flow cytometer. The acquired data were analyzed with FlowJo v10.7.1.

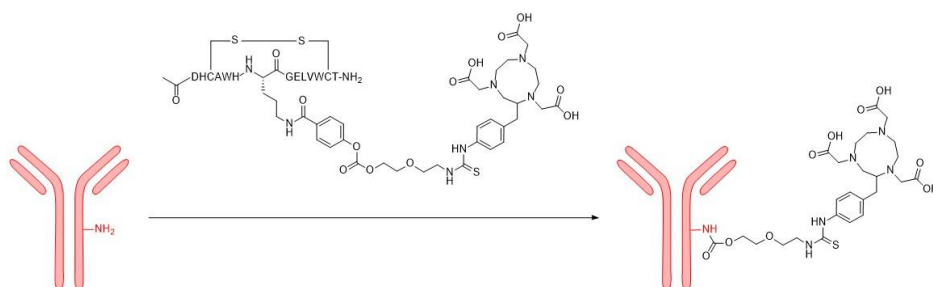


Figure S 1 AbYlink™ technology for Fc-site specific antibody conjugation. Patent application WO 2022/079031.

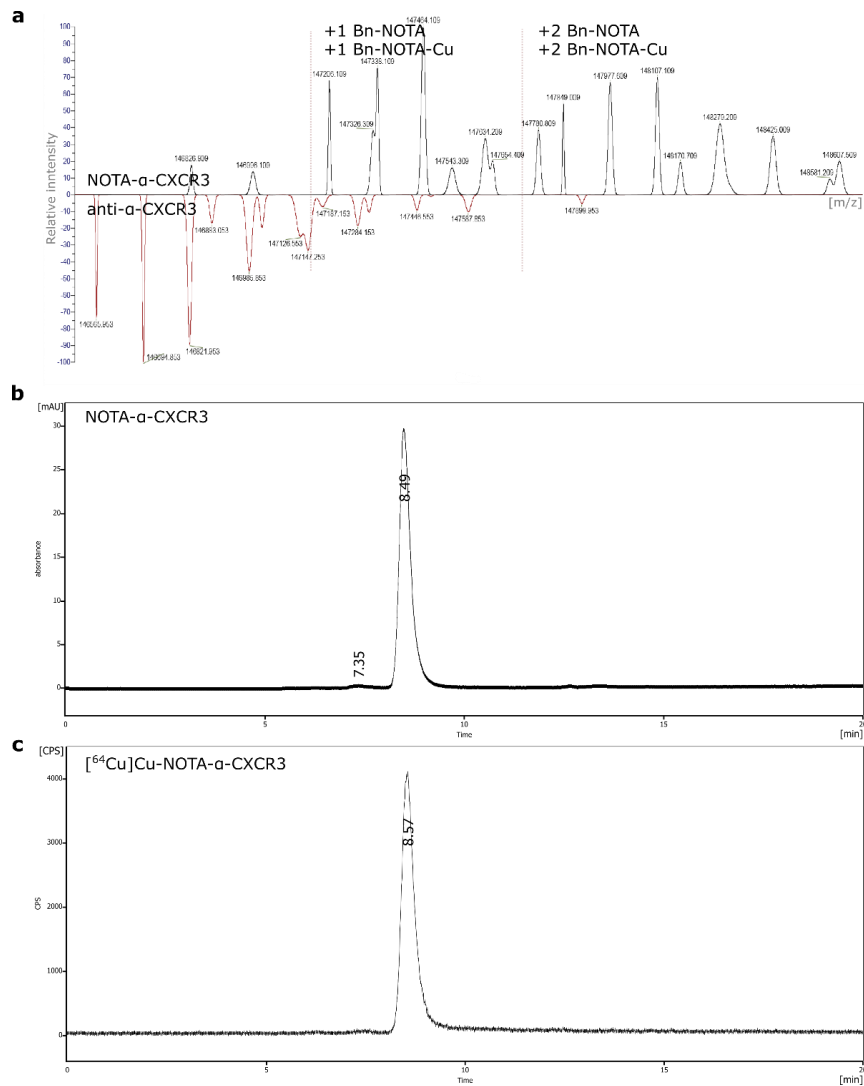


Figure S 2: **(a)** Evaluation of the degree of conjugation (DoC) through mass spectrometry. The NOTA-conjugated antibody is illustrated on the top and on the bottom the un conjugated antibody as control. Bn-NOTA: +582 m/z , and BN-NOTA-Cu: +643 m/z . **(b)** SEC-chromatogram of NOTA- α -CXCR3 in labeling buffer (0.1 M NaOAc, pH 5.5), R_t 8.49 min; **(c)** Radio-SEC chromatogram of [64 Cu]Cu-NOTA- α -CXCR3, R_t 8.57 min.

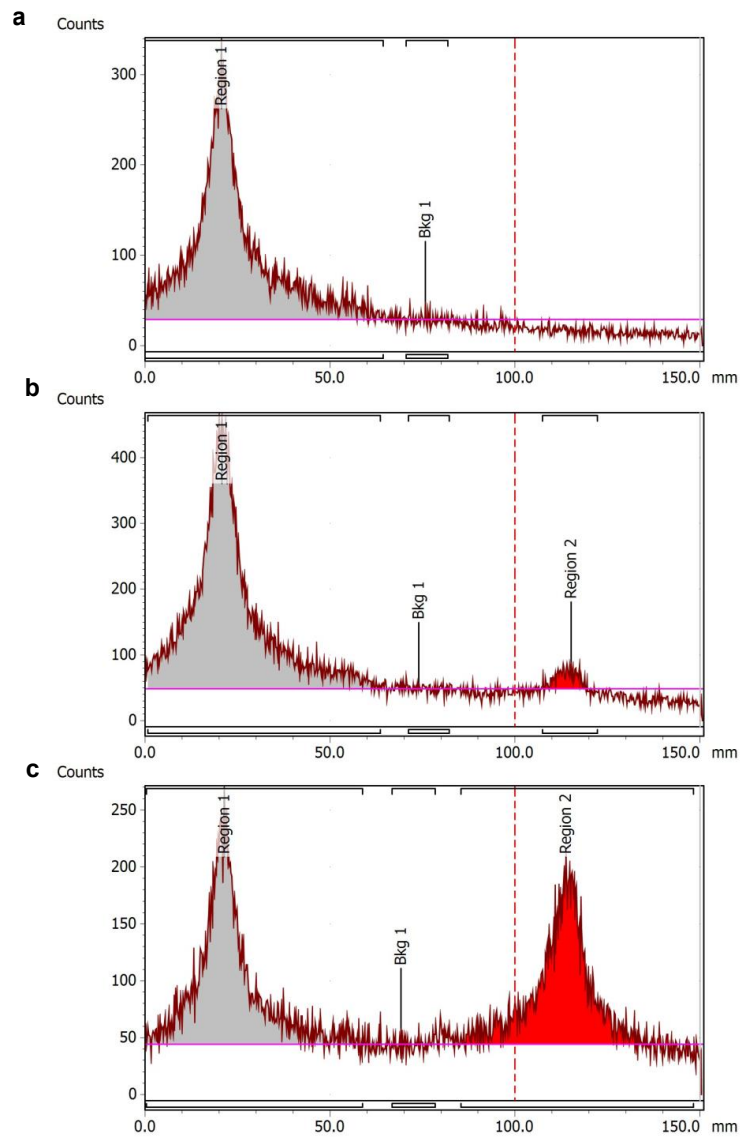


Figure S 3: iTLC chromatograms of $[^{64}\text{Cu}]\text{Cu-NOTA-}\alpha\text{-CXCR3}$ radiolabeled with increasing activities of ^{64}Cu . Region 1: $[^{64}\text{Cu}]\text{Cu-NOTA-}\alpha\text{-CXCR3}$; Region 2: $[^{64}\text{Cu}]\text{Cu-EDTA}$; Bkg1: Background region. (a) Radiolabeling to MA of 538 GBq/ μmol ; (b) MA of 690 GBq/ μmol ; (c) MA of 1250 GBq/ μmol .

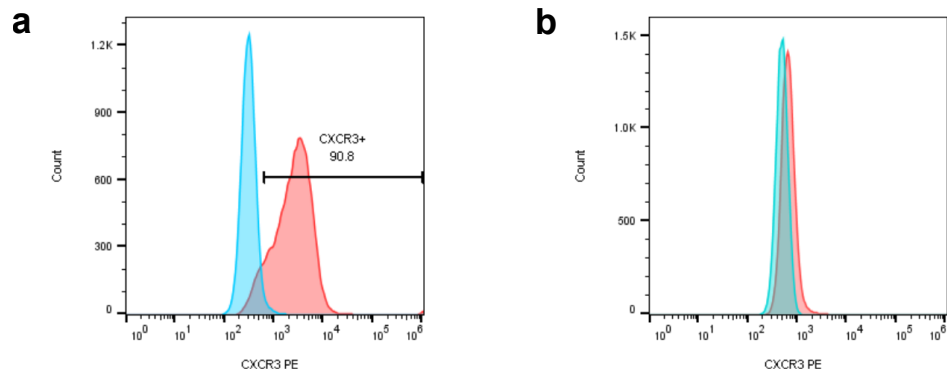


Figure S 5: Flow cytometry analysis. Anti-mouse-CXCR3-PE stained cells in red, unstained cells in blue. (a) Transfected CHO cells expressing murine CXCR3; (b) MC38 tumor cells.

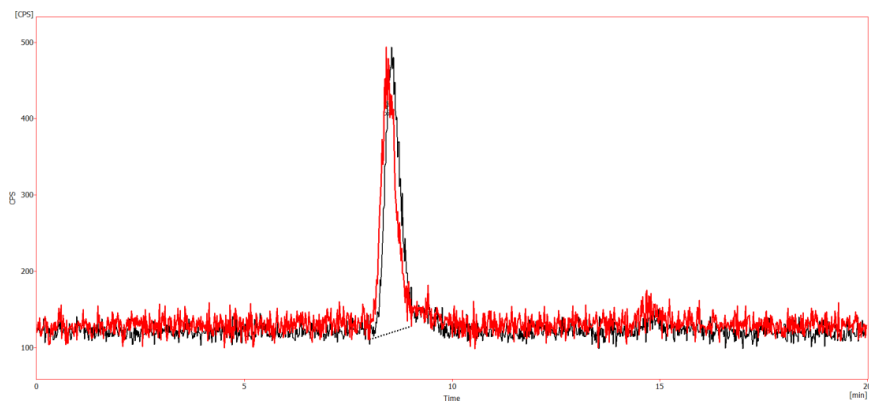


Figure S 4: Stability of $[^{64}\text{Cu}]\text{Cu-NOTA-}\alpha\text{-CXCR3}$ in human serum. Overlay of SEC analyses after 24 hours (red) and 48 hours (black) of incubation at 37°C .

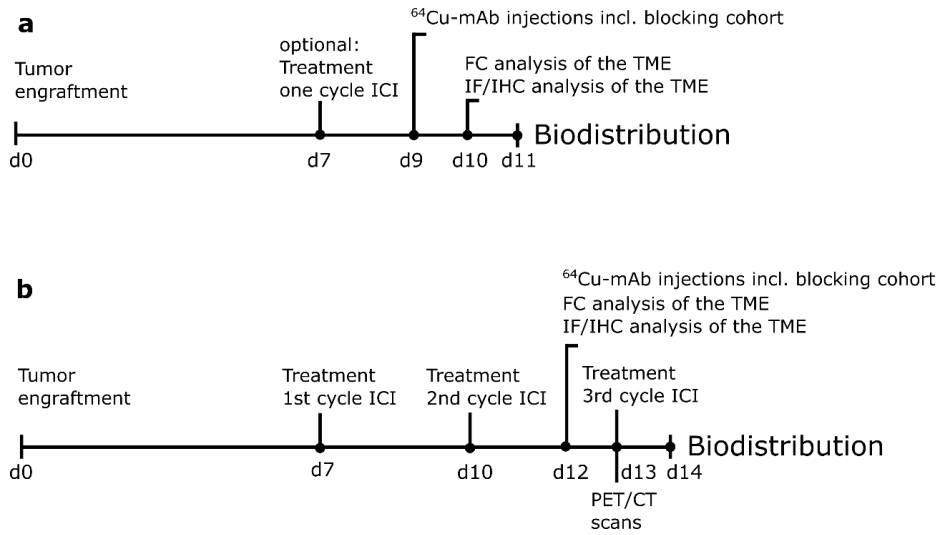


Figure S 6: ICI treatment schedule for MC38 tumor bearing mice. ICI: immune checkpoint inhibitor, IF: immunofluorescence, mAb: monoclonal antibody. (a) Schedule for untreated mice and mice treated with one dose of ICI. (b) Schedule for mice which received two or three doses of ICI.

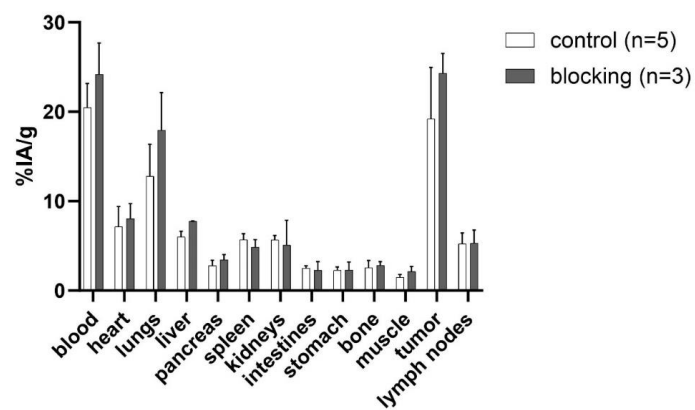


Figure S 7: Biodistribution of $[^{64}\text{Cu}]\text{Cu-NOTA-}\alpha\text{-CXCR3}$ (10 GBq/ μmol , 15 μg mAb/mouse) at 24h p.i. in untreated MC38 tumor bearing mice.

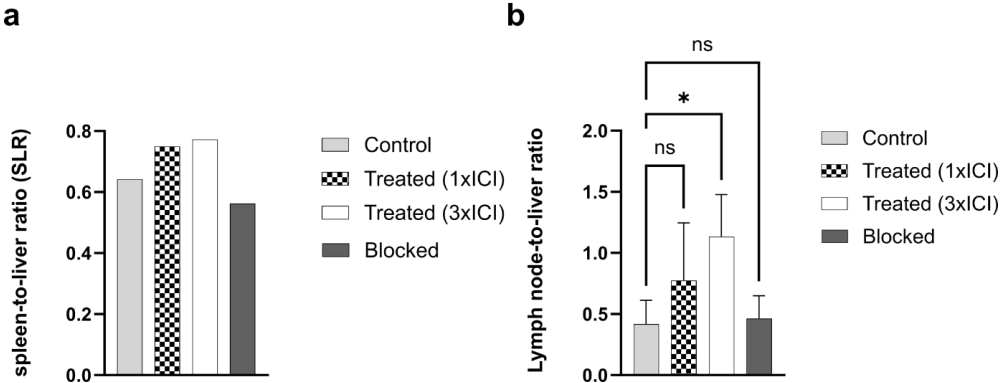


Figure S 8: (a) Spleen-to-liver ratios as determined from VOI evaluation of the representative PET/CT images (n=1 each condition); (b) Lymph node-to-liver ratios as determined from the Biodistribution data (Table 1).

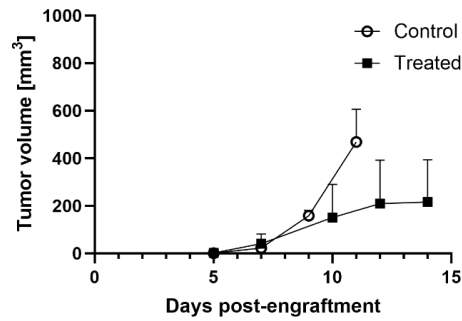


Figure S 9: Growth kinetics of MC38 tumors in CB57Bl/6 mice. Tumors (2×10^6 cells) were engrafted subcutaneously on the right flank. Immune checkpoint inhibitor treatment using α PD1 and α CTLA-4 was applied on day 7, 10 and 13 post-enuftment.

6 Exploiting CXCR4 as target for imaging and radioligand therapy

CXCR4 is a highly relevant molecular target for PET/CT imaging and RLT. Currently, a potent theranostic concept using [^{68}Ga]Ga-PentixaFor and [^{177}Lu]Lu/[^{90}Y]Y-PentixaTher is available and clinically implemented [91]. Nevertheless, optimizations on different levels are being constantly pursued: (a) understanding regulation of CXCR4 expression in cancer, for example of chemotherapeutic drugs, because they can interfere with successful RLT (see section 6.5), and (b) ongoing optimization of tracers expanding the spectrum of available labeling method by structural optimization.

The successful development of [$^{99\text{m}}\text{Tc}$]Tc-PentixaTec was facilitated by the introduction of the novel structural moiety L6-CPCR4, which allows for the incorporation of bulkier groups on the L6 linker without compromising affinity towards CXCR4 [37, 103]. First-in-human SPECT using [$^{99\text{m}}\text{Tc}$]Tc-PentixaTec in patients with hematological cancers demonstrated high-contrast delineation of CXCR4 expressing tumors [37]. To further expand the scope of potential applications, we synthesized highly potent tracers capable of utilizing [^{18}F]AlF chemistry, as well as hybrid ligands suitable for fluorescence and nuclear imaging. All of these tracers were developed based on the L6-CPCR4 moiety.

6.1 Development of CXCR4-directed ligands

Recently, PentixaFor analogs containing an optimized linker moiety, called L6 (Abz-D-Ala-D-Arg-dap), which increases the affinity towards CXCR4 (mouse/human), was developed. The L6-CPCR4 scaffold now tolerates the attachment of bulky groups to the L6-linker modality without compromising affinity and thus greatly improves flexibility with respect to the choice of chelator and labeling methodology [103]. Based on this scaffold, novel chelator-conjugated analogs (**NOTA-L6-CPCR4** and **NODAGA-L6-CPCR4**) for [^{18}F]AlF labeling, a fluorescent compound (**SulfoCy5-L6-CPCR4**), and a hybrid compound (**SulfoCy5-dap(DOTA)-L6-CPCR4**) were synthesized and evaluated in vitro which are presented in Figure 6.1.

6.2 Synthesis of L6-CPCR4 derivatives

The semi-protected building block L6-CPCR4 (Cyclo(D-Tyr-NMe-D-Orn(D-Dap(Boc)-D-Arg(Pbf)-D-Ala-4-Abz)-Arg(Pbf)-2-Nal-Gly) was used as the starting material to conjugate either the macrocyclic chelators (NOTA-bis(tert-Butyl)ester, NCS-MP-NODA, NODA-GA-NHS ester) and/or the Sulfo-Cyanine5 NHS ester to obtain the compounds. The deprotection yielding **NODA-L6-CPCR4** was not possible since the thiourea group of the **NODA-L6-CPCR4** was unstable even under mild acidic conditions using 1% TFA at 60 °C for the final deprotection step.

Given that only the two other derivatives, **NODAGA-L6-CPCR4** and **NOTA-L6-CPCR4**, exhibited stability under acidic conditions, only these were synthetically accessible in reasonable yields. The synthesis of the respective cold Al^{nat}F reference compounds was only successful in the case of [$^{\text{nat}}\text{F}$]AlF-**NOTA-L6-CPCR4**. In contrast, the NODAGA-based compound **NODAGA-L6-CPCR4** showed only the formation of **Al-NODAGA-L6-CPCR4** (758.7 [M+2]²⁺). This can be attributed to NODA-GA (3N, 3O) saturating the coordination sphere of Al³⁺ forming stable hexadentate complexes. In previous labeling studies of NODAGA-conjugated peptides with [^{18}F]AlF, this preferential 3N, 3O coordination of Al³⁺ had already led to poor ra-

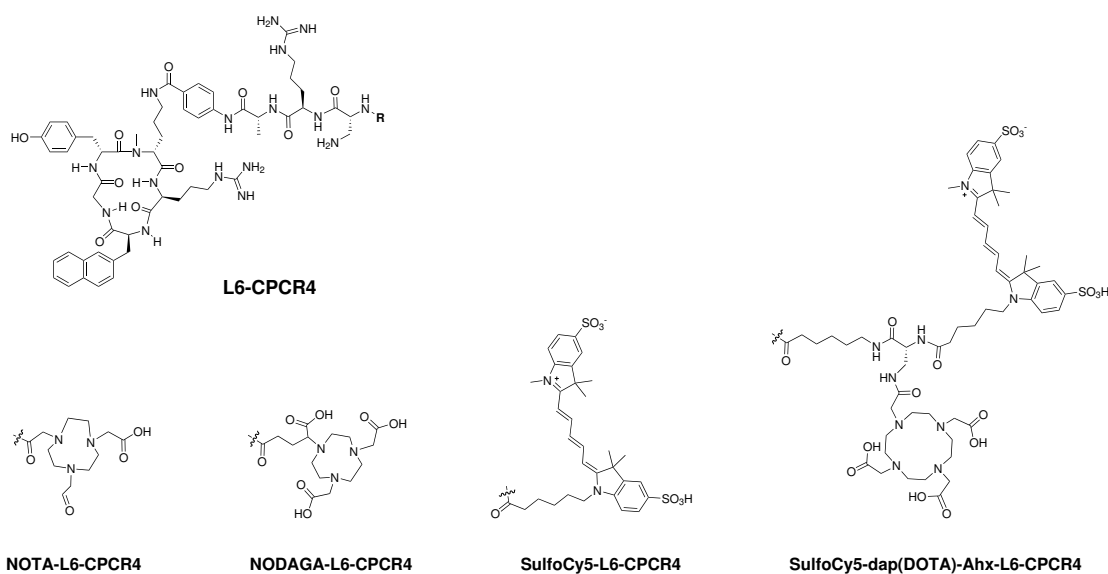


Figure 6.1: Synthesized CXCR4 inhibitors based on the L6-CPCR4 moiety. The highly potent L6-CPCR4 moiety was recently developed by Konrad et al. [37].

radiochemical yields of the desired [¹⁸F]AIF complex (maximal 20%), challenging the suitability of NODA-GA for AIF-labeling [121]. However, **NODAGA-L6-CPCR4** may still be considered useful for labeling with other isotopes like ⁶⁴Cu or ⁶⁸Ga. To demonstrate that this derivative in principle shows high affinity to CXCR4, compound **A1-NODAGA-L6-CPCR4** was characterized *in vitro* alongside [^{nat}F]AIF-**NOTA-L6-CPCR4**.

6.3 IC₅₀ determinations of L6-CPCR4 derivatives

Competitive binding assays were performed using radioligand [¹²⁵I]I-FC131 for Jurkat cells (human CXCR4) and [¹²⁵I]I-CPC4.3 for the HEK cell line (mouse CXCR4), respectively. Table 6.1 summarizes all obtained IC₅₀ values. Not unexpectedly, all tested compounds showed a superior affinity to human CXCR4 compared to the current gold standard of CXCR4-directed imaging [⁶⁸Ga]Ga-PentixaFor. With an IC₅₀ of 0.28 nM, [^{nat}F]AIF-**NOTA-L6-CPCR4** revealed the highest affinity to human CXCR4 which is 150-fold increased compared to [⁶⁸Ga]Ga-PentixaFor. Since the homology between human and mouse CXCR4 is low (91% [122]) and the L6-CPCR4-based peptides are not optimized for mouse CXCR4 affinity, all investigated compounds showed significantly lower affinities on the mouse CXCR4 receptor. However,

Table 6.1: Affinities of CXCR4-targeted peptides on Jurkat cells (human CXCR4) and transfected HEK cells (mouse CXCR4). IC₅₀ values were obtained using [¹²⁵I]I-CPCR4 (mouse CXCR4, 0.1 nM) and [¹²⁵I]I-FC131 (human CXCR4, 0.1 nM).

Compound	mouse CXCR4 [nM]	human CXCR4 [nM]
FC131	119 ± 69 ^a	12.4 ± 3.1 ^a
CPCR4.3	0.8 ± 0.1 ^a	2.8 ± 1.1 ^a
[^{nat} Ga]Ga-PentixaFor	>1000 ^a	42.4 ± 11.6 ^a
AI-NODAGA-L6-CPCR4	366.0 (n = 1)	0.53 ± 0.15 (n = 2)
[^{nat}F]AlF-NOTA-L6-CPCR4	649.7 ± 270.3 (n = 3)	0.28 ± 0.12 (n = 3)
SulfoCy5-L6-CPCR4	466.2 (n = 1)	0.81 (n = 1)
SulfoCy5-dap([^{nat}Ga]Ga-DOTA)-L6-CPCR4	2515.5 ± 1279.0 (n = 6)	3.0 ± 0.7 (n = 4)

^a Data taken from Schottelius et al. [123]

except for the hybrid compound **SulfoCy5-dap([⁶⁸Ga]Ga-DOTA)-L6-CPCR4**, all tested compounds showed improved affinity towards mouse CXCR4 compared to [⁶⁸Ga]Ga-PentixaFor. Overall, this in vitro target validation shows that CXCR4-inhibitors based on the L6-CPCR4 scaffold allowed the conjugation of bulky groups without perturbing their affinity to human CXCR4.

6.4 Internalization studies

As opposed to [⁶⁸Ga]Ga-PentixaFor and [¹⁷⁷Lu]Lu-PentixaTher, which, due to their antagonistic profile show only moderate CXCR4-mediated internalization, peptides containing the L6 linker usually display very efficient internalization [101, 37], hinting towards an agonistic profile. Since at the time of the investigation, the [¹⁸F]AlF-labeling protocol had not yet been established by our collaboration partners in Vienna (Prof. Verena Pichler), an internalization study could not yet be conducted for the lead compound, **NOTA-L6-CPCR4**. However, the internalization kinetics of the hybrid ligand **SulfoCy5-dap([^{nat}Ga]Ga-DOTA)-L6-CPCR4**

was investigated both via fluorescence microscopy using eGFP-CXCR4 expressing MDA-MB-231 X4 cells and via a dual tracer internalization study using the CXCR4-positive breast cancer cell line MCF-7. The compound showed increasing and specific cellular binding after 15 min at 37 °C. Progressive internalization was observed over the whole observation period, with more and more highly fluorescent intracellular vesicles appearing. At all times, red Cy5-fluorescence (ligand) was almost exclusively co-localized with the receptor (eGFP signal), indicative of strong ligand receptor interaction and efficient endocytosis of the receptor-ligand-complex (see Figure 6.2). Next, the internalization of the corresponding radiolabeled peptide **SulfoCy5-dap([⁶⁸Ga]Ga-DOTA)-L6-CPCR4** (1 nM) was investigated in the MCF-7 cell line over a period of 90 min. The assay was conducted as a dual tracer internalization study, with [¹²⁵I]I-FC131 (0.1 nM) as an internal reference (see Figure 6.3). At 60 min of incubation, radioligand internalization plateaued, with app. 8% of the added ⁶⁸Ga-activity internalized, and 12% total cellular binding (internalized + membrane-bound ligand). Compared to the internal standard [¹²⁵I]I-FC131, the internalization of **SulfoCy5-dap([⁶⁸Ga]Ga-DOTA)-L6-CPCR4** was slightly decreased (app. 5% lower internalization and total cellular binding). Unfortunately, further preclinical studies of the evaluated radiotracers were not compatible with the time line of this thesis, but will be pursued in a subsequent project by our laboratory to expand the scope of highly potent CXCR4-directed pharmaceuticals for imaging and therapy.

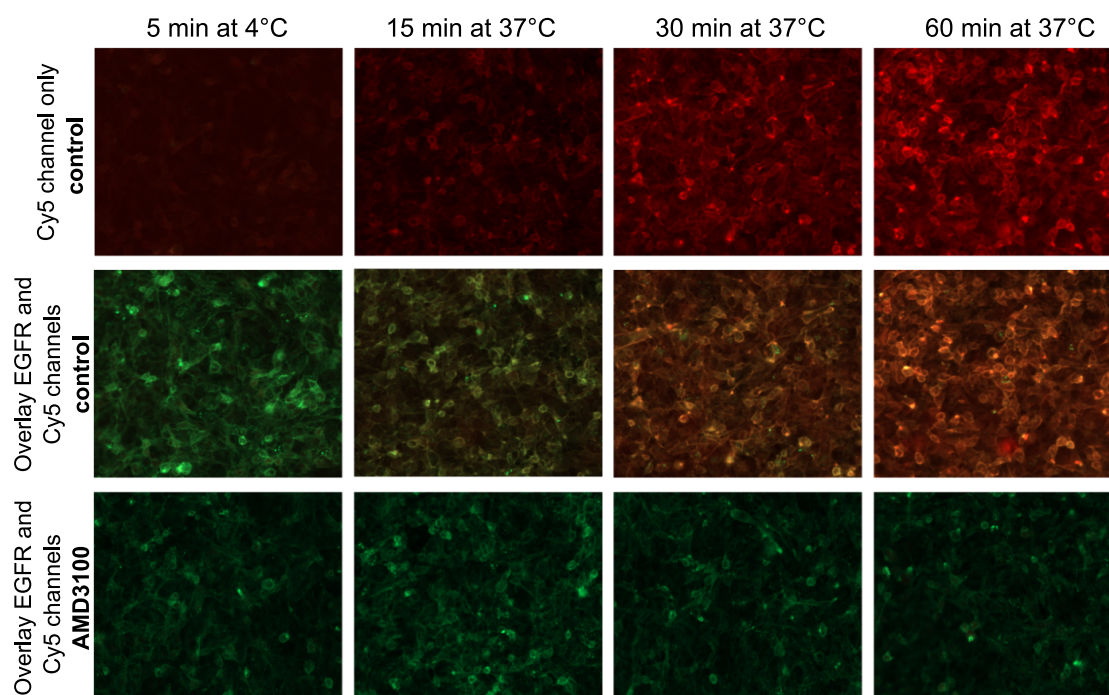


Figure 6.2: Internalization kinetics of hybrid compound **SulfoCy5-dap**($[^{nat}\text{Ga}]\text{Ga-DOTA}$)-**L6-CPCR4** in MDA-MB-231 X4-eGFP expressing cells. Immunofluorescence channels were eGFP (green) and Cy5 (red). Blocking was conducted using AMD3100 (0.1 mM).

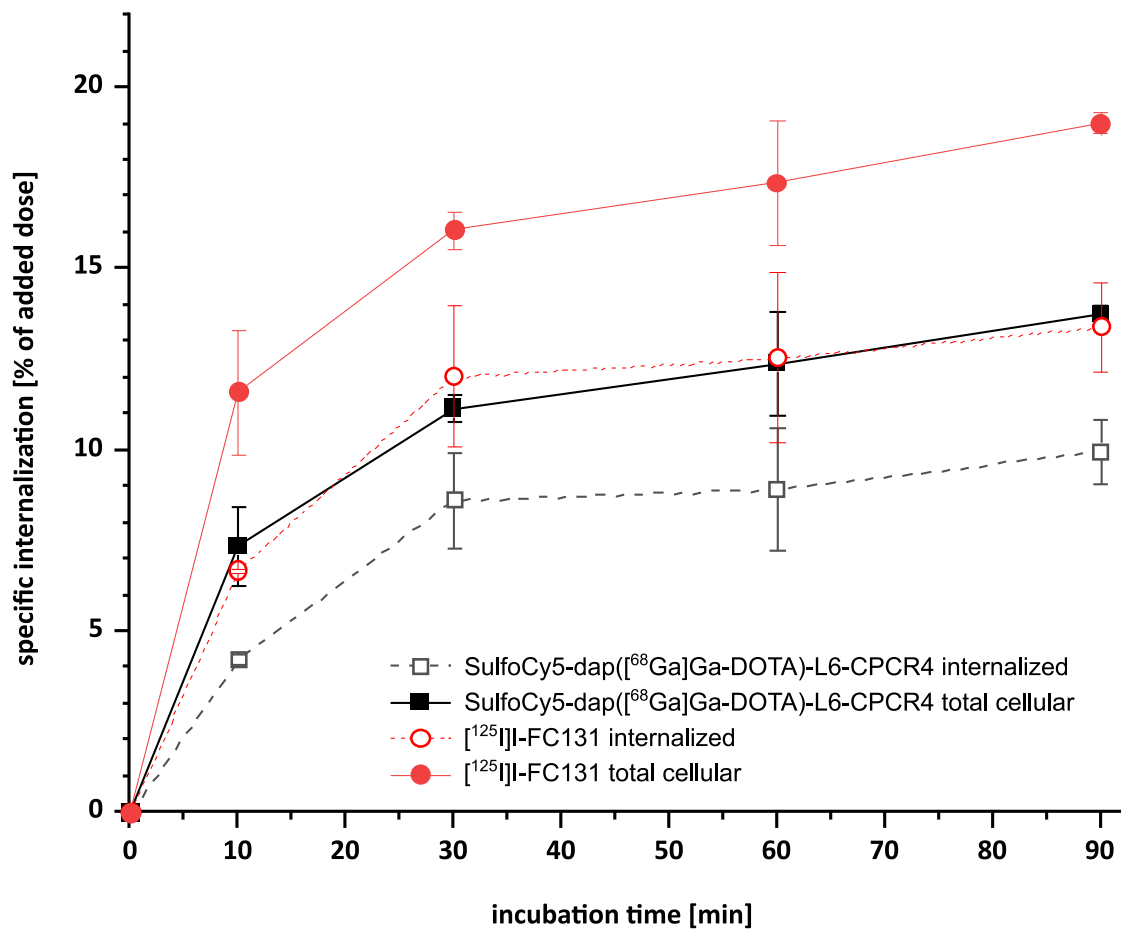


Figure 6.3: Specific internalization of the radiolabeled hybrid compound **SulfoCy5-dap(^{68}Ga)Ga-DOTA)-L6-CPCR4** on MCF-7 cells. Internal reference ^{125}I -FC131 was applied for comparison. Radioligand concentrations were at 1 nM (^{68}Ga -labeled tracer) and 0.1 nM (^{125}I -labeled tracer), respectively.


6.5 Influence of corticosteroid treatment on CXCR4 expression in DLBCL

SHORT COMMUNICATION

Open Access



Influence of corticosteroid treatment on CXCR4 expression in DLBCL

Sebastian Martin^{1,2,3}, David Viertl^{1,2,3}, Anna Janz⁴, Stefan Habringer^{5,6,7}, Ulrich Keller^{5,6,7} and Margret Schottelius^{1,2,3*} 

Abstract

Background CXCR4-targeted radioligand therapy (RLT) with [¹⁷⁷Lu]Lu/[⁹⁰Y]Y-PentixaTher has recently evolved as a promising therapeutic option for patients with advanced hematological cancers. Given their advanced disease stage, most patients scheduled for PentixaTher RLT require concomitant or bridging chemotherapy to prevent intermittent tumor progression. These (mostly combination) therapies may cause significant downregulation of tumoral CXCR4 expression, challenging the applicability of PentixaTher RLT. This study therefore aimed at investigating the influence of corticosteroids, a central component of these chemotherapies, on CXCR4 regulation in diffuse large B cell lymphoma (DLBCL).

Methods Different DLBCL cell lines (Daudi, OCI-LY1, SUDHL-4, -5-, -6 and -8) as well as the human T-cell lymphoma cell line Jurkat were incubated with Dexamethasone (Dex; 0.5 and 5 μM, respectively) and Prednisolone (Pred; 5 and 50 μM, respectively) for different time points (2 h, 24 h). Treatment-induced modulation of cellular CXCR4 surface expression was assessed via flow cytometry (FC) and compared to untreated cells. A radioligand binding assay with [¹²⁵I]CPC4.3 was performed in parallel using the same cells. To quantify potential corticosteroid treatment effects on tumoral CXCR4 expression in vivo, OCI-LY1 bearing NSG mice were injected 50 μg Dex/mouse i.p. (daily for 6 days). Then, a biodistribution study (1 h p.i.) using [⁶⁸Ga]PentixaTher was performed, and tracer biodistribution in treated (n = 5) vs untreated mice (n = 5) was compared.

Results In the in vitro experiments, a strongly cell line-dependent upregulation of CXCR4 was observed for both Dex and Pred treatment, with negligible differences between the high and low dose. While in Jurkat, Daudi and SUDHL-8 cells, CXCR4 expression remained unchanged, a 1.5- to 3.5-fold increase in CXCR4 cell surface expression was observed for SUDHL-5 < SUDHL-4 / -6 < OCI-LY1 via FC compared to untreated cells. This increase in CXCR4 expression was also reflected in correspondingly enhanced [¹²⁵I]CPC4.3 accumulation in treated cells, with a linear correlation between FC and radioligand binding data. In vivo, Dex treatment led to a general increase of [⁶⁸Ga]PentixaTher uptake in all organs compared to untreated animals, as a result of a higher tracer concentration in blood. However, we observed an overproportionally enhanced [⁶⁸Ga]PentixaTher uptake in the OCI-LY1 tumors in treated (21.0 ± 5.5%ID/g) vs untreated (9.2 ± 2.8%ID/g) mice, resulting in higher tumor-to-background ratios in the treatment group.

Conclusion Overall, corticosteroid treatment (Dex/Pred) consistently induced an upregulation of CXCR4 expression DLBCL cells in vitro, albeit in a very cell line-dependent manner. For the cell line with the most pronounced Dex-induced CXCR4 upregulation, OCI-LY1, the in vitro findings were corroborated by an in vivo biodistribution study. This confirms that at least the corticosteroid component of stabilizing chemotherapy regimens in DLBCL patients prior to [¹⁷⁷Lu]Lu-PentixaTher RLT does not lead to downregulation of the molecular target CXCR4 and may even have a

*Correspondence:

Margret Schottelius
margret.schottelius@chuv.ch

Full list of author information is available at the end of the article



© The Author(s) 2023. **Open Access** This article is licensed under a Creative Commons Attribution 4.0 International License, which permits use, sharing, adaptation, distribution and reproduction in any medium or format, as long as you give appropriate credit to the original author(s) and the source, provide a link to the Creative Commons licence, and indicate if changes were made. The images or other third party material in this article are included in the article's Creative Commons licence, unless indicated otherwise in a credit line to the material. If material is not included in the article's Creative Commons licence and your intended use is not permitted by statutory regulation or exceeds the permitted use, you will need to obtain permission directly from the copyright holder. To view a copy of this licence, visit <http://creativecommons.org/licenses/by/4.0/>.

beneficiary effect. However, further studies are needed to investigate if and to what extent the other commonly used chemotherapeutic agents affect CXCR4 expression on DLBCL to ensure the choice of an appropriate treatment regimen prior to [¹⁷⁷Lu]Lu/[⁹⁰Y]Y-PentixaTher RLT.

Keywords CXCR4, Chemokine receptor regulation, Cortisol, Corticosteroids, PentixaTher, Radioligand therapy

Background and study design

CXCR4-targeted radioligand therapy (RLT) with [¹⁷⁷Lu]Lu/[⁹⁰Y]Y-PentixaTher (Yttrium (⁹⁰Y) anditixaforotide) has recently evolved as a promising therapeutic option for patients with advanced hematological cancers such as multiple myeloma (MM), diffuse large B cell lymphoma (DLBCL) or acute lymphoblastic leukemia (ALL) [1–3]. Generally, a prerequisite for patient eligibility for [¹⁷⁷Lu]Lu/[⁹⁰Y]Y-PentixaTher RLT is high tumoral CXCR4 expression, confirmed by high uptake of the companion diagnostic, [⁶⁸Ga]Ga-PentixaFor (Gallium (⁶⁸Ga) boclatixaforotide), in the respective tumor lesions by pre-therapeutic PET/CT. However, as most patients scheduled for PentixaTher RLT suffer from advanced stages of their disease, concomitant or bridging chemotherapy to prevent tumor progression between diagnostic imaging and RLT is often required. That these intermittent therapeutic regimens may have significant impact on tumoral CXCR4 expression has recently been demonstrated. For three patients with different hematological malignancies, substantial downregulation of CXCR4 expression in response to bridging chemotherapy was observed [4], rendering [¹⁷⁷Lu]Lu/[⁹⁰Y]Y-PentixaTher RLT unsuitable or possibly much less effective.

To date, the mechanisms of this CXCR4 downregulation are unclear, and the observed effects are all the more surprising since two of the reported patients received Dexamethasone (albeit in conjunction with cyclophosphamide or other chemotherapeutic agents [4]). Dexamethasone was shown to substantially increase surface expression of CXCR4 in MM cells [4, 5], in murine B-cells [6] and in human T-cells [7]. In view of the implementation of an early phase clinical study on [¹⁷⁷Lu]Lu/[⁹⁰Y]Y-PentixaTher RLT in patients with DLBCL, it is of particular importance to understand the role of corticosteroid treatment on the regulation of CXCR4 expression in this malignancy. Such information could possibly guide the safe use of bridging chemotherapies prior to considering the patients for CXCR4-targeted [¹⁷⁷Lu]Lu/[⁹⁰Y]Y-PentixaTher RLT.

Thus, this study aimed at investigating the influence of corticosteroid (Dexamethasone, Prednisolone) treatment on CXCR4 expression in a panel of DLBCL cell lines (Daudi, OCI-LY1, SUDHL-4, SUDHL-5, SUDHL-6, SUDHL-8) with different baseline CXCR4 expression

levels. The human T-cell leukemia cell line Jurkat with high CXCR4 expression was also included.

Clinically, in the management of DLBCL, the combination of CHOP (Cyclophosphamide, Doxorubicin, Vincristine and Prednisone^a) and rituximab is considered a standard first-line treatment [8], whereas modified/extended DHAP (Dexamethasone, Cytarabine, Cisplatin) protocols are used as second-line chemotherapies [9]. Since patients with DLBCL eligible for [¹⁷⁷Lu]Lu/[⁹⁰Y]Y-PentixaTher RLT are very likely to undergo/have undergone one of these treatments, Prednisolone¹ and Dexamethasone were both included into this investigation.

To ensure the reliability of the in vitro data, the concentrations for Dexamethasone and Prednisolone were chosen such as to resemble as closely as possible to the maximum plasma concentrations observed in humans receiving standard treatments (i.e., 40 mg Dexamethasone/day [9] and 100 mg Prednisone/day [8]). On the basis of this dosing, the corresponding maximum plasma concentrations for Dexamethasone and Prednisolone were found to be approximately 0.5 μM [10] and 5 μM [11], respectively. Thus, these concentrations were used consistently throughout the study. In some experiments, however, to assess a potential concentration dependence of the (up)regulation of CXCR4 and of cell viability, a ten-fold concentration of the chosen corticosteroids was also investigated.

Data from the literature indicate variable kinetics of CXCR4 upregulation in different cell types, with the first detection of receptor upregulation ranging from 1 to 3 h [6, 7] to 24 h of incubation [5]. We therefore performed initial pilot studies to establish the most suitable incubation time for detecting potential effects of corticosteroid treatment on CXCR4 expression in the different DLBCL cell lines. Ultimately, after having established appropriate experimental conditions, a second set of experiments was performed, in which the changes in CXCR4 expression observed in flow cytometry were correlated with changes in radioligand binding induced by corticosteroid therapy. Given the particularly high sensitivity of [¹²⁵I]CPCR4.3 for quantifying different CXCR4 expression

¹ Prednisolone is the actual active compound; Prednisone (administered in CHOP) is the prodrug for Prednisolone and is metabolized to Prednisolone in the liver.

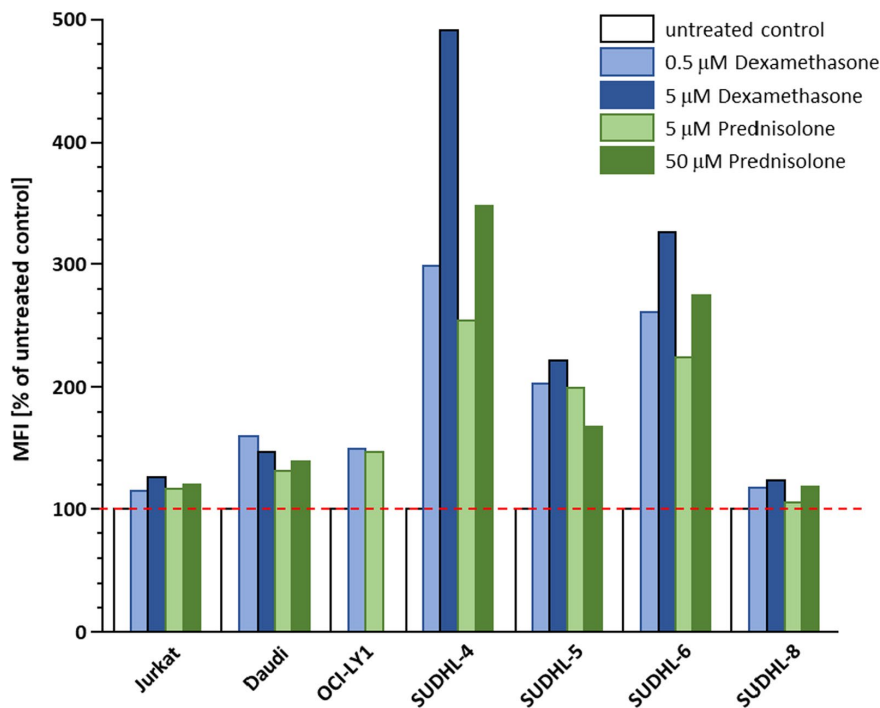


Fig. 1 Dependence of CXCR4 upregulation on drug concentration. Data are shown as the mean fluorescence intensity observed by flow cytometry for each of the cell lines at different concentrations (low and high dose) of Dexamethasone and Prednisolone, respectively, after 24 h of incubation in percent of untreated controls ($n=1$)

levels in vitro [12], this ligand was used instead of [^{177}Lu] Lu-PentixaTher for the in vitro studies.

Results

Pilot studies—time dependence and concentration dependence

In a first set of experiments, the time dependence of CXCR4 (up)regulation by corticosteroid treatment was investigated. As opposed to results from the literature [6, 7], an incubation time of 2 h at 37 °C with both the high dose (5 μ M Dexamethasone, 50 μ M Prednisolone) and the respective low-dose mimicking plasma concentration (0.5 μ M Dexamethasone, 5 μ M Prednisolone) did not induce any notable change in CXCR4 expression in any of the cell lines investigated (data not shown). However, after 24 h of incubation, flow cytometry analysis revealed increased CXCR4 surface expression levels for Daudi, OCI-LY1, SUDHL-4, SUDHL-5 and SUDHL-6 cells at both drug concentrations (Fig. 1). Consequently, an incubation time of 24 h was selected for all subsequent experiments.

Importantly, the effect of corticosteroid treatment on CXCR4 surface expression was highly variable between cell lines (Fig. 1). For SUDHL-4, SUDHL-5 and SUDHL-6 cells, substantial CXCR4 upregulation by treatment with Dexamethasone and Prednisolone was observed, which was also found to be dependent on drug concentration in the case of SUDHL-4 and SUDHL-6 cells. Only moderate, concentration-independent CXCR4 upregulation was observed for Daudi and OCI-LY1 cells, whereas the treatment effect was negligible for Jurkat and SUDHL-8 cells. Overall, there was a slight trend toward a more notable CXCR4 upregulation by Dexamethasone than by Prednisolone in the responding cell lines (Daudi, OCI-LY1, SUDHL-4, -5 and -6). However, since these pilot experiments were performed only once for estimation of effects ($n=1$), their significance is limited and does not allow conclusive interpretation. Despite the observed variability between different cell lines in response to corticosteroid treatment, however, no negative effect of Dexamethasone and Prednisolone on CXCR4 surface expression was detected.

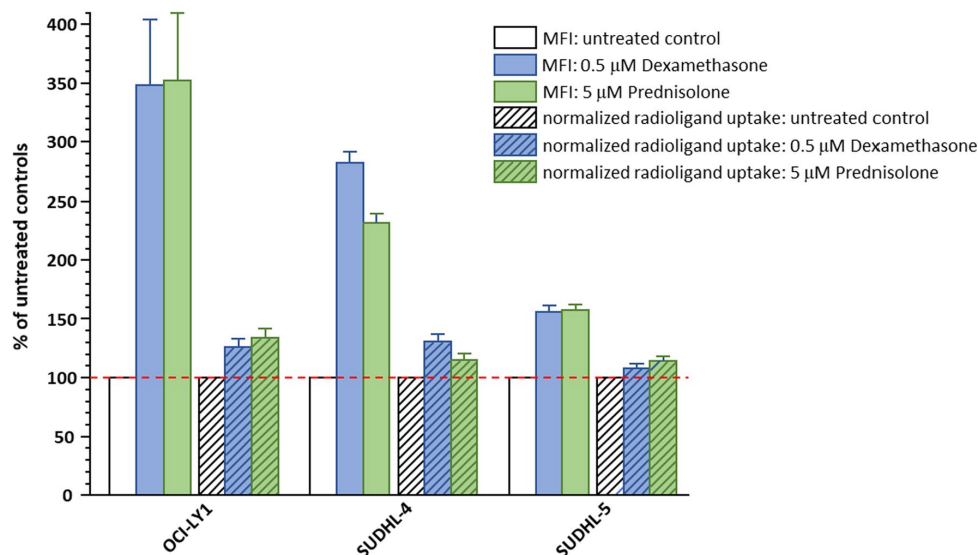


Fig. 2 CXCR4 upregulation by corticosteroid treatment as assessed in parallel by flow cytometry and a radioligand binding study using [125 I]CPCR4.3. All data are shown in percent of the values obtained for untreated control cells. Flow cytometry data are shown as relative mean fluorescence intensity (MFI) values and are means \pm SD from 3–4 separate determinations with $n=3$, respectively. Radioligand binding data are shown as relative normalized uptake values (% of added dose bound per 1 Mio live cells) and are means \pm SD from 2 separate determinations with $n=3$, respectively

Correlation of treatment effects observed by flow cytometry with radioligand binding data

Based on the above pilot experiments, OCI-LY1, SUDHL-4 and SUDHL-5 cells were selected for more in-depth evaluation of the association of steroid pre-treatment, CXCR4 expression and CXCR4 radioligand uptake, based on their gradual response to corticosteroid treatment (SUDHL-4 > SUDHL-5 > OCI-LY1). Despite pronounced CXCR4 upregulation by corticosteroid treatment, SUDHL-6 cells were not included due to practical considerations.

To be able to assess the influence of the CXCR4 upregulation observed via flow cytometry on radioligand uptake an additional set of experiments was performed. Aliquots of the same treated cells (24 h, 37 °C) were analyzed in parallel via flow cytometry and via incubation with [125 I]CPCR4.3 to quantify CXCR4 expression. Results are summarized in Fig. 2.

Interestingly, the extent of CXCR4 upregulation observed by flow cytometry for the three selected cell lines was quite different from the pilot experiments, with the responsiveness to therapy being now in the order of OCI-LY1 > SUDHL-4 > SUDHL-5. Another unexpected finding is the fact that the increase in cellular uptake of [125 I]CPCR4.3 was much less pronounced than the change in CXCR4 surface expression observed by flow

cytometry. However, as shown in Fig. 3, there is a linear correlation between the relative changes in CXCR4 expression determined by flow cytometry and via [125 I]CPCR4.3 binding. This correlation on the one hand corroborates the initial observation (see pilot experiments), that corticosteroid treatment does increase CXCR4 expression in DLBCL cell lines. However, the extent of this effect is strongly cell line dependent. The observed increase in radioligand uptake in cell lines with a strong CXCR4 upregulation upon corticosteroid treatment may even prove beneficial in the context of RLT with [177 Lu]Lu/[90 Y]Y-PentixaTher.

In vivo assessment of the effect of Dexamethasone treatment on tumoral CXCR4 expression

To verify this hypothesis, mice bearing subcutaneous OCI-LY1 DLBCL xenografts were randomized into a control group (no treatment) and a treatment group (50 μg Dexamethasone i.p. for 6 consecutive days), and a comparative biodistribution study using [68 Ga]Ga-PentixaTher was carried out at the end of the treatment period. Of note, since at the time of the experiment, [177 Lu]Cl $_3$ was not available from the manufacturer due to production shortages, [68 Ga]-labeled PentixaTher was chosen as a substitute for the therapeutic agent [177 Lu]Lu-PentixaTher.

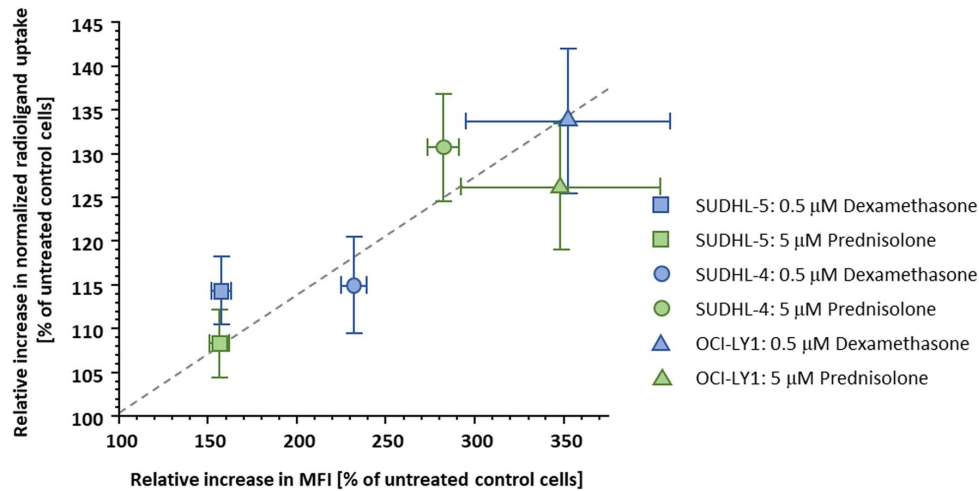


Fig. 3 Correlation of CXCR4 upregulation by corticosteroid treatment quantified by flow cytometry and via a radioligand binding study, respectively. All data are shown in percent of the values obtained for untreated control cells. Flow cytometry data are shown as relative MFI values and are means \pm SD from 3–4 separate determinations with $n=3$, respectively. Radioligand binding data using [125 I]CPC4.3 are shown as relative normalized uptake values (% of added dose bound per 1 Mio live cells) and are means \pm SD from 2 separate determinations with $n=3$, respectively

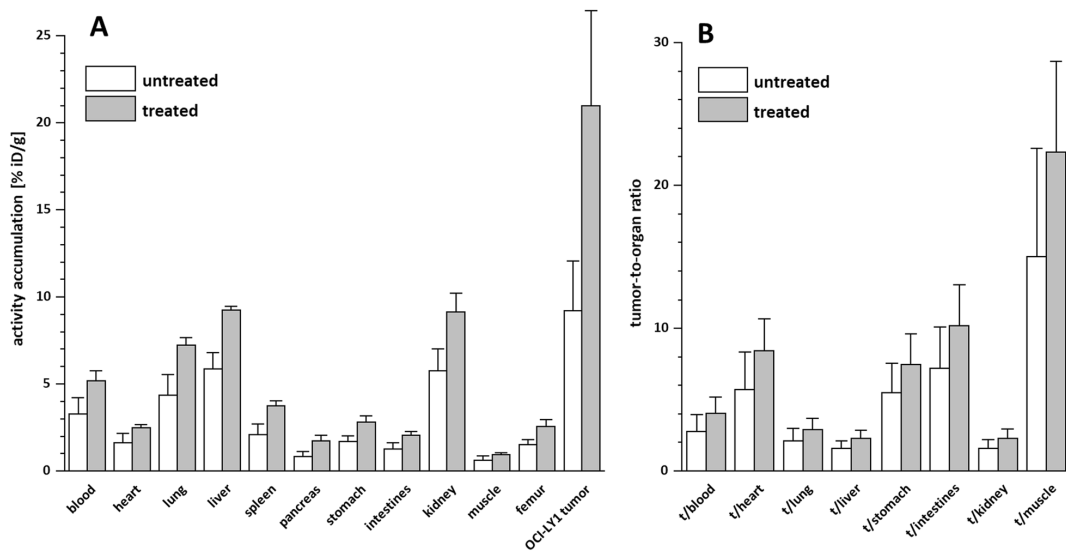


Fig. 4 Biodistribution (A) and Tumor-to-organ ratios (B) of [68 Ga]Ga-PentixaTher in OCI-LY1 DLBCL xenograft bearing NSG mice at 1 h p.i.. The treatment group ($n=5$) received 50 μ g Dexamethasone i.p. for 6 consecutive days before tracer injection. The biodistribution data are given in % injected dose per gram tissue (%ID/g) and are means \pm SD ($n=5$ animals/group)

As summarized in Fig. 4, Dexamethasone treatment (dosing as in [6]) had a pronounced effect on the overall biodistribution of [68 Ga]Ga-PentixaTher. The observed increased concentration of the tracer in blood (increase

by 58% in treated vs untreated animals) was reflected by a 53–68% higher absolute tracer uptake in all organs in the treated animals. The only exception from this consistent general effect was the OCI-LY1 xenograft,

with an increase in [⁶⁸Ga]Ga-PentixaTher uptake by 128% compared to untreated animals. As of now, the reasons for the tendency toward an increased blood concentration of [⁶⁸Ga]Ga-PentixaTher are unclear; it may either be the result of a delayed blood clearance as a side effect of corticosteroid treatment, or be related to an upregulation of mCXCR4 expression on circulating mouse immune cells (T-lymphocytes, B-cells [6]). [¹⁷⁷Lu]Lu-PentixaTher is known to display moderate affinity toward mCXCR4 [13], and it is highly probable that the mCXCR4 affinity of [⁶⁸Ga]Ga-PentixaTher lies in the same range, and thus, the increased [⁶⁸Ga]Ga-PentixaTher concentration in blood in treated animals may thus be related to specific tracer binding. However, further experiments are needed to confirm this hypothesis.

In contrast, however, the over-proportional increase in tracer accumulation in the OCI-LY1 xenograft is in line with our *in vitro* findings, i.e., a dexamethasone-treatment induced CXCR4 upregulation on the tumor cells. This is further underlined by the consistently higher tumor/organ ratios observed for the treated animals (Fig. 4). Although the differences in tumor/background ratios between the treated and the untreated animals are not statistically significant ($P=0.4-0.8$ for all organs) due to the relatively high standard deviation of the absolute tumor uptake value for the treatment group, our data nevertheless indicate a clear trend, which is in accordance with our *in vitro* observations.

In summary, we observed that corticosteroid treatment (Dexamethasone, Prednisolone) consistently induced an upregulation of CXCR4 expression DLBCL cells *in vitro*. Of note, the effect varied significantly between cell lines, the increase ranging from 20 to 300% of baseline CXCR4 expression. For the cell line with the most pronounced response to Dexamethasone treatment, OCI-LY1, the *in vitro* findings could also be recapitulated in the corresponding *in vivo* xenograft model. This confirms that at least the corticosteroid component of stabilizing chemotherapy regimens in DLBCL patients [8, 9] prior to CXCR4-targeted RLT with [¹⁷⁷Lu]Lu-PentixaTher does not lead to downregulation of the molecular target CXCR4 and may even have a contrary, beneficiary effect. However, it needs to be investigated in more detail to which extent rituximab or the other chemotherapeutic agents used in CHOP or DHAP treatment protocols affect CXCR4 expression, since these effects may limit the use of CXCR4-targeted diagnostics and/or CXCR4-targeted therapies [4]. A better understanding of CXCR4 (de)regulation by DLBCL lymphoma directed chemotherapies may help to ensure the choice of an appropriate treatment regimen prior to [¹⁷⁷Lu]Lu/[⁹⁰Y]Y-PentixaTher RLT in these diseases.

Materials and methods

Cell culture

Jurkat human T-cell leukemia cells were cultured in RPMI-1640 medium, supplemented with 10% FCS. All DLBCL cell lines, namely Daudi, OCI-LY1, SUDHL-4, -5, -6 and -8, were kindly supplied by Prof. Ulrich Keller, Department of Hematology and Oncology, Charité, Berlin, Germany, and were grown in RPMI-1640 medium, supplemented with 20% FCS. All cell lines were maintained at 37 °C in a humidified 5% CO₂ atmosphere. Media and supplements were obtained from Biochrom (Berlin, Germany) or Gibco (life technologies, Darmstadt, Germany). For cell counting, an automated CytoSMART Lux cell counter (Axion BioSystems, Atlanta, USA) was used.

For treatment with Dexamethasone and Prednisolone (obtained as suspensions/solutions for oral application from the clinical pharmacy at CHUV), the respective cell suspensions were centrifuged (3 min, 1300 rcf, Megafuge 1.0, Heraeus Thermo Scientific). The culture medium was removed and the cell pellet was resuspended in assay medium (DMEM/F-12 medium with Glutamax-1 (1:1) supplemented with 5% BSA) to yield a cell suspension with a concentration of app. $5-7 \cdot 10^6$ cells/ml. For treatment, either 140 µL of assay medium (untreated control cells) or 140 µL of tenfold concentrated solutions of Dexamethasone and Prednisolone (5 µM and 50 µM as well as 50 µM and 500 µM, respectively) was added to 1.26 mL of cell suspension. After incubation of the cells at 37° for 24 h in an incubator, the cells were centrifuged, washed once with assay medium, and resuspended in assay medium to a concentration of $5 \cdot 10^6$ cells/mL. This suspension was either used directly for the radioligand binding assay or processed further for flow cytometry analysis.

Flow cytometry

The treated and untreated cells were washed twice with cold flow cytometry buffer (5% fetal bovine serum in PBS). For the staining, triplicates of $1 \cdot 10^6$ cells were prepared and incubated 45 min on ice with a concentration of 1 µg/mL PE anti-human CD184 CXCR4 antibody (BioLegend) or PE mouse IgG2a isotype control (BioLegend) in 100 µL FACS buffer. Next, the cells were spun down at 300×g and the staining agent was discarded. The cells were washed twice and were resuspended in 500 µL of cold FACS buffer. In addition, DAPI was added to each sample shortly before the analysis to yield a final concentration of 0.5 µg/mL. The flow cytometry analyses were conducted immediately on a Beckman Coulter Gallios flow cytometer. The acquired data were analyzed with FlowJo v10.7.1.

Radioligand binding assay

Radiiodination of CXCR4.3 was carried out using the IodoGen[®] method as described previously [12].

For the binding assay, samples containing app. $1 \cdot 10^6$ cells in assay medium were incubated with [¹²⁵I]CPCR4.3 (0.2 nM) at RT for 60 min in the presence (non-specific binding) or absence (control) of 100 μM unlabeled CPCR4.3 (n=3 per condition, total sample volume: 250 μL). After incubation, the tubes were centrifuged (3 min, 1300 rcf, Megafuge 1.0, Heraeus Thermo Scientific) and the supernatant was carefully removed. The cells were washed once with 200 μL of cold HBSS, and the supernatant of the washing step was pooled with the supernatant from the previous step (free ligand). Then, the amount of bound radioligand in the cell pellet as well as the amount of free radioligand in the combined supernatants was quantified using a γ-counter (WALLAC; 1480 WIZARD™ 3"). For each sample, the cellular uptake in % of total added dose was calculated and then used for further data processing.

Tumor model and in vivo biodistribution studies

For induction of tumor growth, female NSG mice (6–8 weeks) were subcutaneously injected with 5×10^6 OCI-LY1 cells in HBSS/Matrigel (1:1). After 25 days, small palpable tumors had grown in all animals, and animals were divided into a control group (no treatment, n=5) and a treatment group (n=5). Treated animals received 50 μg Dexamethasone in 100 μL PBS as an i.p. injection for 6 consecutive days (day 25-day 30 post tumor implant). The following day, all animals were injected intravenously with 3–4 MBq (0.16–0.18 nmol) [⁶⁸Ga]Ga-PentixaTher, and a biodistribution study was carried out. The animals were sacrificed at 1 h post injection (p.i.), and the organs of interest were dissected. The radioactivity was measured in weighted tissue samples using a γ-counter. Data are expressed in % ID/g tissue (mean ± SD).

Author contributions

SM, DV and MS carried out the in vitro and in vivo experiments. AJ, SH, UK and MS designed the study, and MS wrote the manuscript. All authors were involved in the analysis and interpretation of the data and in revising the manuscript. All authors read and approved the final manuscript.

Funding

Open access funding provided by University of Lausanne. This study was conducted within the setting of a service contract between CHUV and PentixaPharm.

Availability of data and materials

All data generated or analyzed during this study are included in this published article.

Declarations**Ethical approval and consent to participate**

All in vivo experiments were conducted in compliance with the ARRIVE guidelines and according to the Swiss Federal Veterinary Office guidelines and were approved by the Cantonal Veterinary Office (permit number VD3595).

Consent to participate

Not applicable.

Consent for publication

Not applicable.

Competing interests

PentixaPharm GmbH is the exclusive IP license holder for PentixaFor and PentixaTher (WO/2020/053256A1, EP/2019/074196W; WO/2015/185162A1, EP2014/061875; WO/2011/131735, EP2011/056358). M.S. is listed as a coinventor on the respective patents. M.S. and U.K. are scientific advisors for PentixaPharm GmbH. Anna Janz is an employee of PentixaPharm GmbH.

Author details

¹Translational Radiopharmaceutical Sciences, Department of Nuclear Medicine and Department of Oncology, Centre Hospitalier Universitaire Vaudois (CHUV), University of Lausanne, Rue du Bugnon 25A, Agora, CH-1011 Lausanne, Switzerland. ²AGORA, Pôle de Recherche Sur Le Cancer, 1011 Lausanne, Switzerland. ³SCCL Swiss Cancer Center Leman, 1011 Lausanne, Switzerland. ⁴PentixaPharm GmbH, 97080 Würzburg, Germany. ⁵Department of Hematology, Oncology and Cancer Immunology, Campus Benjamin Franklin, Charité - Universitätsmedizin Berlin, corporate member of Freie Universität Berlin and Humboldt-Universität zu Berlin, Berlin, Germany. ⁶German Cancer Consortium (DKTK), German Cancer Research Center (DKFZ), Heidelberg, Germany. ⁷Max Delbrück Center (MDC), 13092 Berlin, Germany.

Received: 20 March 2023 Accepted: 2 May 2023

Published online: 10 May 2023

References

- Buck AK, Serfling SE, Lindner T, Hänscheid H, Schirbel A, Hahner S, Fassnacht M, Einsele H, Werner RA. CXCR4-targeted theranostics in oncology. *Eur J Nucl Med Mol Imag.* 2022;49(12):4133–44.
- Lapa C, Hänscheid H, Kircher M, Schirbel A, Wunderlich G, Werner RA, Samnick S, Kotzerke J, Einsele H, Buck AK, Wester HJ, Grigoleit GU. Feasibility of CXCR4-directed radioligand therapy in advanced diffuse large B-cell lymphoma. *J Nucl Med.* 2019;60:60–4.
- Lapa C, Herrmann K, Schirbel A, Hänscheid H, Luckerath K, Schottelius M, Kircher M, Werner RA, Schreder M, Samnick S, Kropf S, Knop S, Buck AK, Einsele H, Wester HJ, Kortum KM. CXCR4-directed endoradiotherapy induces high response rates in extramedullary relapsed multiple myeloma. *Theranostics.* 2017;7:1589–97.
- Lapa C, Luckerath K, Kircher S, Hänscheid H, Grigoleit GU, Rosenwald A, Stolzenburg A, Kropf S, Einsele H, Wester HJ, Buck AK, Kortum KM, Schirbel A. Potential influence of concomitant chemotherapy on CXCR4 expression in receptor directed endoradiotherapy. *Br J Haematol.* 2019;184:440–3.
- Kim SW, Kim HY, Lee HJ, Yun HJ, Kim S, Jo DY. Dexamethasone and hypoxia upregulate CXCR4 expression in myeloma cells. *Leuk Lymphoma.* 2009;50:1163–73.
- Cain DW, Bortner CD, Diaz-Jimenez D, Petrillo MG, Gruver-Yates A, Cidlowski JA. Murine glucocorticoid receptors orchestrate B cell migration selectively between bone marrow and blood. *J Immunol.* 2020;205:619–29.
- Besedovsky L, Linz B, Dimitrov S, Groch S, Born J, Lange T. Cortisol increases CXCR4 expression but does not affect CD62L and CCR7 levels on specific T cell subsets in humans. *Am J Physiol Endocrinol Metab.* 2014;306:E1322–1329.
- Pfeundschuh M, Trumper L, Osterborg A, Pettengell R, Trneny M, Imrie K, Ma D, Gill D, Walewski J, Zinzani PL, Stahel R, Kvaloy S, Shpilberg O, Jaeger

- U, Hansen M, Lehtinen T, Lopez-Guillermo A, Corrado C, Scheliga A, Milpied N, Mendila M, Rashford M, Kuhnt E. MabThera International Trial G. CHOP-like chemotherapy plus rituximab versus CHOP-like chemotherapy alone in young patients with good-prognosis diffuse large-B-cell lymphoma: a randomised controlled trial by the MabThera International Trial (MinT) Group. *Lancet Oncol.* 2006;7:379–91.
9. Hu J, Wang X, Chen F, Ding M, Dong M, Yang W, Yin M, Wu J, Zhang L, Fu X, Sun Z, Li L, Wang X, Li X, Guo S, Zhang D, Lu X, Leng Q, Zhang M, Zhu L, Zhang X, Chen Q. Combination of decitabine and a modified regimen of cisplatin, cytarabine and dexamethasone: a potential salvage regimen for relapsed or refractory diffuse large B-cell lymphoma after second-line treatment failure. *Front Oncol.* 2021;11:687374.
 10. Subramaniam SL, R. Application number: 211379Orig1s000. Center for Drug Evaluation and Research. 2019, Reference ID: 4493351.
 11. i MN, Pinilla E, Paulos C, Chavez J, Puelles V, Arancibia A. Determination of prednisolone and prednisone in plasma, whole blood, urine, and bound-to-plasma proteins by high-performance liquid chromatography. *J Chromatogr Sci.* 2005;43:201–6.
 12. Schottelius M, Ludescher M, Richter F, Kapp TG, Kessler H, Wester HJ. Validation of $[(125)I]CPCr4.3$ as an investigative tool for the sensitive and specific detection of hCXCR4 and mCXCR4 expression in vitro and in vivo. *EJNMMI Res.* 2019;9:75.
 13. Schottelius M, Osl T, Poschenrieder A, Herrmann K, Lapa C, Hoffmann F, Schwaiger M, Lassmann M, Buck A, Wester H. [177 Lu-pentixather: pre-clinical and first patient results with a highly promising CXCR4-directed endoradiotherapeutic agent. *J Nucl Med.* 2015;56:339–339.

Publisher's Note

Springer Nature remains neutral with regard to jurisdictional claims in published maps and institutional affiliations.

Submit your manuscript to a SpringerOpen[®] journal and benefit from:

- Convenient online submission
- Rigorous peer review
- Open access: articles freely available online
- High visibility within the field
- Retaining the copyright to your article

Submit your next manuscript at ► [springeropen.com](https://www.springeropen.com)

7 Methodological developments

During this thesis, two methodologies were developed. The first established method involves direct conjugation of unprotected macrocyclic chelators such as DOTA or NOTA to immobilized peptides on 2CTC resin. Through this method, the radiotracer precursors **DOTA-RAP-103** and **CC-1** to **CC-7** as well as the clinically relevant compound **PSMA-617** were successfully synthesized (see section 7.1). The second method allowed simultaneous purification and formulation of peptide radiopharmaceuticals in physiologic solution using size exclusion cartridges (G10, 700 kDa cut-off). This method was established with a set of various radiotracers (e.g., monomer vs trimer) as well as relevant radionuclides in the field of nuclear imaging (see section 7.2).

7.1 Conjugation of macrocyclic chelators using solid-phase peptide synthesis

This article is in preparation for the submission to Tetrahedron Letters.

Conjugation of unprotected macrocyclic chelators using solid-phase peptide synthesis

Sebastian Martin^a, Tobias Stemler^b and Margret Schottelius^{a*}^a Department of Nuclear Medicine and Molecular Imaging, Lausanne University Hospital, Rue de Bugnon 25A, CH-1011 Lausanne, Switzerland^b Department of Nuclear Medicine, Saarland University – Medical Center, Kirrbergerstrasse, D-66421, Homburg, Germany

ARTICLE INFO

ABSTRACT

Article history:

Keywords:

DOTA coupling

NOTA coupling

Peptide radiotracer

Solid-phase peptide synthesis (SPPS)

An alternative method for the solid phase coupling of unprotected 1,4,7,10-Tetraazacyclododecane-1,4,7,10-tetraacetic acid (DOTA) and 2,2',2''-(1,4,7-triazacyclononane-1,4,7-triyl)triacetic acid (NOTA) during solid phase peptide synthesis (SPPS). This method uses unprotected chelators DOTA and NOTA, a THF/H₂O based solvent system and 1-Ethyl-3-(3-dimethylaminopropyl)carbodiimide (EDC) as activating agent to obtain chelator-bearing radiolabeling precursors by SPPS. Beside the synthesis of the established PSMA-targeted ligand PSMA-617, the method was expanded to a variety of small receptor targeted peptides with aminohexanoic linker moieties. In contrast to the established use of monoreactive DOTA-tris(tert-butyl)- or NOTA-bis(tert-butyl) ester, this method has the distinct advantage of avoiding a subsequent deprotection step and represents an economic small-scale synthesis method for peptide based radiotracer precursors.

1. Introduction

The undisputed clinical success of peptide-based radiotracers such as the PSMA-targeted inhibitor PSMA-617 or the SST2-targeted ligand DOTA-TATE is based on some unique features associated with using peptides as targeting vectors: due to their small size, they usually show fast clearance from non-target tissue, low background accumulation and, based on their relative hydrophilicity, predominant renal excretion. Additionally, their relatively easy chemical accessibility via SPPS and subsequent functionalization allows precise fine-tuning of their respective receptor affinity and pharmacokinetic profile.^{1,2}

Most peptide tracers that have found their way into clinical routine are conjugated with a bifunctional chelator such as DOTA, NOTA or DOTAGA, allowing fast and efficient radiolabeling with diagnostic and therapeutic radionuclides, e.g. ⁶⁸Ga, ¹⁷⁷Lu or ⁶⁴Cu.³

Usually, to introduce these chelators, monoreactive, triply tBu-protected DOTA or NOTA derivatives are used for peptide derivatization on solid-phase due to their compatibility with standard SPPS conditions such as solvents and coupling reagents. However, the final deprotection of the tert-butyl groups requires harsh conditions (e.g. 1:1 TFA/DCM or TFA/TRIS/H₂O 95:2.5:2.5). Due to the slow cleavage rates of tert-butyl ester groups in DOTA(tBu)₃ and NOTA(tBu)₃, final deprotection is frequently inefficient and require prolonged acidolysis which can lead to undesired side products or a progressive degradation of the bioactive peptide sequence. Problems with a sluggish cleavage rate of tert-butyl esters are frequently reported in the literature.⁴⁻⁷ To circumvent drawbacks during synthesis, we have developed an alternative method to obtain DOTA or NOTA bioconjugates using the unprotected bifunctional chelators as reagents during SPPS. As an exemplary, clinically relevant labeling precursor, PSMA-617 was synthesized using this approach, and the complementary NOTA was also prepared to confirm the versatility of the approach. Furthermore, various small peptides bearing aminohexanoic linkers were also functionalized.

2. Results

Initially, the novel DOTA-conjugation method was investigated in the synthesis of the established radiolabeling precursor PSMA-617. To obtain the urea based binding motif EuK (Glu-urea-Lys) we used 1,1'-Carbonyldiimidazole (CDI). That agent is less toxic compared to the triphosgene, which was used in previous studies.^{8, 9} The CDI activated Lysine derivative was purified by chromatography to gain the PSMA binding motif EuK highly pure and in high coupling yields of 65% on 2CTC resin. Subsequently, the linker moiety consisting of D-naphthyl alanine and trans-4-aminocyclohexanoic acid was conjugated on the binding motif by applying SPPS.

In contrast to current standard protocols using DOTA(tBu)₃ ester for the final coupling^{8, 10, 11}, we simplified the synthesis by using a THF/H₂O solvent mixture, which allowed us to conjugate unprotected DOTA directly to the resin bound N-terminal amino group of the linker. To this aim, DOTA was pre-activated using 1-Ethyl-3-(3-dimethylaminopropyl)carbodiimide (EDCI) and Pentafluorophenol (Pfp). A content of 15-30% H₂O in THF (v/v) was identified as optimal for efficient coupling rates, whereas less than 15% of water led to a persisting precipitation of the chelator from the solvent mixture. Under these conditions chelator pre-activation with EDCI, DIPEA and Pfp led to a complete disappearance of occurring precipitation after 10 minutes of stirring. Next, the activated DOTA was added directly to the pre-soaked resin, which was forming small droplets through the polar protic solvent. In contrast, synthesis approaches using ACN or DMF as organic solvents in 15-30% water resulted in irreversible precipitation and few product formation. The reagents were incubated for 3 hours to achieve coupling rates between 6-20%. A direct comparison of the synthesis of PSMA-617 via (a) the DOTA-tris-butyl/TBTU and (b) the unprotected DOTA/EDCI method on the 2CTC resin with an initial load of 0.82 mmol/g revealed that the established protocol has no disadvantage regarding the final yield of the purified radiotracer precursor. After semipreparative HPLC work-up of PSMA-617, the conventional method (a) revealed an average yield of 3.7±1.7 mg per 100 mg of

*corresponding author: margret.schottelius@chuv.ch

resin (n=3), while method (b) showed a yield of 7.2±2.0 mg per 100 mg of resin (n=3) using the same resin as starting material.

Additionally, we successfully tested this method with NOTA as chelating moiety to synthesize NOTA-PSMA-617 and validated the method using the DOTA chelator on various peptide sequences with similar outcome (see Table 1). By using nearly equimolar amounts of chelator and the coupling reagent EDCI, however, the formation of the product peak was restricted to a maximum of roughly 30-60% AUC. Another limitation was the utilized resin. Applying this synthesis protocol on rink-amide resin the coupling was unsuccessful. Noteworthy, the conventional method already showed low yields on peptide DOTA-208, indicating that the sequence may be challenging. The coupling on compound DOTA-208 failed using the DOTA/EDCI based method.

Overall, we were able to show that coupling of unprotected macrocyclic chelators such as DOTA and NOTA to 2CTC-resin bound peptide precursors is feasible in satisfactory yields using

almost equimolar amounts of chelator and coupling reagent and an appropriate solvent system (THF/water). Final isolated yields are comparable to those obtained by using monoreactive DOTA as well as in solution phase chemistry (cleavage of the crude peptide and subsequent solution phase coupling of DOTA in DMF/H₂O as previously published¹²). Hence, on-resin coupling of unprotected chelators in aqueous solvent systems represents a straightforward, easy-to-implement strategy for the full SPPS synthesis of peptides. On the one hand, it obliterates issues of the final DOTA deprotection, which can be accompanied by substantial losses in product yield, and secondly, use of the less costly unprotected DOTA or NOTA. Thus, this method may be very well suited as cost-effective alternative delivering peptide precursors for radiometal labeling by SPPS in a small scale.

Table 1. Peptides synthesized by direct coupling with DOTA or NOTA using 2CTC resin and EDCI in THF/water.

Compound	Sequence ^a	Applied protocol	Coupling yield (n=3) [%±SD] ^b	Initial resin load [mmol/g]	Yield per 100 mg of resin [mg] ^c
PSMA-617	E-u-K-Nal-AMCHC-DOTA	Resin-based	14.7±6.6	0.82	7.2±2.0
PSMA-617	E-u-K-Nal-AMCHC-DOTA	Conventional	14.5±1.2	0.82	3.7±1.7
NOTA-PSMA-617	E-u-K-Nal-AMCHC-NOTA	Resin-based	n/a	0.82	n/a
DOTA-RAP-103	t-t-n-y-t-Ahx-DOTA	Resin-based	n/a	0.99	12.43
CC-1	r-y-t-s-s-Ahx-DOTA	Resin-based	n/a	0.92	10.1
CC-2	t-y-s-t-t-Ahx-DOTA	Resin-based	n/a	1.23	9.73
CC-3	t-y-n-d-i-Ahx-DOTA	Resin-based	n/a	0.54	4.14
CC-4	t-y-n-d-i-Ahx-DOTA	Resin-based	n/a	1.23	8.95
CC-5	r-y-s-t-n-Ahx-DOTA	Resin-based	n/a	0.92	8.67
CC-6	t-y-n-n-i-Ahx-DOTA	Resin-based	n/a	1.23	4.24
CC-7	g-y-s-t-n-Ahx-DOTA	Resin-based	n/a	1.27	8.23
CC-8	s-y-w-t-e-Ahx-DOTA	Conventional	n/a	0.96	3.28

^aOne letter code of Amino acids. Small letters signify amino acids in D-configuration, capital letters for amino acids in S-configuration. For u: Urea; Nal: Naphthyl alanine; AMCHC = trans-4-Aminocyclohexanoic acid; Ahx = Aminohexanoic acid.

^bThe coupling yield corresponds to the SPPS based coupling between the peptide and the chelator DOTA.

^cYield after semi-preparative HPLC work-up of 100mg of cleaved resin.

Acknowledgments

Not applicable.

References

- Osl, T.; Schmidt, A.; Schwaiger, M.; Schottelius, M.; Wester, H.-J., A new class of PentixaFor- and PentixaTher-based theranostic agents with enhanced CXCR4-targeting efficiency. *Theranostics* **2020**, *10* (18), 8264-8280.
 - Benešová, M.; Bauder-Wüst, U.; Schäfer, M.; Klika, K. D.; Mier, W.; Haberkorn, U.; Kopka, K.; Eder, M., Linker Modification Strategies To Control the Prostate-Specific Membrane Antigen (PSMA)-Targeting and Pharmacokinetic Properties of DOTA-Conjugated PSMA Inhibitors. *Journal of Medicinal Chemistry* **2016**, *59* (5), 1761-1775.
 - Drude, N.; Tienken, L.; Mottaghy, F. M., Theranostic and nanotheranostic probes in nuclear medicine. *Methods* **2017**, *130*, 14-22.
 - Knör, S.; Modlinger, A.; Poethko, T.; Schottelius, M.; Wester, H. J.; Kessler, H., Synthesis of novel 1,4,7,10-tetraazacyclodecane-1,4,7,10-tetraacetic acid (DOTA) derivatives for chemoselective attachment to unprotected polyfunctionalized compounds. *Chemistry* **2007**, *13* (21), 6082-90.
 - Mier, W.; Zitzmann, S.; Krämer, S.; Reed, J.; Knapp, E.-M.; Altmann, A.; Eisenhut, M.; Haberkorn, U., Influence of Chelate
- *corresponding author: margret.schottelius@chuv.ch

Conjugation on a Newly Identified Tumor-Targeting Peptide. *Journal of Nuclear Medicine* **2007**, *48* (9), 1545-1552.

- Wängler, B.; Beck, C.; Wagner-Utermann, U.; Schirmacher, E.; Bauer, C.; Rösch, F.; Schirmacher, R.; Eisenhut, M., Application of tris-allyl-DOTA in the preparation of DOTA-peptide conjugates. *Tetrahedron Letters* **2006**, *47* (33), 5985-5988.
- Mier, W.; Graham, K. A. N.; Wang, Q.; Krämer, S.; Hoffend, J.; Eisenhut, M.; Haberkorn, U., Synthesis of peptide conjugated chelator oligomers for endoradiotherapy and MRT imaging. *Tetrahedron Letters* **2004**, *45* (28), 5453-5455.
- Benešová, M.; Schäfer, M.; Bauder-Wüst, U.; Afshar-Oromieh, A.; Kratochwil, C.; Mier, W.; Haberkorn, U.; Kopka, K.; Eder, M., Preclinical Evaluation of a Tailor-Made DOTA-Conjugated PSMA Inhibitor with Optimized Linker Moiety for Imaging and Endoradiotherapy of Prostate Cancer. *J Nucl Med* **2015**, *56* (6), 914-20.
- Greifenstein, L.; Engelbogen, N.; Lahnif, H.; Sinnes, J.-P.; Bergmann, R.; Bachmann, M.; Rösch, F., Synthesis, Labeling and Preclinical Evaluation of a Squaric Acid Containing PSMA Inhibitor Labeled with ⁶⁸Ga: A Comparison with PSMA-11 and PSMA-617. *ChemMedChem* **2020**, *15* (8), 695-704.
- Ginj, M.; Maecke, H. R., Synthesis of trifunctional somatostatin based derivatives for improved cellular and subcellular uptake. *Tetrahedron Letters* **2005**, *46* (16), 2821-2824.
- Roosenburg, S.; Laverman, P.; Joosten, L.; Eek, A.; Oyen, W. J. G.; de Jong, M.; Rutjes, F. P. J. T.; van Delft, F. L.; Boerman, O. C., Stabilized ¹¹¹In-Labeled sCCK8 Analogues for Targeting

CCK2-Receptor Positive Tumors: Synthesis and Evaluation.
Bioconjugate Chemistry **2010**, *21* (4), 663-670.

12. Schottelius, M.; Schwaiger, M.; Wester, H.-J., Rapid and high-yield solution-phase synthesis of DOTA-Tyr3-octreotide and DOTA-Tyr3-octreotate using unprotected DOTA. *Tetrahedron Letters* **2003**, *44* (11), 2393-2396.

Supplementary Material

Supplementary material provided.

Supplementary Information

Conjugation of unprotected macrocyclic chelators using solid-phase peptide synthesis

Martin Sebastian^a*, Tobias Stemler^b and Margret Schottelius^a*

^a *Department of Nuclear Medicine and Molecular Imaging, Lausanne University Hospital, Rue de Bugnon 25A, CH-1011 Lausanne, Switzerland*

^b *Department of Nuclear Medicine, Saarland University – Medical Center, Kirrbergerstrasse, D-66421, Homburg, Germany*

* Corresponding author. margret.schottelius@chuv.ch

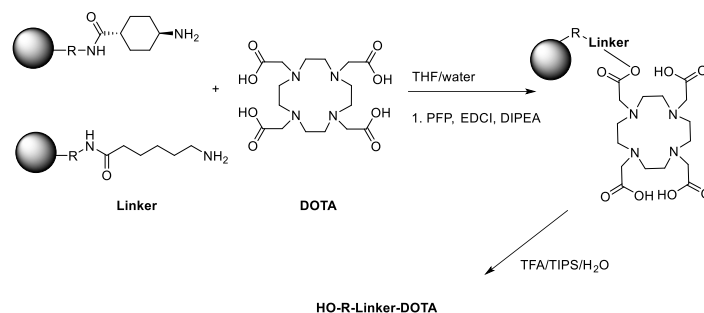


Figure 1 Reaction scheme of the established resin-based methodology.

Resin-based methodology

DOTA (2 eq) was dissolved in water (0.25 mmol DOTA per mL). Pentafluorophenol (PFP) (2.5 eq) was dissolved in Tetrahydrofuran (THF) (1 mL/g) and the appropriate volume was given into the dissolved DOTA solution. EDCI (2.5 eq) was dissolved in THF/water (1:1, v/v) to a final concentration of 0.3-0.7 mmol/mL, DIPEA (20 eq) was added and the mixture was added stepwise to the DOTA solution under vigorous stirring. After 5 min both reactants were mixed, THF was added slowly (100 μ L per step) over a period of another 5 min so that the reaction mixture contained approximately 30-50% of THF. Next, the pre-activated DOTA mixture was given to the resin in THF containing usually 3-5 mL of THF. The resin was agitated for 2 hours and then washed 2 times in THF and DMF, respectively.

Conventional method

DOTA-tris(tert-butyl ester) was activated using 2-(1H-Benzotriazole-1-yl)-1,1,3,3-tetramethylammonium tetrafluoroborate (TBTU) (2 eq), HOBT (2 eq) and DIPEA (4.5 eq) in DMF for 5 min. Subsequently, the preactivated agent was added to the resin which was then shaken for 2 hours.

Cleavage and crude preparation

A mixture of Trifluoroacetic acid (TFA), Triisopropyl silane (TIPS), water (95:2.5:2.5, v/v/v) was utilized to cleave and deprotect the peptides three times for 15 min, while the liquid was collected to remove the TFA under nitrogen flow. After 45 min, the remaining cleavage agent was filled up to a volume of approximately 1 mL with methanol and given to 45 mL of cold Diethylether (DEE). The precipitated peptide was centrifuged (3 min, 3000 rpm). The pellet was redissolved in approximately 1 mL of methanol and filtered through a 0.2 μ m Ministart RC4 filter.

Product isolation and analysis

High performance liquid chromatography (HPLC) was conducted on a Shimadzu LC-40D equipped with a SPD-M40 DAD UV detector (UV detection at 220 nm) a DGU-405 degassing unit and a CTO-40C column oven (column temperature at 40°C). For all HPLC measurements, the solvent system was A = 0.1% TFA in H₂O; B = 0.1% TFA in acetonitrile. For analytical measurements 1a a 150x4.6mm MultiKrom 100-5 C18 (CS Chromatographie Service GmbH, Langerwehre) was used. Analytical HPLC: 0-1 min 5% B, 1-25 min 5-40% B, 25-30 min 40-90% B, 26-28 min 80% B, 28-32 min 90% B, 32-35 min 90-5% B, 35-37 min 5% B at a flow rate of 1 mL min⁻¹. For crude purification the 250x10mm MultoKrom 100-5 C18 (CS-Chromatographie Service GmbH, Langwehre) column was installed. Gradient: 0-1 min 5% B, 1-15 min 5-20% B, 15-16 min 20-80% B, 16-18 min 80% B, 18-19 min 80-5% B, 19-22 min 5% B at a flow rate of 4 mL min⁻¹. Mass spectrometry was performed on a Advion Express ESI system.

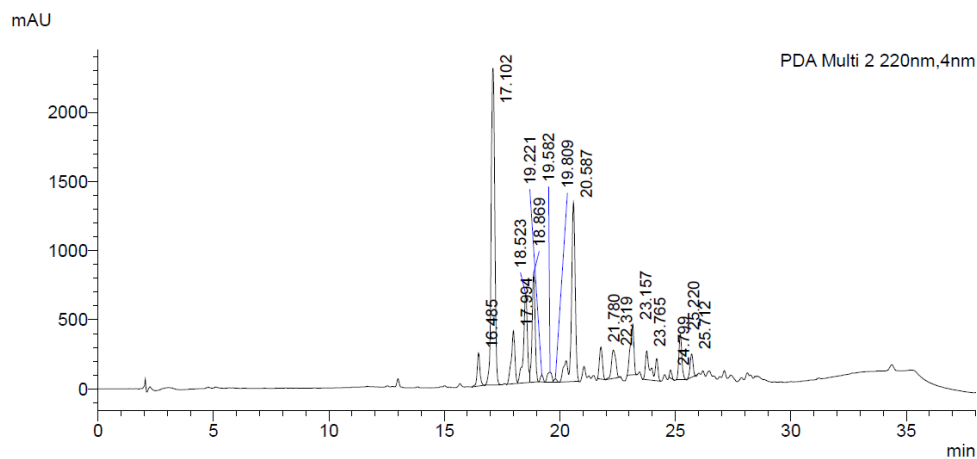


Figure 2 Analytical chromatogram of crude PSMA-617 synthesized applying the alternative DOTA/EDCI protocol. 30.4% AUC of main product peak at 17.10 min. HPLC gradient 1a.

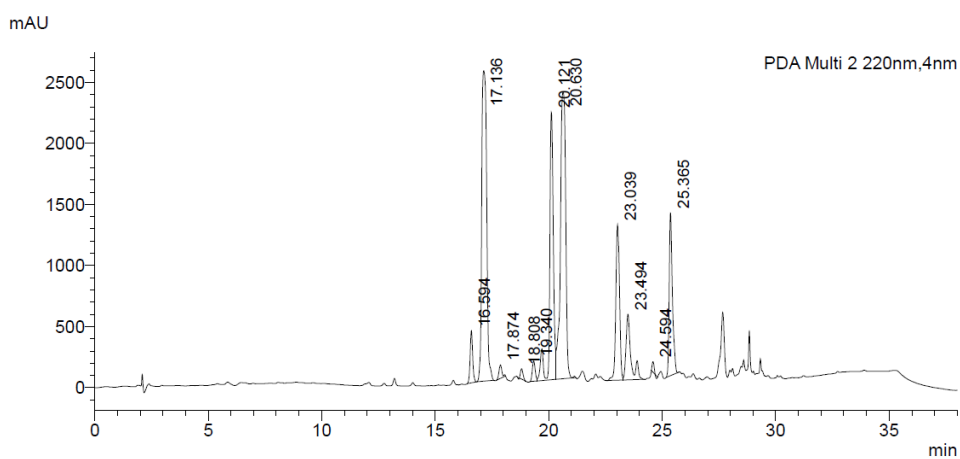


Figure 3 Analytical chromatogram of crude PSMA-617 synthesized applying the conventional synthesis protocol using DOTA-tris(tertbutyl ester). 26.9% AUC of main product peak at 17.13 min. HPLC gradient 1a.

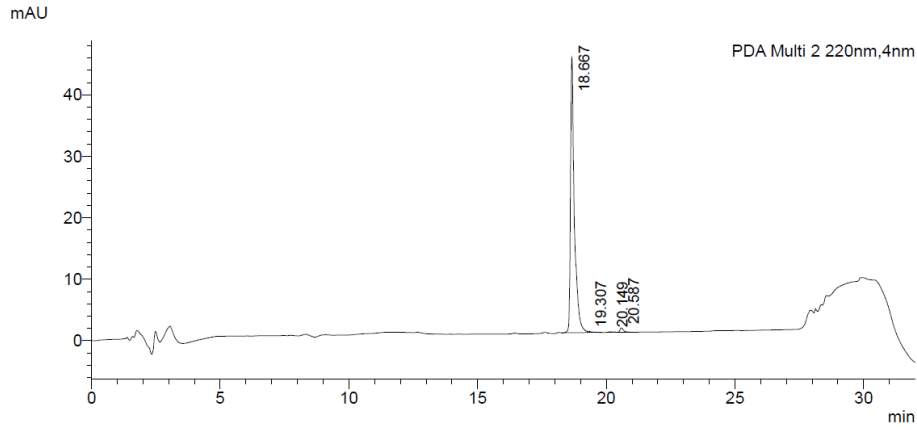


Figure 4 Analytical chromatogram of purified PSMA-617. Product peak at 18.7 min (97.9% purity).

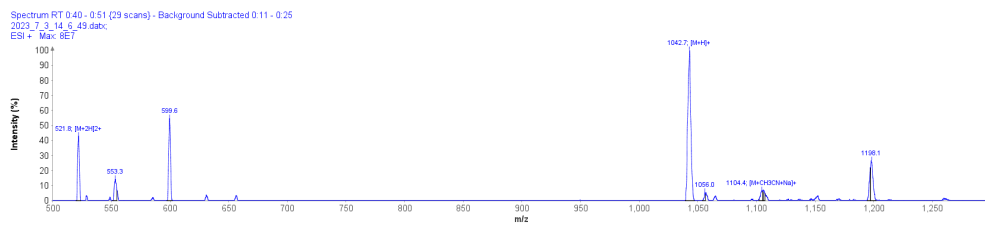


Figure 5 MS spectrum of purified PSMA-617.

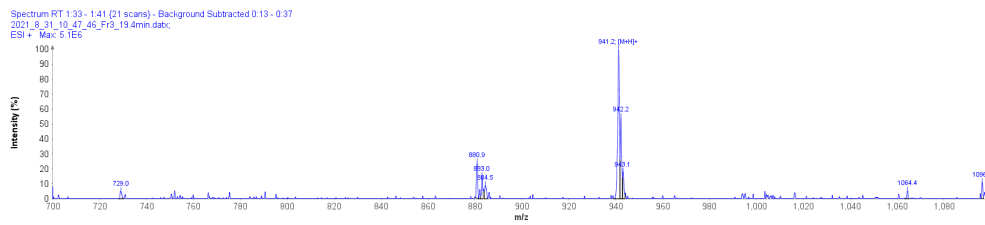


Figure 6 MS spectrum of purified NOTA-PSMA-617.

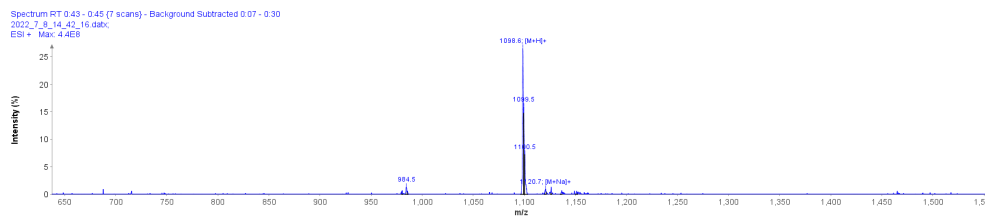


Figure 7 MS spectrum of purified DOTA-RAP-103.

**7.2 Validation of a size exclusion method for concomitant
purification and formulation of peptide
radiopharmaceuticals**

Reproduced with permission of Springer Nature.

METHODOLOGY

Open Access



Validation of a size exclusion method for concomitant purification and formulation of peptide radiopharmaceuticals

Sebastian Martin^{1,2,3} , Lennard Wendlinger^{1,2,3} , Alexandra Litvinenko^{1,2,3} , Radmila Faizova^{1,2,3} and Margret Schottelius^{1,2,3*}

*Correspondence:
Margret Schottelius
margret.schottelius@chuv.ch
¹Translational Radiopharmaceutical Sciences, Department of Nuclear Medicine and Department of Oncology, Centre Hospitalier Universitaire Vaudois (CHUV) and University of Lausanne (UNIL), Rue du Bugnon 25A, Agora, Lausanne CH-1011, Switzerland
²AGORA, Pôle de recherche sur le cancer, Lausanne 1011, Switzerland
³SCCL Swiss Cancer Center Leman, Lausanne 1011, Switzerland

Abstract

Background Both in clinical routine and in preclinical research, the established standard procedure for the final purification of radiometal-labeled peptide radiopharmaceuticals is cartridge-based reversed-phase (RP) solid phase extraction (SPE). It allows the rapid and quantitative separation of the radiolabeled peptide from hydrophilic impurities and easy integration into automated synthesis procedures. However, product elution from RP cartridges necessitates the use of organic solvents and product recovery is sometimes limited. Thus, an alternative purification method based on commercially available size exclusion cartridges was investigated.

Results Since most peptide radiopharmaceuticals have a molecular weight > 1 kDa, Sephadex G10 cartridges with a molecular size cut-off of 700 Da were used for the final purification of a broad palette of ⁶⁸Ga-, ⁶⁴Cu- and ^{99m}Tc-labeled experimental peptide radiotracers as well as the clinically relevant ligand PSMA-617. Results (radiochemical purity (RCP, determined by ITLC), recovery from the solid support) were compared to the respective standard RP-SPE method. Generally, retention of unreacted ⁶⁸Ga, ⁶⁴Cu and ^{99m}Tc salts on the G10 cartridges was quantitative up to the specified elution volume (1.2 mL) for ⁶⁸Ga and ^{99m}Tc and 99.6% for ⁶⁴Cu. Even at increased elution volumes of 1.5–2 mL, RCPs of the eluted ⁶⁸Ga- and ^{99m}Tc -radiopeptides were > 99%. For all peptides with a molecular weight ≥ 2 kDa, product recovery from the G10 cartridges was consistently > 85% upon respective adjustment of the elution volume. Product recovery was lowest for [⁶⁸Ga]Ga-PSMA-617 (67%, 1.2 mL to 84%, 2 mL). The pH of the final product solution was found to be volume-dependent (1.2 mL: pH 6.3; 1.5 mL: pH 5.9; 2 mL: pH 5.5). Notably, the G10 cartridges were reused up to 20 times without compromising performance, and implementation of the method in an automated radiosynthesis procedure was successful.

Conclusions Overall, size exclusion purification yielded all peptide radiopharmaceuticals in excellent radiochemical purities (> 99%) in saline within 10–12 min. Although product recovery is marginally inferior to classical SPE purifications, this method has the advantage of completely avoiding organic solvents and representing a cost-effective, easy-to-implement purification approach for automated radiotracer synthesis.



© The Author(s) 2024. **Open Access** This article is licensed under a Creative Commons Attribution 4.0 International License, which permits use, sharing, adaptation, distribution and reproduction in any medium or format, as long as you give appropriate credit to the original author(s) and the source, provide a link to the Creative Commons licence, and indicate if changes were made. The images or other third party material in this article are included in the article's Creative Commons licence, unless indicated otherwise in a credit line to the material. If material is not included in the article's Creative Commons licence and your intended use is not permitted by statutory regulation or exceeds the permitted use, you will need to obtain permission directly from the copyright holder. To view a copy of this licence, visit <http://creativecommons.org/licenses/by/4.0/>.

Keywords Size-exclusion cartridge, Peptide radiopharmaceutical, Tracer, Purification, Sephadex G10

Background

The widely established standard labeling protocols for ^{68}Ga -, ^{64}Cu - or $^{99\text{m}}\text{Tc}$ -labeling of chelator functionalized peptides usually provide excellent radiolabeling yields, with frequently >97% of incorporated radionuclide. Nevertheless, both in clinical routine production and in preclinical research, the preparation of radiometal-labeled peptide radiopharmaceuticals almost always involves a last purification step using (reversed phase (RP)) solid phase extraction (SPE) cartridges (Neels et al., 2018; Decristoforo et al., 2007; Hennrich & Benešová, 2020; Hennrich & Eder, 2022; Hennrich & Eder, 2021). This step ensures quantitative removal of free radionuclide or radionuclide colloids and of non-physiological, potentially toxic labeling buffer components, such as HEPES (Nelson et al., 2022). However, product elution requires organic solvents like ethanol (Decristoforo et al., 2007; Hennrich & Eder, 2021; Nelson et al., 2022). Additionally, acidic conditions may prove indispensable to obtain sufficient product recovery from the solid phase (Robu et al., 2017). This, in turn, entails additional processing steps, such as solvent evaporation, neutralization or dilution to meet the specifications for injectable solutions (pH 4–8, ethanol $\leq 10\%$ v/v) (Hennrich & Eder, 2021; Serdons et al., 2008). Although small amounts of ethanol are accepted in the final formulation of peptide radiopharmaceuticals, the presence of ethanol can lead to pain and haemolysis at the injection site (Serdons et al., 2008). On the other hand, evaporation of the organic solvent by heat under nitrogen flow is time consuming (10–20 min) and leads to a loss of activity, especially when working with short-lived radioisotopes such as ^{68}Ga . In some cases, another drawback of SPE purification consists in the poor recovery of the final product from the solid support. This has been shown for ^{68}Ga -DOTA-TBIA101 (Mokaleng et al., 2015), for which low recovery limited the overall yield of the final product.

To circumvent the complications associated with the use of RP-SPE cartridges, we investigated the use of size exclusion chromatography (SEC) cartridges as an alternative, organic-solvent-free purification method for radiometal-labeled peptide radiopharmaceuticals. Since most peptide radiotracers have a molecular weight >1 kDa, Sephadex G10 cartridges with a molecular weight cut-off of 700 Da (for a sample volume of 1 mL) were chosen for this study. After assessing the retention capacities of the material for free $^{68}\text{GaCl}_3$, $^{64}\text{CuCl}_2$ and $^{99\text{m}}\text{TcO}_4^-$, the size exclusion purification method was investigated for the post-labeling workup of a variety of ^{68}Ga -, ^{64}Cu - and $^{99\text{m}}\text{Tc}$ -labeled peptide radiopharmaceuticals in a molecular weight range of 1–3 kDa. ^{68}Ga -PSMA-617 was included as a clinically relevant reference. Key parameters such as radiochemical purity (RCP) after purification and recovery from the cartridge material were quantified and compared to the respective results obtained by SPE purification. In a last step, the SEC-based purification was implemented in a semi-automated synthesis protocol.

Results

The results obtained for the retention capacity of the G10 cartridges for the free ^{68}Ga -, ^{64}Cu - and $^{99\text{m}}\text{Tc}$ -radionuclide salts are summarized in Fig. 1A. All reaction mixtures were applied to the cartridge in a fixed volume of 0.5 mL and in the respective radiolabeling

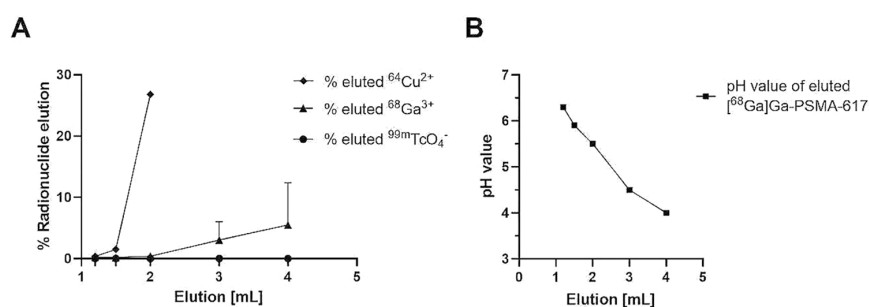


Fig. 1 (A) Retention capacity of the G10 size exclusion cartridge for the free ^{68}Ga , ^{64}Cu and $^{99\text{m}}\text{Tc}$ -radiionuclide salts as present in the radiolabeling mixture. Saline (0.9% NaCl) was used for elution. (B) Exemplary correlation between elution volume and pH of the final product [^{68}Ga]Ga-PSMA-617 in labeling buffer (1 M NaOAc, pH 4.5)

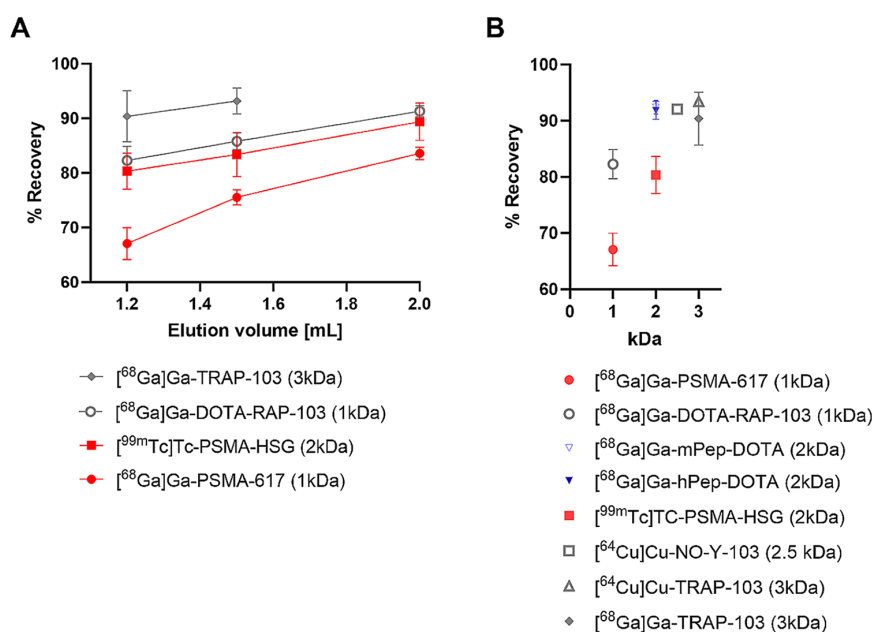


Fig. 2 Assessment of the recovery using a G10 cartridge. Gray: radiotracers with neutral binding motif; Red: radiotracers with anionic binding motif; Blue: radiotracers with cationic binding motif. (A) Recovery of selected peptide radiopharmaceuticals as a function of elution volume. (B) Recovery of the investigated peptide radiopharmaceuticals at a fixed elution volume of 1.2 mL as a function of molecular weight

buffer (no colloid formation). In the case of ^{68}Ga , quantitative retention of the free radio-nuclide was observed for a 1.2 mL elution volume, and only $0.4 \pm 0.2\%$ of free ^{68}Ga was eluted, when the elution volume was increased to 2 mL. In contrast, for ^{64}Cu , 0.4% of the activity were already eluted with 1.2 mL 0.9% NaCl, increasing to $>1\%$ and $>25\%$ of the initial activity, respectively, when elution volumes of 1.5 and 2 mL were used. Interestingly, $^{99\text{m}}\text{Tc}$ -pertechnetate showed quantitative retention on the size exclusion cartridge, both when applied in radiolabeling buffer and as pure generator eluate (in saline), even when the elution volume was increased to 4 mL. Retention of freshly generated $^{99\text{m}}\text{Tc}$ -tin colloid was slightly less efficient (see materials and methods). While 98% of the $^{99\text{m}}\text{Tc}$ -tin colloid remained trapped on the G10 column, $1.0 \pm 0.7\%$ were eluted using a

2 mL elution volume. For $^{68}\text{GaOH}_3$ colloid, app. 50% of the activity were eluted using an elution volume of 1.2 mL.

Next, the buffer exchange capacity of the used G10 cartridges was investigated by pH measurements of the eluate at different elution volumes. The pH values were determined both by pH paper strips and a pH electrode. After the radiolabeling of PSMA-617 in sodium acetate buffer (1 M, pH=4.5) as an exemplary tracer, the pH of the eluate remained stable at pH 6.2 ± 0.1 , when 1.2 mL of 0.9% NaCl (pH 6.3) were used for product elution. A slight decrease in pH was observed at an elution volume of 1.5 mL (pH 5.9 ± 0.1), while increasing the elution volume to 2 mL decreased the pH to 5.5 (see Fig. 1B). This decrease is due to the co-elution of the acidic labeling buffer. Thus, to achieve a physiological pH of the final product formulation, 300 μL of phosphate buffer (0.5 M, pH 8) had to be added to the eluate. In contrast, since $^{99\text{m}}\text{Tc}$ -labeling of PSMA-HSG was carried out in phosphate buffer (pH 7.5), the pH of the column eluate remained neutral throughout the elution (1.2-2 mL 0.9% NaCl) of the radiolabeled peptide.

After this initial validation of the G10 cartridge-based SEC method for the size exclusion purification of radiometal-labeled peptides, its suitability for the post-labeling work-up of several ^{68}Ga -, ^{64}Cu - and $^{99\text{m}}\text{Tc}$ -labeled peptides in a molecular weight range from 1 to 3 kDa was investigated. The used peptide radiopharmaceuticals include the reference compound [^{68}Ga]Ga-PSMA-617 (app. 1 kDa), the CCR5-targeted ligands including unpublished compounds [^{68}Ga]Ga-DOTA-Rap-103 (app. 1 kDa) and its trimeric counterparts [^{68}Ga]Ga-TRAP-103 (app. 3 kDa), [^{64}Cu]Cu-TRAP-103 (app. 3 kDa) and [^{64}Cu]Cu-NO-Y-103 (app. 2.5 kDa), the PD-1 targeted peptides [^{68}Ga]Ga-mPep-DOTA (app. 2 kDa) and [^{68}Ga]Ga-hPep-DOTA (app. 2 kDa) (Hu et al., 2020) as well as the novel hybrid PSMA-tracer [$^{99\text{m}}\text{Tc}$]Tc-PSMA-HSG (app. 2 kDa) (manuscript in preparation). The structures of all ligands are provided in the supplementary information (Supp. Figure S1-S7).

The most important parameters in this part of the evaluation were the recovery of the radiolabeled peptide from the size exclusion material as well as the radiochemical purity (RCP) of the final product. For an elution volume of 1.2 mL, RCPs >99% (as determined by ITLC or HPLC) were observed for all peptides, independently of the radionuclide or the molecular weight of the peptide precursor. An increase of the elution volume to 2 mL still provided the respective peptide radiopharmaceuticals in >99% RCP (see Supp. Fig. S8-S11), allowing the adjustment of the elution volume to the retention behaviour of the specific peptide.

That this is highly relevant in terms of recovery from the SEC cartridge, is shown in Fig. 2A. For all peptides investigated, increasing the elution volume led to improved tracer recoveries from the SEC cartridge. This effect was much more pronounced for the low-molecular-weight compounds [^{68}Ga]Ga-DOTA-RAP-103 (1 kDa) and [^{68}Ga]Ga-PSMA-617 (1 kDa) compared to their higher-molecular-weight counterparts [^{68}Ga]Ga-TRAP-103 (3 kDa) and [$^{99\text{m}}\text{Tc}$]Tc-PSMA-HSG (2 kDa), respectively. Recoveries of the trimeric RAP-103-analogs [^{68}Ga]Ga-TRAP-103, [^{64}Cu]Cu-TRAP-103 and [^{64}Cu]Cu-NO-Y-103 were all comparable and high at 1.2 mL elution volume (91.1, 93.5 and 92.1%, respectively; see Fig. 2B), while an elution volume of 2 mL was required for a similar recovery of the structurally related monomer [^{68}Ga]Ga-DOTA-RAP-103 (Fig. 2A).

To further improve recoveries, alternative elution buffers (saline containing different additives, see Supp. Table S1) were used for the SEC purification of the exemplary compounds [^{68}Ga]Ga-PSMA-617 and [^{68}Ga]Ga-TRAP-103. However, neither the addition of 5% ethanol nor the addition of the chaotropic agent guanidine (50 mM) nor of 0.5% of the non-ionic surfactant polysorbate 80 had any noteworthy influence of tracer recovery.

Finally, the recoveries obtained using the G10 cartridge based purification method were compared to the most-commonly used RP-SPE purification method for selected compounds ([^{68}Ga]Ga-PSMA-617, [^{68}Ga]Ga-TRAP-103, [^{68}Ga]Ga-mPep-DOTA and [$^{99\text{m}}\text{Tc}$]Tc-PSMA-HSG). For the elution of [^{68}Ga]Ga-PSMA-617 and [^{68}Ga]Ga-TRAP-103, 1.5 mL of a 4:1 ethanol/water mixture was used, and for the elution of [^{68}Ga]Ga-mPep-DOTA and [$^{99\text{m}}\text{Tc}$]Tc-PSMA-HSG, 0.5 mL 0.1% TFA in acetonitrile were used. For all compounds except [^{68}Ga]Ga-PSMA-617, product recovery from the C18 cartridge material under the chosen conditions was 3–10% higher than from the G10 size exclusion cartridge. For [^{68}Ga]Ga-PSMA-617, SPE work-up afforded a significantly higher recovery of >95%, while SEC elution using 1.5 mL 0.9% NaCl had provided a recovery of only $75.5 \pm 1.4\%$.

To demonstrate the ease of implementation of the G10-cartridge based SEC purification method into automated radiosynthesis protocols, [^{68}Ga]Ga-TRAP-103 was also synthesized and purified using a automated radiosynthesis module (Scintomics GRP series, see Supp. Figure S12) and NaCl elution of SCX-bound ^{68}Ga (Mueller et al., 2012). The final automated SEC purification of the reaction mixture (1 mL) provided a product recovery of $80.0 \pm 2.5\%$ ($n=3$) in 1.2 mL elution volume, which was comparable to the observed recovery obtained during manual synthesis using 1.0 mL reaction volume (81.9%).

Discussion

Using commercially available SEC cartridges with a molecular cut-off of 700 kDa, we systematically investigated the purification of peptide radiotracers of different charge and size labeled with ^{64}Cu , ^{68}Ga , and $^{99\text{m}}\text{Tc}$ -pertechnetate. With respect to the retention capacity of the SEC cartridge for unreacted radionuclide, only ^{64}Cu showed comparably low retention by the cartridge. This could be attributed to the increased molecular size of the copper acetate complex formed in the acetate labeling buffer as a stabilized intermediate during ^{64}Cu -labeling (Kyuzou et al., 2010). In contrast, the $^{99\text{m}}\text{Tc}$ -pertechnetate in radiolabeling buffer was retained quantitatively by the size-exclusion material. This hints towards non-size effects in the retention of the $^{99\text{m}}\text{Tc}$ -pertechnetate anion that have already been described for Sephadex material, where increasing ionic strength of eluent was found to substantially increase the retention of $^{99\text{m}}\text{Tc}$ -pertechnetate on the size exclusion material (Harms et al., 1996). Surprisingly, the free $^{68}\text{Ga}^{3+}$ was also retained with >99% even when using 2 mL of elution volume, while colloidal $^{68}\text{GaOH}_3$ was poorly retained on the cartridge. This is in accordance with a study using PD-10 size exclusion cartridges to separate $^{68}\text{GaOH}_3$ colloids from the radiotracer ^{68}Ga -DOTA-exendin-3, where (co)elution of $^{68}\text{GaOH}_3$ colloids was equally observed (Brom et al., 2016). In contrast, and probably due to charge effects, colloidal $^{99\text{m}}\text{Tc}$ -tin showed very high (>98%), but not quantitative retention on the G10 cartridge. It is important to note, however, that usually, when widely established, optimized radiolabeling conditions are used, the formation of colloidal species is efficiently suppressed and should thus not interfere

with size-exclusion-based purification methods. Overall, these combined observations allowed the adaptation of the elution volume for ^{68}Ga - and $^{99\text{m}}\text{Tc}$ -labeled peptides to higher elution volumes (2 mL), which in turn resulted in improved recovery rates of the final product to >90%, with RCPs always $\geq 99\%$.

For all peptides investigated, an increased elution volume consistently led to improved tracer recoveries from the SEC cartridge. According to the principle of size exclusion chromatography, larger-molecular-weight compounds elute in lower volume and sharper peaks than smaller compounds. This explains why recoveries of the trimeric RAP-103-analogs [^{68}Ga]Ga-TRAP-103, [^{64}Cu]Cu-TRAP-103, and [^{64}Cu]Cu-NO-Y-103 were all comparable and high, while an elution volume of 2 mL was required for a similar recovery of the structurally related monomer [^{68}Ga]Ga-DOTA-RAP-103. However, non-size-related structural effects also play a role in the recovery of radiometal-labeled peptide radiopharmaceuticals from the G10 cartridges used in this study. Both anionic PSMA-ligands show substantially lower recovery from the Sephadex material than their respective comparable molecular weight counterparts with neutral as well as cationic net charge. Most probably this is a result of the high number of anionic charges in the targeting moiety of the PSMA-ligands, leading to increased adsorption to the gel material due to increased hydrogen bonding as opposed to end-capped silica material used in SPE.

In summary, the SEC based purification method has distinct advantages and disadvantages over conventional SPE methods. The reusability of size exclusion cartridges for up to 20 cycles without compromising RCP and recovery of the eluted products, provides a cost-effective and sustainable alternative to single-use SPE cartridges. With respect to overall synthesis time, the presented gravity-based purification method (10–12 min) is more time-consuming than SPE purification (4–5 min). However, SEC purification represents an advantage over RP-SPE purification, especially in the preclinical tracer synthesis setting, where lengthy organic solvent evaporation and reconstitution steps can be omitted (Hörmann et al., 2022). Despite these strengths, it is crucial to acknowledge the associated minor limitations in product recovery, which have been found to be slightly superior for RP-SPE methods, as well as the dependence of product recovery on the molecular weight, charge and charge distribution of the respective peptide radiopharmaceutical. However, the major advantage of the SEC purification method presented in this study is the direct elution of the radiolabeled product in a physiological buffer or saline. Of note, direct product elution without organic solvents is also feasible using an SPE purification method based on cation exchange cartridges. For example, [^{68}Ga]Ga-FAPI-046 was obtained in excellent yields and purities using cation exchange cartridge purification, with efficient retention of free ^{68}Ga (Spreckelmeyer et al., 2020). However, the efficiency and performance of cation exchange-based separation methods are largely dependent on the net charge and structure of the specific tracer molecule, and the G10-based size exclusion method presented in this study benefits from a much greater versatility and broader applicability.

With respect to clinical application, the G10 cartridges require more extensive validation. Similar Sephadex-based cartridges (PD-10) have been successfully utilized to purify the radiolabeled monoclonal antibody ^{211}At -BC8-B10, meeting the cGMP requirements (pyrogen-free and >95% purity) for subsequent human trials (Spreckelmeyer et al., 2020). In principle, the present G10-based method may thus also be suited for clinical

application, and since the content of organic solvent contaminants in the final radiopharmaceutical formulation is a decisive release criterion (Chi et al., 2014; Agency EM., 2019), the possibility to perform an organic-solvent-free purification represents a major simplification.

Conclusions

The use of size exclusion cartridges for the purification of radiometal-labeled peptide radiopharmaceuticals represents a valuable alternative to conventional RP-SPE purification methods. Especially for the investigated radiotracers at a molecular weight ≥ 2 kDa, SEC purification was found to reliably provide structurally diverse peptide tracers in consistently high yields ($\geq 80\%$ recovery from the SEC cartridge) and excellent RCPs ($\geq 99\%$) in a ready-to-inject physiological formulation. Its easy implementation into an automated synthesis protocol, its sustainability, and particularly the fact that the SEC-cartridge based tracer purification is inherently an organic-solvent-free procedure make it highly attractive for routine implementation in preclinical research and clinical tracer production.

Methods

Quality control

Thin layer chromatography

The RCP was determined by instant thin layer chromatography (ITLC) using a ScanRAM radio-TLC scanner (LabLogic) and Laura software (LabLogic, Version 6.0.3). ITLC analyses were performed on dried ITLC-SG Glass microfiber chromatography paper coated with silica gel (Agilent Technologies, Folsom, CA 95,630). The radiotracers were analyzed by a retention factor (R_f), reflecting the migration distance of the compound relative to the spotting line.

Reversed phase high performance liquid chromatography (RP-HPLC)

Upon SEC purification, selected peptide tracers were also analyzed via RP-HPLC using a Shimadzu LC-20AT Gradient HPLC system equipped with an SPD-M20A UV/VIS detector and a Gabi Na(I) well-type scintillation detector (Elysia-Raytest). Either a chromolith RP-18e, 100 \times 4.6 mm (Merck KGaA, Darmstadt) column (flow rate: 2 mL/min) or a MultiKrom 100-5 C18, 150 \times 4.6 mm (CS-Chromatographie Service GmbH, Langerwehe) column (flow rate: 1 mL/min) was used. Peptides were eluted using different gradients of solvent B (acetonitrile, 0.1% TFA) in solvent A (0.1% TFA in water). Specific gradients are cited in the text.

Radiolabeling and radiotracer purification

⁶⁸Ga-radiolabeling

For ⁶⁸Ga-labeling, a slightly modified protocol based on the method developed by Mueller et al. (2012) was used. Briefly, 10 nmol (TRAP-103) or 25 nmol (NO-Y-103, hPep-DOTA, mPep-DOTA, DOTA-RAP-103, PSMA-617) of peptide precursor (1–5 mM stock concentration) were added to 350–450 μ L of NaOAc buffer (1 M, pH 4.5). The ⁶⁸GaCl₃ eluate from a ⁶⁸Ge/⁶⁸Ga generator (Eckert & Ziegler AG, activity 500 MBq) was either collected by fractionated elution, or the entire eluate (6 mL) was passed through a SCX cartridge (Waters), which had been preconditioned with 1 M HCl (1 mL) and

deionized water (10 mL) and dried with air (10 mL). For the manual synthesis, the SCX cartridge was eluted with 500 μL 5 M NaCl/134 mM HCl. A fraction of the purified $^{68}\text{GaCl}_3$ solution (50–100 MBq, 50–150 μL) was then used for radiolabeling, with a final volume of 0.5 mL of the total labeling mixture. The mixture was then heated to 85–90 °C for 12 min. ITLC before and after the purification was performed with a solution of NH_4OAc buffer (1 M, pH 4.5) in methanol (1:1 v/v). (Colloidal $^{68}\text{GaOH}_3$ and $^{68}\text{GaCl}_3$, $R_f = 0$, ^{68}Ga -labeled peptide $R_f = 1$).

Automated ^{68}Ga -radiolabeling and purification

For the automated radiosynthesis Scintomics GRP V3 module (see Supp. Fig. S9) was used. The ^{68}Ga was eluted from a SCX cartridge using 700 μL NaCl/HCl (5 M NaCl/134 mM HCl). The automated SEC purification was carried out as described, using a fixed volume of 1.2 mL of 0.9% NaCl for product elution. ITLC analysis before and after the purification was performed using the buffer system cited above.

Colloidal $^{68}\text{GaOH}_3$

$^{68}\text{GaOH}_3$ was prepared similarly to Brom et al. with minor changes (2016). Briefly, 1 mL of a 1:2 (v/v) mixture of ^{68}Ga generator-eluate (50–80 MBq in 0.1 N HCl) and phosphate buffer (0.2 M, pH 7.4) was heated to 90 °C for 10 min. The resulting colloidal $^{68}\text{GaOH}_3$ (500 μL) was added to a G10 column and the elution was performed as described. Colloidal $^{68}\text{GaOH}_3$ was verified by ITLC using 0.1 M EDTA in NH_4OAc (0.25 M, pH 5.5) as mobile phase (R_f $^{68}\text{GaOH}_3$ colloid=0, R_f $^{68}\text{Ga-EDTA}$ =1). ^{64}Cu -radiolabeling $^{64}\text{CuCl}_2$ was provided by the Arronax (Nantes, France) cyclotron facility. ^{64}Cu -labeling was carried out in 450 μL of labeling buffer (0.1 M NaOAc, pH 5.5) containing 10 nmol of peptide precursor. The total reaction volume was 0.5 mL, and the radiolabeling was performed at 85 °C for 12 min. Pure $^{64}\text{CuCl}_2$ solutions (for analysis of the elution profile of the radionuclide from G-10 cartridges) were prepared by adding 50 μL of eluate to the labeling buffer to achieve a final volume of 500 μL . ITLC before and after the purification was performed using 0.1 M citrate buffer (pH 5) as mobile phase. A volume of 5 μL EDTA (1 mM) was added to the sample before the analysis. ($^{64}\text{CuCl}_2$, $R_f = 1$, ^{64}Cu -labeled peptide $R_f = 0$).

$^{99\text{m}}\text{Tc}$ -radiolabeling

Lyophilized kits containing 10 nmol of PSMA-HSG peptide precursor (manuscript in preparation) were prepared according to Robu et al. (2017). A volume of 0.5 mL of $^{99\text{m}}\text{Tc}$ -pertechnetate was added to the vial and heated to 90 °C for 15 min.

Pure $^{99\text{m}}\text{Tc}$ -pertechnetate solutions (for analysis of the elution profile of the radionuclide from G-10 cartridges) were prepared by addition of the generator eluate to precursor-free labelling kits. The final pH of all preparations was 7–7.5. ITLC before and after G10 purification was performed using 2-Butanone (colloidal $^{99\text{m}}\text{TcO}_2$ and $^{99\text{m}}\text{Tc}$ -labeled peptide $R_f = 0$, $^{99\text{m}}\text{Tc}$ -pertechnetate $R_f = 1$) and $\text{NH}_4\text{OAc}/\text{DMF}$ (1:1) (colloidal $^{99\text{m}}\text{TcO}_2$, $R_f = 0$, $^{99\text{m}}\text{Tc}$ -pertechnetate and $^{99\text{m}}\text{Tc}$ -labeled peptide $R_f = 1$) as mobile phases to discriminate between colloidal, free $^{99\text{m}}\text{Tc}$ -pertechnetate, and the labeled peptide.

Colloidal ^{99m}Tc -tin

Colloidal ^{99m}Tc -tin was prepared similarly to a reported Kit-preparation with minor changes (Gil Valenzuela et al., 2008). Briefly, 100 μl SnCl_2 (0.3 mg in 0.02 N HCl) and 100 μl of a solution containing NaCl (3.6 mg) and NaF (1.0 mg) were added to an Eppendorf tube. Subsequently, ^{99m}Tc -pertechnetate (2 mL, approximately 100 MBq) was added and incubated for 20 min at room temperature. The pH of the mixture was verified with pH paper strips (pH 5–6). A volume of 500 μl of this mixture was added to the G10 cartridge and the elution was performed as described. Colloidal ^{99m}Tc -tin was identified by ITLC using saline as mobile phase ($R_f^{99m}\text{Tc-tin-colloid}=0$, $R_f^{99m}\text{Tc-pertechnetate}=1$).

G10 elution protocol

After equilibration of the Sephadex PD MidiTRAP G10 (Cytiva MiniTrap G-10, #Cat: 28,918,011) with 20 mL of saline, 0.5–1 mL of the respective crude radiolabeling mixture was added to the cartridge. The liquid was allowed to sink completely into the bed. The required volume of eluent (0.9% NaCl) for the subsequent column wash was determined by subtracting the already added sample volume from 1.7 mL of total volume required. After collection of the wash eluate, up to 2 mL of saline were used to elute the respective radiolabeled peptide. For elution volumes ≥ 1.5 mL, the final pH of the eluate was adjusted to pH 6–7 by using phosphate buffer (0.5 M, 300 μL , pH 8).

Measurement of activity and recovery rates

Recovery rates were determined by measuring the residual activity on the column, the activity in the initial 1.7 mL column wash and the product eluate. An α - β - γ Raditec acti-meter with an IBC-LITE software was used for activity quantification. All values were decay-corrected.

Abbreviations

SEC	Size exclusion chromatography
SPE	Solid phase extraction
RCP	Radiochemical purity
RCC	Radiochemical conversion
RP	Reverse phase
PSMA	Prostate specific membrane antigen
SCX	Solid cationic exchange
ITLC	Instant thin layer chromatography
Rf	Retention factor
HPLC	High performance liquid chromatography
Rt	Retention time
ACN	Acetonitrile

Supplementary Information

The online version contains supplementary material available at <https://doi.org/10.1186/s41181-024-00254-2>.

Supplementary Material 1

Acknowledgements

Not applicable.

Authors' contributions

SM, LW, AL and MS were involved in the conceptualization and experimental design of this study. SM and LW carried out the labeling procedures, prepared the draft, collected, and analyzed the data. SM, LW, AL, RF and MS contributed to the writing and revision of the manuscript. All authors have read and agreed to the current version of the manuscript.

Funding

Not applicable.

Open access funding provided by University of Lausanne

Data availability

All data generated and analysed during this study are included in this published article and its supplementary information.

Declarations**Ethics approval and consent to participate**

Not applicable.

Consent for publication

Not applicable.

Competing interests

The authors declare that they have no competing interests.

Received: 25 January 2024 / Accepted: 15 March 2024

Published online: 21 March 2024

References

- Agency EM. ICH guideline Q3C (R6) on impurities: guideline for residual solvents ema.europa.eu2019 [Available from: https://www.ema.europa.eu/en/documents/scientific-guideline/international-conference-harmonisation-technical-requirements-registration-pharmaceuticals-human-use_en-33.pdf].
- Brom M, Franssen GM, Joosten L, Gotthardt M, Boerman OC. The effect of purification of Ga-68-labeled exendin on in vivo distribution. *EJNMMI Res.* 2016;6(1):65.
- Chi YT, Chu PC, Chao HY, Shieh WC, Chen CC. Design of CGMP production of 18F- and 68Ga-radiopharmaceuticals. *Biomed Res Int.* 2014;2014:680195.
- Decristoforo C, Knopp R, von Guggenberg E, Rupprich M, Dreger T, Hess A et al. A fully automated synthesis for the preparation of 68Ga-labelled peptides. *Nucl Med Commun.* 2007;28(11).
- Gil Valenzuela MC, Mikolajczak JKM. In: Ozker K, editor. Meera Venkatesh. Technetium-99m radiopharmaceuticals: manufacture of kits. International Atomic Energy Agency; 2008.
- Neels O, Martin R, Cardinale J, Smits R, Schaefer M, Hoepping A, et al. GMP-compliant fully automated single-step radiosynthesis of [18F]PSMA-1007 using SPE cartridge purification. *J Nucl Med.* 2018;59(supplement 1):402.
- Harms AV, van Elteren JT, Claessens HA. Technetium speciation: non-size effects in size-exclusion chromatography. *J Chromatogr A.* 1996;755(2):219–25.
- Henrich U, Benešová M. [68Ga]Ga-DOTA-TOC: the first FDA-Approved 68Ga-Radiopharmaceutical for PET imaging. *Pharmaceuticals.* 2020;13(3):38.
- Henrich U, Eder M. [(68)Ga]Ga-PSMA-11: the first FDA-Approved (68)Ga-Radiopharmaceutical for PET imaging of prostate Cancer. *Pharmaceuticals (Basel).* 2021;14(8).
- Henrich U, Eder M. [177Lu]Lu-PSMA-617 (PluvictoTM): the first FDA-Approved Radiotherapeutic for treatment of prostate Cancer. *Pharmaceuticals.* 2022;15(10):1292.
- Hu K, Xie L, Hanyu M, Zhang Y, Li L, Ma X, et al. Harnessing the PD-L1 interface peptide for positron emission tomography imaging of the PD-1 immune checkpoint. *RSC Chem Biology.* 2020;1(4):214–24.
- Hörmann AA, Plhak E, Klingler M, Rangger C, Pfister J, Schwach G, et al. Automated synthesis of 68Ga-Labeled DOTA-MGS8 and preclinical characterization of Cholecystokinin-2 receptor targeting. *Molecules.* 2022;27(6):2034.
- Kyuzou M, Mori W, Tanaka J. Electronic structure and spectra of cupric acetate mono-hydrate revisited. *Inorg Chim Acta.* 2010;363(5):930–4.
- Mokaleng BB, Ebenhan T, Ramesh S, Govender T, Kruger HG, Parboosing R, et al. Synthesis, 68Ga-radiolabeling, and preliminary in vivo assessment of a depsipeptide-derived compound as a potential PET/CT infection imaging agent. *Biomed Res Int.* 2015;2015:284354.
- Mueller D, Klette I, Baum RP, Gottschaldt M, Schultz MK, Breeman WAP. Simplified NaCl based 68Ga concentration and labeling Procedure for Rapid Synthesis of 68Ga Radiopharmaceuticals in High Radiochemical Purity. *Bioconjug Chem.* 2012;23(8):1712–7.
- Nelson BJB, Andersson JD, Wuest F, Spreckelmeyer S. Good practices for 68Ga radiopharmaceutical production. *EJNMMI Radiopharmacy Chem.* 2022;7(1):27.
- Robu S, Schottelius M, Eiber M, Maurer T, Gschwend J, Schwaiger M, et al. Preclinical evaluation and first patient application of 99mTc-PSMA-i&S for SPECT Imaging and Radioguided surgery in prostate Cancer. *J Nucl Med.* 2017;58(2):235–42.
- Serdons K, Verbruggen A, Bormans G. The Presence of ethanol in Radiopharmaceutical injections. *J Nucl Med.* 2008;49(12):2071.
- Spreckelmeyer S, Balzer M, Poetzsch S, Brenner W. Fully-automated production of [(68)Ga]Ga-FAPI-46 for clinical application. *EJNMMI Radiopharm Chem.* 2020;5(1):31.

Publisher's Note

Springer Nature remains neutral with regard to jurisdictional claims in published maps and institutional affiliations.

Supporting Information**Validation of a size exclusion method for concomitant purification and formulation of peptide radiopharmaceuticals**

Sebastian Martin^{1,2,3}, Lennard Wendlinger^{1,2,3}, Alexandra Litvinenko^{1,2,3}, Radmila Faizova^{1,2,3}, Margret Schottelius^{1,2,3,*}

- 1 Translational Radiopharmaceutical Sciences, Department of Nuclear Medicine and Department of Oncology, Centre Hospitalier Universitaire Vaudois (CHUV) and University of Lausanne (UNIL), 1011 Lausanne, Switzerland
- 2 AGORA, Pôle de recherche sur le cancer, 1011 Lausanne, Switzerland
- 3 SCCL Swiss Cancer Center Leman, 1011 Lausanne, Switzerland

***Corresponding Author**

Prof. Dr. Margret Schottelius
Translational Radiopharmaceutical Sciences
Department of Nuclear Medicine, CHUV
Department of Oncology, UNIL
Rue du Bugnon 25A, Agora
CH-1011 Lausanne
Switzerland
Phone +41.21.545.1120
Mobile +41.79.556.0143
Email: margret.schottelius@chuv.ch

Contents

Figure S1 Structure of PSMA-HSG.	3
Figure S2 Structure of PSMA-617.	3
Figure S3 Structure of hPep-1-DOTA.	4
Figure S4 Structure of mPep-1-DOTA.	4
Figure S5 Structure of DOTA-RAP-103.	5
Figure S6 Structure of NO-Y-103.	5
Figure S7 Structure of TRAP-103.	6
Figure S 8 Analytical chromatogram of radiotracer [⁶⁸ Ga]Ga-TRAP-103.	7
Figure S 9 Analytical chromatogram radiotracer [⁶⁸ Ga]Ga-DOTA-RAP-103.	7
Figure S 10 Analytical chromatogram of radiotracer [⁶⁴ Cu]Cu-NO-Y-103.	7
Figure S 11 Analytical chromatogram of radiotracer [^{99m} Tc]Tc-PSMA-HSG.	7
Figure S12 Scheme of a semi-automated implementation of a G10 column on a Scintomics GRP V3 synthesizer module.	8
Table S1 Investigated elution buffers of ⁶⁸ Ga-labeled peptides using a G10 column.	8

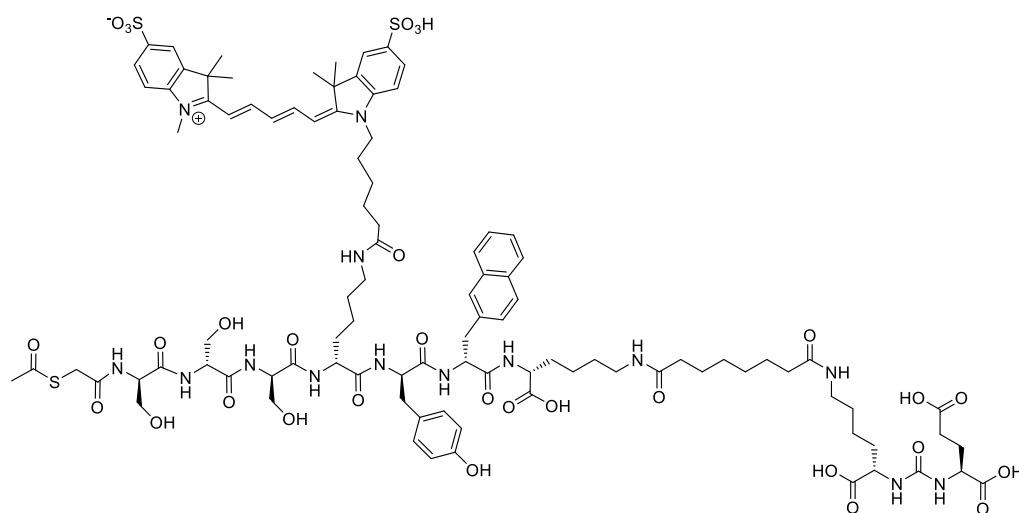


Figure S1 Structure of PSMA-HSG.

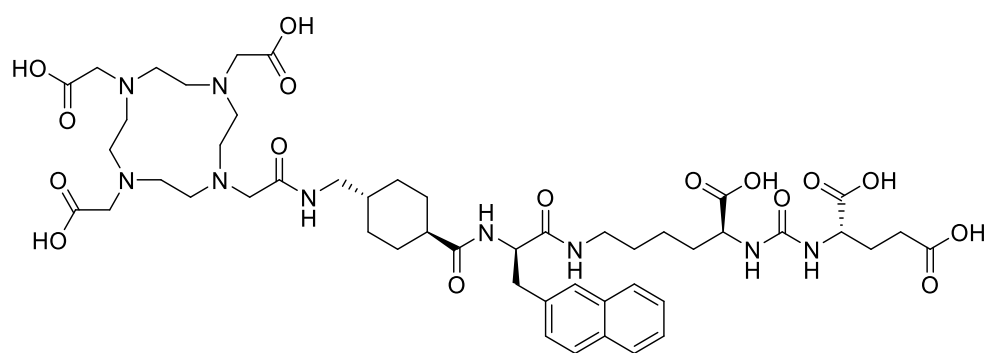


Figure S2 Structure of PSMA-617.

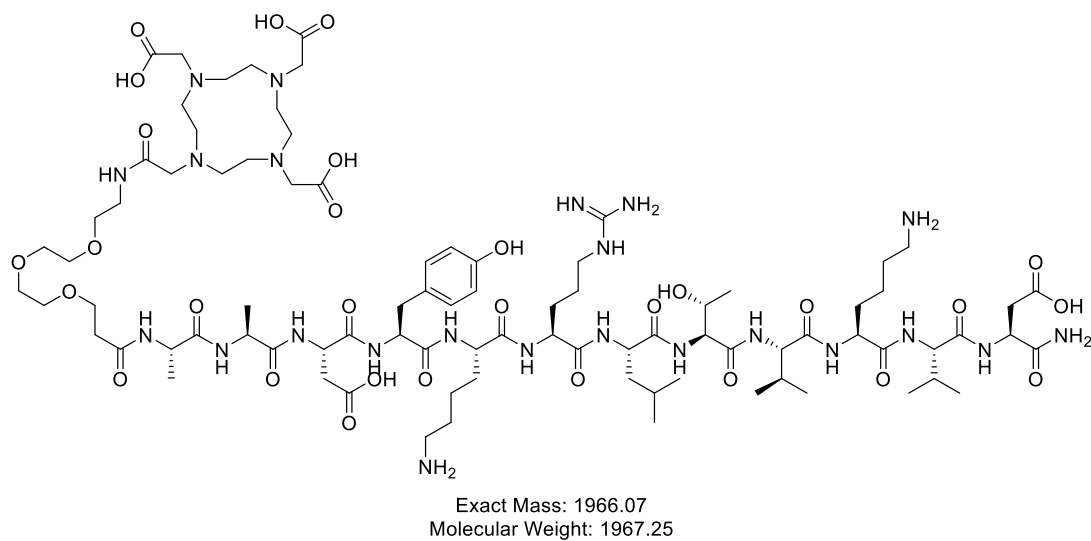


Figure S3 Structure of hPep-1-DOTA.

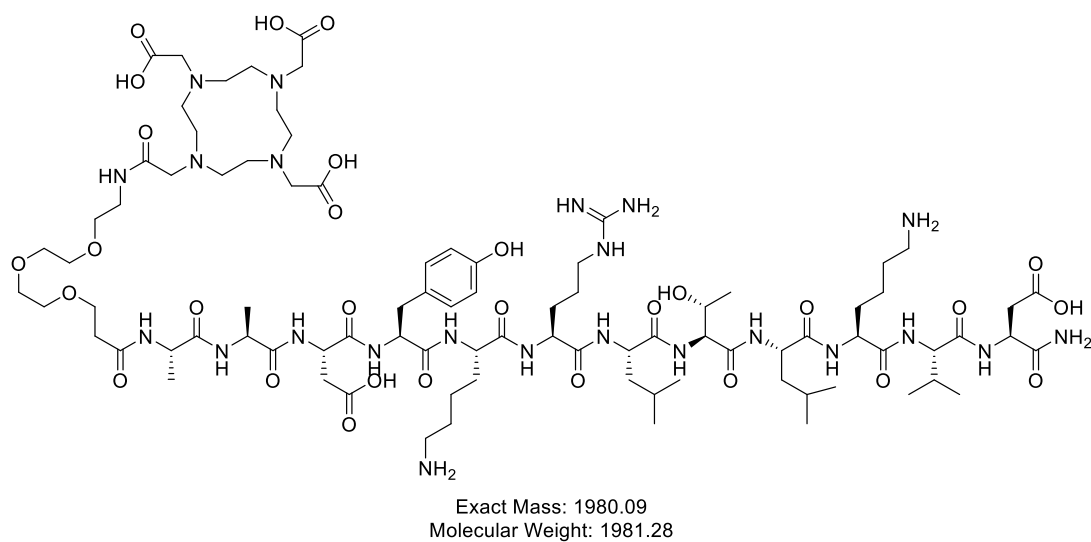
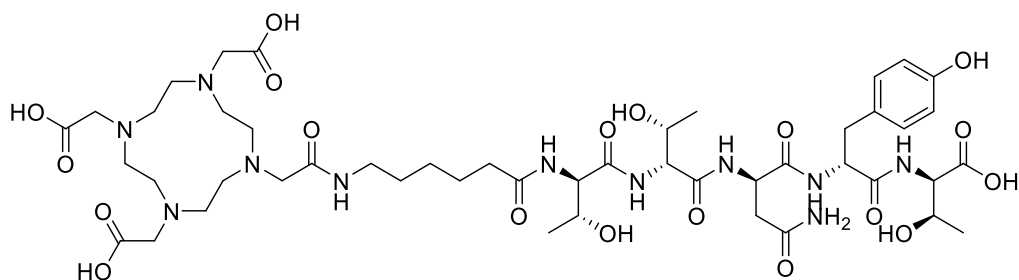
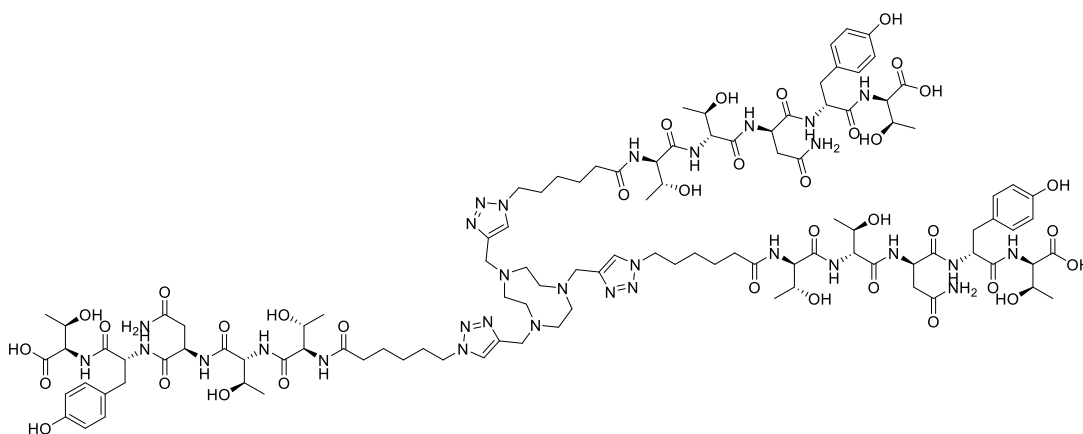


Figure S4 Structure of mPep-1-DOTA.



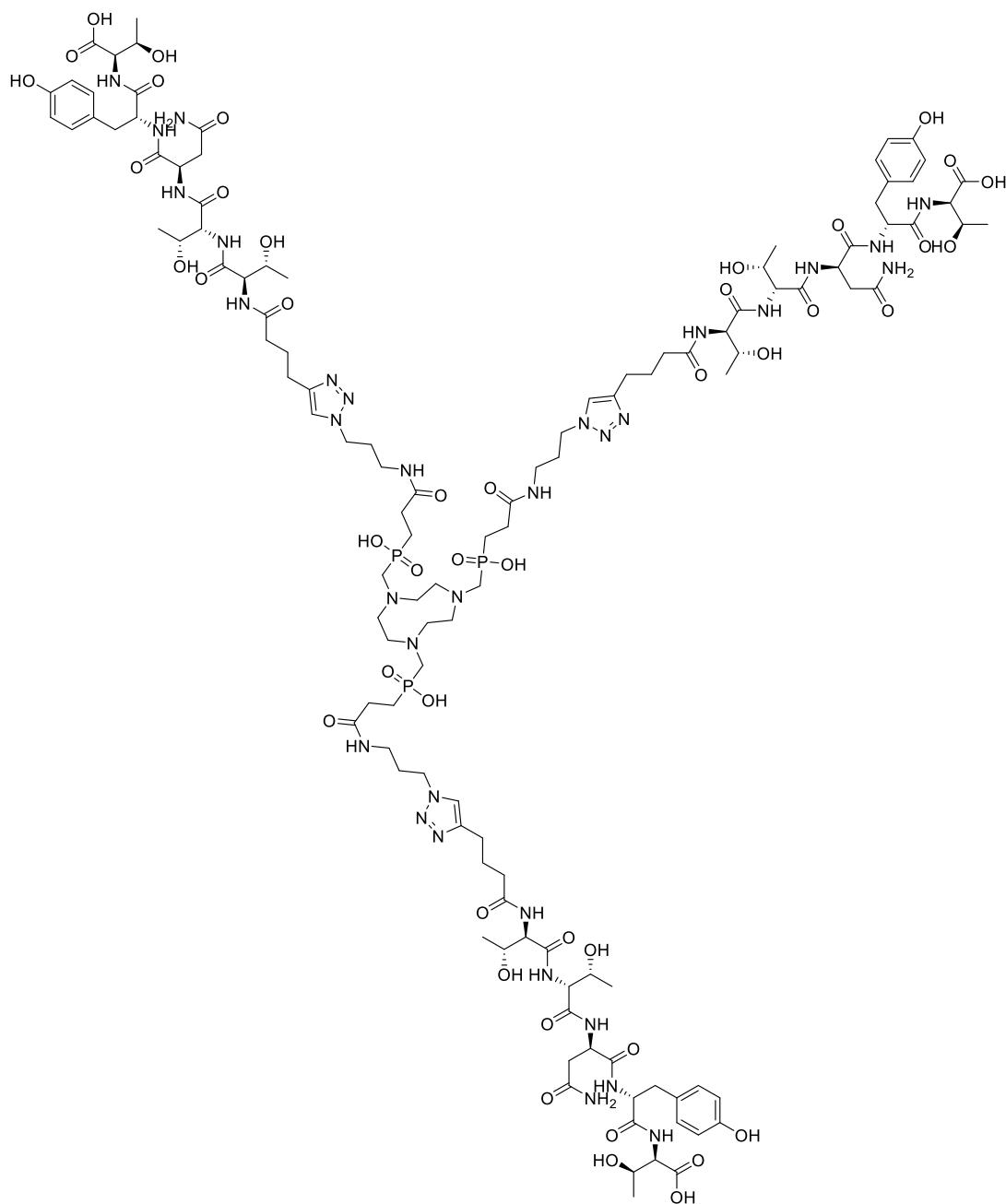
Chemical Formula: $C_{47}H_{75}N_{11}O_{19}$
Molecular Weight: 1098.18

Figure S5 Structure of DOTA-RAP-103.



Chemical Formula: $C_{108}H_{162}N_{30}O_{36}$
Molecular Weight: 2456.66

Figure S6 Structure of NO-Y-103.



Chemical Formula: $C_{120}H_{186}N_{33}O_{45}P_3$
Molecular Weight: 2903.92

Figure S7 Structure of TRAP-103.

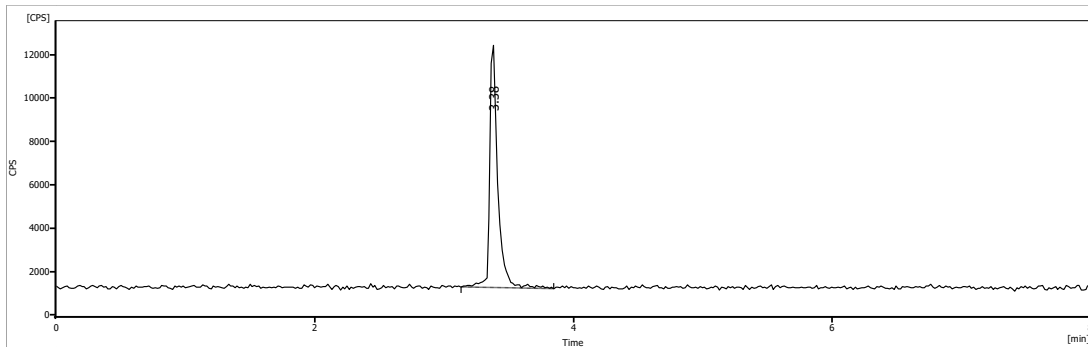


Figure S 8 Analytical chromatogram of radiotracer $[^{68}\text{Ga}]\text{Ga-TRAP-103}$. Chromolith column, gradient of 10-70% B in 15 min., R_t 3.4 min, RCP >99%.

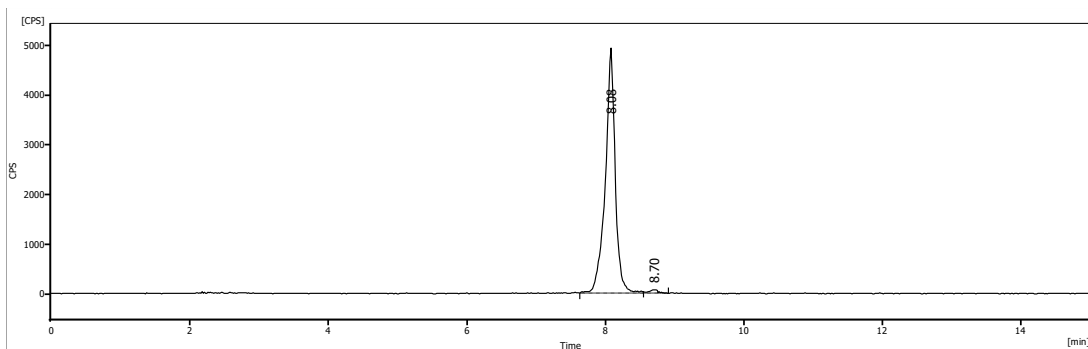


Figure S 9 Analytical chromatogram radiotracer $[^{68}\text{Ga}]\text{Ga-DOTA-RAP-103}$. MultiChrom column, gradient of 5-50% B in 10 min., R_t 8.1 min, RCP >99%.

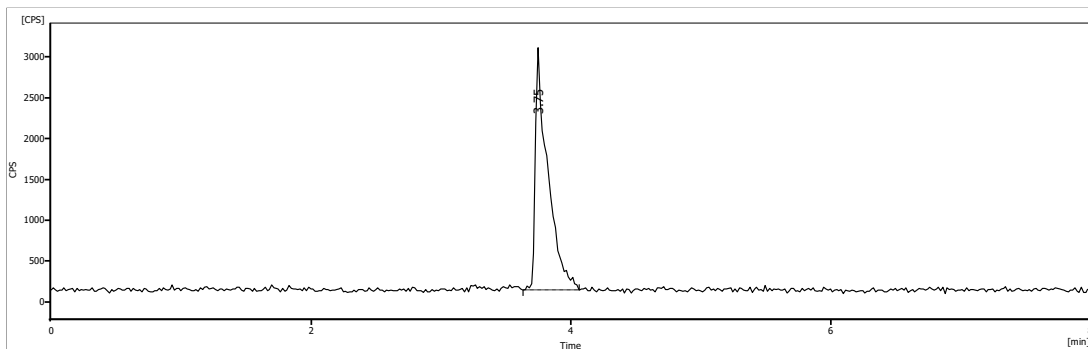


Figure S 10 Analytical chromatogram of radiotracer $[^{64}\text{Cu}]\text{Cu-NO-Y-103}$. Chromolith column, gradient of 10-70% B in 15 min., R_t 3.8 min, RCP >99%.

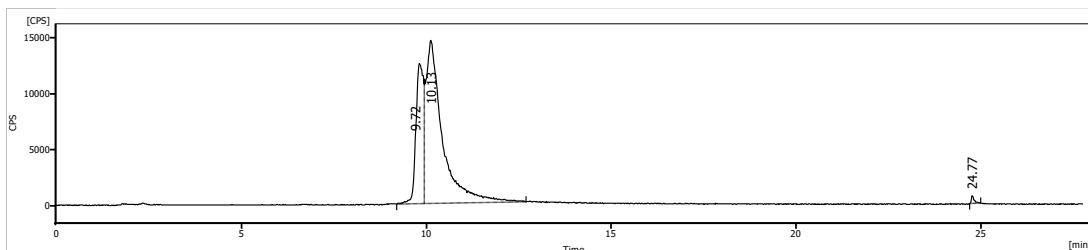


Figure S 11 Analytical chromatogram of radiotracer $[^{99\text{m}}\text{Tc}]\text{Tc-PSMA-HSG}$. Typical double peak observed by the two conformations formed with the mas_3 chelator. MultoKrom column, Gradient 10-90% B in 15 min, R_t 9.7 and 10.1 min, RCP >99%.

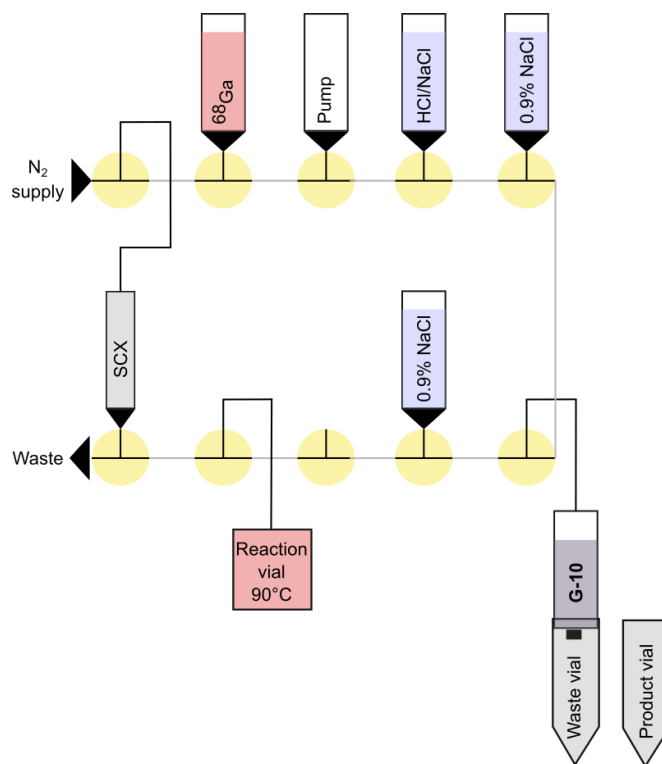


Figure S 12 Scheme of a semi-automated implementation of a G10 column on a Scintomics GRP V3 synthesizer. Step 1: The ^{68}Ga is eluted in 0.1M HCl and passed through the activated SCX cartridge. Step 2: The ^{68}Ga is eluted with 0.7-0.75 mL HCl/NaCl into the reaction vial containing 5-10nmol the radiotracer precursor and 350 μL 1M NaOAc. Step 3: The reaction vial is heated for 5 min at 90°C. Step 4: The crude is added to the column. Step 5: The wash is performed with 0.7 mL of 0.9% NaCl. Step 6: After changing to the product vial the product is eluted using 1.2 mL of 0.9% NaCl. Overall synthesis time 35 minutes.

Table S1 Investigated elution buffers of ^{68}Ga -labeled peptides using a G10 column for the radiotracer work-up.

Utilized buffers	Supplemented agent	^{68}Ga]Ga-PSMA617		^{68}Ga]Ga-TRAP-103	
		elution vol. [mL]	Recovery [%]	elution vol. [mL]	Recovery [%]
0.9% NaCl	-	1.2	67.1 \pm 2.9	1.2	90.4 \pm 4.7
0.9% NaCl	-	1.5	75.5 \pm 1.4	1.5	93.2 \pm 2.4
0.9% NaCl	-	2	83.6 \pm 1.2	-	-
0.9%NaCl	5%EtOH	2	81.0	1.5	90.8
0.9%NaCl	50mM Guanidine	1.2	66.3	1.5	n/a
0.9%NaCl	0.5% PS80	1.2	62.8	1.5	90.1

8 Discussion

8.1 Targeting chemokine receptors for molecular imaging and radioligand therapy

For optimal uptake of radiopharmaceuticals in target tissues, the molecular target should exhibit several key characteristics. These include a high expression level, specificity for the observed biological process, a high positivity rate among patients expressing the target protein, and favorable target accessibility for the radiotracer (e.g., intra- vs extracellular) [124]. The four major chemokine receptor families are GPCRs and typically offer good accessibility for the radiotracer binding on the cell surface. Among these receptors, CXCR4 demonstrates both good specificity and positivity rates, along with high expression levels (e.g., number of binding sites per cell (B_{\max}) $> 10^6$ receptors/cell on T cell lymphoma [125]), particularly in various hematologic cancers [36]. This allows specific targeting with the development of potent radiotracers for imaging and RLT (chapter 6). Physiological CXCR4 expression is ubiquitous across nearly all leukocyte subpopulations, including B cells, T cells, and NK cells [33]. During CXCR4-directed RLT, off-target leukocyte binding becomes critical, leading to the reported toxicity of the radiopharmaceuticals [^{177}Lu]Lu/[^{90}Y]Y-PentixaTher [91]. This toxicity is characterized by cytopenia, which is caused by the depletion of healthy leukocytes in the bone marrow [126]. Notably, these myeloablative effects are clinically well controlled

by hematopoietic stem cell transplantation [91]. In the context of CXCR4-directed PET imaging using [^{68}Ga]Ga-PentixaFor, this is leading to background uptake in organs with high leukocyte presence such as the bone marrow, albeit with no pharmacological effect.

This inherent physiological CXCR4 expression can be therefore exploited for inflammation imaging. Although highly diluted in the blood pool, inflamed tissues show sufficient leukocyte infiltration to allow the monitoring of inflammation using the CXCR4-specific radiotracer [^{68}Ga]Ga-PentixaFor, thereby expanding the field of applications from cancer imaging to inflammation imaging [127, 128]. Imaging readouts in patients with atherosclerosis showed superior detection of inflammatory lesions with CXCR4-directed imaging in comparison to 2- ^{18}F FDG [128]. Thus, [^{68}Ga]Ga-PentixaFor PET/CT is currently under clinical investigation in the context of myocardial inflammations such as acute cellular graft rejection, cardiac sarcoidosis, and myocarditis due to drug administration (NCT05499637, NCT05519735).

As a consequence of CXCR4 overexpression in various cancers themselves, TME imaging of leukocyte infiltration in tumor with CXCR4-directed radiotracers is not practicable. Therefore, we investigated alternative targets meeting the requirements for leukocyte imaging in cancer. One such target is CCR5, which shows expression in various leukocyte populations [31]. The potential of exploiting CCRs to image lymphocyte infiltration has already been studied in recent preclinical investigations [108, 61, 49]. We aimed to exploit this general approach to visualize and quantify leukocyte infiltration in tumors using peptide radiotracers, which may be useful for differentiating between the immune-infiltrated and immune-desert cancer phenotypes. Unfortunately, the synthesized radiotracers (**[^{68}Ga]Ga-DOTA-DAPTA**, **[^{68}Ga]Ga-DOTA-RAP-103**, **[^{68}Ga]Ga-TRAP-103**) did not show specific uptake in tumors or in lymphoid organs, despite previously established presence of CCR5-positive immune cells in the TME. Likely, both the CCR5-affinity and the CCR5-expression levels on leukocytes were low, and thus, specific radiotracer uptake could not be achieved in sufficiently high levels for detection.

Another chemokine receptor with potential utility to monitor leukocytes in the TME is CXCR3. Predominantly expressed on activated T cells [43], CXCR3 upregulation presents as

a promising biomarker for inflammation [78, 77] and T cell activation imaging. Therefore, we thoroughly investigated this receptor to monitor T cell activation *in vivo*. In conjunction with the in-depth TME analysis *ex vivo*, we were able to confirm (1) radiotracer specificity in lymphoid organs and (2) systemic response during ICI treatment using the radiotracer [⁶⁴Cu]Cu-NOTA- α -CXCR3. Despite the presence of CD3⁺CXCR3⁺ expressing T cells within MC38 tumors and their significant increase during immune checkpoint inhibitor (ICI) treatment, specific radiotracer uptake was not observed. This observation may be attributed to several factors. One of them is the apparently low biomarker expression on T cells as well as the low target cell presence (<20.000 CXCR3⁺ T cells per tumor) leading to very small radiotracer binding. In addition, the high unspecific uptake of the ⁶⁴Cu-mAb radiotracer (>10%IA/g, blocking cohort) likely contributed to the high standard deviations, potentially masking small but significant radiotracer uptake.

Both the study on CCR5 tracer development (chapter 4) and the validation of CXCR3 as a potential imaging biomarker for T cell activation (chapter 5) were facing several common pitfalls: Lack of established and commercially available *in vitro* binding assays, low expression levels of the biomarker, low target cell number in the tumor, the pharmacokinetics of the radiotracer (very rapid vs slow clearance), or insufficient binding affinity for TME imaging. In the next section, the most common challenges will be discussed in more detail.

8.2 The challenges of tumor micro-environment imaging

The validation of CXCR3 as a biomarker for T cell activation exemplified the challenges in TME imaging using PET radiotracers. These challenges comprise (1) the target expression and the cellular density, (2) the pharmacokinetics- and dynamics of the radiotracer, and (3) the molar activity of the radiotracer preparation (see Figure 8.1).

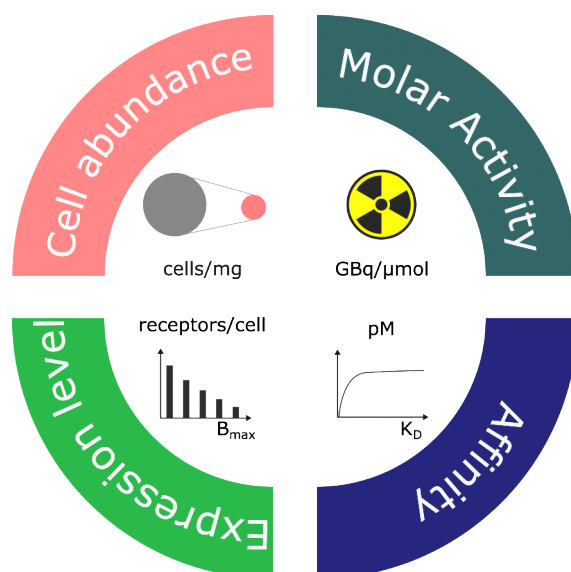


Figure 8.1: Challenges of tumor micro-environment (TME) imaging using PET radiotracers. Compared to tumor cells, a small immune cell fraction is present in the tumor (cells/mg). The B_{\max} values (receptors per cell) of immune cell biomarkers can be low and dynamic (e.g., depending on the activation state). The molar activity (MA) of a radiotracer (ideally >100 GBq/ μmol) and an extremely high binding affinity of the radiotracer (ideally pM) are crucial to obtain a specific signal.

8.2.1 Challenge 1: Target expression and cell abundance

Target density is a crucial parameter that significantly influences the specific uptake achievable for a radiotracer. This comprises the expression levels of the molecular target on cells (B_{\max}) as well as the abundance of the target cells in the tissue (cells per mg of target tissue). Thus, the average number of binding sites in a tissue ($\text{av}B_{\max}$) is dependent on both parameters. In the context of cancer cell imaging, this is usually no concern. Despite possible intra- and inter-lesion heterogeneity of target expression, many cells in the tumor bulk do express the target, and receptor numbers per cell usually range from 50.000 to >1 Mio. In contrast, immune cells typically constitute a much smaller cellular proportion of the entire tumor. For example, in the CT26 tumor model, approximately 12% of the cells in the TME are immune cells, while the rest of the tumor consists of other cell types like cancer cells and stromal cells [129]. The immune-cell fraction can be further subdivided according to their function or activation state [130] (e.g., $\text{CD8}^+\text{CXCR3}^-$ T cells vs activated $\text{CD8}^+\text{CXCR3}^+$ T cells), leading to

a very low overall target presence on the entire tissue (<20.000 CXCR3⁺ T cells per tumor), which results in a low avB_{\max} . Nevertheless, there may be a very small proportion of specific tracer binding present, but this is easily masked by high background noise occasioned for example by high blood concentrations of the enhanced permeability and retention (EPR) effect (for macromolecular tracers).

8.2.2 Challenge 2: The pharmacokinetic and -dynamic properties of a radiotracer

Dealing with low target densities in the tissue requires the development of high affinity radiotracers with optimized pharmacokinetic properties. A low number of binding sites can only be compensated for by extremely high tracer affinities (picomolar range), which then provides sufficient receptor occupation at tracer concentrations. In conjunction with low unspecific uptake and rapid elimination small but significant differences, for example between baseline expression and therapy-induced receptor upregulation, may not be masked by the background noise. The ⁶⁴Cu-mAb radiotracer targeting CXCR3 used in this work showed a binding affinity of 3.3 nM. This affinity is well-suited for tumor cell imaging, but is apparently insufficient to monitor T cell activation in the TME. However, in organs with lower background accumulation (spleen and lymph nodes), ICI-induced CXCR3 upregulation could be specifically detected. Thus, the performance of a tracer for visualizing small immune cell subpopulations in the TME not only depends on its affinity, but is largely dominated by its pharmacokinetic properties. In the case of the ⁶⁴Cu-mAb, the slow elimination EPR effect [131] and Fc γ -receptor binding [132] led to substantial background activity, even at late time points. Using a small molecular weight tracers with optimized pharmacokinetics and picomolar affinity, CXCR3 upregulation in the TME might be specifically visualized by PET imaging.

8.2.3 Challenge 3: The molar activity of a radiotracer preparation

One of the core specifications of a radiotracer is the molar activity which directly influences the injected ligand dose during the *in vivo* study and consequently the specific tracer uptake. For example, a study has shown that PD-1 is rapidly saturated by high injected doses of [⁶⁴Cu]Cu-NOTA-PD-1 mAb [133]. Thus, imaging of PD-1 was only feasible with an injected dose of 10 pmol of radiotracer (injected activity 1.44 MBq, molar activity (MA) 144 GBq μ mol⁻¹). Similar effects were observed during the CXCR3 target evaluation. As the target density (avB_{max}) of CXCR3 is very low, a radiotracer preparation with a MA of 15 GBq μ mol⁻¹ (15 μ g injected dose) showed no specific uptake of the radiotracer in spleen and lymph nodes. However, a MA of 300 GBq μ mol⁻¹ (1.5 μ g injected dose) avoided the target saturation by unlabeled radiotracer precursor and provided a CXCR3-specific signal in lymphoid organs. Thus, high molar activities (above 100 GBq μ mol⁻¹) are desirable to allow a reasonable reduction of injected radiotracer doses for achieving specific radiotracer uptake in tissues with low avB_{max} .

Taken together, all points combined are a decisive criterion whether specific binding can be achieved. However, the increased MA of the mAb radiotracer preparation could not counteract the inherently low target presence in MC38 tumors. The low cellular density of CXCR3⁺ cells in the TME (app. 2000-10.000 cells/tumor) with assumable low expression levels (B_{max}) both contribute to low available binding sites (avB_{max}) and consequently result in low uptake values. In addition to the low avB_{max} , the pharmacokinetic properties of antibodies are unfavorable, leading to high background noise, which complicates the validation of small but significant differences. Adding to the unfavorable pharmacokinetics of antibodies, the temporal dynamics of biomarker expression may further challenge mAb imaging due to the extended timelines between injection and image acquisition [134]. This requires continuous T cell activation to ensure specific accumulation while the tracer molecules are circulating. Ideally, high-affinity radiotracers with rapid elimination and high MA would allow small but significant tracer uptake in tumors. With this, a robust clinical implementation is feasible.

8.3 Outlook of chemokine receptor targeting

Chemokine receptors stand as highly relevant drug targets in the field of immuno-oncology. Notably, [⁶⁸Ga]Ga-PentixaFor (PET) and [¹⁷⁷Lu]Lu/[⁹⁰Y]Y-PentixaTher (RLT), alongside the latest addition, [^{99m}Tc]Tc-PentixaTec (SPECT), have paved the way for potent CXCR4-directed applications for both imaging and RLT, making significant progress for clinical implementation [36, 38, 37]. With the next generation of CXCR4-specific molecules bearing the L6-linker moiety, highly potent tracers offer promising advancements for imaging and therapy. Alongside nuclear medicine, pharmacological investigations on chemokine receptors continue to provide encouraging results, improving the efficacy of immunotherapy. Notably, synergistic effects have been observed with the combination of STING agonist and α -CXCR3 mAb, offering a compelling strategy to overcome anti-PD-L1 resistance [135]. Similarly, the inhibition of CXCR4 (Peptide-R54 [47]), CCR5 (maraviroc [136]), or CCR2 (RS504393 [137]) enhances the efficacy of ICI therapy, revealing the multifaceted potential of chemokine receptor modulation in augmenting immunotherapeutic outcomes. Targeting CCR8 with nanobodies depletes CCR8⁺ Tregs in the TME and synergizes with anti-PD-1 therapy [138]. Yet, their role in the TME often remains ambiguous. More detailed studies in the context of molecular imaging has the potential to provide more conclusive insights in their localization and expression dynamics. Therefore, finding high-affinity radiotracers in conjunction with an appropriate chemokine receptor holds promise for several key reasons: (a) aiding in the selection of a potent therapy, (b) providing evidence of efficacy during the treatment, and (c) facilitating the potential development of RLT targeting tumor suppressive cells such as CCR8⁺ Tregs, or via CXCR4-directed RLT in conjunction with immunotherapy. This has the potential to accelerate the development of potent drugs and to improve immunotherapy treatment outcomes, thus advancing the overarching objective of achieving a therapeutic benefit.

Bibliography

- [1] *World Health Organization (WHO)*. URL: <https://www.who.int/>.
- [2] Amanda Leiter, Rajwanth R. Veluswamy, and Juan P. Wisnivesky. “The global burden of lung cancer: current status and future trends”. In: *Nature Reviews Clinical Oncology* 2023 20.9 (July 2023), pp. 624–639. ISSN: 1759-4782. DOI: 10.1038/s41571-023-00798-3.
- [3] Oleg Gaidai, Ping Yan, and Yihan Xing. “Future world cancer death rate prediction”. In: *Scientific Reports* 2023 13.1 (Jan. 2023), pp. 1–9. ISSN: 2045-2322. DOI: 10.1038/s41598-023-27547-x.
- [4] Min Hwa Shin et al. “Recent Advances in CAR-Based Solid Tumor Immunotherapy”. In: *Cells* 12.12 (June 2023). ISSN: 20734409. DOI: 10.3390/CELLS12121606.
- [5] Norah A. Alturki. “Review of the Immune Checkpoint Inhibitors in the Context of Cancer Treatment”. In: *Journal of Clinical Medicine* 12.13 (July 2023), p. 4301. ISSN: 20770383. DOI: 10.3390/JCM12134301.
- [6] Kathleen Madden and Mary Kate Kasler. “Immune Checkpoint Inhibitors in Lung Cancer and Melanoma”. In: *Seminars in Oncology Nursing* 35.5 (Oct. 2019), p. 150932. ISSN: 0749-2081. DOI: 10.1016/J.SONCN.2019.08.011.
- [7] J. Larkin et al. “Combined nivolumab and ipilimumab or monotherapy in untreated Melanoma”. In: *New England Journal of Medicine* 373.1 (July 2015), pp. 23–34. ISSN: 15334406. DOI: 10.1056/NEJMoa1504030.
- [8] Alyson Haslam and Vinay Prasad. “Estimation of the Percentage of US Patients With Cancer Who Are Eligible for and Respond to Checkpoint Inhibitor Immunotherapy

- Drugs”. In: *JAMA network open* 2.5 (May 2019), e192535. ISSN: 25743805. DOI: 10.1001/jamanetworkopen.2019.2535.
- [9] Maria de Miguel and Emiliano Calvo. “Clinical Challenges of Immune Checkpoint Inhibitors”. In: *Cancer Cell* 38.3 (Sept. 2020), pp. 326–333. ISSN: 18783686. DOI: 10.1016/j.ccell.2020.07.004.
- [10] Robert C. Sterner and Rosalie M. Sterner. “CAR-T cell therapy: current limitations and potential strategies”. In: *Blood Cancer Journal* 2021 11.4 (Apr. 2021), pp. 1–11. ISSN: 2044-5385. DOI: 10.1038/s41408-021-00459-7.
- [11] Sofia Bruni et al. “Cancer immune exclusion: breaking the barricade for a successful immunotherapy”. In: *Frontiers in Oncology* 13 (May 2023), p. 1135456. ISSN: 2234943X. DOI: 10.3389/FONC.2023.1135456.
- [12] Habib Sadeghi Rad et al. “Understanding the tumor microenvironment in head and neck squamous cell carcinoma”. In: *Clinical & Translational Immunology* 11.6 (Jan. 2022), e1397. ISSN: 2050-0068. DOI: 10.1002/CTI2.1397.
- [13] Yuan Tong Liu and Zhi Jun Sun. “Turning cold tumors into hot tumors by improving T-cell infiltration”. In: *Theranostics* 11.11 (Mar. 2021), pp. 5265–5286. ISSN: 1838-7640. DOI: 10.7150/THNO.58390.
- [14] Donovan Drouillard, Brian T. Craig, and Michael B. Dwinell. “Physiology of chemokines in the cancer microenvironment”. In: *American journal of physiology. Cell physiology* 324.1 (Jan. 2023), pp. C167–C182. ISSN: 1522-1563. DOI: 10.1152/AJPCELL.00151.2022.
- [15] Samuel J. Klempner et al. “Tumor Mutational Burden as a Predictive Biomarker for Response to Immune Checkpoint Inhibitors: A Review of Current Evidence”. In: *The oncologist* 25.1 (Jan. 2020), e147–e159. ISSN: 1549-490X. DOI: 10.1634/THEONCOLOGIST.2019-0244.
- [16] Chang L et al. “Microsatellite Instability: A Predictive Biomarker for Cancer Immunotherapy”. In: *Applied immunohistochemistry & molecular morphology : AIMM* 26.2 (2018), e15–e21. ISSN: 1533-4058. DOI: 10.1097/PAL.0000000000000575.

Bibliography

- [17] Liang Chen et al. “Comprehensive analyses of a CD8+ T cell infiltration related gene signature with regard to the prediction of prognosis and immunotherapy response in lung squamous cell carcinoma”. In: *BMC Bioinformatics* 24.1 (Dec. 2023), pp. 1–21. ISSN: 14712105. DOI: 10.1186/S12859-023-05302-3.
- [18] Dongqiang Zeng et al. “Macrophage correlates with immunophenotype and predicts anti-PD-L1 response of urothelial cancer”. In: *Theranostics* 10.15 (2020), p. 7002. ISSN: 18387640. DOI: 10.7150/THNO.46176.
- [19] Alexander Haragan et al. “Heterogeneity of PD-L1 expression in non-small cell lung cancer: Implications for specimen sampling in predicting treatment response”. In: *Lung cancer (Amsterdam, Netherlands)* 134 (Aug. 2019), pp. 79–84. ISSN: 1872-8332. DOI: 10.1016/J.LUNGCAN.2019.06.005.
- [20] Pok Fai Wong et al. “Multiplex quantitative analysis of cancer-associated fibroblasts and immunotherapy outcome in metastatic melanoma”. In: *Journal for immunotherapy of cancer* 7.1 (July 2019). ISSN: 2051-1426. DOI: 10.1186/S40425-019-0675-0.
- [21] Philippe L. Bedard et al. “Tumour heterogeneity in the clinic”. In: *Nature* 2013 501:7467 501.7467 (Sept. 2013), pp. 355–364. ISSN: 1476-4687. DOI: 10.1038/nature12627.
- [22] Gilbert Bigras et al. “Small Biopsies Misclassify up to 35% of PD-L1 Assessments in Advanced Lung Non-Small Cell Lung Carcinomas”. In: *Applied Immunohistochemistry and Molecular Morphology* 26.10 (Nov. 2018), pp. 701–708. ISSN: 15334058. DOI: 10.1097/PAI.0000000000000698.
- [23] Emelie Berglund et al. “Spatial maps of prostate cancer transcriptomes reveal an unexplored landscape of heterogeneity”. In: *Nature Communications* 2018 9.1 (June 2018), pp. 1–13. ISSN: 2041-1723. DOI: 10.1038/s41467-018-04724-5.
- [24] Marius Ilie et al. “Assessment of the PD-L1 status by immunohistochemistry: challenges and perspectives for therapeutic strategies in lung cancer patients”. In: *Virchows Archiv* 468.5 (May 2016), pp. 511–525. ISSN: 0945-6317. DOI: 10.1007/s00428-016-1910-4.

- [25] Taha Rakhshandehroo et al. “Molecular Immune Targeted Imaging of Tumor Microenvironment”. In: *Nanotheranostics* 6.3 (2022), pp. 286–305. ISSN: 2206-7418. DOI: 10.7150/ntno.66556.
- [26] Lesley Seymour et al. “iRECIST: guidelines for response criteria for use in trials testing immunotherapeutics”. In: *The Lancet. Oncology* 18.3 (Mar. 2017), e143–e152. ISSN: 1474-5488. DOI: 10.1016/S1470-2045(17)30074-8.
- [27] Larissa B. Costa et al. “Reassessing Patterns of Response to Immunotherapy with PET: From Morphology to Metabolism”. In: *Radiographics : a review publication of the Radiological Society of North America, Inc* 41.1 (Jan. 2021), pp. 120–143. ISSN: 1527-1323. DOI: 10.1148/RG.2021200093.
- [28] Julian L. Goggi et al. “Examining Immunotherapy Response Using Multiple Radio-tracers”. In: *Molecular Imaging and Biology* 22.4 (Aug. 2020), pp. 993–1002. ISSN: 18602002. DOI: 10.1007/s11307-020-01477-w.
- [29] Heather M. Gibson et al. “IFN γ PET Imaging as a Predictive Tool for Monitoring Response to Tumor Immunotherapy”. In: *Cancer research* 78.19 (Oct. 2018), pp. 5706–5717. ISSN: 1538-7445. DOI: 10.1158/0008-5472.CAN-18-0253.
- [30] Kimberly J. Edwards et al. “Using CD69 PET Imaging to Monitor Immunotherapy-Induced Immune Activation”. In: *Cancer Immunology Research* 10.9 (Sept. 2022), pp. 1084–1094. ISSN: 2326-6066. DOI: 10.1158/2326-6066.CIR-21-0874.
- [31] Francoise Bachelerie et al. “International Union of Basic and Clinical Pharmacology. LXXXIX. Update on the Extended Family of Chemokine Receptors and Introducing a New Nomenclature for Atypical Chemokine Receptors”. In: *Pharmacological Reviews* 66.1 (Jan. 2014). Ed. by Eliot H. Ohlstein, pp. 1–79. ISSN: 0031-6997. DOI: 10.1124/pr.113.007724.
- [32] Catherine E. Hughes and Robert J.B. Nibbs. *A guide to chemokines and their receptors*. Aug. 2018. DOI: 10.1111/febs.14466.

Bibliography

- [33] Jason W. Griffith, Caroline L. Sokol, and Andrew D. Luster. “Chemokines and Chemokine Receptors: Positioning Cells for Host Defense and Immunity”. In: *Annual Review of Immunology* 32.1 (Mar. 2014), pp. 659–702. ISSN: 0732-0582. DOI: 10.1146/annurev-immunol-032713-120145.
- [34] William G. Glass et al. “Reduced Macrophage Infiltration and Demyelination in Mice Lacking the Chemokine Receptor CCR5 Following Infection with a Neurotropic Coronavirus”. In: *Virology* 288.1 (Sept. 2001), pp. 8–17. ISSN: 00426822. DOI: 10.1006/viro.2001.1050.
- [35] Jong Youl Kim et al. “CCR4 and CCR5 Involvement in Monocyte-Derived Macrophage Migration in Neuroinflammation”. In: *Frontiers in Immunology* 13 (May 2022). ISSN: 1664-3224. DOI: 10.3389/fimmu.2022.876033.
- [36] Andreas K. Buck et al. “Imaging of C-X-C Motif Chemokine Receptor 4 Expression in 690 Patients with Solid or Hematologic Neoplasms using 68Ga-PentixaFor PET”. In: *Journal of Nuclear Medicine* (Mar. 2022), jnumed.121.263693. ISSN: 0161-5505. DOI: 10.2967/jnumed.121.263693.
- [37] Matthias Konrad et al. “[99mTc]Tc-PentixaTec: development, extensive pre-clinical evaluation, and first human experience”. In: *European Journal of Nuclear Medicine and Molecular Imaging* 50.13 (Nov. 2023), p. 3937. ISSN: 16197089. DOI: 10.1007/S00259-023-06395-X.
- [38] Andreas K. Buck et al. “C-X-C Motif Chemokine Receptor 4–Targeted Radioligand Therapy in Patients with Advanced T-Cell Lymphoma”. In: *Journal of Nuclear Medicine* 64.1 (Jan. 2023), pp. 34–39. ISSN: 0161-5505. DOI: 10.2967/JNUMED.122.264207.
- [39] Margret Schottelius, Ken Herrmann, and Constantin Lapa. “In Vivo Targeting of CXCR4—New Horizons”. In: *Cancers* 13.23 (Nov. 2021), p. 5920. ISSN: 2072-6694. DOI: 10.3390/cancers13235920.
- [40] Dangaj D et al. “Cooperation between Constitutive and Inducible Chemokines Enables T Cell Engraftment and Immune Attack in Solid Tumors”. In: *Cancer cell* 35.6 (June 2019), pp. 885–900. ISSN: 1878-3686. DOI: 10.1016/J.CCELL.2019.05.004.

- [41] Melvyn T. Chow et al. “Intratumoral Activity of the CXCR3 Chemokine System Is Required for the Efficacy of Anti-PD-1 Therapy”. In: *Immunity* 50.6 (June 2019), pp. 1498–1512. ISSN: 10747613. DOI: 10.1016/j.immuni.2019.04.010.
- [42] Julien Schmidt et al. “Neoantigen-specific CD8 T cells with high structural avidity preferentially reside in and eliminate tumors”. In: *Nature Communications* 14.1 (June 2023), p. 3188. ISSN: 2041-1723. DOI: 10.1038/s41467-023-38946-z.
- [43] Joanna R. Groom and Andrew D. Luster. *CXCR3 in T cell function*. Mar. 2011. DOI: 10.1016/j.yexcr.2010.12.017.
- [44] Toshiki Iwai et al. “Both T cell priming in lymph node and CXCR3-dependent migration are the key events for predicting the response of atezolizumab”. In: *Scientific Reports 2021* 11.1 (July 2021), pp. 1–15. ISSN: 2045-2322. DOI: 10.1038/s41598-021-93113-y.
- [45] Kelli A. Connolly et al. “Increasing the efficacy of radiotherapy by modulating the CCR2/CCR5 chemokine axes”. In: *Oncotarget* 7.52 (Dec. 2016), pp. 86522–86535. ISSN: 1949-2553. DOI: 10.18632/oncotarget.13287.
- [46] Joanna Kowal, Mara Kornete, and Johanna A Joyce. “Re-education of macrophages as a therapeutic strategy in cancer”. In: *Immunotherapy* 11.8 (June 2019), pp. 677–689. ISSN: 1750-743X. DOI: 10.2217/imt-2018-0156.
- [47] Crescenzo D’Alterio et al. “Targeting CXCR4 potentiates anti-PD-1 efficacy modifying the tumor microenvironment and inhibiting neoplastic PD-1”. In: *Journal of Experimental & Clinical Cancer Research* 38.1 (Dec. 2019), p. 432. ISSN: 1756-9966. DOI: 10.1186/s13046-019-1420-8.
- [48] Aleksandra J. Ozga, Melvyn T. Chow, and Andrew D. Luster. “Chemokines and the immune response to cancer”. In: *Immunity* 54.5 (May 2021), pp. 859–874. ISSN: 1074-7613. DOI: 10.1016/J.IMMUNI.2021.01.012.
- [49] Liu Y et al. “PET imaging of chemokine receptors in vascular injury-accelerated atherosclerosis”. In: *Journal of nuclear medicine : official publication, Society of Nu-*

Bibliography

- clear Medicine* 54.7 (July 2013), pp. 1135–1141. ISSN: 1535-5667. DOI: 10.2967/JNUMED.112.114777. URL: <https://pubmed.ncbi.nlm.nih.gov/23658218/>.
- [50] Denis R. Beckford Vera et al. “Immuno-PET imaging of tumor-infiltrating lymphocytes using zirconium-89 radiolabeled anti-CD3 antibody in immune-competent mice bearing syngeneic tumors”. In: *PLoS ONE* 13.3 (Mar. 2018). ISSN: 19326203. DOI: 10.1371/journal.pone.0193832.
- [51] Benjamin M. Larimer et al. “Quantitative CD3 PET imaging predicts tumor growth response to anti-CTLA-4 therapy”. In: *Journal of Nuclear Medicine* 57.10 (Oct. 2016), pp. 1607–1611. ISSN: 2159662X. DOI: 10.2967/jnumed.116.173930.
- [52] W Evan Secor et al. “Increased Density of Human Immunodeficiency Virus Type 1 Coreceptors CCR5 and CXCR4 on the Surfaces of CD4 T Cells and Monocytes of Patients with *Schistosoma mansoni* Infection”. In: *INFECTION AND IMMUNITY* 71.11 (2003), pp. 6668–6671. DOI: 10.1128/IAI.71.11.6668-6671.2003.
- [53] Maria T. Polianova et al. “Chemokine receptor-5 (CCR5) is a receptor for the HIV entry inhibitor peptide T (DAPTA)”. In: *Antiviral Research* 67.2 (Aug. 2005), pp. 83–92. ISSN: 01663542. DOI: 10.1016/j.antiviral.2005.03.007.
- [54] Marta Arimont et al. *Structural Analysis of Chemokine Receptor-Ligand Interactions*. June 2017. DOI: 10.1021/acs.jmedchem.6b01309.
- [55] Patrick Dorr et al. “Maraviroc (UK-427,857), a potent, orally bioavailable, and selective small-molecule inhibitor of chemokine receptor CCR5 with broad-spectrum anti-human immunodeficiency virus type 1 activity”. In: *Antimicrobial Agents and Chemotherapy* 49.11 (Nov. 2005), pp. 4721–4732. ISSN: 00664804. DOI: 10.1128/AAC.49.11.4721-4732.2005.
- [56] M R Ruff et al. “Pharmacokinetics of peptide T in patients with acquired immunodeficiency syndrome (AIDS).” In: *Progress in neuro-psychopharmacology & biological psychiatry* 15.6 (1991), pp. 791–801. ISSN: 0278-5846. DOI: 10.1016/0278-5846(91)90008-o.

- [57] Michael Ruff. *US20140322252A1 - Peptides for Treating Alzheimers's Disease and Related Conditions - Google Patents*. URL: <https://patents.google.com/patent/US20140322252>.
- [58] Satyanarayana S.V. Padi et al. "Attenuation of rodent neuropathic pain by an orally active peptide, RAP-103, which potently blocks CCR2- and CCR5-mediated monocyte chemotaxis and inflammation". In: *Pain* 153.1 (Jan. 2012), pp. 95–106. ISSN: 03043959. DOI: 10.1016/j.pain.2011.09.022.
- [59] Mami Noda et al. "Neuropathic pain inhibitor, RAP-103, is a potent inhibitor of microglial CCL1/CCR8". In: *Neurochemistry International* 119 (Oct. 2018), pp. 184–189. ISSN: 01970186. DOI: 10.1016/j.neuint.2017.12.005.
- [60] Lihui Wei et al. "Development of an inflammation imaging tracer, ¹¹¹In-DOTA-DAPTA, targeting chemokine receptor CCR5 and preliminary evaluation in an ApoE^{-/-} atherosclerosis mouse model". In: *Journal of Nuclear Cardiology* 26.4 (Aug. 2019), pp. 1169–1178. ISSN: 15326551. DOI: 10.1007/s12350-018-1203-1.
- [61] Yongjian Liu et al. "PET-based imaging of chemokine receptor 2 in experimental and Disease-related lung inflammation". In: *Radiology* 283.3 (June 2017), pp. 758–768. ISSN: 15271315. DOI: 10.1148/radiol.2016161409.
- [62] Gyu Seong Heo et al. "Targeted PET Imaging of Chemokine Receptor 2+ Monocytes and Macrophages in the Injured Heart". In: *Journal of Nuclear Medicine* (May 2020), jnumed.120.244673. ISSN: 0161-5505. DOI: 10.2967/jnumed.120.244673.
- [63] Sebastian Martin et al. "Proof-of-Concept Study of the NOTI Chelating Platform: Preclinical Evaluation of ⁶⁴Cu-Labeled Mono- and Trimeric c(RGDfK) Conjugates". In: *Molecular Imaging and Biology* 23.1 (Feb. 2021), pp. 95–108. ISSN: 1536-1632. DOI: 10.1007/s11307-020-01530-8.
- [64] Hans Raskov et al. "Cytotoxic CD8+ T cells in cancer and cancer immunotherapy". In: *British Journal of Cancer* 2020 124:2 124.2 (Sept. 2020), pp. 359–367. ISSN: 1532-1827. DOI: 10.1038/s41416-020-01048-4.

Bibliography

- [65] Jarem Edwards et al. “CD103+ Tumor-Resident CD8+ T Cells Are Associated with Improved Survival in Immunotherapy-Naïve Melanoma Patients and Expand Significantly During Anti-PD-1 Treatment”. In: *Clinical Cancer Research* 24.13 (July 2018), pp. 3036–3045. ISSN: 1078-0432. DOI: 10.1158/1078-0432.CCR-17-2257.
- [66] Israt S. Alam et al. “Imaging activated T cells predicts response to cancer vaccines”. In: *Journal of Clinical Investigation* 128.6 (June 2018), pp. 2569–2580. ISSN: 15588238. DOI: 10.1172/JCI98509.
- [67] Zunyu Xiao et al. “ICOS Is an Indicator of T-cell-Mediated Response to Cancer Immunotherapy”. In: *Cancer Research* 80.14 (July 2020), pp. 3023–3032. ISSN: 0008-5472. DOI: 10.1158/0008-5472.CAN-19-3265.
- [68] S. V. Hartimath et al. “Noninvasive monitoring of cancer therapy induced activated T cells using [18F]FB-IL-2 PET imaging”. In: *OncoImmunology* 6.1 (Jan. 2017), e1248014. ISSN: 2162-402X. DOI: 10.1080/2162402X.2016.1248014.
- [69] Benjamin M. Larimer et al. “Granzyme B PET Imaging as a Predictive Biomarker of Immunotherapy Response”. In: *Cancer Research* 77.9 (May 2017), pp. 2318–2327. ISSN: 0008-5472. DOI: 10.1158/0008-5472.CAN-16-3346.
- [70] Jelena Levi et al. “Imaging of Activated T Cells as an Early Predictor of Immune Response to Anti-PD-1 Therapy”. In: *Cancer Research* 79.13 (July 2019), pp. 3455–3465. ISSN: 0008-5472. DOI: 10.1158/0008-5472.CAN-19-0267.
- [71] Jeremy Gungabeesoon et al. “A neutrophil response linked to tumor control in immunotherapy”. In: *Cell* 186.7 (Mar. 2023), pp. 1448–1464. ISSN: 00928674. DOI: 10.1016/j.cell.2023.02.032.
- [72] M Loetscher et al. “Chemokine receptor specific for IP10 and mig: structure, function, and expression in activated T-lymphocytes.” In: *Journal of Experimental Medicine* 184.3 (Sept. 1996), pp. 963–969. ISSN: 0022-1007. DOI: 10.1084/jem.184.3.963.

- [73] Nathan Karin. “CXCR3 Ligands in Cancer and Autoimmunity, Chemoattraction of Effector T Cells, and Beyond”. In: *Frontiers in Immunology* 11 (May 2020). DOI: 10.3389/FIMMU.2020.00976.
- [74] Mikucki ME et al. “Non-redundant requirement for CXCR3 signalling during tumoricidal T-cell trafficking across tumour vascular checkpoints”. In: *Nature communications* 6 (June 2015). ISSN: 2041-1723. DOI: 10.1038/NCOMMS8458.
- [75] Kenji Chamoto et al. “Mitochondrial activation chemicals synergize with surface receptor PD-1 blockade for T cell-dependent antitumor activity”. In: *Proceedings of the National Academy of Sciences* 114.5 (Jan. 2017), E761–E770. ISSN: 0027-8424. DOI: 10.1073/PNAS.1620433114.
- [76] Andrew D. Luster and Philip Leder. “IP-10, a -C-X-C- chemokine, elicits a potent thymus-dependent antitumor response in vivo”. In: *Journal of Experimental Medicine* 178.3 (Sept. 1993), pp. 1057–1065. DOI: 10.1084/JEM.178.3.1057.
- [77] Hukui Sun et al. “Monitoring Early-Stage Acute Rejection by Imaging CXCR3-Positive Cell Infiltration: Evaluation of ¹²⁵Iodine-Labeled CXCL10.” In: *Experimental and clinical transplantation : official journal of the Middle East Society for Organ Transplantation* 18.3 (June 2020), pp. 368–374. ISSN: 2146-8427. DOI: 10.6002/ect.2019.0346.
- [78] Santosh R. Alluri et al. “Synthesis and preclinical evaluation of a novel fluorine-18 labeled small-molecule PET radiotracer for imaging of CXCR3 receptor in mouse models of atherosclerosis”. In: *EJNMMI Research* 13.1 (July 2023), p. 67. ISSN: 2191-219X. DOI: 10.1186/s13550-023-01017-x.
- [79] Viktoriia Postupalenko et al. “Template directed synthesis of antibody Fc conjugates with concomitant ligand release”. In: *Chemical Science* 13.14 (2022), pp. 3965–3976. ISSN: 2041-6520. DOI: 10.1039/D1SC06182H.
- [80] Molly A. Taylor et al. “Longitudinal immune characterization of syngeneic tumor models to enable model selection for immune oncology drug discovery”. In: *Journal for ImmunoTherapy of Cancer* 7.1 (Nov. 2019). ISSN: 20511426. DOI: 10.1186/s40425-019-0794-7.

Bibliography

- [81] Mark J. Selby et al. “Preclinical Development of Ipilimumab and Nivolumab Combination Immunotherapy: Mouse Tumor Models, In Vitro Functional Studies, and Cynomolgus Macaque Toxicology”. In: *PLOS ONE* 11.9 (Sept. 2016), e0161779. ISSN: 1932-6203. DOI: 10.1371/JOURNAL.PONE.0161779.
- [82] Chung-Her Jenh et al. “A selective and potent CXCR3 antagonist SCH 546738 attenuates the development of autoimmune diseases and delays graft rejection”. In: *BMC Immunology* 13 (Jan. 2012), p. 2. DOI: 10.1186/10.1186/1471-2172-13-2.
- [83] Rosanna Mezzapelle et al. “CXCR4/CXCL12 Activities in the Tumor Microenvironment and Implications for Tumor Immunotherapy”. In: *Cancers* 14.9 (May 2022), p. 2314. ISSN: 2072-6694. DOI: 10.3390/cancers14092314.
- [84] Christine Feig et al. “Targeting CXCL12 from FAP-expressing carcinoma-associated fibroblasts synergizes with anti-PD-L1 immunotherapy in pancreatic cancer”. In: *Proceedings of the National Academy of Sciences* 110.50 (Dec. 2013), pp. 20212–20217. ISSN: 0027-8424. DOI: 10.1073/pnas.1320318110.
- [85] Luigi Portella, Anna Maria Bello, and Stefania Scala. “CXCL12 Signaling in the Tumor Microenvironment”. In: 2021, pp. 51–70. DOI: 10.1007/978-3-030-62658-7{_}5.
- [86] Gary D Luker et al. “At the Bench: Pre-clinical evidence for multiple functions of CXCR4 in cancer”. In: *Journal of Leukocyte Biology* 109.5 (May 2021), pp. 969–989. ISSN: 0741-5400. DOI: 10.1002/JLB.2BT1018-715RR.
- [87] Hongli Zhao et al. “CXCR4 over-expression and survival in cancer: A system review and meta-analysis”. In: *Oncotarget* 6.7 (Mar. 2015), pp. 5022–5040. ISSN: 1949-2553. DOI: 10.18632/oncotarget.3217.
- [88] Li Bao et al. “CXCR4 is a good survival prognostic indicator in multiple myeloma patients”. In: *Leukemia Research* 37.9 (Sept. 2013), pp. 1083–1088. ISSN: 01452126. DOI: 10.1016/j.leukres.2013.06.002.

- [89] Jeong Yeal Ahn et al. "The Prognostic Value of CXCR4 in Acute Myeloid Leukemia". In: *Applied Immunohistochemistry & Molecular Morphology* 21.1 (Jan. 2013), pp. 79–84. ISSN: 1541-2016. DOI: 10.1097/PAI.0b013e3182606f4d.
- [90] Ravi Salgia et al. "A randomized phase II study of LY2510924 and carboplatin/etoposide versus carboplatin/etoposide in extensive-disease small cell lung cancer". In: *Lung Cancer* 105 (Mar. 2017), pp. 7–13. ISSN: 01695002. DOI: 10.1016/j.lungcan.2016.12.020.
- [91] Andreas K. Buck et al. "CXCR4-targeted theranostics in oncology". In: *European Journal of Nuclear Medicine and Molecular Imaging* 49.12 (Oct. 2022), pp. 4133–4144. ISSN: 1619-7070. DOI: 10.1007/s00259-022-05849-y.
- [92] Malte Kircher et al. "CXCR4-directed theranostics in oncology and inflammation". In: *Annals of Nuclear Medicine* 32.8 (Oct. 2018), pp. 503–511. ISSN: 0914-7187. DOI: 10.1007/s12149-018-1290-8.
- [93] Constantin Lapa et al. "Potential influence of concomitant chemotherapy on CXCR4 expression in receptor directed endoradiotherapy". In: *British Journal of Haematology* 184.3 (Feb. 2019), pp. 440–443. ISSN: 0007-1048. DOI: 10.1111/bjh.15096.
- [94] Seong-Woo Kim et al. "Dexamethasone and hypoxia upregulate CXCR4 expression in myeloma cells". In: *Leukemia & Lymphoma* 50.7 (Jan. 2009), pp. 1163–1173. ISSN: 1042-8194. DOI: 10.1080/10428190902893801.
- [95] Grzegorz Mazur et al. "Decreased Expression of CXCR4 Chemokine Receptor in Bone Marrow after Chemotherapy in Patients with Non-Hodgkin Lymphomas Is a Good Prognostic Factor". In: *PLoS ONE* 9.5 (May 2014), e98194. ISSN: 1932-6203. DOI: 10.1371/journal.pone.0098194.
- [96] Michael Pfreundschuh et al. "CHOP-like chemotherapy plus rituximab versus CHOP-like chemotherapy alone in young patients with good-prognosis diffuse large-B-cell lymphoma: a randomised controlled trial by the MabThera International Trial (MInT) Group". In: *The Lancet Oncology* 7.5 (May 2006), pp. 379–391. ISSN: 14702045. DOI: 10.1016/S1470-2045(06)70664-7.

Bibliography

- [97] Junxia Hu et al. "Combination of Decitabine and a Modified Regimen of Cisplatin, Cytarabine and Dexamethasone: A Potential Salvage Regimen for Relapsed or Refractory Diffuse Large B-Cell Lymphoma After Second-Line Treatment Failure". In: *Frontiers in Oncology* 11 (June 2021). ISSN: 2234-943X. DOI: 10.3389/fonc.2021.687374.
- [98] María Nella Gai et al. "Determination of Prednisolone and Prednisone in Plasma, Whole Blood, Urine, and Bound-to-Plasma Proteins by High-Performance Liquid Chromatography". In: *Journal of Chromatographic Science* 43.4 (Apr. 2005), pp. 201–206. ISSN: 0021-9665. DOI: 10.1093/CHROMSCI/43.4.201.
- [99] Elena V. Mishina and Tapash K. Gosh. *Center for Drug Evaluation and Research Application Number: 22-512 Clinical Pharmacology and Biopharmaceutics Review*. Tech. rep. 2010.
- [100] Andreas Poschenrieder et al. "The influence of different metal-chelate conjugates of pentixafor on the CXCR4 affinity". In: *EJNMMI Research* 6.1 (Dec. 2016), p. 36. ISSN: 2191-219X. DOI: 10.1186/s13550-016-0193-8.
- [101] Theresa Osl et al. "A new class of PentixaFor- and PentixaTher-based theranostic agents with enhanced CXCR4-targeting efficiency". In: *Theranostics* 10.18 (2020), pp. 8264–8280. ISSN: 1838-7640. DOI: 10.7150/thno.45537.
- [102] Oliver Demmer et al. "PET Imaging of CXCR4 Receptors in Cancer by a New Optimized Ligand". In: *ChemMedChem* 6.10 (Oct. 2011), pp. 1789–1791. ISSN: 1860-7179. DOI: 10.1002/cmdc.201100320.
- [103] Matthias Lorenz Konrad. "Cyclic pentapeptide-based CXCR4 ligands for various applications within cancerous malignancies". PhD thesis. 2021.
- [104] Margret Schottelius, Markus Schwaiger, and Hans Jürgen Wester. "Rapid and high-yield solution-phase synthesis of DOTA-Tyr3-octreotide and DOTA-Tyr3-octreotate using unprotected DOTA". In: *Tetrahedron Letters* 44.11 (Mar. 2003), pp. 2393–2396. ISSN: 00404039. DOI: 10.1016/S0040-4039(03)00221-1.

- [105] Matthias Glaser and Erik Årstad. “Click labeling’ with 2-[18F]fluoroethylazide for positron emission tomography”. In: *Bioconjugate Chemistry* 18.3 (May 2007), pp. 989–993. ISSN: 10431802. DOI: 10.1021/bc060301j.
- [106] Dong Zhou et al. “Facile purification and click labeling with 2-[18F]fluoroethyl azide using solid phase extraction cartridges”. In: *Tetrahedron Letters* 56.7 (Feb. 2015), pp. 952–954. ISSN: 18733581. DOI: 10.1016/j.tetlet.2014.10.126.
- [107] Margret Schottelius et al. “Twins in spirit - episode I: comparative preclinical evaluation of [68Ga]DOTATATE and [68Ga]HA-DOTATATE”. In: *EJNMMI Research* 5.1 (Dec. 2015), p. 22. ISSN: 2191-219X. DOI: 10.1186/s13550-015-0099-x.
- [108] Weijun Wei et al. *Noninvasive PET Imaging of T cells*. May 2018. DOI: 10.1016/j.trecan.2018.03.009. URL: [http://www.cell.com/article/S2405803318300803/fulltext%20http://www.cell.com/article/S2405803318300803/abstract%20https://www.cell.com/trends/cancer/abstract/S2405-8033\(18\)30080-3](http://www.cell.com/article/S2405803318300803/fulltext%20http://www.cell.com/article/S2405803318300803/abstract%20https://www.cell.com/trends/cancer/abstract/S2405-8033(18)30080-3).
- [109] Johannes Notni, Karolin Pohle, and Hans-Jürgen Wester. “Be spoilt for choice with radiolabelled RGD peptides: Preclinical evaluation of 68Ga-TRAP(RGD)3”. In: *Nuclear Medicine and Biology* 40.1 (Jan. 2013), pp. 33–41. ISSN: 09698051. DOI: 10.1016/j.nucmedbio.2012.08.006.
- [110] Zsolt Baranyai et al. “A shortcut to high-affinity Ga-68 and Cu-64 radiopharmaceuticals: one-pot click chemistry trimerisation on the TRAP platform”. In: *Dalton Transactions* 44.24 (June 2015), pp. 11137–11146. ISSN: 1477-9234. DOI: 10.1039/C5DT00576K.
- [111] Alexander Schmidtke et al. “Gallium Complexation, Stability, and Bioconjugation of 1,4,7-Triazacyclononane Derived Chelators with Azaheterocyclic Arms”. In: *Inorganic Chemistry* 56.15 (Aug. 2017), pp. 9097–9110. ISSN: 0020-1669. DOI: 10.1021/acs.inorgchem.7b01129.
- [112] Johannes Notni, Karolin Pohle, and Hans-Jürgen Wester. “Comparative gallium-68 labeling of TRAP-, NOTA-, and DOTA-peptides: practical consequences for the future of gallium-68-PET”. In: *EJNMMI Research* 2.1 (June 2012), p. 28. ISSN: 2191-219X. DOI: 10.1186/2191-219X-2-28.

Bibliography

- [113] Neil Gerard Quigley et al. "PET/CT imaging of head-and-neck and pancreatic cancer in humans by targeting the "Cancer Integrin" $\alpha v\beta 6$ with Ga-68-Trivehexin". In: *European Journal of Nuclear Medicine and Molecular Imaging* (Sept. 2021), pp. 1–12. ISSN: 16197089. DOI: 10.1007/S00259-021-05559-X.
- [114] Graham Simmons et al. "Potent inhibition of HIV-1 infectivity in macrophages and lymphocytes by a novel CCR5 antagonist". In: *Science* 276.5310 (Apr. 1997), pp. 276–279. ISSN: 00368075. DOI: 10.1126/science.276.5310.276.
- [115] Pia C Jensen et al. "Positive versus negative modulation of different endogenous chemokines for CC-chemokine receptor 1 by small molecule agonists through allosteric versus orthosteric binding". In: *Journal of Biological Chemistry* 283.34 (2008), pp. 23121–23128. ISSN: 00219258. DOI: 10.1074/jbc.M803458200.
- [116] Cédric Blanpain et al. "CCR5 Binds Multiple CC-Chemokines: MCP-3 Acts as a Natural Antagonist". In: *Blood* 94.6 (Sept. 1999), pp. 1899–1905. ISSN: 0006-4971. DOI: 10.1182/blood.v94.6.1899.
- [117] Yolande Chvatchko et al. "Inhibition of Airway Inflammation by Amino-Terminally Modified RANTES/CC Chemokine Ligand 5 Analogues Is Not Mediated through CCR3". In: *The Journal of Immunology* 171.10 (Nov. 2003), pp. 5498–5506. ISSN: 0022-1767. DOI: 10.4049/jimmunol.171.10.5498.
- [118] Maria T. Polianova et al. "Chemokine receptor-5 (CCR5) is a receptor for the HIV entry inhibitor peptide T (DAPTA)". In: *Antiviral Research* 67.2 (Aug. 2005), pp. 83–92. ISSN: 01663542. DOI: 10.1016/j.antiviral.2005.03.007.
- [119] Jason G. Cyster. "Chemokines and Cell Migration in Secondary Lymphoid Organs". In: *Science* 286.5447 (Dec. 1999), pp. 2098–2102. ISSN: 0036-8075. DOI: 10.1126/science.286.5447.2098.
- [120] Olga Schulz et al. "Chemokines and Chemokine Receptors in Lymphoid Tissue Dynamics". In: *Annual Review of Immunology* 34.1 (May 2016), pp. 203–242. ISSN: 0732-0582. DOI: 10.1146/annurev-immunol-041015-055649.

- [121] Cyril Fersing et al. "A Comprehensive Review of Non-Covalent Radiofluorination Approaches Using Aluminum [¹⁸F]fluoride: Will [¹⁸F]AlF Replace ⁶⁸Ga for Metal Chelate Labeling?" In: *Molecules* 24.16 (Aug. 2019), p. 2866. ISSN: 1420-3049. DOI: 10.3390/molecules24162866.
- [122] Maria José Costa et al. "A mouse model for evaluation of efficacy and concomitant toxicity of anti-human CXCR4 therapeutics". In: *PloS one* 13.3 (Mar. 2018). ISSN: 1932-6203. DOI: 10.1371/JOURNAL.PONE.0194688. URL: <https://pubmed.ncbi.nlm.nih.gov/29554149/>.
- [123] Margret Schottelius et al. "Validation of [¹²⁵I]CPCR4.3 as an investigative tool for the sensitive and specific detection of hCXCR4 and mCXCR4 expression in vitro and in vivo". In: *EJNMMI Research* 9.1 (Dec. 2019), p. 75. ISSN: 2191-219X. DOI: 10.1186/s13550-019-0545-2.
- [124] Xinyu Wang et al. "Druggability of Targets for Diagnostic Radiopharmaceuticals". In: *ACS pharmacology & translational science* 6.8 (Aug. 2023), pp. 1107–1119. ISSN: 2575-9108. DOI: 10.1021/ACSPTSCI.3C00081.
- [125] Ute Hennrich et al. "Synthesis and in vitro evaluation of ⁶⁸Ga-DOTA-4-FBn-TN14003, a novel tracer for the imaging of CXCR4 expression". In: *Bioorganic & Medicinal Chemistry* 20.4 (Feb. 2012), pp. 1502–1510. ISSN: 09680896. DOI: 10.1016/j.bmc.2011.12.052.
- [126] Sabine Maurer et al. "Side Effects of CXC-Chemokine Receptor 4-Directed Endoradiotherapy with Pentixather Before Hematopoietic Stem Cell Transplantation". In: *Journal of Nuclear Medicine* 60.10 (Oct. 2019), p. 1399. ISSN: 2159662X. DOI: 10.2967/JNUMED.118.223420.
- [127] Ismaheel O Lawal et al. "[⁶⁸Ga]Ga-Pentixafor for PET Imaging of Vascular Expression of CXCR-4 as a Marker of Arterial Inflammation in HIV-Infected Patients: A Comparison with ¹⁸F[FDG] PET Imaging". In: 10 (2020). DOI: 10.3390/biom10121629.


Bibliography

- [128] Malte Kircher et al. “Imaging Inflammation in Atherosclerosis with CXCR4-Directed ⁶⁸Ga-Pentixafor PET/CT: Correlation with ¹⁸F-FDG PET/CT”. In: *Journal of nuclear medicine : official publication, Society of Nuclear Medicine* 61.5 (May 2020), pp. 751–756. ISSN: 1535-5667. DOI: 10.2967/JNUMED.119.234484.
- [129] Daniel S. Chen and Ira Mellman. *Elements of cancer immunity and the cancer-immune set point*. Jan. 2017. DOI: 10.1038/nature21349. URL: <https://pubmed.ncbi.nlm.nih.gov/28102259/>.
- [130] Jong W. Yu et al. “Tumor-immune profiling of murine syngeneic tumor models as a framework to guide mechanistic studies and predict therapy response in distinct tumor microenvironments”. In: *PLOS ONE* 13.11 (Nov. 2018), e0206223. ISSN: 1932-6203. DOI: 10.1371/journal.pone.0206223.
- [131] Elly L van der Veen et al. “⁸⁹Zr-pembrolizumab biodistribution is influenced by PD-1-mediated uptake in lymphoid organs”. In: *Journal for ImmunoTherapy of Cancer* 8.2 (Oct. 2020), e000938. ISSN: 2051-1426. DOI: 10.1136/jitc-2020-000938.
- [132] Delphine Vivier et al. “The Impact of FcγRI Binding on Immuno-PET”. In: *Journal of Nuclear Medicine* 60.8 (Aug. 2019), pp. 1174–1182. ISSN: 0161-5505. DOI: 10.2967/jnumed.118.223636.
- [133] Michael Hettich et al. “High-Resolution PET Imaging with Therapeutic Antibody-based PD-1/PD-L1 Checkpoint Tracers”. In: *Theranostics* 6.10 (2016), p. 1629. ISSN: 18387640. DOI: 10.7150/THNO.15253.
- [134] Mohammad O. Sako and Benjamin M. Larimer. “Imaging of Activated T Cells”. In: *Journal of Nuclear Medicine* 64.1 (Jan. 2023), pp. 30–33. ISSN: 0161-5505. DOI: 10.2967/jnumed.122.264097.
- [135] Lingling Zhu et al. “Combination of STING agonist and CXCR3 antagonist disrupts immune tolerance to overcome anti-PD-L1 resistance in lung adenocarcinoma under oxidative stress”. In: *Gene* 851 (Jan. 2023), p. 146962. ISSN: 03781119. DOI: 10.1016/j.gene.2022.146962.


- [136] Georg Martin Haag et al. “Combined PD-1 inhibition (Pembrolizumab) and CCR5 inhibition (Maraviroc) for the treatment of refractory microsatellite stable (MSS) metastatic colorectal cancer (mCRC): First results of the PICCASSO phase I trial.” In: *Journal of Clinical Oncology* 38.15_suppl (May 2020), pp. 3010–3010. ISSN: 0732-183X. DOI: 10.1200/JCO.2020.38.15{_}suppl.301.
- [137] Megan M. Tu et al. “Inhibition of the CCL2 receptor, CCR2, enhances tumor response to immune checkpoint therapy”. In: *Communications Biology* 3.1 (Nov. 2020), p. 720. ISSN: 2399-3642. DOI: 10.1038/s42003-020-01441-y.
- [138] Helena Van Damme et al. “Therapeutic depletion of CCR8 + tumor-infiltrating regulatory T cells elicits antitumor immunity and synergizes with anti-PD-1 therapy”. In: *Journal for ImmunoTherapy of Cancer* 9.2 (Feb. 2021). ISSN: 20511426. DOI: 10.1136/JITC-2020-001749.

Curriculum Vitae

ADDRESS

 Rue du Bugnon 25A,
1005 Lausanne

PHONE


 +41 (0) 21 545 11 22


EMAIL


 sebastian.martin@chuv.ch

LINKS

 www.chuv.ch/trs

 [LinkedIn](#)

 [ORCID](#)

 [Researchgate](#)

LANGUAGES

German (native) - English (C1) -
French (C1)

Soft-skills

teamplayer - time management -
curiosity - endurance

INTERESTS AND HOBBIES

Sailing - skiing - triathlon -
medicine - nature - biology

Curriculum Vitae

Sebastian Martin

PhD candidate in Translational Radiopharmaceutical
Sciences

Oct 2019 - expected June 2024
PhD candidate at CHUV, Department of Nuclear
Medicine and Molecular Imaging.

Thesis title: "Exploiting chemokines and their receptors for non-
invasive imaging in cancer and immunology."

Subjects: Bioconjugation of antibody-drug-conjugates (ADCs),
peptide synthesis, preclinical radiotracer development,
immuno-oncology.

EDUCATION

2015-2018 Master of Pharmaceutical Sciences, Albert-Ludwigs
University of Freiburg, Germany

[Certificate](#) - [Alumni Award](#) - [DPhG Award](#)

2011-2015 Bachelor of Pharmaceutical Sciences, Albert-Ludwigs
University of Freiburg, Germany

[Certificate](#)

EXPERIENCE

Mar 2019 - Aug 2019
Internship at [Lonza Bioconjugates](#), CH (Valais).

GMP-conform quality control of ADCs. Techniques: HPLC, drug-
to-antibody ratio via UV spectroscopy, Empower.

[Lean six sigma certificate](#) - [Phenomenex training](#)

Nov 2017 - Jun 2018
Master thesis at the University Hospital Freiburg,
Department of Nuclear Medicine.

Preclinical development of trimeric triazole-based inhibitors for
theranostic applications. Techniques: Organic synthesis,
radiolabeling, in vitro binding studies, in vivo imaging.

[Publication](#) - [Reference \(Letter of Recommendation\)](#)

Mar 2017 - Jul 2017
Erasmus Plus internship at the Linköping University
Hospital (Sweden), Department of Nuclear Medicine.

Production and quality control of FDG (2-Deoxy-2-[¹⁸F]fluoro-
D-glucose). Techniques: GC, HPLC, cyclotron based
radiolabeling.

[PET-OC certificate](#) - [GC/HPLC certificate](#)

List of publications

Martin, Sebastian, et al. (2024), "Validation of a size exclusion method for concomitant purification and formulation of peptide radiopharmaceuticals." EJNMMI Radiopharmacy and Chemistry.

Martin, S et al. (2023). 'Influence of corticosteroid treatment on CXCR4 expression in DLBCL'. EJNMMI research.

Martin, S et al. (2021), 'Identification, Characterization, and Suppression of Side Products Formed during the Synthesis of [177Lu]Lu-PSMA-617', Journal of Medicinal Chemistry.

Martin, S. et al. (2020) 'Proof-of-Concept Study of the NOTI Chelating Platform: Preclinical Evaluation of 64Cu-Labeled Mono- and Trimeric c(RGDfK) Conjugates', EJNMMI Molecular Imaging and Biology.

Talks

International Symposium on Radiopharmaceutical Sciences (ISRS), Nantes, May 2022, "Development and preclinical evaluation of PSMA-targeting trimers based on the NOTI chelating platform."